The non-mass-dependent isotopic composition of ozone and its photochemical transfer to stratospheric CO_2: Unexpected variations in stratospheric CO_2 and the unusual role of collisional quenching efficiencies in photochemistry experiments and kinetics modeling

By

Aaron Andrew Wiegel

A dissertation submitted in partial satisfaction of the

requirements for the degree of

Doctor of Philosophy

in

Chemistry

in the

Graduate Division

of the

University of California, Berkeley

Committee in charge:

Professor Kristie A. Boering, Chair

Professor Ronald C. Cohen

Professor Ronald Amundson

Fall 2013

The non-mass-dependent isotopic composition of ozone and its photochemical transfer to stratospheric CO_2: Unexpected variations in stratospheric CO_2 and the unusual role of collisional quenching efficiencies in photochemistry experiments and kinetics modeling

Aaron Andrew Wiegel

Abstract

The non-mass-dependent isotopic composition of ozone and its photochemical transfer to stratospheric CO_2: Unexpected variations in stratospheric CO_2 and the unusual role of collisional quenching efficiencies in photochemistry experiments and kinetics modeling

by

Aaron Andrew Wiegel

Doctor of Philosophy in Chemistry

University of California, Berkeley

Professor Kristie A. Boering, Chair

Atypically large and non-mass-dependent kinetic isotope effects (KIEs) in the three-body ozone formation reaction, $O(^3P) + O_2 \rightarrow O_3^* + M \rightarrow O_3 + M^*$, lead to a non-mass-dependent oxygen isotopic composition for O_3 observed in both the laboratory and the atmosphere. Theoretical work has suggested that a dynamically-driven, quantum symmetry isotope effect in the lifetime of the excited ozone complex O_3^* or its collisional stabilization is responsible, although the underlying chemical physics has remained mysterious. Stratospheric CO_2 also has a non-mass-dependent oxygen isotopic composition that is thought to be transferred from ozone by photolysis to form $O(^1D)$ followed by the $O(^1D) + CO_2$ isotope exchange reaction. However, the non-mass-dependent isotopic compositions of CO_2 measured either in UV photochemistry experiments or in stratospheric air samples could not easily be explained by isotope effects in ozone formation, leading some to claim that additional anomalous isotope effects must exist in ozone photolysis or in the $O(^1D) + CO_2$ isotope exchange reaction. In the research results presented here, I detail several significant advances in the understanding of the non-mass-dependent isotopic composition of ozone and its transfer to stratospheric CO_2. I made these advances through new measurements and kinetics modeling of the isotopic composition of O_3 and CO_2 in photochemistry experiments in which mixtures of O_2, CO_2, and other bath gases were irradiated with UV light from a mercury lamp as well as comparisons of these results with the latitude, altitude, and seasonal dependence of the isotopic composition of stratospheric CO_2.

For application to the non-mass-dependent isotopic composition of stratospheric CO_2, I show using a kinetics model that the non-mass-dependent isotope effects in ozone formation alone can quantitatively account for the non-mass-dependent isotopic composition of CO_2 in laboratory measurements of UV-irradiated mixtures of O_2 and CO_2 at atmospheric mixing ratios. I then used the kinetics model to provide a conceptual framework for understanding the significant differences in the non-mass-dependent isotopic composition of CO_2 between the laboratory experiments and the stratosphere and between different regions of the stratosphere that I discovered in the atmospheric measurements. Based on model sensitivities to the temperature dependence of the ozone KIEs and mass-dependent isotope effects in ozone photolysis, differences in temperature and in the relative rate of ozone photolysis are found to be the likely sources of the differences in the non-mass-dependent isotopic composition of CO_2 between the laboratory and the stratosphere and between different regions of the stratosphere.

Having accounted for the non-mass-dependent isotopic composition of CO_2 at an atmospheric O_2/CO_2 mixing ratio, I performed additional laboratory measurements of the non-mass-dependent isotopic composition of CO_2 as a function of the O_2/CO_2 mixing ratio to explore the dramatic decrease in the non-mass-dependent ^{17}O and ^{18}O enrichments in CO_2 as the O_2/CO_2 mixing ratio decreases found in previous experiments. Kinetics modeling shows that expected changes in the non-mass-dependent KIEs in ozone formation as O_2/CO_2 decreases cannot explain the O_2/CO_2 dependence of the non-mass-dependent enrichments in CO_2, so a number of different potential chemical mechanisms with non-mass-dependent isotope effects were tested using the model. Of the mechanisms tested, only inclusion of non-thermal rate coefficients for the reactions of $^{16}O(^1D)$, $^{17}O(^1D)$, and $^{18}O(^1D)$ with O_2, CO_2, and O_3 led to any significant decrease in the non-mass-dependent isotopic composition of CO_2 as the O_2/CO_2 mixing ratio is decreased in the model. These non-thermal rate coefficients were derived from non-thermal kinetic energy distributions for $^{16}O(^1D)$, $^{17}O(^1D)$, and $^{18}O(^1D)$ that were calculated using the hard sphere approximation for collisional energy transfer between $O(^1D)$ and O_2 and between $O(^1D)$ and CO_2 and the initial energy distributions from O_3 photolysis. While the inclusion of the non-thermal rate coefficients in the model produced an O_2/CO_2 mixing ratio dependence that is still approximately 5 times smaller than the experimentally observed O_2/CO_2 mixing ratio dependence (i.e. -5‰ instead of -50‰ from high to low O_2/CO_2), that the non-thermal reactions involving $^{16}O(^1D)$, $^{17}O(^1D)$, and $^{18}O(^1D)$ could produce non-mass-dependent isotopic compositions even though the corresponding thermal reactions are mass-dependent is novel and, to our knowledge, has not been explored thoroughly in any previous work.

Because of the role that collisional energy plays in the isotope exchange between $O(^1D)$ and CO_2, I also conducted measurements of the isotopic composition of O_3 formed in different bath gases, M, to test how the efficiency of collisional energy transfer between O_3* and M in ozone formation affects the non-mass-dependent isotopic composition of the resulting O_3. New measurements and kinetics modeling of the isotopic composition of O_3 formed in an air-like mixture of O_2/N_2 show statistically significant differences between the non-mass-dependent isotopic composition of O_3 formed in pure O_2 and in an air-like mixture of O_2 and N_2. Using a kinetics model, I explore possible origins for these differences in in these experiments and in experiments involving O_3 photolysis or O_3 formation in SF_6. The combined results comparing the model results with the measurements suggest that mass-dependent KIEs in the $O_2(^1\Sigma) + O_3$ reaction can likely be ruled out and that the radical complex mechanism for O_3 formation (as opposed to the energy transfer mechanism) may indeed play a role in generating the differences in the isotopic composition of O_3 formed in different bath gases.

For James Henry

Table of Contents

List of Figures

List of Tables

Acknoledgements

I am very grateful to many different people who have helped make the research in this dissertation possible. Of course, I would like to thank my adviser, Kristie Boering, for taking a chance on me as a student and for helping me through my research and this process. I also would like to thank my committee members, Ron Cohen and Ron Amundson, for reading this work, especially given the unusual circumstances near my graduation. I am also grateful to many other collaborators on my research, including Eliot Atlas and Sue Schauffler. I am also very grateful for the time I spent in Utrecht at IMAU working with Thomas Röckmann and Christof Janssen along with many helpful discussions regarding my research.

All of the Boering group members I worked with over the years have also made graduate school easier and more fun, including Emily, Lauren, John, Amadu, and Mica. All of my coworkers at IMAU, including Dorota, Supun, Christiana, Carlos, and many others also made my short stay there both scientifically and personally valuable. Some of my initial mentors at the Boering Group such as Amanda, Annalise, Phil, and Kate were very helpful in getting my started on my research. I would also like to thank my friend Michael for suggesting that I learn Python for my research, especially since it helped improve my calculations. A special thanks goes to Karen Feilberg, whom with I had many useful and fun discussions about chemistry and many other things.

I would also like to thank my parents for their strong commitment to education that they passed on to me from their parents. In particular, my mom taught me the importance of thinking outside the box and challenging people, and my father taught me the importance not only of hard work but also of taking pride in what you do. Several of my other family members, especially my sister, have been very supportive over the years There are probably many other people who helped me in ways big and small during my Ph.D. and I wish I could go into a completely exhaustive list of each one. Finally, though, I would like to thank David, for having the patience to listen to all my nonsensical rambling and for all his support. Without the support of everyone here, none of this would have been possible.

Chapter 1
Introduction

The stable isotope ratios of chemical compounds can often provide useful information about chemical, biological, and geophysical processes that cannot be understood by using concentrations alone. For example, the concentrations of ethanol and water in a bottle of wine do not provide much information beyond the extent of fermentation. However, an analysis of the $^{2}H/^{1}H$ and $^{13}C/^{12}C$ ratios of the ethanol and the $^{18}O/^{16}O$ ratio of the water is used by European Union regulators to detect adulteration and to verify the region of origin because the fermentation process, local climate, and other factors generate specific isotopic signals in the wine.[1,2] For oxygen-containing compounds, the relative abundance of ^{18}O to ^{16}O is usually measured, but in a few unusual cases, the relative abundance of ^{17}O to ^{16}O also provides additional information about the physical and chemical mechanisms acting on that compound. These relative abundances of ^{17}O and ^{18}O are reported relative to an international standard using the following notation where ^{x}O is either ^{17}O or ^{18}O:

$$\ln{}^{x}\mathrm{O} = \ln\left[\frac{\left({}^{x}\mathrm{O}/{}^{16}\mathrm{O}\right)_{\text{sample}}}{\left({}^{x}\mathrm{O}/{}^{16}\mathrm{O}\right)_{\text{standard}}}\right] = \ln(1+\delta\,{}^{x}\mathrm{O}) \tag{1}$$

In most oxygen-containing chemical compounds, $\ln^{17}O$ and $\ln^{18}O$ are correlated by a factor $\lambda_{MD} \approx 0.5$ because the chemical and physical processes that act on a compound scale with the differences in masses between ^{16}O, ^{17}O, and ^{18}O , so that the $\ln^{17}O$ values are approximately half the $\ln^{18}O$ values, as shown in Eq. (2).[3]

$$\ln{}^{17}\mathrm{O} = 0.5 \times \ln{}^{18}\mathrm{O} \tag{2}$$

More specifically, these "mass-dependent" cases result from the fact that the molecular velocities, rotational energies, and vibrational energies of the reactants, transition states, or products and thus chemical equilibria or the rates of reactions scale with the relative differences in mass upon isotopic substitution of ^{17}O or ^{18}O for one of the ^{16}O isotopes in the compound.[4] Because of this mass-dependent relationship between ^{16}O, ^{17}O, and ^{18}O, the measurement of ^{17}O is usually redundant.

However, measurements of the isotopic composition of ozone formed in the laboratory and the atmosphere showed quite unusual isotope enrichments in ^{17}O and ^{18}O relative to ^{16}O; the enrichments were not only large but also did not scale with the differences in masses between the isotopes.[5–7] These enrichments were called "non-mass-dependent" or "anomalous" because they deviated from the typical mass-dependent relationship of $\lambda_{MD} \approx 0.5$ and thus had a non-zero ^{17}O isotope anomaly $\Delta^{17}O$ as defined in Eq. (3).

$$\Delta^{17}\mathrm{O} = \ln{}^{17}\mathrm{O} - \lambda_{\mathrm{MD}} \times \ln{}^{18}\mathrm{O} \tag{3}$$

Through a number of different experiments,[8–12] these large, non-mass-dependent enrichments for ^{17}O and ^{18}O of ozone were eventually traced to unusual isotope effects in the three-body ozone recombination reaction (R1):

(R1) $O(^3P) + O_2 \rightarrow O_3^* + M \rightarrow O_3 + M^*$

Measurements of the kinetic isotope effects (KIEs) in the ozone formation reaction (R1) showed that the rate coefficients relative to $^{16}O^{16}O^{16}O$ were both unusually large for some of the isotopic-specific ozone formation pathways and had an unusual relationship to molecular symmetry. For example, the three ozone recombination reactions involving one ^{18}O atom that can form ozone are shown in reactions (R2), (R3), or (R4) along with their KIEs relative to formation of $^{16}O^{16}O^{16}O$.[9]

(R2) $^{18}O^{16}O + {}^{16}O + M \rightarrow {}^{18}O^{16}O^{16}O$ KIE = 1.45

(R3) $^{18}O + {}^{16}O^{16}O + M \rightarrow {}^{18}O^{16}O^{16}O$ KIE = 0.92

(R4) $^{16}O + {}^{18}O^{16}O + M \rightarrow {}^{16}O^{18}O^{16}O$ KIE = 1.08

While the asymmetric isotopologue $^{18}O^{16}O^{16}O$ could be formed by either reaction (R2) or (R3), the relative rate coefficient for (R2) of 1.45 was surprisingly large for an element heavier than hydrogen, but the relative rate coefficient for (R3) was only 0.92.[9] Furthermore, the formation of the symmetric isotopologue $^{16}O^{18}O^{16}O$ through reaction (R4) showed a rate coefficient enhancement of 1.08 relative to $^{16}O^{16}O^{16}O$. Marcus and co-workers[13–16] explained these KIEs for ozone formation using a combination of two isotope effects in semi-empirical RRKM calculations. The first isotope effect is a large, mass-dependent isotope effect in the formation of the asymmetric isotopologues of ozone that depends sensitively on the zero-point energy difference (ΔZPE) between the ground vibrational states of the two O_2 isotopologues from which the asymmetric ozone isotopologues could be formed. For example, $^{18}O^{16}O^{16}O$ could be formed from either $^{18}O^{16}O$ in (R2) or $^{16}O^{16}O$ in (R3), so the ΔZPE refers to the difference between the zero point energies of $^{16}O^{16}O$ and $^{18}O^{16}O$. This isotope effect cancels out under "scrambled" conditions when ozone formation can form from both $^{16}O^{16}O$ and $^{18}O^{16}O$, such as in the atmosphere or typical bulk photochemistry experiments. The second isotope effect is called the "η-effect" and its origins remain unexplained. The η effect was named after the *ad hoc* non-statistical factor η applied to the effective densities of states in O_3^* for formation of symmetric ozone isotopologues (e.g. $^{16}O^{18}O^{16}O$) relative to that for asymmetric isotopologues (e.g., $^{18}O^{16}O^{16}O$) used by Marcus and co-workers[13–16] in their semi-empirical RRKM calculations. This ad hoc reduction in the densities of states for symmetric O_3^* isotopologues leads to an 18% reduction in the relative rate coefficients for the formation of the symmetric isotopologues of O_3. This same phenomenological factor η was also found to be necessary in semi-classical trajectory[17,18] calculations to match the isotope-specific rate coefficients for ozone formation measured in Mauersberger et al.[8] The η-effect originates in differences between the symmetric and asymmetric isotopologues of O_3 through differences between the apparent lifetimes for the symmetric and asymmetric metastable O_3^* complexes, through differences in the efficiencies of collisional stabilization of the symmetric and asymmetric isotopologues by the bath gas M, or through both.[13,17] However, a theoretical basis for the chemical physics of the η effect has so far remained elusive. As such, additional experiments investigating the non-mass-dependent isotopic composition of ozone, including its bath gas and pressure dependence, as well as investigations

of other species that exhibit non-mass-dependent isotopic compositions could provide new insights into the physical chemical origin of the η-effect and provide new benchmarks for theory.

In addition to the isotopic composition of O_3, measurements of the isotopic composition of CO_2 in the stratosphere have shown that it is also non-mass-dependently enriched in ^{17}O and ^{18}O.[19–22] The ^{17}O isotope anomaly in stratospheric CO_2 has been thought[23] to originate at least in part through the KIEs in ozone formation (R1), followed by ultraviolet photolysis of ozone to form $O(^1D)$ (R5) and then isotope exchange between $O(^1D)$ and CO_2 (R6).

(R5) $O_3 + h\nu \rightarrow O(^1D) + O_2(^1\Delta)$ $\lambda < 310nm$

(R6) $O(^1D) + CO_2 \rightarrow CO_3^* \rightarrow O(^3P) + CO_2$

(R7) $O(^1D) + CO_2 \rightarrow CO_3^* \rightarrow O(^1D) + CO_2$

Isotope exchange between $O(^1D)$ and CO_2 was also found to occur via the non-quenching pathway (R7) that becomes important at higher collision energies.[24,25] To investigate whether transfer of the ^{17}O anomaly from ozone to CO_2 can be explained by this mechanism, in previous studies,[26–29] mixtures of O_2, CO_2, and in some cases, O_3, were irradiated with UV light, and the isotopic compositions of the CO_2 were measured or inferred. However, neither the resulting isotopic compositions of CO_2 nor the three isotope slopes (i.e. $\lambda = \Delta\ln^{17}O/\Delta\ln^{18}O$) for CO_2 could be easily explained by isotope effects in ozone formation, leading some to claim that additional anomalous isotope effects must exist in (R5), (R6), or (R7).[26,28,29] Furthermore, the three isotope slopes λ for CO_2 from these experimental studies were also near 1.0 and thus lower than the observed λ for the stratosphere that ranged from 1.2 to 1.7.[19–22] Thus, whether the reactions (R1), (R5), (R6), and (R7) and their associated isotope effects could quantitatively account for the observed λ in stratospheric CO_2 or for the differences in the value of λ between the laboratory and stratosphere was unknown.

At least part of the muddled interpretation of the differences in the three isotope slope λ for CO_2 between experiments in different research groups and between experiments and the stratosphere arose from the unusual dependence of the isotopic composition of CO_2 on the O_2/CO_2 mixing in the photochemical experiments, which was only relatively recently brought to light. Shaheen et al.[28] were the first to show systematically that the $\ln^{17}O$, $\ln^{18}O$, and $\Delta^{17}O$ values for CO_2 decrease dramatically with decreasing O_2/CO_2 mixing ratio in these experiments and that this O_2/CO_2 dependence could explain some of the differences in λ between different experiments. However, in investigating the O_2/CO_2 mixing ratio dependence of the isotopic composition of CO_2 systematically, Shaheen et al.[28] uncovered a new dilemma: they argued that some additional isotope effect(s) in addition to the KIEs in ozone formation was necessary to explain the dependence of the isotopic composition of CO_2 on the O_2/CO_2 mixing ratio. The measured values of $\Delta^{17}O$ in CO_2 decreased from ~60‰ at high O_2/CO_2 mixing ratios of 100 to ~30‰ at a low O_2/CO_2 mixing ratio of 0.1. Their new data led them to postulate that a non-mass-dependent isotope effect in addition to O_3 formation must exist in the UV photochemistry experiments performed at low O_2/CO_2 mixing ratios. They suggested that $O(^1D)$ at low O_2/CO_2 mixing ratios could have a large excess of kinetic energy (~20 kJ/mol) compared with thermal energies (~2kJ/mol) that would in turn allow more $O(^1D)$ to react with CO_2 via the non-quenching isotope exchange reaction (R7). How an increase in the population of high kinetic energy $O(^1D)$ and thus an increase in the relative importance of (R7) at low O_2/CO_2 could lead to a O_2/CO_2 dependence in the value of $\Delta^{17}O$ was not explored, however. Calculations of the non-

thermal kinetic energy distributions for $O(^1D)$ at various O_2/CO_2 mixing ratios might resolve whether such an effect is relevant to the non-mass-dependent isotopic composition of CO_2.

To further investigate the non-mass-dependent isotopic compositions of O_3 and CO_2 and to understand the underlying non-mass-dependent isotope effects, I measured the isotopic compositions of O_2, O_3, or CO_2 in laboratory experiments in which mixtures of gases were irradiated with UV light. The gases were separated cryogenically and were then analyzed for their triple isotope composition by dual inlet isotope ratio mass spectrometry. To compare the measurements in experiments and in stratospheric O_3 and CO_2 and to better understand the underlying chemistry and isotope effects, I then optimized and extended a photochemical kinetics model previously developed to describe photochemistry experiments of ozone photolysis and $O(^1D) + CO_2$ isotope exchange.[29,30] New features in the model included the pressure, bath gas, and temperature dependences of the KIEs in O_3 formation derived from the isotopic composition of O_3 under known conditions, mass-dependent isotope effects in several different reactions, some of which had not been considered before, and non-thermal rate coefficients for the reactions of $^{16}O(^1D)$, $^{17}O(^1D)$, and $^{18}O(^1D)$ with O_2, O_3, and CO_2. I derived these isotope-specific non-thermal rate coefficients by integrating energy-dependent reaction cross sections and branching ratios with kinetic energy distributions for $^{16}O(^1D)$, $^{17}O(^1D)$, and $^{18}O(^1D)$ that were calculated from the initial translational energy distribution of $O(^1D)$ from O_3 photolysis[31] and the hard sphere approximation for elastic and inelastic collisions.[32] The combined experimental measurements, stratospheric observations, and model results were compared to elucidate mechanisms for the differences in the triple isotope composition of O_2, O_3, and CO_2under various experimental and atmospheric conditions. Using these methods, I made several significant advances in understanding the origin of the non-mass-dependent isotopic compositions of both CO_2 and O_3. These findings are summarized for each chapter below.

In Chapter 2, I discovered systematic variations in the three isotope slope λ for CO_2 from new observations of stratospheric CO_2 with latitude, altitude, and season and used the results from photochemistry experiments with UV-irradiated mixtures of O_2 and CO_2 at an atmospheric O_2/CO_2 mixing ratio and from a photochemical kinetics model to understand the origins of these variations. Importantly, I was able to quantitatively predict both the ^{17}O isotope anomaly and the three isotope slope λ for CO_2 in the laboratory experiments at two different total pressures using a kinetics model. These results demonstrated that — for experiments at an atmospheric O_2/CO_2 mixing ratio at least — additional non-mass-dependent isotope effects beyond the KIEs in O_3 formation were not necessary to explain the isotopic compositions of CO_2 in the laboratory. The three isotope slope λ of CO_2 in these experiments was still only 1.0 compared with the slope of 1.2 to 1.7 previously observed in the stratosphere, however;[19–22] furthermore, the new observations showed that λ reached values of nearly 2.2 in some regions of the stratosphere. Having successfully predicted the isotopic composition and ^{17}O isotope anomaly of CO_2 in the laboratory experiments, I then used the model to show that differences in the three isotope slope between the experiments and the stratosphere and between the different regions of the stratosphere are qualitatively consistent with the temperature dependence of the O_3 KIEs and with changes in the relative importance of mass-dependent isotope effects in reactions, particularly O_3 photolysis. These model sensitivities provide a stronger physical chemistry framework for understanding the non-mass-dependent isotopic compositions of CO_2 than the crude analysis of the three isotope slopes that had been used in the past. In particular, the photochemical kinetics model provides an analytical tool for investigating the impact of changes

in the relative importance of the non-mass-dependent and mass-dependent isotope effects that lead to differences in the non-mass-dependent isotopic composition and the three isotope slope λ for CO_2. These results have provided a paradigm shift in the understanding of the non-mass-dependent isotopic composition of stratospheric CO_2 and its transfer from ozone, and a sounder foundation for the various biogeochemical and paleoclimate applications based on the ^{17}O isotope anomaly of stratospheric CO_2, such as estimating biosphere productivity from changes in the ^{17}O isotope anomaly of O_2.[33]

In Chapter 3, I extended the experiments and modeling from Chapter 2 to explore how and why the triple isotope composition of CO_2 and its ^{17}O anomaly change dramatically as the O_2/CO_2 mixing ratio in the experiment is varied. I measured the triple isotope compositions of O_2 and CO_2 as a function of the O_2/CO_2 mixing ratio at two different pressures, particularly at O_2/CO_2 mixing ratios in which the isotopic compositions are changing rapidly, thus significantly extending the number of available measurements. Kinetics modeling of these experiments confirmed that the dramatic O_2/CO_2 dependence of the ^{17}O anomaly in CO_2 cannot be explained by expected changes in the non-mass-dependent KIEs in O_3 formation in a CO_2 bath. Many different possible mechanisms were included in various model scenarios to explore what processes might produce a large dependence of the ^{17}O isotope anomaly on the O_2/CO_2 ratio. The mechanisms explored included CO_2 photolysis, photochemical reactions with residual water in the reactor and the small, non-mass-dependent isotope effects in CO + OH, and many others (not all of which are explicitly documented in Chapter 3). Of all the mechanisms tested in the model, the only mechanism that showed a O_2/CO_2 dependence in the values of $\ln^{17}O$, $\ln^{18}O$, and $\Delta^{17}O$ for CO_2 was the inclusion of isotope-specific non-thermal rate coefficients for the reactions of $O(^1D)$ with O_2, O_3, and CO_2. These non-thermal rate coefficients were calculated from integration of the energy dependence of the reaction cross sections over the translational energy distributions for $^{16}O(^1D)$, $^{17}O(^1D)$, and $^{18}O(^1D)$ that were calculated using the hard sphere approximation for elastic and inelastic collisions.[32] The calculated kinetic energy distributions at low O_2/CO_2 mixing ratios showed that over 50% of $O(^1D)$ in CO_2-dominated mixtures has kinetic energy in excess of $5k_bT$ (~10 kJ/mol), compared with 10% of $O(^1D)$ for the kinetic energy distribution at high O_2/CO_2 mixing ratios, so that non-quenching isotope exchange reaction between $O(^1D)$ and CO_2 (R7) becomes more important at low O_2/CO_2 mixing ratios, as hypothesized by Shaheen et al.[28] Analysis of the kinetics model results for the isotopic composition of CO_2 for various scenarios in which the non-thermal rate coefficients were calculated in various ways from the isotope-specific translational energy distributions showed that the translational energy distributions of $^{17}O(^1D)$ and $^{18}O(^1D)$ diverge from the translational energy distribution of $^{16}O(^1D)$, especially at low O_2/CO_2 mixing ratios because of the increased importance of the non-quenching $O(^1D) + CO_2$ isotope exchange reaction (R7). This divergence of the translational energy distributions for $^{17}O(^1D)$ and $^{18}O(^1D)$ from the distribution for $^{16}O(^1D)$ leads to non-thermal rate coefficients that can produce a O_2/CO_2 dependence in the $\Delta^{17}O$ values for CO_2 calculated in the model. Despite the factor of 5 smaller magnitude of the O_2/CO_2 dependence for values of $\Delta^{17}O$ of CO_2 calculated in the model compared with the experiments, the divergence of the translational energy distributions for the rare isotopes $^{17}O(^1D)$ and $^{18}O(^1D)$ from the translational energy distribution for the common isotope $^{16}O(^1D)$ due to non-thermal isotope exchange reactions is a novel mechanism for producing unexpected non-mass-dependent isotope fractionation that has not been described before. Importantly, this mechanism for non-mass-dependent fractionation is not related to the non-mass-dependent KIEs in O_3 formation. Thus, in principle, this type of non-mass-dependent fractionation could occur in any isotope

exchange reaction involving high kinetic energy oxygen atoms, such as in the upper atmosphere of Earth[34] or the atmosphere of Mars.[35,36] or Venus.[37]

In addition to the role that energy transfer in collisions of $O(^1D)$ with CO_2 plays in the isotopic composition of CO_2 at low O_2/CO_2 mixing ratios, experiments near the beginning of the research presented here showed that the non-mass-dependent isotopic composition of O_3 was affected by differences in the efficiency of collision energy transfer. In Feilberg, Wiegel, and Boering,[38] I contributed to the interpretation of these new measurements of the pressure dependence of the non-mass-dependent isotopic composition of ozone in different bath gases. The isotopic composition of ozone formed by irradiating O_2 with UV light showed that the values of $\ln^{17}O$, $\ln^{18}O$, and $\Delta^{17}O$ for O_3 formed in a bath gas at a given pressure follow the pattern $Ar > O_2 > CO_2 > SF_6$.[38] This order is expected based on the efficiency of quenching of the metastable O_3*[39] by collisions with each bath gas (i.e. the average energy transferred per collision, $<\Delta E>$, derived from kinetics experiments for ozone formation is 18 cm^{-1}, 25 cm^{-1}, 150 cm^{-1}, and 260 cm^{-1} for Ar, O_2 (assuming it is similar to N_2), CO_2, and SF_6 respectively).[39] Remarkably, though, the difference between $\Delta^{17}O$ of O_3 formed in CO_2 and that formed in SF_6 was extremely large while the difference between $\Delta^{17}O$ of O_3 formed in O_2 and that formed in CO_2 was quite small, even though $<\Delta E>$ for both CO_2 and SF_6 are quite large. I concluded that the large difference between the isotopic composition of O_3 formed in CO_2 versus in SF_6 suggested that collisions between O_3* and SF_6 were particularly effective at probing the region of the O_3 potential energy surface that was most sensitive to the non-mass-dependent KIEs, while CO_2 is not despite its relatively large $<\Delta E>$ compared with Ar and N_2. Several theorists are now working to see if they can calculate these large differences in the non-mass-dependent isotopic composition of ozone formed in CO_2 versus in SF_6 bath gases. Measurements of the isotopic composition of O_3 formed in additional bath gases beyond those measured in Feilberg, Wiegel, and Boering[38] may therefore provide some insight into the mechanism for the dramatic difference in the ^{17}O isotope anomaly between O_3 formed in CO_2 and in SF_6.

Therefore, in Chapter 4, based on the need for additional bath gas measurements from my work in Feilberg, Wiegel, and Boering,[38] I measured the isotopic composition of O_3 formed in an air-like mixture of O_2 and N_2 at several different pressures. The values of $\ln^{17}O$, $\ln^{18}O$, and $\Delta^{17}O$ for O_3 at most of the pressures measured showed small, but statistically significant differences from O_3 formed in a pure O_2 bath. Importantly, I used a kinetics model of these experiments to show that the inclusion of the KIEs measured or derived for O_3 formation at 40 Torr O_2 and 160 Torr N_2 by Mauersberger et al.[8,9] lead to a quantitative prediction for $\Delta^{17}O$ of O_3 in my experiments using the same partial pressures of O_2 and N_2 as in the Mauersberger experiments. These results showed directly with evidence from both measurements and a kinetics model that non-mass-dependent isotope effects in the UV photolysis of O_3, such as the ones suggested by Chakraborty and Bhattacharya,[40] do not exist. Because the model successfully predicted the value of $\Delta^{17}O$ for O_3 at 40 Torr of O_2 and 160 Torr of N_2, I then used the kinetics model to explore the mechanisms that could lead to differences in the triple isotope composition of O_3 formed in N_2 and O_2. The sensitivity of the isotopic composition of O_3 in the model to mass-dependent isotope effects in O_3 photolysis and other reactions in pure O_2 and in an air-like mixture of O_2 and N_2 showed that many of the calculated photolysis cross sections for different isotopologues of O_3[41,42] are likely to be too small compared to the experimental measurements. Furthermore, using both my model and my experimental results, I identified reactions with mass-dependent isotope effects that are important for determining the bulk isotopic composition of O_3

as well as the isotopic composition of any other chemical species that obtains its anomalous isotopic composition through reactions with O_3, such as CO_2. Finally, along with the results of Feilberg, Wiegel, and Boering,[38] I showed that differences in the relative importance of the radical complex mechanism for O_3 formation (as opposed to the energy transfer mechanism), even between two very similar gases such as O_2 and N_2, may have some impact on the non-mass-dependent KIEs in O_3 formation.

In summary, I have made significant advances in the understanding of the non-mass-dependent isotopic compositions of O_3 and CO_2 using a kinetics model to analyze new measurements of the triple isotope composition of CO_2 in photochemistry experiments and in the stratosphere I also showed that differences in the efficiency of collisional energy transfer can play an important role in non-mass-dependent KIEs in O_3 formation and can even generate non-mass-dependent fractionation due to differences in the non-thermal translational energy distributions for $^{16}O(^1D)$, $^{17}O(^1D)$, and $^{18}O(^1D)$. When the translational energy distributions for $^{16}O(^1D)$, $^{17}O(^1D)$, and $^{18}O(^1D)$ were integrated with the energy-dependent branching ratios for various reactions with different chemical species, the resulting non-thermal rate coefficients produce non-mass-dependent fractionation due to changes in the relative rates of isotope exchange that no longer scale with the isotopic mass differences. Together, these results provide critical new experimental insights into and constraints on the underlying physical chemical origin of the η-effect in O_3 formation and of the origins and some novel mechanisms of non-mass-dependent fractionation in general. In each chapter, I have shown that a kinetics model is an indispensable tool for analyzing and deriving a mechanistic understanding of non-mass-dependent isotopic compositions and isotope effects, especially as previous research studies often relied on flawed assumptions[40] or superficial analyses of three isotope slopes.[26,27]

The work in this dissertation also points to specific photochemistry experiments and kinetics modeling efforts that can be pursued to further our understanding of the non-mass-dependent isotopic compositions of O_3 and CO_2 to address remaining uncertainties. In particular, experiments and kinetics modeling of how the isotopic compositions of O_3 and CO_2 are affected by collisional quenching of O_3* and the isotope-specific translational energy distributions of $O(^1D)$ could help further improve the theoretical basis for non-mass-dependent isotope effects — some of which were discovered here — and how and why they occur. For O_3, measurements of the isotopic composition of O_3 formed in different bath gases, particularly one with an efficiency of collisional quenching of O_3* in between those for CO_2 and SF_6, could provide a better understanding for the dramatic difference in $\Delta^{17}O$ of O_3 formed in SF_6 versus Ar, O_2, N_2, or CO_2. For CO_2, experiments in which $O(^1D)$ is produced with "hotter" or "colder" initial energy distributions could be used to probe the sensitivity of the O_2/CO_2 mixing ratio dependence in the values of $\ln^{17}O$, $\ln^{18}O$, and $\Delta^{17}O$ for CO_2 to differences in the translational energy distributions of $^{16}O(^1D)$, $^{17}O(^1D)$, and $^{18}O(^1D)$ in the bulk photochemical system. Along with these new experiments, calculations of how the isotope-specific kinetic energy distributions vary by using more accurate elastic and inelastic scattering than the hard sphere approximation are needed, as indicated by the model sensitivity studies in Chapter 3. Such calculations might help narrow the discrepancies for the O_2/CO_2 mixing ratio dependence of the $\ln^{17}O$, $\ln^{18}O$, $\Delta^{17}O$ values for CO_2 between the model and experiments and provide a more robust framework for the non-mass-dependent isotope fractionation discovered in these studies based on the isotope-specific non-thermal rate coefficients for $O(^1D)$ isotope exchange reactions. With these additional experiments and modeling, a more complete theoretical framework for these interesting and

unusual isotope effects may in turn lead to an even better understanding of the origins of the non-mass-dependent isotopic compositions of O_3 and CO_2 in planetary atmospheres.

References

[1] A. Rossmann, Food Rev. Int. **17**, 347 (2001).

[2] D.M.A.M. Luykx and S.M. van Ruth, Food Chem. **107**, 897 (2008).

[3] M.H. Thiemens, Annu. Rev. Earth Planet. Sci. **34**, 217 (2006).

[4] J. Bigeleisen and M.G. Mayer, J. Chem. Phys. **15**, 261 (1947).

[5] M.H. Thiemens and J.E. Heidenreich, Science **219**, 1073 (1983).

[6] K. Mauersberger, Geophys. Res. Lett. **8**, 935 (1981).

[7] K. Mauersberger, Geophys. Res. Lett. **14**, 80 (1987).

[8] K. Mauersberger, B. Erbacher, D. Drankowsky, J. Gunther, and R. Nickel, Science **283**, 370 (1999).

[9] C. Janssen, J. Guenther, K. Mauersberger, and D. Krankowsky, Phys. Chem. Chem. Phys. **3**, 4718 (2001).

[10] J. Morton, J. Barnes, B. Schueler, and K. Mauersberger, J. Geophys. Res. **95**, 901 (1990).

[11] K. Mauersberger, S.M. Anderson, D. Hu, and D. Hulsebusch, J. Chem. Phys. **107**, 5385 (1997).

[12] J.E. Heidenreich and M.H. Thiemens, J. Chem. Phys. **84**, 2129 (1986).

[13] Y.Q. Gao and R.A. Marcus, Science **293**, 259 (2001).

[14] Y.Q. Gao and R.A. Marcus, J. Chem. Phys. **127**, 244316 (2007).

[15] Y.Q. Gao and R.A. Marcus, J. Chem. Phys. **116**, 137 (2002).

[16] Y.Q. Gao, W.-C. Chen, and R.A. Marcus, J. Chem. Phys. **117**, 1536 (2002).

[17] R. Schinke, S.Y. Grebenshchikov, M. V Ivanov, and P. Fleurat-Lessard, Annu. Rev. Phys. Chem. **57**, 625 (2006).

[18] R. Schinke and P. Fleurat-Lessard, J. Chem. Phys. **122**, 094317 (2005).

[19] M.H. Thiemens, T. Jackson, E.C. Zipf, P.W. Erdman, and C. Van Egmond, Science **270**, 969 (1995).

[20] P. Lämmerzahl, T. Röckmann, C.A.M. Brenninkmeijer, D. Krankowsky, and K. Mauersberger, Geophys. Res. Lett. **29**, 1582 (2002).

[21] B. Alexander, M.K. Vollmer, T. Jackson, and R.F. Weiss, J. Geophys. Res. **28**, 4103 (2001).

[22] S. Kawagucci, U. Tsunogai, S. Kudo, F. Nakagawa, H. Honda, S. Aoki, T. Nakazawa, M. Tsutsumi, and T. Gamo, Atmos. Chem. Phys. **8**, 6189 (2008).

[23] Y.L. Yung, a Y. Lee, F.W. Irion, W.B. DeMore, and J. Wen, J. Geophys. Res. **102**, 10857 (1997).

[24] M.J. Perri, A.L. Van Wyngarden, K.A. Boering, J.J. Lin, and Y.T. Lee, J. Chem. Phys. **119**, 8213 (2003).

[25] M.J. Perri, A.L. Van Wyngarden, J.J. Lin, Y.T. Lee, and K.A. Boering, J. Phys. Chem. A **108**, 7995 (2004).

[26] J. Wen and M.H. Thiemens, J. Geophys. Res. **98**, 12801 (1993).

[27] S. Chakraborty and S.K. Bhattacharya, J. Geophys. Res. **108**, 4724 (2003).

[28] R. Shaheen, C. Janssen, and T. Röckmann, Atmos. Chem. Phys. **7**, 495 (2007).

[29] J.C. Johnston, T. Röckmann, and C.A.M. Brenninkmeijer, J. Geophys. Res. **105**, 15213 (2000).

[30] A.S. Cole and K.A. Boering, J. Chem. Phys. **125**, 184301 (2006).

[31] S.M. Dylewski, J.D. Geiser, and P.L. Houston, J. Chem. Phys. **115**, 7460 (2001).

[32] V. Kharchenko and A. Dalgarno, J. Geophys. Res. **109**, 1 (2004).

[33] B. Luz, E. Barkan, M.L. Bender, M.H. Thiemens, and K.A. Boering, Nature **400**, 547 (1999).

[34] N. Balakrishnan, V. Kharchenko, and A. Dalgarno, J. Geophys. Res. **103**, 23393 (1998).

[35] M.H. Thiemens, T.L. Jackson, and C.A.M. Brenninkmeijer, Geophys. Res. Lett. **22**, 255 (1995).

[36] C. Barth and C. Hord, Science **173**, 197 (1971).

[37] F. Montmessin, J.-L. Bertaux, F. Lefèvre, E. Marcq, D. Belyaev, J.-C. Gérard, O. Korablev, a. Fedorova, V. Sarago, and a. C. Vandaele, Icarus **216**, 82 (2011).

[38] K.L. Feilberg, A.A. Wiegel, and K.A. Boering, Chem. Phys. Lett. **556**, 1 (2013).

[39] K. Luther, K. Oum, and J. Troe, Phys. Chem. Chem. Phys. **7**, 2764 (2005).

[40] S. Chakraborty and S.K. Bhattacharya, J. Chem. Phys. **118**, 2164 (2003).

[41] S.A. Ndengué, F. Gatti, R. Schinke, H.-D. Meyer, and R. Jost, J. Phys. Chem. A **114**, 9855 (2010).

[42] M.-C. Liang, G.A.G. Blake, and Y.L.Y. Yung, J. Geophys. Res. **109**, D10308 (2004).

Chapter 2
Unexpected variations in the triple oxygen isotope composition of stratospheric carbon dioxide

Adapted from an article with the same title, published in *Proc. Natl. Acad. Sci. U. S. A.* ***110****, 17680 (2013)*, authored by A.A. Wiegel, A.S. Cole, K.J. Hoag, E.L. Atlas, S.M. Schauffler, and K.A. Boering

Abstract

We report observations of stratospheric CO_2 that reveal surprisingly large anomalous enrichments in ^{17}O that vary systematically with latitude, altitude, and season. The triple isotope slopes reached 1.95±0.05(1σ) in the middle stratosphere and 2.22±0.07 in the Arctic vortex versus 1.71±0.03 from previous observations and a remarkable factor of 4 larger than the mass-dependent value of 0.52. Kinetics modeling of laboratory measurements of photochemical ozone-CO_2 isotope exchange demonstrates that non-mass-dependent isotope effects in ozone formation alone quantitatively account for the ^{17}O anomaly in CO_2 in the laboratory, resolving long-standing discrepancies between models and laboratory measurements. Model sensitivities to hypothetical mass-dependent isotope effects in reactions involving O_3, $O(^1D)$, or CO_2 and to an empirically-derived temperature dependence of the anomalous kinetic isotope effects in ozone formation then provide a conceptual framework for understanding the differences in the isotopic composition and the triple isotope slopes between the laboratory and the stratosphere and between different regions of the stratosphere. This understanding in turn provides a firmer foundation for the diverse biogeochemical and paleoclimate applications of ^{17}O anomalies in tropospheric CO_2, O_2, mineral sulfates, and fossil bones and teeth, which all derive from stratospheric CO_2.

Main text

For most materials containing oxygen, the relative abundances of its three stable isotopes (^{16}O, ^{17}O, and ^{18}O) fall on a "mass-dependent" fractionation line (1) with a $\ln^{17}O$-$\ln^{18}O$ three-isotope slope[1] near 0.5, which is well-predicted by statistical thermodynamics (3) and chemical reaction rate theories (4). In other words, ^{17}O is usually one-half as depleted or enriched as ^{18}O when measured relative to ^{16}O and relative to those same ratios in an international standard. Discoveries of large deviations from a mass-dependent slope of 0.5 in meteorites (5) and ozone (6, 7), resulting in non-zero ^{17}O anomalies (i.e., $\Delta^{17}O=\ln^{17}O-0.52\ln^{18}O\neq 0$), have led to many applications tracing the histories and inventories of materials throughout the solar system (1), despite continuing debate about their chemical or physical origins (e.g., 1, 8).

For ozone, the non-mass-dependent enrichments in ^{17}O and ^{18}O have a three-isotope slope of 0.65 to 1.0 (e.g., 9) and have been traced to anomalous kinetic isotope effects (KIEs) in O_3 formation:

---

[1] Isotopic compositions are often reported as "δ" values but a short-hand logarithmic notation is used here, as recommended by Luz and Barkan (2) both for convenience and to avoid unnecessary and uninteresting curvature that the use of δ values can cause in three isotope plots for the large laboratory enrichments measured. This logarithmic notation is defined as $\ln^{18}O = \ln[(^{18}O/^{16}O)_{sample}/(^{18}O/^{16}O)_{standard}] = \ln[\delta^{18}O + 1]$ where $(^{18}O/^{16}O)_i$ is the ratio of the number of atoms of ^{18}O to ^{16}O in a sample or standard and $\delta^{18}O = [\{(^{18}O/^{16}O)_{sample}/(^{18}O/^{16}O)_{standard}\}-1]$, and similarly for $\ln^{17}O$ and $\delta^{17}O$.

$$O(^3P)+O_2+M \rightarrow O_3^*+M \rightarrow O_3+M^* \quad (1)$$

where M is any collision partner (10-12). While much progress has been made in understanding ozone's non-mass-dependent isotopic composition (12-14), the theoretical basis in chemical physics is still unresolved (15-17). In addition, whether ^{17}O anomalies in other species – such as CO_2, N_2O, sulfates, and nitrates (e.g., 18) – result solely from transfer from O_3 or from additional anomalous KIEs remains unclear. Stratospheric CO_2, for example, attains at least part of its observed non-mass-dependent isotopic composition (19-24) via reactions 2-3 (25-28):

$$O_3+h\nu \rightarrow O(^1D)+O_2(^1\Delta) \quad (2)$$

$$O(^1D)+CO_2 \rightarrow CO_3^* \rightarrow O(^3P)+CO_2 \quad (3a)$$

$$O(^1D)+CO_2 \rightarrow CO_3^* \rightarrow O(^1D)+CO_2 \quad (3b)$$

The observed $\ln^{17}O/\ln^{18}O$ slope for stratospheric CO_2 ranges from ~1.2 to 1.7, much larger than for O_3. To explain the difference, non-mass-dependent isotope effects beyond O_3 formation have been postulated (19, 29), including a coincidental near-resonance for $^{17}O^{12}C^{16}O_2^*$ or a nuclear spin/spin-orbit coupling effect in 3a. In addition, $\ln^{17}O/\ln^{18}O$ slopes for CO_2 measured in laboratory mixtures of UV-irradiated O_2 or O_3 and CO_2 (29-32), slopes calculated from photochemical models of laboratory experiments (30) and the stratosphere (27, 28), and slopes from observations show remarkable disagreements. For example, three-isotope slopes for CO_2 in laboratory experiments typically vary from about 0.8 to 1.0 (29, 30, 32) not the value of 1.7 that has come to be expected for the stratosphere (22, 33). Although one laboratory study has yielded a slope up to 1.8 (31), the experiment was performed at unrealistically high O_3/CO_2 ratios and shows unusual behavior relative to all other published experiments; experiments under nearly identical conditions but longer irradiation times (32) yielded a slope near 1, suggesting that the higher slope in the high O_3/short irradiation time experiments likely results from non-mass-dependent isotope effects in O_3 photodissociation due to O_3 self-shielding, which is not relevant for atmospheric conditions; thus, the apparent agreement with previous stratospheric observations is arguably fortuitous, as discussed further below. In addition, $\ln^{17}O$ was measured directly in only one previous laboratory study (32), while it was inferred from mass balance in all others, which adds additional uncertainty (e.g., if unknown ^{13}C isotope effects might affect the results due to the isobaric interference between $^{13}C^{16}O^{16}O$ and $^{12}C^{17}O^{16}O$ in mass spectrometry measurements). Finally, Liang *et al.* (27, 28) calculate a three-isotope slope of 1.5 for CO_2 in their model at latitudes >25°N that shows little temporal or spatial variation in the lower and middle stratosphere. The current level of disagreement between experiments, atmospheric observations, and atmospheric modeling shows that isotope exchange between O_3 and CO_2 is still not well understood.

Here, we report measurements of $\ln^{17}O$ and $\ln^{18}O$ of stratospheric CO_2 that reveal much larger three-isotope slopes than expected and their systematic variation with latitude, altitude, and season. We also report time-dependent laboratory and modeling results that demonstrate for the first time that anomalous KIEs in O_3 formation alone quantitatively account for the triple isotope composition of CO_2 in the laboratory. Combining laboratory and stratospheric results, we show that differences in temperature, relative rates of mass-dependent reactions, and vertical versus quasi-horizontal transport rates can plausibly explain differences in the $\ln^{17}O/\ln^{18}O$ relationships between the laboratory and stratosphere and within the stratosphere. The results thus provide a deeper understanding of contemporary stratospheric CO_2 isotope variations, the underlying isotope chemistry, and a sounder foundation for the biogeochemical, paleoclimate,

and paleoatmospheric applications of ^{17}O anomalies in materials that derive their signals from stratospheric CO_2 (34-40).

Stratospheric CO_2 was separated cryogenically from whole air samples collected by NASA ER-2 aircraft (41) in winter 1999-2000 during the SOLVE mission (42) and a September 2004 balloon flight (43) at 34°N. The isotopic composition was measured on a Finnigan MAT 252 isotope ratio mass spectrometer using the CeO_2 equilibration technique (44). Additional sampling and measurement details are provided in ***Materials and Methods*** and ***SI Appendix***. Results are shown in Fig. 2-1 and the SI Appendix (Tables 2-S1 through 2-S4). Samples of high latitude air (>55°N) determined to be in the polar vortex from nitrous oxide (N_2O) and potential temperature (θ) measurements (45) (SI Appendix (Fig. 2-S1)) exhibit a three-isotope slope from a bivariate linear least-squares regression of 2.22±0.07(1σ). Samples collected at midlatitudes (25-55°N) and in "midlatitude-like" (i.e., non-vortex) air at high latitudes (based on N_2O and θ) yield a three-isotope slope of 1.95±0.05. These slopes are significantly larger (Table 2-1) than the expected value of 1.71±0.03 from Lämmerzahl *et al.* (22), with homogeneity of regression tests demonstrating that these differences with respect to the *Lämmerzahl* data are both significant at the 99% confidence interval (SI Appendix (Table 2-S5)). If only the new lower stratospheric (<21 km) samples are included in our midlatitude regression, the slope is 1.7±0.2, closer to expectations but more variable. We believe this increased variability in the lower stratosphere is real (see below), although additional uncertainty from a smaller regression range may also contribute.

Additional insight into the regional differences in slope is gained by examining $\Delta\ln^{17}O/\Delta\ln^{18}O$ (i.e., the slope of a line defined by two points: the $\ln^{17}O$ and $\ln^{18}O$ isotopic composition of a sample and the isotopic composition of tropospheric CO_2 with $\ln^{17}O$=21.1‰ and $\ln^{18}O$=40.2‰) for individual datapoints from the rocket (19) and 2004 balloon datasets. Vertical profiles of CH_4, N_2O and θ suggest the influence of air transported from more equatorial regions (SI Appendix (Figs. 2-S2, 2-S3; Table 2-S3)). The $\Delta\ln^{17}O/\Delta\ln^{18}O$ values for these tropically-influenced samples are typically larger than for samples with more midlatitude-like character based on CH_4, N_2O, and θ. These differences suggest that even larger slopes may be observable in the deep tropics and that transport and mixing of tropical air to 34°N contributes to the $\Delta\ln^{17}O/\Delta\ln^{18}O$ variability in these profiles.

These systematic variations in $\Delta\ln^{17}O/\Delta\ln^{18}O$ and three-isotope slopes with latitude, altitude and season are not inconsistent with the previous observations of Lämmerzahl *et al.* (22) at 44°N and 68°N. The narrow range in slope of 1.71±0.03 they measured has been considered the "standard" against which other measurements and model predictions should match (22, 33). However, the *Lämmerzahl* flights, based on their timing, would have likely always intercepted non-vortex extratropical air, yielding a relatively homogeneous three-isotope slope not necessarily representative of other regions, similar to how the long-lived tracers CH_4 and N_2O exhibit homogeneous non-vortex extratropical slopes distinct from tropical and vortex slopes. Satellite measurements of CH_4 and N_2O show CH_4:N_2O relationships that are compact (i.e., homogeneous) and distinct between three regions: the tropics, the extratropics, and the polar vortices after significant descent has occurred (46). In contrast, the region at 25±10°N exhibits CH_4:N_2O correlations that are much less compact, consisting of inhomogeneous mixtures of tropical and midlatitude air (46). The CO_2 isotopic composition is also a long-lived tracer (23, 27, 28) since the lifetime for isotope exchange with O_3 is always at least an order of magnitude longer than stratospheric transport timescales, even at 45 km where $O(^1D)$ peaks (27, 28); thus transport and mixing affect it similarly to CH_4 and N_2O. By analogy, homogeneous three-isotope

slopes for CO_2 can be observed polewards of 35°N except in Arctic vortex air in January-March (42); the tropical and late vortex $\ln^{17}O/\ln^{18}O$ slopes can be distinct from the non-vortex/extratropical relationships; and the 25±10°N "mixed region" would be an inhomogeneous mixture, as observed. These variations in three-isotope slopes thus appear to be explicable and robust across high precision CO_2 datasets.

These systematic variations with latitude and season we observe may also account for at least some of the variability in what have been considered to be the noisier datasets shown in Figure 2-1 (20, 21, 24). For example, the dataset of Alexander *et al.* (21) consists of 6 samples that were collected in or near the polar vortex and which indeed show a higher three-isotope slope of 2.1±0.6(1σ, N=6), although the variability is high and the uncertainty in slope means it is not statistically different from the previous, lower slope datasets. It is not clear whether the variability is due to the small number of samples and real atmospheric variability (such as moving in and out of vortex air) or to possible measurement artifacts. Our vortex data and interpretation presented here suggest that at least some of the variability may be real. Similarly, some of the Kawagucci *et al.* datapoints (24) overlap with our larger slope datapoints, but they report themselves that a linear fit to their data yields a slope of 1.63±0.05(1σ, N=58) and that their slope and data in general are not statistically nor characteristically different from the Lämmerzahl *et al.* dataset. If additional unpublished trace gas data and geophysical parameters are available for their samples, it may be possible to investigate their outliers at larger or smaller $\Delta\ln^{17}O/\Delta\ln^{18}O$ values. Otherwise, whether these outliers are explained by atmospheric variability or by a lower measurement precision for their online CuO equilibration IRMS technique (as the much more scattered relationship between their $\Delta^{17}O$ of CO_2 and N_2O mixing ratio measurements may suggest (SI Appendix (Fig. 2-S4)) is unclear. Homogeneity of regression tests demonstrate that the differences in slope between our "vortex" and the *Kawagucci* data and between our "midlatitude" and the *Kawagucci* data are statistically significant at the 99% and 95% confidence intervals, respectively (SI Appendix (Table 2-S5)). Finally, the rocket dataset reported by Zipf and Erdman (20), which also lacks information on other long-lived tracer and potential temperature data, overlaps with our dataset, showing a curvilinear $\ln^{17}O$-$\ln^{18}O$ relationship that links our lower and middle stratospheric data with the middle and upper stratospheric rocket data reported by Thiemens *et al.* (19); this dataset is thus also consistent with the idea that we put forth here that a linear $\ln^{17}O/\ln^{18}O$ relationship of 1.7 with a small standard deviation of <0.1 cannot represent the entire stratosphere, in contrast to the now widely-held assumption that it does.

To investigate processes that could lead to the larger $\Delta\ln^{17}O/\Delta\ln^{18}O$ values and three-isotope slopes we observe, O_2 and CO_2 mixtures near atmospheric mixing ratios were irradiated with UV light (see **Materials and Methods** and **SI Appendix**). The CO_2 isotopic composition was measured (SI Appendix (Table 2-S7)) and compared to results from a time-dependent photochemical kinetics model we developed using KINTECUS (SI Appendix (Tables 2-S9 and 2-S10)). The model accurately predicts both the time dependence and the steady-state values for $\ln^{17}O$, $\ln^{18}O$ and $\Delta^{17}O$ of CO_2 (Fig. 2-2; Table 2-2). These results demonstrate for the first time that anomalous KIEs in O_3 formation can quantitatively explain the triple isotope composition of CO_2 in the laboratory at atmospherically-relevant O_2, O_3, and CO_2 mixing ratios without invoking additional anomalous KIEs or other unknown effects to account for the data. Importantly, the model uses molecular level rate coefficients without employing empirical or phenomenological parameterizations of how the transfer of the anomaly from CO_2 to O_3 occurs at steady-state used in previous work (28, 32). These results also demonstrate that slopes close to

1 are to be expected in most laboratory experiments using mercury lamps at atmospherically-relevant O_2/CO_2 ratios and pressures below 150 Torr. Indeed, even the very high O_3/CO_2 experiments of Shaheen *et al.* performed for long irradiation times (32) resulted in an experimental slope near 1, as did our photochemical model run under conditions similar to theirs, unlike the slope of 1.8 measured at very high O_3/CO_2 mixing ratios for short irradiation times (31). The short irradiation times combined with the narrow lines of a Hg lamp, large reactor volume, and very high amounts of O_3 in the *Chakraborty and Bhattacharya* experiments (31) suggest that their 1.8 slope for CO_2 results from non-mass-dependent isotopic self-shielding by O_3 during O_3 photodissociation and subsequent transfer to CO_2 (32) rather than to processes simulating stratospheric isotope photochemistry in their experiment. In other words, isotopic self-shielding by O_3 does not occur at the O_3/CO_2 levels in the atmosphere or in the near-atmospheric mixing ratio laboratory experiments, or even at the longer irradiation times in the high O_3/CO_2 experiments of Shaheen *et al.*; thus the apparent agreement between the $\ln^{17}O/\ln^{18}O$ slope for CO_2 of 1.8 with the previously expected value of 1.7 is likely fortuitous.

The three-isotope slopes near 1.1 in experiments without isotopic self-shielding artifacts, however, are still much smaller than stratospheric observations. To investigate the possible origins of the laboratory-stratosphere differences in $\Delta\ln^{17}O/\Delta\ln^{18}O$ values, we tested the sensitivity of the photochemical model to various inputs and processes (Fig. 2-2; Table 2-2). Initializing the model with the tropospheric isotopic compositions of O_2 and CO_2 increases the slope from 1.067 to 1.24, a sensitivity previously noted (28, 31, 32). As the model temperature decreases to stratospheric values, the modeled slope increases further, to 1.84 at 200K, based on several temperature-dependent O_3 KIE measurements (47) and our estimates of others not yet measured (see SI Appendix). The temperature decrease changes the predicted magnitudes of the O_3 formation KIEs, which in turn alter the non-mass-dependent isotopic compositions of O_3 and $O(^1D)$ and hence both the three-isotope slope and $\Delta^{17}O$ of CO_2. Introduction of mass-dependent isotope effects in any number of reactions can also change the three-isotope slope but leaves $\Delta^{17}O$ effectively unchanged (Fig. 2-2CD; Table 2-2). For example, a mass-dependent O_3 photolysis isotope effect at the experimental wavelength of 254 nm that isotopically depletes the remaining O_3 (48, 49) will mass-dependently enrich $O(^1D)$ and CO_2 and thus decreases the three-isotope slope. Similarly, but with opposite effect, a hypothetical mass-dependent isotope effect that isotopically enriches O_3 will deplete $O(^1D)$ and CO_2, thereby increasing the three-isotope slope. Broadband O_3 photolysis in the stratosphere appears to mass-dependently enrich the remaining O_3 (9) which would increase the slope for CO_2. (Note that the existence of non-mass-dependent isotope effects in ozone photolysis have been proposed (50), but subsequent analysis (51) of those experimental results demonstrated that ozone formation was in fact responsible for the non-mass-dependent enrichments observed.) These experimental and modeling results support the hypothesis (18, 32) that temperature dependence of the O_3 formation KIEs and mass-dependent O_3 photolysis isotope effects likely cause the laboratory-stratosphere differences in the three-isotope slope for CO_2, although differences in the importance of other mass-dependent isotope effects between the laboratory and stratosphere leading to isotopic depletions in $O(^1D)$ or CO_2 cannot be ruled out.

Because the modeled $\ln^{17}O$-$\ln^{18}O$ relationship for CO_2 depends on temperature and O_3 photolysis wavelengths and rates, which vary with altitude and latitude, these variables are the likely origin of the observed regional differences in stratospheric $\ln^{17}O$-$\ln^{18}O$ relationships. Indeed, the O_3 isotopic composition in the upper stratosphere shows regional differences attributed to UV photolysis (9), which was estimated to contribute 25-30% of the total

enrichments in tropical O_3 versus only 20-25% at midlatitudes. Our model sensitivities suggest that larger tropical O_3 enrichments would increase the three-isotope slope of tropical CO_2 relative to the extratropics, consistent with inferences from our "mixed region" observations.

With larger three-isotope slopes in upper tropical CO_2, transport and mixing (which are much faster than CO_2-O_3 isotope exchange) then redistribute this tropical signal to other regions yet keep the slopes distinct, as for the CH_4:N_2O slopes. The larger tropical $\Delta\ln^{17}O/\Delta\ln^{18}O$ values are transported into the "mixed region" at 25±10°N at 25-40 km and will decrease as mixing into extratropical air proceeds (see below). Similarly, transport of this tropical upper stratospheric air by the residual circulation into the polar vortex generates the high $\Delta\ln^{17}O/\Delta\ln^{18}O$ values there, similar to the winter build-up of O_3 at high latitudes from the tropics (42). Since little photochemistry and vertical mixing occurs in the vortex, and a dynamic barrier at the vortex edge blocks most mixing with midlatitude air, the larger $\Delta\ln^{17}O/\Delta\ln^{18}O$ tropical values are maintained in the vortex. When the vortex breaks up in spring, vortex and midlatitude air mix, decreasing the slope to the extratropical value. For example, apparent vortex remnants sampled in May 1998 at 22 km show a slope of 1.7 (22). Tracer measurements in similar vortex remnants in 1997 demonstrate that such remnants have mixed extensively with midlatitude air by May-June (42, 52). End member mixing of high-N_2O and low-N_2O air produces a mixing line of slope 1.7 (Fig. 2-1; SI Appendix (Table 2-S6)) using two samples with ranges of N_2O concentrations similar to air that mixed during and after the 1997 vortex break-up (42, 52) and, more generally, similar to the mixing of low-N_2O and high-N_2O air that occurs on much larger spatial and temporal scales that are known to result in different CH_4:N_2O relationships in the tropics and extratropics (46).

Transport and mixing can also explain the larger scatter in slope in the lower stratosphere noted above. For example, $\Delta\ln^{17}O/\Delta\ln^{18}O$ values for N_2O<~220 ppbv are >1.7, but for N_2O>~220 ppbv they vary between ~0.5 and 1.7, are roughly inversely correlated with N_2O, and increase with increasing $\Delta^{17}O$ (Fig. 2-3). Moreover, the few outliers to the $\Delta^{17}O$ and inverse N_2O trends can be explained by (1) the degree of mixing of lower-N_2O air from higher altitudes with higher-N_2O air at lower altitudes, or (2) the fact that the samples are from the lowermost stratosphere (θ<380K), which is a mixture of stratospheric air with air recently transported from the troposphere. These characteristics suggest that such lower stratospheric mixing creates real atmospheric variability in $\Delta\ln^{17}O/\Delta\ln^{18}O$ values ranging between the entry (tropospheric) value of ~0.5 to values $\geq$1.7 (see also **SI Appendix**).

In summary, we have shown that room temperature laboratory measurements of CO_2-O_3 isotope exchange near an atmospheric O_2/CO_2 mixing ratio can be quantitatively predicted with a first principles photochemical model and results in a linear $\ln^{17}O$-$\ln^{18}O$ relationship for CO_2 of 1.2 (starting with tropospheric O_2 and CO_2 isotopic compositions), while the $\ln^{17}O$-$\ln^{18}O$ relationship for stratospheric CO_2 can vary systematically with latitude, altitude, and time, ranging up to 2.2 in a sometimes curvilinear manner. Model sensitivities suggest that the laboratory-stratosphere and regional stratospheric differences originate from differences in mass-dependent isotope fractionation in O_3 photolysis and in temperature due to the temperature dependence of the non-mass-dependent isotope effects in O_3 formation. The latitude, altitude, and seasonal dependence of the observed three-isotope slopes suggests that stratospheric transport and mixing act to redistribute air with higher $\Delta\ln^{17}O/\Delta\ln^{18}O$ values for CO_2 from the tropical source region to the subtropics and into the polar vortex and then homogenize these higher values to the extratropical background of 1.7. Additional CO_2 isotope measurements in the tropics could validate our hypothesis that the three isotope slopes are greater there and

provide additional constraints on photolysis isotope effects and the temperature dependence of the O_3 formation KIEs, which also need further laboratory investigations. 2D and 3D atmospheric models that include the latitude and altitude dependencies of the isotope chemistry inferred here and that can simulate realistic transport barriers are also needed. For ^{17}O anomalies in tropospheric CO_2 (34), in O_2 on short (35, 36) and glacial-interglacial (37, 38) timescales, in ancient mineral sulfates (39), and in fossilized bioapatite (40), we note the following: On one hand, productivity estimates for the current terrestrial and oceanic biospheres are on sounder footing since the isotope chemistry is no longer mysterious. Furthermore, these large three-isotope slopes do not affect previous estimates of the annual mean flux of $\Delta^{17}O$ of CO_2 to the troposphere since $\Delta^{17}O$ is still similarly well-correlated with N_2O in the lower stratosphere (SI Appendix (Fig. 2-S4)) (23). Importantly, the magnitude of $\Delta^{17}O$ matters more than the magnitude of the three-isotope slopes, a point which is often overlooked. On the other hand, a sensitivity of $\Delta^{17}O$ of CO_2 to the temperature dependence of the anomalous O_3 KIEs represents a possible caveat for longer timescale variations in $\Delta^{17}O$ of O_2, mineral sulfates, and bioapatite. While Luz *et al.* (37) already elucidated the need to consider past changes in O_3 and CO_2 levels on $\Delta^{17}O$ of O_2, variations in stratospheric temperatures as climate changed may also affect $\Delta^{17}O$ anomalies, especially if the temperature dependencies of the O_3 KIEs are larger than estimated here.

Materials and Methods

Atmospheric Samples: Air samples were collected between 29 and 79°N and 11 and 21 km by the Whole Air Sampler instrument during the SOLVE mission (42) in January–March 2000 and at 34.5°N between 27 and 33 km by the Cryogenic Whole Air Sampler instrument aboard a high-altitude scientific balloon (43) launched from Fort Sumner, NM, in September 2004. Mixing ratios of trace gases in the samples were measured at the University of Miami or the National Center for Atmospheric Research (NCAR), including N_2O and CH_4 using an HP5890 II+ series GC, prior to shipment to UC Berkeley. At UC Berkeley, CO_2 was separated from air and any residual water in a series of 5 liquid N_2 and –75.5ºC ethanol–LN_2 traps, respectively. The resulting aliquots of 30–60 μmol of CO_2 were flame sealed into glass ampoules for subsequent IRMS analysis. Several samples exhibited water levels higher than stratospheric air (typically <10 ppmv), indicating the sampler manifolds may have been temporarily contaminated with water. To eliminate potential artifacts from isotope exchange between CO_2 and H_2O either in the sample canisters or during the cryogenic separation that could increase $\Delta\ln^{17}O/\Delta\ln^{18}O$ values, samples with residual water > 20 ppmv have been eliminated from analysis (See **SI Appendix**).

Laboratory Experiments: Mixtures of O_2 (Scott Specialty Gases, 99.999%) and CO_2 (Scott Specialty Gases, 99.998%) close to the atmospheric ratio ($O_2/CO_2 \approx 450$) were introduced into a 2.2L borosilicate glass bulb fitted with a fused quartz (Heraeus-Amersil, Inc.) "finger" extending into the interior of the bulb. A low-pressure Hg/Ar pen lamp (Oriel Instruments) with major emission lines at 184.9 nm and 253.7 nm was placed in the quartz finger to irradiate the bulb from the center. After irradiation for 0 to 190 hours, the CO_2 and resulting O_3 were separated cryogenically from O_2 using liquid nitrogen and were transferred to a sample tube containing nickel shavings. After heating at 60°C for 15 minutes to decompose O_3, the CO_2 was separated cryogenically from the resulting O_2 with liquid nitrogen and then measured by IRMS. In some experiments, the isotopic composition of O_3 was determined by measuring the O_2 from O_3 decomposition at m/z values of 32, 33, and 34 by IRMS.

IRMS Measurements: The triple oxygen isotope composition of CO_2 was measured on a Finnigan MAT 252 isotope ratio mass spectrometer at UC Berkeley using the CeO_2 equilibration technique (44) on 12-18 μmol aliquots of the purified CO_2 from the whole air samples or the purified CO_2 from the laboratory experiments. Corrections to the IRMS signals for the presence of N_2O in the stratospheric CO_2 samples prior to CeO_2 equilibration were made using measurements of the mixing ratio and isotopic composition of N_2O made directly on the stratospheric whole air samples. External 1σ measurement precisions (N=104 over 2 years) for $\ln^{18}O$, $\ln^{17}O$, and $\Delta^{17}O$ of CO_2 were ±0.05‰, ±0.2‰, and ±0.2‰, respectively, where $\Delta^{17}O=\ln^{17}O-0.528\ \ln^{18}O$. Including accuracy (see **SI Appendix**) yields overall 1σ uncertainties of ±0.1‰, ±0.5‰, and ±0.5‰, respectively.

Photochemical Kinetics Model: The isotope-specific reaction kinetics occurring in the laboratory reaction bulb were predicted with KINTECUS software (53) using the Modified Bader-Deuflhard integrator to solve the system of stiff differential equations. The model is based on a previous model of O_2-O_3 isotope photochemistry (51) modified to include reactions relevant for CO_2. In the "base model," only KIEs in O_3 formation and $O+O_2$ isotope exchange were included, as measured or derived in earlier studies (10, 11). The pressure dependence of the O_3 formation KIEs was derived from the O_3 formation KIEs at low pressure and the pressure dependence of the O_3 isotopic enrichments (54-56). In the model runs investigating sensitivity to temperature, the temperature dependence of the O_3 formation KIEs was based on a combination of measurements of the temperature dependence of the KIEs for formation of the ^{18}O-containing O_3 isotopomers (47) and the temperature dependence of the ^{18}O and ^{17}O enrichments in O_3 (9, 47) In model runs investigating sensitivity to possible isotope effects in O_3 photolysis, a theoretical value at 254 nm from Liang *et al.* (48, 49) was used, as well as hypothetical limiting values for normal and inverse isotope effects. See the **SI Appendix** for more details regarding the measurements and calculations.

References

1. Thiemens MH (2006) History and applications of mass-independent isotope effects. *Ann. Rev. Earth Planetary Sci.* 34:217-262.
2. Luz B & Barkan E (2005) The isotopic ratios $^{17}O/^{16}O$ and $^{18}O/^{16}O$ in molecular oxygen and their significance in biogeochemistry. *Geochim. Cosmochim. Acta* 69(5):1099-1110.
3. Urey HC (1947) The thermodynamic properties of isotopic substances. *J. Am. Chem. Soc.*:562-581.
4. Bigeleisen J & Goeppert Mayer M (1947) Calculation of equilibrium constants for isotopic exchange reactions. *J. Chem. Phys.* 15(5):261-267.
5. Clayton RN, Grossman L, & Mayeda TK (1973) Component of primitive nuclear composition in carbonaceous meteorites. *Science* 182(4111):485-488.
6. Thiemens MH & Heidenreich JE, III (1983) The mass-independent fractionation of oxygen: a novel isotope effect and its possible cosmochemical implications. *Science* 219:1073-1075.
7. Mauersberger K (1987) Ozone isotope measurements in the stratosphere. *Geophys. Res. Lett.* 14:80-83.
8. Clayton RN (2002) Solar System - Self-shielding in the solar nebula. *Nature* 415(6874):860-861.
9. Krankowsky D, *et al.* (2007) Stratospheric ozone isotope fractionations derived from collected samples. *J. Geophys. Res.* 112(D8):D08301.
10. Mauersberger K, Erbacher B, Krankowsky D, Gunther J, & Nickel R (1999) Ozone isotope enrichment: Isotopomer-specific rate coefficients. *Science* 283:370-372.
11. Janssen C, Guenther J, Mauersberger K, & Krankowsky D (2001) Kinetic origin of the ozone isotope effect: a critical analysis of enrichments and rate coefficients. *Phys. Chem. Chem. Phys.* 3(21):4718-4721.
12. Mauersberger K, Krankowsky D, Janssen C, & Schinke R (2005) Assessment of the ozone isotope effect. *Adv. Atomic Molec. Optical Phys.*, eds Bederson B & Walther H (Elsevier Academic Press Inc.), Vol 50, pp 1-54.
13. Gao YQ & Marcus RA (2001) Strange and unconventional isotope effects in ozone formation. *Science* 293(5528):259-263.
14. Schinke R, Grebenshchikov SY, Ivanov MV, & Fleurat-Lessard P (2006) Dynamical studies of the ozone isotope effect: A status report. *Ann. Rev. Phys. Chem.* 57:625-661.
15. Ivanov MV, Grebenshchikov SY, & Schinke R (2009) Quantum mechanical study of vibrational energy transfer in Ar-O_3 collisions: Influence of symmetry. *J. Chem. Phys.* 130(17):174311.
16. Kryvohuz M & Marcus RA (2010) Coriolis coupling as a source of non-RRKM effects in ozone molecule: Lifetime statistics of vibrationally excited ozone molecules. *J. Chem. Phys.* 132(22):224305.
17. Ghaderi N & Marcus RA (2011) Bimolecular Recombination Reactions: Low Pressure Rates in Terms of Time-Dependent Survival Probabilities, Total J Phase Space Sampling of Trajectories, and Comparison with RRKM Theory. *J. Phys. Chem. B* 115(18):5625-5633.
18. Brenninkmeijer CAM, *et al.* (2003) Isotope effects in the chemistry of atmospheric trace compounds. *Chem. Rev.*103(12):5125-5161.

19. Thiemens MH, Jackson T, Zipf EC, Erdman PW, & van Egmond C (1995) Carbon dioxide and oxygen isotope anomalies in the mesosphere and stratosphere. *Science* 270:969-972.
20. Zipf E & Erdman PW (1994) Trace constituents in the upper stratosphere and mesosphere using cryogenic whole sampling techniques. *1992-1993 UARP Research Summaries: Report to Congress*.
21. Alexander B, Vollmer MK, Jackson T, Weiss RF, & Thiemens MH (2001) Stratospheric CO_2 isotopic anomalies and SF_6 and CFC tracer concentrations in the Arctic polar vortex. *Geophys. Res. Lett.* 28(21):4103-4106.
22. Lammerzahl P, Rockmann T, Brenninkmeijer CAM, Krankowsky D, & Mauersberger K (2002) Oxygen isotope composition of stratospheric carbon dioxide. *Geophys. Res. Lett.* 29(12):1582.
23. Boering KA, *et al.* (2004) Observations of the anomalous oxygen isotopic composition of carbon dioxide in the lower stratosphere and the flux of the anomaly to the troposphere. *Geophys. Res. Lett.* 31(3):L03109.
24. Kawagucci S, *et al.* (2008) Long-term observation of mass-independent oxygen isotope anomaly in stratospheric CO_2. *Atm. Chem. Phys.* 8:6189-6197.
25. Yung YL, Lee AYT, Irion FW, DeMore WB, & Wen J (1997) Carbon dioxide in the atmosphere: Isotopic exchange with ozone and its use as a tracer in the middle atmosphere. *J. Geophys. Res.* 102(DD9):10857-10866.
26. Perri MJ, Van Wyngarden AL, Boering KA, Lin JJ, & Lee YT (2003) Dynamics of the $O(^1D)+CO_2$ oxygen isotope exchange reaction. *J. Chem. Phys.* 119(16):8213-8216.
27. Liang MC, Blake GA, Lewis BR, & Yung YL (2007) Oxygen isotopic composition of carbon dioxide in the middle atmosphere. *Proc. Nat. Acad. Sci.* 104(1):21-25.
28. Liang MC, Blake GA, & Yung YL (2008) Seasonal cycle of $C^{16}O^{16}O$, $C^{16}O^{17}O$, and $C^{16}O^{18}O$ in the middle atmosphere: Implications for mesospheric dynamics and biogeochemical sources and sinks of CO_2. *J. Geophys. Res.* 113:D12305.
29. Wen J & Thiemens MH (1993) Multi-isotope study of the $O(^1D) + CO_2$ exchange and stratospheric consequences. *J. Geophys. Res.* 98(D7):12801-12808.
30. Johnston JC, Rockmann T, & Brenninkmeijer CAM (2000) $CO_2 + O(^1D)$ isotopic exchange: Laboratory and modeling studies. *J. Geophys. Res.* 105(D12):15213-15229.
31. Chakraborty S & Bhattacharya SK (2003) Experimental investigation of oxygen isotope exchange between CO_2 and $O(^1D)$ and its relevance to the stratosphere. *J. Geophys. Res.* 108(D23):4724.
32. Shaheen R, Janssen C, & Rockmann T (2007) Investigations of the photochemical isotope equilibrium between O_2, CO_2 and O_3. *Atm. Chem. Phys.* 7:495-509.
33. Mauersberger K, Krankowsky D, & Janssen C (2003) Oxygen isotope processes and transfer reactions. *Space Sci. Rev.* 106(1-4):265-279.
34. Hoag KJ, Still CJ, Fung IY, & Boering KA (2005) Triple oxygen isotope composition of tropospheric carbon dioxide as a tracer of terrestrial gross carbon fluxes. *Geophys. Res. Lett.* 32(2):L02802.
35. Luz B & Barkan E (2000) Assessment of oceanic productivity with the triple-isotope composition of dissolved oxygen. *Science* 288:2028-2031.
36. Juranek LW, *et al.* (2012) Biological production in the NE Pacific and its influence on air-sea CO_2 flux: Evidence from dissolved oxygen isotopes and O_2/Ar. *J. Geophys. Res. Oceans* 117:23.

37. Luz B, Barkan E, Bender ML, Thiemens MH, & Boering KA (1999) Triple-isotope composition of atmospheric oxygen as a tracer of biosphere productivity. *Nature* 400(6744):547-550.
38. Blunier T, Barnett B, Bender ML, & Hendricks MB (2002) Biological oxygen productivity during the last 60,000 years from triple oxygen isotope measurements. *Global Biogeochem Cycles* 16(3):1029.
39. Bao HM, Lyons JR, & Zhou CM (2008) Triple oxygen isotope evidence for elevated CO_2 levels after a Neoproterozoic glaciation. *Nature* 453(7194):504-506.
40. Gehler A, Tuetken T, & Pack A (2011) Triple oxygen isotope analysis of bioapatite as tracer for diagenetic alteration of bones and teeth. *Palaeogeography Palaeoclimatology Palaeoecology* 310(1-2):84-91.
41. Flocke F, *et al.* (1999) An examination of chemistry and transport processes in the tropical lower stratosphere using observations of long-lived and short-lived compounds obtained during STRAT and POLARIS. *J. Geophys. Res.* 104:26625-26642.
42. Newman PA, *et al.* (2002) An overview of the SOLVE/THESEO 2000 campaign. *J. Geophys. Res.* 107(D20):8259.
43. Froidevaux L, *et al.* (2006) Early validation analyses of atmospheric profiles from EOS MLS on the Aura satellite. *IEEE Trans. Geosci. Remote Sensing* 44(5):1106-1121.
44. Assonov SS & Brenninkmeijer CAM (2001) A new method to determine the ^{17}O isotopic abundance in CO_2 using oxygen isotope exchange with a solid oxide. *Rapid Comm. Mass Spectrom.* 15(24):2426-2437.
45. Greenblatt JB, *et al.* (2002) Tracer-based determination of vortex descent in the 1999/2000 Arctic winter. *J. Geophys. Res.* 107(D20):8279.
46. Michelsen HA, Manney GL, Gunson MR, & Zander R (1998) Correlations of stratospheric abundances of CH_4 and N_2O derived from ATMOS measurements. *Geophys. Res. Lett.* 25:2777-2780.
47. Janssen C, Guenther J, Krankowsky D, & Mauersberger K (2003) Temperature dependence of ozone rate coefficients and isotopologue fractionation in ^{16}O-^{18}O oxygen mixtures. *Chem. Phys. Lett.* 367(1-2):34-38.
48. Liang MC, Blake GA, & Yung YL (2004) A semianalytic model for photo-induced isotopic fractionation in simple molecules. *J. Geophys. Res.* 109(D10):D10308.
49. Liang MC, *et al.* (2006) Isotopic composition of stratospheric ozone. *J. Geophys. Res.* 111:D02302.
50. Chakraborty S & Bhattacharya SK (2003) Oxygen isotopic fractionation during UV and visible light photodissociation of ozone. *J. Chem. Phys.* 118(5):2164-2172.
51. Cole AS & Boering KA (2006) Mass-dependent and non-mass-dependent isotope effects in ozone photolysis: Resolving theory and experiments. *J. Chem. Phys.* 125(18):184301.
52. Rex M, *et al.* (1999) Subsidence, mixing, and denitrification of Arctic polar vortex air measured During POLARIS. *J. Geophys. Res.* 104(D21):26611-26623.
53. Ianni JC (Kintecus), Windows Version 3.962.
54. Morton J, Barnes J, Schueler B, & Mauersberger K (1990) Laboratory studies of heavy ozone. *J. Geophys. Res.* 95(D1):901-907.
55. Thiemens MH & Jackson T (1988) New experimental evidence for the mechanism for production of isotopically heavy O_3. *Geophy. Res. Lett.* 15(7):639-642.
56. Thiemens MH & Jackson T (1990) Pressure dependency for heavy isotope enhancement in ozone formation. *Geophys. Res. Lett.* 17(6):717-719.

57. Feilberg KL, Wiegel AA, & Boering KA (2013) Probing the unusual isotope effects in ozone formation: Bath gas and pressure dependence of the non-mass-dependent isotope enrichments in ozone. *Chem. Phys. Lett.* 556:1-8.

Fig. 2-1. Stratospheric CO_2 observations. Three isotope plot for the balloon (34°N) and "SOLVE" aircraft (24-83°N) samples, with previous observations: *Thiemens* (19) and *Zipf & Erdman* (20) are rocket samples from ~34°N. *Lämmerzahl* (22) are balloon samples from 44° and 68°N. *Alexander* (21) are balloon samples from 68°N. *Kawagucci* (24) are balloon samples from 39° and 68°N. Data from *Boering et al.* (23) are not shown because of an analytical mass-dependent artifact that affects $\ln^{17}O$ and $\ln^{18}O$ but not $\Delta^{17}O$. The mass-dependent fractionation line with slope 0.528 (red) and a hypothetical end member mixing line (black) with slope 1.7 (SI Appendix (Table 2-S6)) are also shown. The overall 1σ uncertainties for the SOLVE and Balloon 2004 data including both external precision and accuracy are ±0.1‰ for $\ln^{18}O$ and ±0.5‰ for $\ln^{17}O$.

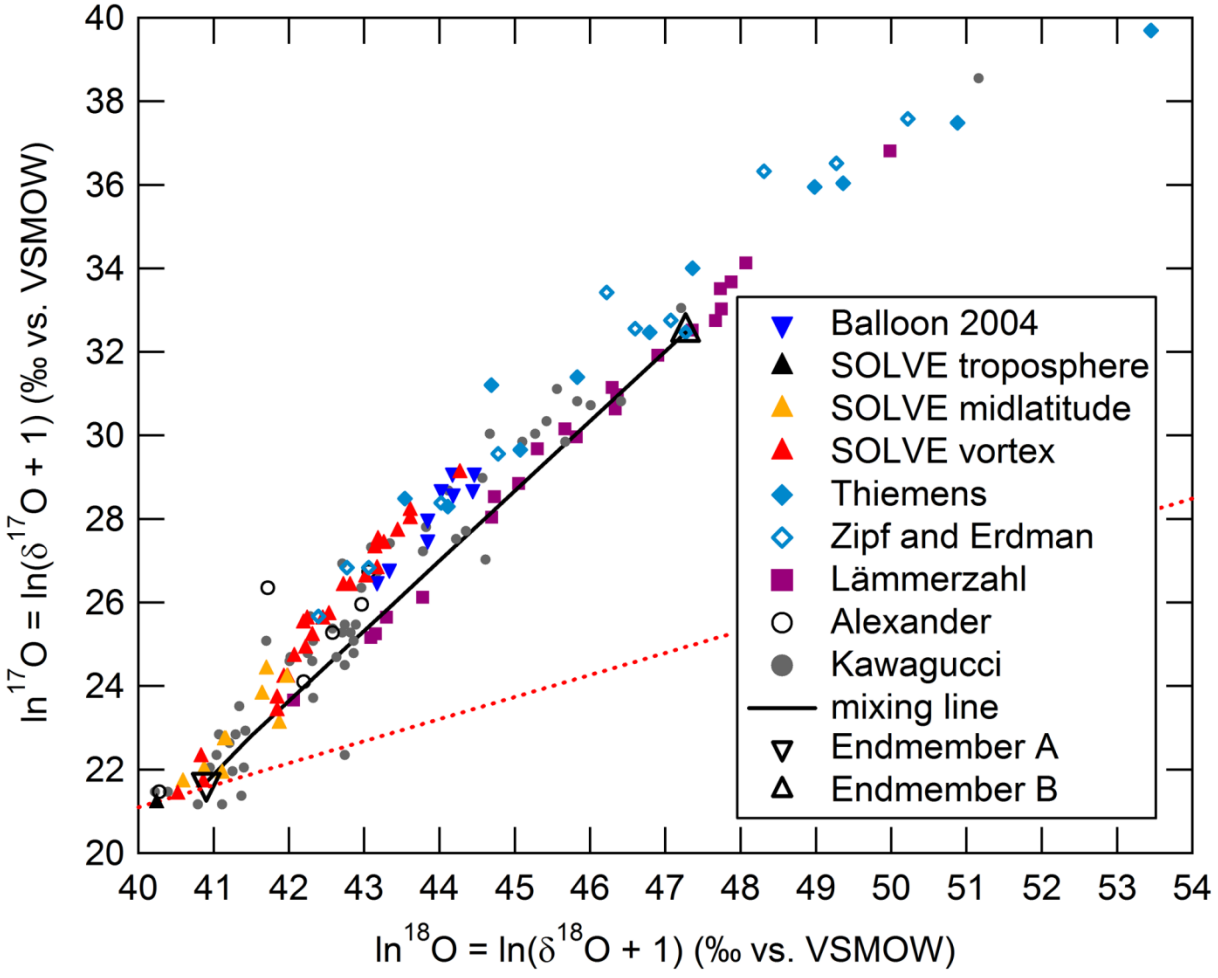

Fig. 2-2. Experimental versus Model Results. Time evolution of the CO_2 isotopic composition for the 50 Torr (**A**) and 100 Torr (**B**) UV irradiation experiments (symbols) and predictions from a photochemical kinetics model (lines). Shaded area shows uncertainty in the base model predictions, dominated by a conservative estimate of the uncertainty in $k_{asymmetric}$ for $^{17}O^{16}O^{16}O$ formation. (**C**) and (**D**): Same as (**A**) and (**B**) in a three-isotope plot. Also included in different model scenarios (SI Appendix (Table 2-S9)) shown here are theoretical mass-dependent ("MD") isotope effects in O_3 photolysis at 254 nm (48); and large, hypothetical "normal" and "inverse" MD O_3 photolysis isotope effects to illustrate how the three-isotope slope for CO_2 is increased ("normal") or decreased ("inverse") along a mass-dependent line of slope 0.528 (red dotted line) as the MD isotope effects change the isotopic composition of O_3 and $O(^1D)$, while leaving $\Delta^{17}O$ (Table 2-2) essentially unchanged (to within small differences in the MD coefficients, λ, in $\Delta^{17}O=\ln^{17}O-\lambda\ln^{18}O$, which can range from 0.500 to 0.529 (2)). Under these laboratory conditions, there is only one $O(^1D)$ isotopic composition, so the CO_2 isotopic composition evolves along a straight line connecting the $O(^1D)$ isotopic composition with that of the initial CO_2.

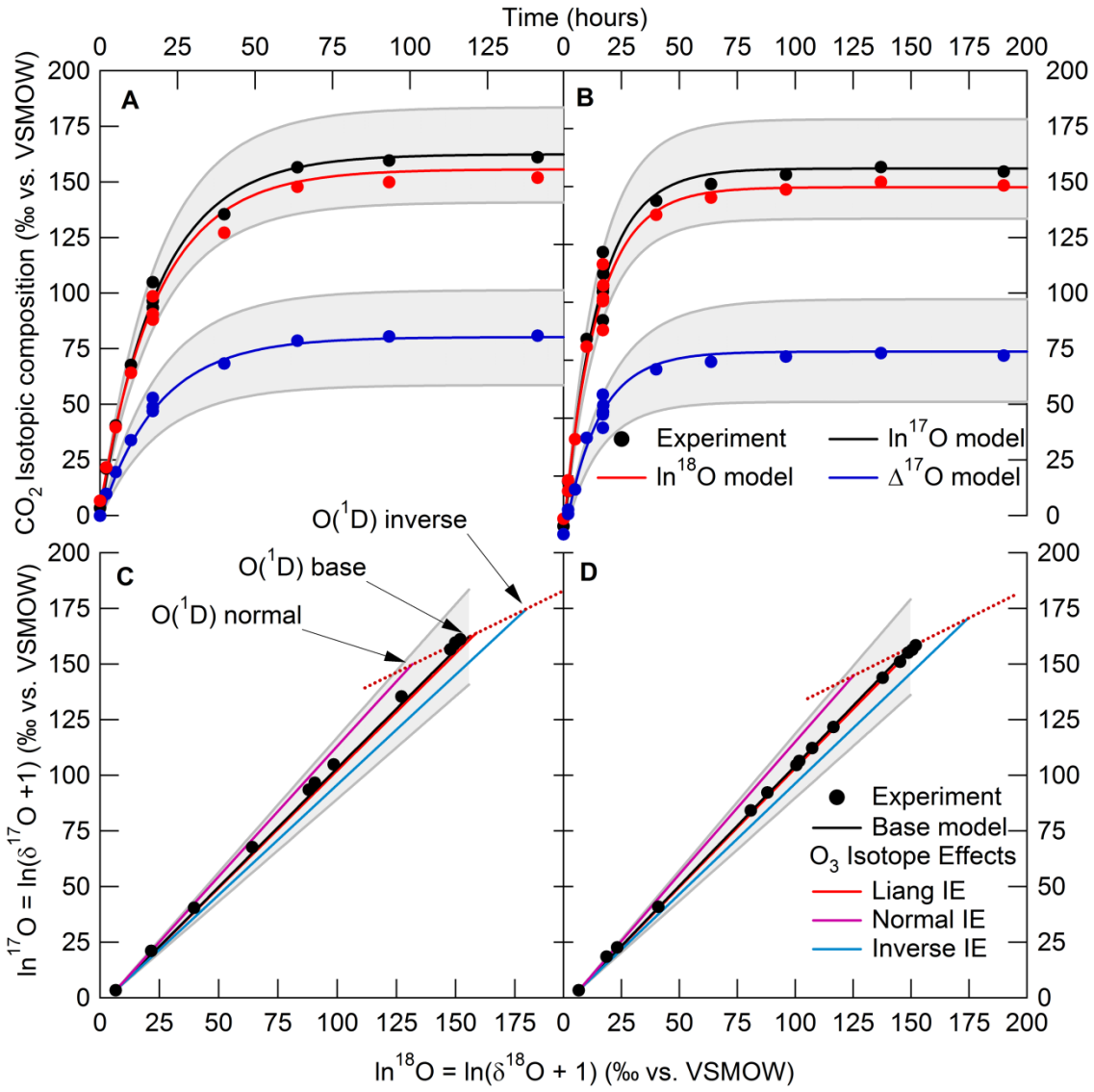

Fig. 2-3. $\Delta\ln^{17}O/\Delta\ln^{18}O$ of CO_2 versus **(A)** N_2O mixing ratio and **(B)** $\Delta^{17}O$ of CO_2; $\Delta\ln^{17}O/\Delta\ln^{18}O = 1.7$ is shown (dashed line) for reference. In general, the $\Delta\ln^{17}O/\Delta\ln^{18}O$ values increase from a tropospheric, near-mass-dependent value to >1.6 as N_2O decreases and $\Delta^{17}O$ of CO_2 increases, explaining at least part of the larger observed variability in $\Delta\ln^{17}O/\Delta\ln^{18}O$ in the lower stratosphere where "younger," high N_2O air mixes with "older," lower N_2O air. Note that, for these samples, the trends in $\Delta\ln^{17}O/\Delta\ln^{18}O$ are still apparent (even though the values change) even if we assume that the entry value for $\ln^{18}O$ of CO_2 entering the stratosphere from the troposphere can vary by ±0.5, either by applying the same offset for every point or by mimicking a seasonal variation within the dataset, and even though the overall 1σ uncertainty in the $\ln^{17}O$ measurements including both accuracy and precision is ±0.5‰.

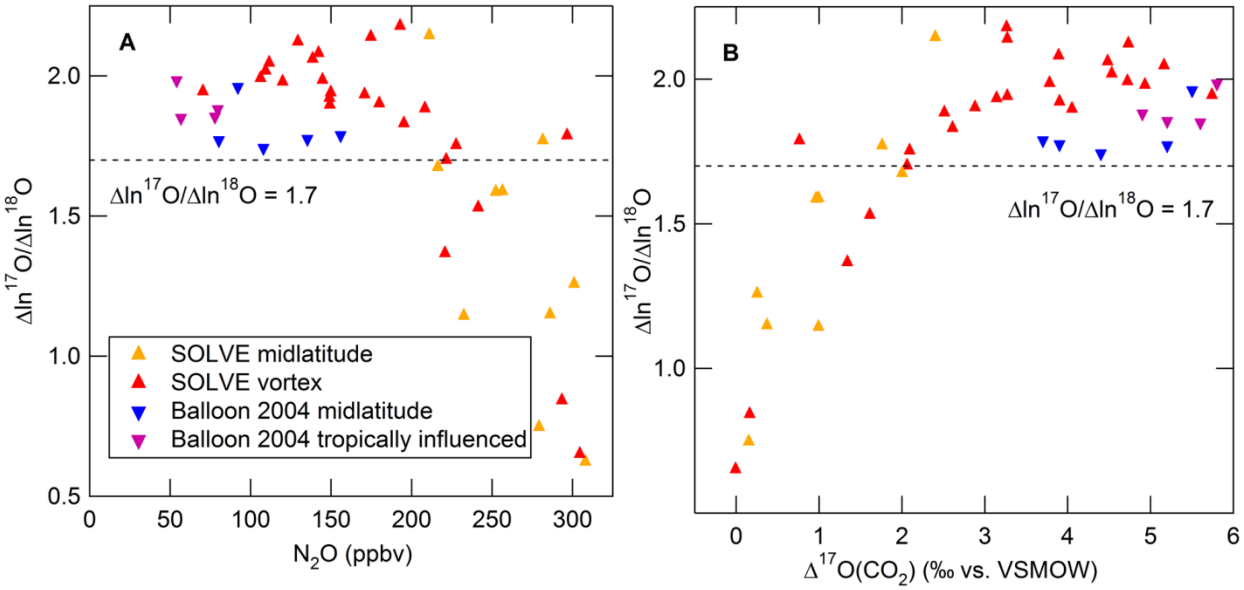

Table 2-1. Summary of $\ln^{17}O/\ln^{18}O$ slopes for stratospheric CO_2

Source	Dates	Region	Altitude (km)	N	Slope (±1σ)
SOLVE	12/99-3/00	High latitude/vortex	11 – 20	24	2.22 ± 0.07
SOLVE	12/99-3/00	High latitude/non-vortex and midlatitude	11 – 20	11	1.7 ± 0.2
SOLVE + Balloon	12/99-3/00, 9/04	High latitude/non-vortex and midlatitude	11 – 33	20	1.95 ± 0.05

Table 2-2. Isotopic compositions from photochemistry experiments and kinetics modeling at 50 Torr on the VSMOW scale. The modeled $O(^1D)$ isotopic composition is identical to that for CO_2 since isotope effects in the $O(^1D) + CO_2$ isotope exchange reaction were not included in these model scenarios. Results for 100 Torr are shown in Table 2-S11.

Description	**CO_2***				**O_3†**			
	$\ln^{17}O$	**$\ln^{18}O$**	**Slope**	**$\Delta^{17}O$‡**	**$\ln^{17}O$**	**$\ln^{18}O$**	**Slope**	**$\Delta^{17}O$‡**
Experiment:	160 ± 1	151 ± 1	1.075 ± 0.004	80.7 ± 1.3	114 ± 7	138 ± 8	0.83 ± 0.07	41 ± 6
Model:								
Base Scenario	163	156	1.067	80.3	113	139	0.81	39.2
Liang photolysis IE §	164	159	1.056	80.2	110	134	0.82	39.3
Normal photolysis IE	150	132	1.172	80.4	119	151	0.79	39.2
Inverse photolysis IE	175	180	0.989	79.7	107	127	0.84	39.5
Tropopause O_2 and CO_2	161	153	1.24	80.4	111	136	0.82	39.4
" " and T = 250K	140	124	1.41	74.5	96	117	0.83	34.8
" " and T = 220K	126	105	1.61	70.7	87	104	0.83	31.8
" " and T = 200K	117	92	1.84	68.0	80	95	0.84	29.7

* Experimental results for CO_2 are an average (N=2, ±1σ) of the measured values at isotopic steady-state.

† Experimental results for O_3 are an average (N=2, ±1σ combined error) of previous results at 50 Torr (54, 57).

‡ $\Delta^{17}O = \ln^{17}O - 0.528 \ln^{18}O$.

§ Theoretical mass-dependent O_3 photolysis isotope effect at 254 nm (48).

SI Appendix

S1.1 Stratospheric samples

Whole air samples were collected by the WAS instrument (1) on board the NASA ER-2 aircraft during the SOLVE mission (2) from flights out of the NASA Dryden Flight Research Center (California, USA, 35°N, 118ºW), Westover Air Reserve Base (Massachusetts, USA, 42° N, 72° W), and Kiruna (Sweden, 68°N, 20°E) and by a new Cryogenic Whole Air Sampler (CWAS) (3), based on an earlier instrument design (4), on a high-altitude scientific balloon flight in September 2004 out of the NASA Scientific Balloon Flight Facility in Fort Sumner (New Mexico, USA, 34°N, 104°W). The WAS instrument consists of 32 electropolished, 1.6 liter, stainless steel canisters connected in series through a manifold to a 4-stage metal-bellows compressor. The compressor draws ambient air in through the instrument inlet and compresses the gas into the manifold; each sample canister valve is actuated under computer control and the cans are each pressurized to 40 psi (~4.4 standard liters). Canister fill times depend on aircraft altitude and range from approximately 45 seconds at 15 km to 180 seconds at 21 km. Canisters are baked and pumped out on a vacuum line prior to flight. For cans intended for the CO_2 oxygen isotope measurements, no additional pre-flight treatment was performed, while cans intended for halocarbon measurements were backflushed with wet air. The WAS samples were not dried during acquisition since the stratosphere is very dry (generally ≤ 10 ppmv water vapor); higher levels of atmospheric water, as in the lower atmosphere, can result in artifacts in the measured isotopic composition of sample CO_2 due to oxygen isotope exchange between CO_2 and H_2O (see Section 1.2 for further discussion). The CWAS instrument consists of a manifold of 26 electropolished, 800mL stainless steel canisters, which are immersed in liquid neon to serve as a cryopump when each motor-driven canister valve is actuated. Airflow into each canister is monitored by pressure changes in the manifold and the canisters are filled to pressures of 245-310 psi. As for the WAS instrument, the samples are not dried during collection. After sample collection, the mixing ratios of a number of trace gases in the whole air samples were measured at the University of Miami or the National Center for Atmospheric Research (NCAR), including N_2O and CH_4 using an HP5890 II+ series GC and NIST-traceable standards to precisions of 0.1% and 0.3%, respectively.

S1.2 CO_2 Isotope Measurements

After trace gas mixing ratio measurements, whole air samples were shipped to UC Berkeley, where ~30-60 µmol of CO_2 (depending on canister size and pressure) was purified cryogenically using liquid nitrogen on five cold traps. The CO_2 was released from each trap using a liquid nitrogen-ethanol slurry at -95°C to trap any residual H_2O. The CO_2 was then measured and flame sealed for storage in ¼-inch OD borosilicate glass ampoules resulting in 47 samples from the SOLVE mission and for 25 CWAS samples from the 2004 balloon flight. On the day of an isotopic measurement, the ampoules were cracked open on a high vacuum line and one-half to one-third of each sample was transferred to a sample tube for the IRMS measurement while the remaining portion was re-sealed in a new ampoule. Measurements of $^{14}N/^{15}N$ ratios of N_2 on a subset of samples confirm that the isotopes should be fractionated by <0.1‰ during the whole air collection process, while an estimate of fractionation for the cryogenic separation and subsequent sample transfers and splitting was found to be <0.1‰ through measurements of CO_2

extracted from a 360ppmv CO_2 laboratory standard of known isotopic composition using the identical processes as for the whole air samples from the balloon and aircraft flights.

To measure $\ln^{17}O$, $\ln^{18}O$, and $\ln^{13}C$ of CO_2, we used the method of Assonov and Brenninkmeijer (5) that requires two separate measurements to be made due to an isobaric interference between $^{13}C^{16}O^{16}O$ and $^{12}C^{16}O^{17}O$. First, the m/z 44, 45 and 46 values of CO_2 were measured on a Finnigan MAT 252 isotope ratio mass spectrometer (IRMS) in dual inlet mode against a working laboratory standard. The working laboratory standard was calibrated by measuring it against three NIST standard reference materials (RM8562=CO_2 Heavy/Paleomarine Origin; RM8563=CO_2 Light/Petrochemical Origin; and RM8564=CO_2 Biogenic/Modern Biomass Origin), yielding an isotopic composition of $\ln^{13}C = -2.40\pm 0.01$ (1σ) ‰ PDB, $\ln^{18}O$ = 28.50 ± 0.06 (1σ) ‰ VSMOW, and $\ln^{17}O$ = 15.05 ± 0.03 (1σ) ‰ VSMOW. Second, the CO_2 was then transferred cryogenically from the IRMS and then equilibrated with powdered CeO_2 on a separate vacuum line for 15 minutes at 650°C. After confirming complete recovery of the sample from the CeO_2 equilibration (with measured yields ranging from 99.8 to 100.2%), the m/z 44, 45 and 46 values were then measured a second time. The final values for $\ln^{13}C$, $\ln^{18}O$ and $\ln^{17}O$ were calculated from equations given in Assonov & Brenninkmeijer (5) using the parameters $^{13}R_{PDBCO2} = 0.0112372$, $^{17}R_{PDBCO2} = 0.00039511$, $^{18}R_{PDBCO2} = 0.00208835$, and λ_{std} = 0.528 (6). Each day that stratospheric samples were run, at least one aliquot of one or more anomalous CO_2 laboratory standards that we produced by irradiating mixtures of O_2 and CO_2 with a mercury lamp were also run. To avoid possible memory effects, the CeO_2 powder was flushed with high purity O_2 after every 14 runs. Repeated measurements (totaling N=104) over 2 years of one mass-dependent (N=26) secondary standard and four anomalous CO_2 standards with $\Delta^{17}O$ values equal to 2.45 (N=44), 4.67 (N=19), 18.18 (N=4) and 22.97 (N=11) yielded an overall external 1σ measurement precision of 0.05‰ for $\ln^{18}O$ and 0.2‰ for $\ln^{17}O$ and $\Delta^{17}O$. Finally, because we have not directly measured the isotopic composition of the commercial CeO_2 used for our measurements (which can have a small ^{17}O anomaly itself on a scale of ~0.1‰ due both to the production process and to flushing with O_2, which also has a small ^{17}O anomaly (7)), we estimate that the overall uncertainty in our reported values for $\ln^{17}O$ and $\Delta^{17}O$, including both accuracy and precision, is ±0.5‰.

Because the stratospheric samples contain a small amount of N_2O, the N_2O isobaric interferences with CO_2 at m/z 44, 45, and 46 must be corrected for in the initial pre-equilibrated IRMS measurements of CO_2. However, because the high-temperature CeO_2 step converts N_2O to N_2 and O_2, N_2O does not interfere with the post-equilibration IRMS measurement (8). Both N_2O mixing ratios and the N_2O isotope ratios (^{45}R and ^{46}R) were measured on the SOLVE and Balloon 2004 samples of this study. Thus, these N_2O measurements, combined with the relative ionization efficiency of N_2O and CO_2 measured for the UCB MAT 252 IRMS (E = 0.6958 ± 0.0066), can therefore be used to correct for this interference for each sample. An "ion productivity" *A* is first calculated using the mixing ratio ρ of N_2O to CO_2:

$$\rho = \frac{[N_2O]}{1000\times[CO_2]}$$
$$A = \frac{\rho \times E}{1+{}^{45}R_{N_2O}+{}^{46}R_{N_2O}} \qquad \text{(S1)}$$

The measured pre-equilibration ln values for CO_2 are then converted to isotope ratios and used to calculate mass correction factors for N_2O.

$$p = A\times({}^{45}R_{pre-uncorr} - {}^{45}R_{N_2O})$$
$$p' = A\times({}^{46}R_{pre-uncorr} - {}^{46}R_{N_2O}) \quad \text{(S2)}$$

These mass correction factors are then used to correct the measured pre-equilibrated ^{45}R and ^{46}R values for the interference from N_2O.

$${}^{45}R_{pre-corr} = \frac{p\times({}^{46}R_{pre-uncorr} + p') + (1-p')\times({}^{45}R_{pre-uncorr} + p)}{(1-p)\times(1-p') - p\times p'}$$
$${}^{46}R_{pre-corr} = \frac{(1-p)\times({}^{46}R_{pre-uncorr} + p') + p'\times({}^{45}R_{pre-uncorr} + p)}{(1-p)\times(1-p') - p\times p'} \quad \text{(S3)}$$

These isotope ratios can then be converted back to δ or ln values for use in the CeO_2 calculations from Assonov and Brennikmeijer (5). For the datasets reported here, the correction ranged from +0.3 to +3‰ for $\ln^{17}O$ and from +0.1 to +0.7‰ for $\ln^{18}O$, with the larger corrections corresponding to samples with higher N_2O mixing ratios. This correction is critically important, since without it tropospheric CO_2 (and "young" stratospheric samples with high N_2O mixing ratios) would have incorrect $\Delta^{17}O$ values of –3‰ and values of $\ln^{17}O$ and $\ln^{18}O$ that would be significantly lower than tropospheric values.

Using the methods described above, the CO_2 isotopic composition was measured on 11 CWAS samples from the 2004 balloon flight and on 47 WAS samples from the SOLVE mission. Although 25 CWAS samples were collected, only 9 samples were found to be as dry as expected for the stratosphere (≤ 10 ppmv of water vapor), as indicated by the total amount of water collected during the extraction procedure and the sample size, suggesting a source of water contamination for a subset of the samples. The excess water may have come from the sample manifold during flight after exposure to atmospheric moisture from lower altitudes or to the water-treated sample canisters, although no pattern of order of sampling or proximity to wet canisters flown has been determined. Water contamination causes mass-dependent fractionation of CO_2 in such samples since water adsorbed on canister or extraction trap surfaces can exchange oxygen isotopes with CO_2 during storage or during the cryogenic extraction. Given the likely ranges of isotopic composition of water contamination and of stratospheric and tropospheric CO_2, such exchange should produce CO_2 that is depleted in ^{17}O and ^{18}O and typically results in a larger three-isotope slope than in the absence of such isotope exchange (until there is also a mass balance issue). Indeed, the CO_2 isotopic composition of two of the subset of "wet" CWAS samples was measured and found to be mass-dependently fractionated in this manner. Of the 47 WAS samples from the SOLVE mission measured for the CO_2 isotopic composition, 12 had excess water above that expected for the stratosphere. Therefore, as an objective criterion for rejection of samples affected by water contamination, samples were excluded from analysis, interpretation, figures and tables here if the extracted water corresponded to >20 ppmv in the canisters; this led to the rejection of 2 balloon samples and 12 SOLVE samples for which the CO_2 isotopic compositions were measured. At <20 ppmv of H_2O and 360-370 ppmv of CO_2, isotope exchange should have a negligible effect on our measured CO_2 isotopic compositions. Indeed, this is consistent with the fact that samples with the lowest canister water concentration also have the highest $\Delta\ln^{17}O/\Delta\ln^{18}O$ values within the subset of "dry" samples that pass our

water threshold criterion. For example, two samples that were not excluded by the water threshold criterion each have a $\Delta^{17}O$ value of 3.3‰, but the sample with the higher water concentration has a $\Delta\ln^{17}O/\Delta\ln^{18}O$ value of 1.94 while the sample with the lower water concentration has a $\Delta\ln^{17}O/\Delta\ln^{18}O$ value of 2.14. Thus, we are confident that real atmospheric variability rather than an artifact from isotope exchange with water in the canisters or during extraction is the source of the greater $\ln^{17}O/\ln^{18}O$ slopes we observe.

While the oxygen isotope measurements are discussed in detail in the main text and below, we note here for completeness that the $\ln^{13}C$ values for stratospheric CO_2 (shown in Tables 2-S1 and S2 below) all fall between −8.04 and −8.16‰ on the PDB scale for the 2004 balloon samples, in line with surface flask measurements by NOAA ESRL (http://www.esrl.noaa.gov/gmd/dv/iadv/graph.php?code=MLO&program=ccgg&type=ts) at Mauna Loa, Hawaii, between 1999 and 2004. These measured $\ln^{13}C$ values fall within the expected range for stratospheric air with mean ages between 0 and 5 years (9) and provide additional confidence in the measurements and sample robustness for samples with H_2O<20 ppmv.

S1.3 Stratospheric Context

To identify possible regional differences in the CO_2 isotope compositions, mixing ratio measurements of trace gases such as N_2O, CH_4, and others were used along with measurements of pressure altitude, latitude, and potential temperature (θ) in order to characterize the air sampled as polar vortex, midlatitude or midlatitude-like, or tropically-influenced. The high latitude (>55°N) SOLVE whole air samples were collected both outside and inside the winter polar vortex in the lower stratosphere, so we separated the vortex or vortex filament samples from midlatitude-like samples using the method of Greenblatt *et al.* (10). We qualitatively identified each sample as "midlatitude-like", "vortex", or "vortex edge" using the distinct correlations of measurements of θ and N_2O mixing ratios inside and outside the vortex (Fig. 3-S1). The vortex and vortex edge samples were then categorized as “polar vortex”, and the midlatitude-like and midlatitude samples were categorized as “midlatitude” in the tables and figures of this study. These regional designations are given in Tables 2-S1 and 2-S2 for each sample. Similarly, vertical profiles near 34°N of CH_4 and N_2O for the rocket samples of Thiemens *et al.* (11) and for our balloon data show that air characteristic of more equatorial regions was sampled at various altitudes on these flights. These more tropical-like filaments of air are evident in excursions of CH_4 and N_2O to higher values, as shown in Fig. 2-S2 and 2-S3 for CH_4.

Once separated into regional subsets, the bivariate linear least squares regressions (12) of the data subsets were calculated. Homogeneity of regression tests (Table 2-S5) indicate that the slopes calculated for the vortex and the midlatitude subsets are statistically different at the 99% confidence interval from the slope of the *Lämmerzahl* dataset (13). In addition, for each air sample, a $\Delta\ln^{17}O/\Delta\ln^{18}O$ slope was calculated relative to tropospheric CO_2, which was taken to be $\ln^{17}O$ = 21.16‰ and $\ln^{18}O$ = 40.18‰ to avoid rounding errors. These $\Delta\ln^{17}O/\Delta\ln^{18}O$ values are given in Tables 2-S1 through 2-S4 and are shown as a function of N_2O mixing ratio and $\Delta^{17}O$ of CO_2 in Figure 2-S5. Because this choice for a CO_2 isotopic composition entering the stratosphere from the troposphere is somewhat arbitrary and because there may be small seasonal variations in its values, we also varied the "entry" tropospheric CO_2 isotopic composition used in the calculation of $\Delta\ln^{17}O/\Delta\ln^{18}O$ by ±0.268‰ ±0.500‰ in $\ln^{17}O$ and $\ln^{18}O$, respectively. These

values represent a conservative estimate for the maximum range of a possible seasonal cycle in tropospheric CO_2 isotopic compositions entering the stratosphere based on surface isotope measurements from NOAA ESRL noted above and the boundary condition for CO_2 mixing ratios entering the stratosphere (9). These variations do affect the magnitude of the $\Delta\ln^{17}O/\Delta\ln^{18}O$ values but not the interpretations of the relative values (i.e., the trends with respect to N_2O or $\Delta^{17}O$ of CO_2) that we present here. Moreover, varying the entry isotopic composition within this range in the photochemistry model affects the overall three-isotope slope from *in situ* photochemistry by less than 0.003.

S1.4 Two-endmember mixing calculations

Isotopic compositions of mixed air masses can be calculated using equations derived from material balance and mixing relationships (14). For a two-endmember system, the isotope ratio R can be expressed as a mass fraction M and concentration C of the two-endmember components A and B.

$$R_{system} = \frac{C_A M_A}{\left(C_A M_A + C_B M_B\right)} R_A + \frac{C_B M_B}{\left(C_A M_A + C_B M_B\right)} R_B \qquad \text{(S4)}$$

For the two-endmember mixing shown in Fig. 2-1 and 2-S1, one datum from SOLVE in the lower stratosphere and one datum from the dataset of Thiemens *et al.* (11) were chosen given the approximate N_2O mixing ratios and corresponding altitudes for air masses that are inferred to have mixed together after the breakup of the polar vortex in 1997 (15); see Table 2-S6, Fig. 2-1, and 2-S6. This mixing scenario qualitatively illustrates how mixing and transport in the absence of chemistry can also affect the three-isotope slope, and specifically how the mixing of lower altitude air with higher altitude air can result in a three-isotope slope of 1.7 when the vortex breaks up in spring.

S1.5 Photochemistry experiments

The Pyrex vacuum line shown in Fig. 2-S5 was designed and built for these and other photochemistry experiments at UC Berkeley. The 2.2 L glass bulb in which the reactions occur, based on a similar design by Johnston *et al.* (16), has a fused quartz (Heraeus-Amersil, Inc., Commercial) "finger" extending into the interior of the bulb and a glass cold finger extending out of the bottom. The bulb was large enough for the pressures in the experiments to avoid significant ozone formation on surfaces (17, 18). Valve stopcocks on either side of the bulb were made of glass and sealed with chemically-resistant Kalrez O-rings to prevent reaction with ozone or UV light. A low-pressure mercury/argon pen lamp (Oriel Instruments) was placed in the quartz finger such that it irradiated the bulb from the center. This lamp has major emission lines at 184.9 nm and 253.7 nm in the ultraviolet region along with several other faint lines. Using the reported lamp irradiance for the 253.7 nm line of 74±12 μW cm^{-2} at 25 cm (19), the transmission coefficient of the quartz of 0.8 at this wavelength (Heraeus-Amersil, Inc.), and the geometry of the bulb, we calculated the average photon flux throughout the bulb at 253.7 nm to be 5.9×10^{15} $cm^{-2}s^{-1}$. Since the intensity of a mercury lamp at 184.9 nm is roughly 4-10 times lower than the intensity at 253.7 nm (20,), and the transmission coefficient of the quartz at 184.9 nm is approximately 0.3, we then estimated an upper bound to the flux at 184.9 nm to be between 2.2×10^{14} and 5.5×10^{14} cm^{-2} s^{-1}. The lamp intensities at these wavelengths were also estimated by performing CO_2 actinometry experiments in the bulb. In these experiments, a trace amount of CO_2 was photolyzed at 185 nm for two to five hours to yield CO and O_2, and the total yield of

the non-condensable CO and O_2 gases was measured. Assuming that the CO and O_2 products were created in stoichiometric amounts, the loss rate of CO_2 was used with the known absorption cross section at 184.9 nm to infer the photon flux, yielding a value of 4.3×10^{13} cm^{-2} s^{-1} at 184.9 nm. Because the measured quantum yields for CO and O_2 in previous photolysis experiments at this wavelength have ranged from 0.2 to 1 and 0.1 to 0.5, respectively, (20) this value represents a lower bound for the actual photon flux. Using the same assumptions above for the relative intensities and quartz transmission coefficients, a lower bound for the 253.7 nm flux was calculated to be between 4.6×10^{14} and 1.1×10^{15} cm^{-2} s^{-1}. We then used these estimates of the lower and upper bounds of the lamp intensities at 184.9 and 253.7 nm to check for consistency with the photolysis rate coefficients for O_2 and O_3 used to simulate the experimental results with the photochemical model described in Section 1.6 below.

The gases used in the experiments were O_2 (Scott Specialty Gases, 99.999%) and CO_2 (Scott Specialty Gases, 99.998%). The isotopic composition of O_2 was measured three times against a laboratory standard using the Finnigan MAT 252 IRMS and was determined to have an average isotopic composition of $\ln^{17}O=13.7\pm0.1‰$ (1σ) and $\ln^{18}O=26.5\pm0.1‰$ (1σ) relative to VSMOW. The initial isotopic composition of CO_2 in the bulb had an average (N=6) isotopic composition of $\ln^{17}O=3.4\pm0.2‰$ (1σ) and $\ln^{18}O=6.6\pm0.3‰$ (1σ) relative to VSMOW, based on three replicate measurements of CO_2 from the source cylinder and three replicate measurements of CO_2 that was processed through the entire experimental procedure without irradiation. We also determined that the O_2 isotopic composition remained constant throughout the irradiation period by collecting aliquots of O_2 from experiments in which the gas mixtures had been irradiated for more than 100 hours. The isotopic composition of these aliquots of O_2 showed a change of only 0.9‰ or smaller, as expected given that O_2 was so much more abundant than CO_2 or any of the trace gases (predominantly O_3) generated photochemically in the bulb during the experiment.

Two sets of irradiation experiments were performed at two different total pressures in the bulb and at near-atmospheric O_2/CO_2 ratios. In the first set, a mixture of an average of 50.0±0.1 (1σ) Torr of O_2 and 110±3 mTorr of CO_2 was used (corresponding to 5.97±0.01 mmol of O_2 and 13.1±0.3 μmol of CO_2 and $\rho = O_2/CO_2 = 456 \pm 11$); see Table 2-S7. In the second set, a mixture of an average of 99.6±0.3 (1σ) Torr of O_2 and 210±6 mTorr of CO_2 was used (corresponding to 11.9±0.1 mmol of O_2 and 25.1±0.7 μmol of CO_2 and $\rho = O_2/CO_2 = 473 \pm 11$). To obtain these partial pressures in the bulb, the desired amount of CO_2 was introduced from the gas cylinder into a section of the vacuum line and then equilibrated for five minutes. The CO_2 was then frozen to a trap using liquid nitrogen, then released with an ethanol slush between -75^oC and -80^oC and transferred to a calibrated volume. In the calibrated volume, the pressure of CO_2 was measured using a Baratron capacitance manometer (MKS Instruments 627B, 0.1% accuracy, 10 Torr or 1000 Torr full-scale depending on sample size), and the CO_2 was then frozen to the cold finger on the glass bulb. While the CO_2 remained frozen, O_2 was added to the bulb through a liquid nitrogen cold trap (to remove trace impurities such as CO_2 or H_2O) at a rate of approximately 1 mmol/min. Once the desired O_2 pressure was reached, the O_2 was allowed to equilibrate for one minute, and then the bulb was closed (We note that the temperature gradient in the bulb during this procedure results in an additional uncertainty in the O_2 pressure of ≤1%). The liquid nitrogen was then removed from the cold finger, and the Hg/Ar lamp was turned on once the finger was at room temperature. A constant flow of nitrogen was used to sweep out the area around the lamp during irradiation in order to prevent the formation of ozone in the laboratory and to prevent overheating of the bulb. Irradiation times ranged from zero to 190 hours.

At the end of the irradiation time, the lamp was turned off and the gas mixture in the bulb was extracted over a liquid nitrogen trap at a rate of approximately 1 mmol/min. The trap was pumped until the pressure above it was less than 0.1 mTorr to remove most of the ozone, which has a vapor pressure of 0.7 mTorr at −196ºC. The liquid nitrogen was replaced with an ethanol slush at −75ºC to release CO_2 and O_3 while keeping any H_2O condensed, and the CO_2 and O_3 were frozen to a glass sample tube containing several shavings of nickel foil. The sample tube was then heated to roughly 60ºC for 15 minutes to decompose any remaining O_3 to O_2 on the nickel catalyst. Repeated heating cycles confirmed that all the O_3 was decomposed under these conditions. Although it is known that this process can result in small isotopic enrichments in CO_2 as the O_3 decomposes on the Ni catalyst in experiments performed at low O_2/CO_2 ratios (16, 21), such an artifact should be negligibly small for the high O_2/CO_2 ratios in our experiments here (21). The CO_2 was then frozen again and the resulting O_2 was pumped away. The CO_2 was then transferred to the same calibrated volume as before the irradiation in order to measure the final CO_2 yield and then frozen to a glass sample tube for IRMS analysis. Results are shown in Table 2-S7.

We also used this apparatus to measure the isotopic composition of ozone formed, both in a separate experiments in which we irradiated O_2/CO_2 mixtures at 100 Torr total pressure (Table 2-S8), and in pure O_2 at 50 and 100 Torr (22). The procedures for collecting O_3, separating it from O_2 (and CO_2 when applicable), and measuring its isotopic composition have been described elsewhere (22). Results are shown in Figure 2-S9, along with previous measurements by Morton *et al.* (17) and Thiemens *et al.* (23, 24). An average of all results at 50 Torr (17, 22) are reported in Table 2-2 and an average of all results at 100 Torr (17, 22, Table 2-S8) are reported in Table 2-S11. The ozone isotopic compositions show more scatter in the experiments than the CO_2 isotopic compositions. Because of the non-negligible vapor pressure of O_3 at liquid nitrogen temperature, cryogenically separating O_3 from O_2 and CO_2 can lead to some loss of O_3, which can result in mass-dependent enrichments in the O_3 collected. We note that the O_3 isotopic compositions reported in Table 2-S8 were measured before we had further optimized the O_3 separation and collection procedures (22) and may therefore be mass-dependently enriched by ~2 to 5‰. Despite the larger uncertainty in precision and accuracy due to this potential artifact for O_3, the combined CO_2 and O_3 results overall indicate a well-behaved system that is well-predicted by the photochemical model (see below).

Finally, we note that, between each irradiation experiment, both the lamp and the quartz finger in which the lamp was placed were cleaned using acetone and an abrasive scrub pad to remove the brown residue that accumulated on the surfaces during each experiment. Despite flushing the area constantly with N_2, organic material from the surrounding air likely reacted with ozone generated around the lamp to create volatile products which then deposited on the lamp and quartz finger and attenuated the lamp flux. Since changes in the lamp flux affect the O_2 and O_3 photolysis rates and, therefore, the rate of increase of the isotope enrichments in CO_2, cleaning before each experiment was necessary in order to keep the experimental conditions as constant as possible. The effect of changes in the lamp flux can be seen from replicate experiments performed at approximately 17 hours of irradiation time (see Fig. 2-2 and Fig. 2-S6). Since the CO_2 enrichment is changing quickly at 17 hours, the values measured at this time are more sensitive to variations in the radiative flux into the bulb compared to those measured at long times, when the CO_2 has reached isotopic steady-state. In addition to accumulating residue, changes in the lamp flux could be due to variability in the lamp irradiance, which was measured to be ±16% (1σ) in similar lamps (19).

S1.6 Photochemical Kinetics Model Description

The experiments described in Section 1.5 were simulated using a detailed photochemical kinetics model coded in KINTECUS (25) and based on one originally developed by Johnston *et. al* (16) and used in a previous publication on the isotopic composition of ozone (26). A complete list of the reactions (Eq. S6 to S22) in the model for ^{16}O species only, along with their rate coefficients, is given in Table 2-S9. In addition to all the reactions listed in Table 2-S9, the model also included all possible variants of these reactions that involved substituting ^{17}O or ^{18}O for one or two of the oxygen atoms. For example, nineteen ozone formation reactions with different isotopic substitutions were included: the unsubstituted reaction (Eq. S7 in Table 2-S9), the six "singly-substituted reactions" shown in Table 2-S10, and the twelve possible "doubly-substituted reactions" that are not shown. Without doubly-substituted reactions in the model, $\Delta^{17}O$ of both $O(^1D)$ and CO_2 changed by 2 to 3‰. This difference was deemed large enough to justify the extra complexity of adding doubly-substituted reactions to the model. Adding triply-substituted species was found to change the model predictions by less than 0.1‰, so these and higher-order substitutions were neglected. We did not include any isotope effects for the doubly-substituted reactions, in large part because so few have been measured. A model scenario that included the huge isotope effects measured for a handful of the doubly-substituted ozone formation reactions (27, 28) was found to have little effect on the model predictions.

S1.6.1 The Base Model in the low pressure limit

The model was initialized with the initial isotopic compositions of CO_2 and O_2 in the experiments, with $\ln^{17}O$=3.4‰ and $\ln^{18}O$=6.6‰ for CO_2 and $\ln^{17}O$=13.7‰ and $\ln^{18}O$=26.5‰ for O_2, all relative to VSMOW. The partial pressures of CO_2 and O_2 in the model corresponded to those measured in the two sets of experiments. Based on these isotopic compositions and pressures, as well as the estimated values for the $^{17}O/^{16}O$ and $^{18}O/^{16}O$ ratios for the VSMOW isotopic standard (6), we calculated the initial concentrations of each isotope-specific species assuming a statistical distribution of the heavy isotopes. All modeled isotopic compositions relative to VSMOW were then calculated at each model output time from the $^{17}O/^{16}O$ and $^{18}O/^{16}O$ ratios of each species. Carbon isotopes were not treated explicitly in this model.

Photolysis rate coefficients (or "J-values") for O_3 and O_2 are required as input to the model. For O_3 photolysis, the lower and upper bounds for the lamp flux at 253.7 nm estimated in Section 1.5 above correspond to O_3 photolysis rate coefficients of 5.3×10^{-3} s^{-1} and 6.7×10^{-2} s^{-1}, respectively, using the O_3 absorption cross section $\sigma_{254} = 1.15\times10^{-17}$ cm^2 (29). The rate of O_3 photolysis at 184.9 nm is negligible compared to the rate at 253.7 nm, with a maximum estimated contribution of 0.4% of the total photolysis rate, so the O_3 photolysis J-value at this wavelength was assumed to be zero in the model. For O_2 photolysis, the lower and upper bounds for the lamp flux at 184.9 nm correspond to O_2 photolysis rate coefficients of 1.6×10^{-7} s^{-1} and 2.1×10^{-6} s^{-1}, respectively, using the O_2 absorption cross section of 3.8×10^{-21} cm^2 (30). If we assume that the ratio of the lamp intensity at 184.9 nm to that at 253.7 nm is 1:10, then the upper bound for the O_2 photolysis J-value drops to 8.4×10^{-7} s^{-1}. In order to choose appropriate J-values as input for the model, the model was run with J-values that fell within the estimated ranges above, and self-consistent J-values were then selected which produced the best fit to the rate of increase of the $\Delta^{17}O$ values for CO_2 in the base model at short irradiation times for the 100 Torr set of experiments. Using this procedure, the J-values used as input for subsequent model runs were 1.80×10^{-2} s^{-1} for O_3 and 2.23×10^{-7} s^{-1} for O_2, which are both well within the range of values predicted by the CO_2 actinometry (lower) and lamp irradiance (upper) estimates given above. We

note that these J-values do not affect the steady-state $\Delta^{17}O$ values or the three-isotope slope for CO_2, only the time it takes to reach steady state. For completeness, we also note here that if a mass-dependent isotope effect is also included in the ozone photolysis (Eq. S8) step of a magnitude predicted by Liang *et al.* (31) at 253.7 nm, the isotope-specific J-values chosen do affect the three-isotope slope for CO_2 but only to a small degree (see, e.g., Figure 2-2).

The base model in the low pressure limit included isotope effects for only two reactions. The first is the very fast isotope exchange between O and O_2 (Eq. S21 in Table 2-S9). The rate coefficient for the $^{17}O+^{16}O^{16}O$ forward reaction was assumed to be the same as that measured for the $^{18}O+^{16}O^{16}O$ reaction (32). The reverse rate coefficients were calculated from the theoretical equilibrium constants (Eq. S22) calculated by Kaye and Strobel (33). The second set of isotope effects included in the base model in the low pressure limit are the ozone formation KIEs. Most of these were measured or derived by Mauersberger and coworkers (27, 28) and are given in Table 2-S10. The exception is our estimate for the relative rate coefficients for the formation of $^{16}O^{17}O^{16}O$ and $^{16}O^{16}O^{17}O$ from the reaction $^{16}O+^{16}O^{17}O$. While the sum of the two rate coefficients has been measured, the individual rate coefficients for formation of the symmetric versus asymmetric $^{49}O_3$ isotopomers have not been. We estimated values for k_{sym} and k_{asym} based on the empirical zero-point energy relationship (28) to be 0.99 and 1.35, respectively, as described in Cole and Boering (26). Using these rate coefficients resulted in an O_3 isotopic composition consistent with previous measurements at low pressures (17, 22-24) and with measurements that show that most of the enrichment and ^{17}O anomaly is carried by the asymmetric ozone isotopomers (34). To evaluate the sensitivity of the isotopic composition of CO_2 to uncertainty in the k_{sym} and k_{asym} estimates for $^{49}O_3$ formation, these rate coefficients were varied by +0.05 and –0.05 in the model and in the derivation for the pressure dependence below. These variations were chosen based on the standard error of the measured average of these rate coefficients and the scatter in the zero point energy relationship. The average of the two rate coefficients, however, was fixed at the experimental value of 1.17 so that the two rate coefficients were not varied independently. Thus, if k_{asym}=1.30, k_{sym} must be 1.04, and if k_{asym}=1.40, k_{sym} must be 0.94. Since the total ^{17}O enrichment in ozone depends only on the average of k_{asym} and k_{sym}, the values of $\ln^{17}O$ and $\Delta^{17}O$ for O_3 are therefore invariant in these three sets of simulations. However, the distribution of ^{17}O in the central and terminal positions of O_3 does change the magnitude of isotope transfer to CO_2 when these two rate coefficients are varied. The sensitivity of the CO_2 isotopic composition to this conservative range of estimated values for k_{asym} and k_{sym} for the $^{16}O+^{16}O^{17}O$ reaction is shown in Fig. 2-S6 in gray shading. The base model predictions in the low pressure limit for the CO_2 isotopic composition are shown along with experimental results in Fig. 2-S6.

S1.6.2 Modeling the pressure dependence

Because the irradiation experiments were conducted at pressures above the low-pressure limit, a pressure dependence for the ozone formation KIEs was included in the model to more accurately predict the experimental results. Precise measurements of the pressure dependence of the kinetic isotope effect for each ozone formation channel are unavailable, so an empirical pressure dependence to the KIEs was derived from the ozone isotope enrichments at various pressures (17, 23, 24) as follows. At isotopic steady state, the ^{18}O enrichments relative to ^{16}O can be expressed in (S23)

$$\frac{[OOQ]+[OQO]}{[OOO]} = \frac{\left(k_{O+OQ}/2 + k_{O+QO}/2\right)[O][OQ] + k_{Q+OO}[Q][OO]}{k_{O+OO}[O][OO]} \quad \text{(S23)}$$

where Q = ^{18}O and O = ^{16}O. Using the equilibrium constant (33)in Eq. S22 in Table 2-S8, the isotopic steady state in Eq. S23 above then simplifies to Eq. S24:

$$\frac{\frac{[OOQ]+[OQO]}{[OOO]}}{\frac{[OQ]}{[OO]}} = \frac{k_{O+OQ}/2 + k_{O+QO}/2 + k_{Q+OO}/K_{eq}}{k_{O+OO}} \quad \text{(S24)}$$

Using the definition of a relative delta value (Eq. S25) – that is, the isotopic composition of O_3 relative to the starting O_2 isotopic composition, then substituting the left-hand side of Eqn S24 into S25, and assuming that formation of OOQ from O+OQ has a significant pressure dependence while formation of OOQ from O+QO and Q+OO do not (35), we can then write Eqn S26:

$$\delta^{18}O_{O_2}(O_3) = \left(\frac{2\left([OOQ]+[OQO]\right)/[OOO]}{3[OQ]/[OO]} - 1\right) \times 1000 \quad \text{(S25)}$$

$$\frac{k_{O+OQ}}{k_{O+OO}}(p) = 3\left(\delta^{18}O_{O_2}(O_3)/1000 + 1\right) - \frac{k_{O+QO}}{k_{O+OO}} - \frac{2k_{Q+OO}}{k_{O+OO}K_{eq}} \quad \text{(S26)}$$

Equation S26 gives the KIE for the O+OQ reaction at a given pressure as a function of the δ^{18}O value of ozone at a given pressure and (assumed) pressure-independent terms for k_{O+QO}/k_{O+OO} and k_{Q+OO}/k_{O+OO}, available from the Mauersberger *et al* (27, 28) low pressure experiments, and the equilibrium constant for isotope exchange, K_{eq}. Using $\ln^{18}$O values for O_3 measured at 50 Torr from earlier experiments (17, 24) in Equation S26 yields a value for k_{O+OQ}/k_{O+OO}(*50 Torr*) of 1.45, consistent with the direct measurement of the KIE for this ozone channel in the low pressure limit (27, 28). To derive an empirical expression for $k_{O+OQ}/k_{O+OO}(p)$ at higher pressures, Eqn S26 was first used to calculate a value for the KIE at each of the higher pressures for which an experimental value for $\ln^{18}$O of O_3 is available. The resulting values for $k_{O+OQ}/k_{O+OO}(p)$ calculated at these different pressures were then fit with a nonlinear least squares fitting method that uses the Levenberg-Marquardt algorithm to find a set of coefficients that minimize chi-squared for the Hill function. The general form of the Hill function is $base + max - base1 + pp0rate$ where p is the variable and *base*, *max*, p_0, and *rate* are the fitted parameters. This procedure yielded the functional form for $k_{O+OQ}/k_{O+OO}(p)$ given in S27:

$$\frac{k_{O+OQ}}{k_{O+OO}}(p) = 1.4538 + \frac{1.0092 - 1.4538}{1 + \left(p/3010.6\right)^{-0.69388}} \quad \text{(S27)}$$

The same calculations and assumptions applied to the KIEs for the corresponding ^{17}O-containing ozone isotopomers yields a value of 1.35 in the low pressure limit for formation of OOP (where P=^{17}O), which is also consistent with our value for that KIE estimated above from the data of

Mauersberger *et al.* in the low pressure limit, and yields the functional form for the pressure dependence of this KIE in S28:

$$\frac{k_{O+OP}}{k_{O+OO}}(p) = 1.3543 + \frac{0.97167 - 1.3543}{1 + \left(p/3576.2\right)^{-0.68094}} \quad \text{(S28)}$$

The photochemical model was then run with Eq. S27 and Eq. S28 at various pressures to test the accuracy of the predicted ozone enrichments versus experimental values (17, 22-24), shown together in Fig. 2-S7.

In addition, the derived value of k_{O+PO}/k_{O+OO} (P = ^{17}O) was also varied from 0.99 by +0.05 and –0.05 in the calculations and pressure fits in order to test the sensitivity of the CO_2 isotopic composition to the choice of value for k_{O+PO}/k_{O+OO}, as discussed in section 1.6.1. These results are shown in gray in Fig. 2-2 of the main text. The model results for the O_3 isotopic composition (shown in Fig. 2-S7) are not sensitive to choice of these values, as noted already in Section 1.6.1 for the low pressure limit.

The photochemistry model described above can predict the CO_2 isotopic composition in the CO_2-O_2 irradiation experiments to a remarkably good degree, especially once the empirical pressure dependence of the ozone KIEs is included in the model (Fig. 2-2; Fig. 2-S8). While this excellent agreement could arguably be somewhat fortuitous, since mass-dependent isotope effects are likely to occur in some of the many reactions detailed in Table 2-S9, it has been postulated that at least some of these isotope effects may roughly cancel each other out under laboratory conditions (16), and many should have quite small magnitudes relative to the large O_3 formation KIEs and their pressure dependence. Ozone photolysis isotope effects, calculated as a function of wavelength by Liang *et al.* (31) and incorporated into our model here, are also predicted to have a small effect on the model predictions and experimental data (e.g., see Fig. 2-2). We do note, however, that the model becomes less accurate for experiments conducted at pressures higher than 100 Torr (21) or for experiments conducted at low O_2/CO_2 mixing ratios (16, 21, 36), variables that we are currently investigating with systematic new laboratory measurements. Indeed, measurements of the anomalous KIEs for each isotope-specific ozone formation channel at various pressures in different bath gases may be needed to improve model predictions for these other types of experiments. Importantly, however, the model can predict the non-mass-dependent isotope enrichments in CO_2 quite well for stratospheric pressures and atmospheric O_2/CO_2 mixing ratios, so that an additional anomalous kinetic isotope effect in the stratosphere is unnecessary even if it cannot be ruled out for experiments at low O_2/CO_2 mixing ratios (21).

S1.6.3 Modeling the temperature dependence

To compare the potential effect of temperature on the three-isotope slope for CO_2, we derived a temperature dependence for the ozone formation KIEs based on experimental measurements of the KIEs for formation of the ^{18}O-containing ozone isotopomers (37). Janssen *et al.* (37) measured the temperature dependence given in (S31) and an average of (S29) and (S30). Here, we assume that k_{O+OQ}/k_{O+OO} (S29) and k_{O+QO}/k_{O+OO} (S30) have the same temperature dependence as the average of the two, which taken together yield the following three temperature-dependent KIEs for each of the three ozone formation channels containing one ^{18}O atom:

$$\frac{k_{O+OQ}}{k_{O+OO}}(T) = 1.45 + 0.0000207 \times (T - 300K) \quad \text{(S29)}$$

$$\frac{k_{O+QO}}{k_{O+OO}}(T) = 1.08 + 0.0000207 \times (T - 300K) \quad \text{(S30)}$$

$$\frac{k_{Q+OO}}{k_{O+OO}}(T) = 0.92 + 0.00103 \times (T - 300K) \quad \text{(S31)}$$

For the ^{17}O-containing isotopomers of ozone, the temperature dependence of the corresponding KIEs has not been measured directly, so here we derive an empirical temperature dependence from laboratory measurements of the ^{17}O enrichments in ozone as a function of temperature (38). First, we rearrange Eq. S26 (with P=^{17}O substituted for Q=^{18}O) to give Eq. S32:

$$\frac{k_{P+OO}}{k_{O+OO}} = \frac{K_{eq}}{2}\left(3\left(\delta^{17}O_{O_2}(O_3)/1000+1\right) - \frac{k_{O+PO}}{k_{O+OO}} - \frac{k_{O+OP}}{k_{O+OO}}\right) \quad \text{(S32)}$$

Assuming that the temperature dependence of both k_{O+PO}/k_{O+OO} and k_{O+OP}/k_{O+OO} are the same as those for the corresponding ^{18}O reactions, and using the calculated temperature dependence of K_{eq} for ^{17}O, the following linear fits to the temperature dependence were derived from the measured ^{17}O enrichments in ozone (38):

$$\frac{k_{O+OP}}{k_{O+OO}}(T) = 1.35 + 0.0000207 \times (T - 300K) \quad \text{(S33)}$$

$$\frac{k_{O+PO}}{k_{O+OO}}(T) = 0.99 + 0.0000207 \times (T - 300K) \quad \text{(S34)}$$

$$\frac{k_{P+OO}}{k_{O+OO}}(T) = 1.03 + 0.000782 \times (T - 300K) \quad \text{(S35)}$$

The temperature-dependent KIEs in Eqns S29-S35 were then used in the model at 200K, 220K, and 250K to investigate the potential sensitivity of the three-isotope slope and $\Delta^{17}O$ of CO_2 to temperatures lower than room-temperature based on the assumptions above; see Tables 2-2 and S11.

The assumption that the KIEs for formation of both the asymmetric and symmetric ozone isotopomers (i.e., in S29 and S30 for $^{50}O_3$ and S33 and S34 for $^{49}O_3$, respectively) share the same temperature dependence may not turn out to be correct. For example, although the Janssen *et al.* (37) measurements showed that the temperature dependence of the average of the reactions in S29 and S30 is smaller than the temperature dependence of the reaction in S31, it is possible that the asymmetric and symmetric formation channels in S29 and S30, respectively, could individually exhibit temperature dependences that, in the extreme, might be larger in magnitude than the average but opposite in sign, thereby leading to the smaller average temperature dependence measured for a combination of S29 and S30 than that measured for S31. Such a scenario would be important for predicting the isotopic composition of CO_2 as a function of

temperature since it would change the predicted distribution of isotopes between the symmetric and asymmetric ozone isotopomers. A change in the intramolecular distributions isotopes in O_3 will in turn affect the isotopic composition of CO_2 since it is the terminal oxygen atom in O_3 which is ejected upon photolysis and then undergoes isotope exchange with CO_2. Thus, although the model using the temperature dependences given in S29-S35 qualitatively predicts an increase in the three-isotope slope with decreasing temperature based on the assumptions given above, measurements of the temperature dependence of the KIEs for each isotope-specific ozone formation channel and additional laboratory measurements of CO_2-O_2 isotope exchange at lower temperatures are needed to further test the assumptions and predictions made here.

1.6.4 Sensitivity to mass-dependent isotope effects

We also investigated additional model scenarios which included possible mass-dependent isotope effects in other reactions beyond ozone formation (Eq. S7 in Table 2-S9) and O+O_2 isotope exchange (Eq. S21 in Table 2-S9) in order to test the sensitivity of the predicted values for $\ln^{18}O$, $\ln^{17}O$, and $\Delta^{17}O$ of CO_2. We investigated the effect of mass-dependent O_3 photolysis isotope effects at 254 nm in the experiment, using the calculated isotope-specific cross sections from Liang *et al.* (31) at this wavelength, as in Cole and Boering (26). In this scenario, the fragmentation of asymmetric $^{16}O^{16}O^{18}O$ was assumed to yield $^{16}O(^1D)$ and $^{18}O(^1D)$ with equal probability. The isotope-specific J-values are given in Table 2-S10. We note that the value for λ_{MD} for these calculated isotope effects is 0.526, slightly smaller than the value of 0.528 that we use throughout this study to calculate $\Delta^{17}O$ using $\Delta^{17}O=\ln^{17}O-0.528\ \ln^{18}O$. Thus, even though mass-dependent, including these photolysis isotope effects leads to a very small change in $\Delta^{17}O$ of −0.1‰ relative to the base model scenario, as shown in Table 2-2.

To show the effect of larger mass-dependent isotope effects in UV photolysis of O_3, a set of hypothetical isotope-specific J-values were also calculated assuming that the bond in an ozone O_2—O "diatomic" molecule is broken. Under this assumption, the relative J-values for ozone photolysis for each isotopologue are given simply by the square root of the ratio of the reduced masses of the O_2 and O fragments of the hypothetical O_2—O diatomic molecule as follows:

$$\frac{J'}{J} = \sqrt{\frac{\mu}{\mu'}} \qquad \text{(S36)}$$

Equation S36 with J' and J corresponding to a heavy and a light O_3 isotopologue, respectively, yields a "normal" isotope effect since J'/J<1 (i.e., the heavy isotopologue photolyzes more slowly than the light isotopologue). An "inverse" isotope effect for which the heavy isotopologue photolyzes more quickly than the light isotopologue is calculated using the reciprocal of Eqn. S36. The values for these hypothetical mass-dependent isotope effects are given in Table 2-S10, and the model results including them are shown in Figure 2-2 and Tables 2-2 and 2-S11. This overly simplified set of scenarios was used merely for illustrative purposes to show the sensitivity of the three-isotope slope and $\Delta^{17}O$ values for CO_2 to large, mass-dependent isotope effects. The $\Delta^{17}O$ values change by less than ±0.5‰ when adding one of these hypothetical mass-dependent isotope effects into the model because the values for λ_{MD} are 0.513 to 0.520 rather than the value of 0.528 that is used to calculate $\Delta^{17}O$.

S2. SI Appendix discussion

S2.1. Further comparisons with three isotope "slopes" in previous data sets

The three isotope slope calculated using bivariate linear least squares regressions for the "vortex" and "vortex edge" SOLVE samples is 2.22 ± 0.07 (1σ, N=25), while that calculated for the combined Balloon 2004 and the midlatitude and "midlatitude-like" SOLVE samples is 1.95 ± 0.05 (1σ, N=19). In comparison, the samples of Lämmerzahl *et al.* (13) from midlatitudes and from non-vortex air at high latitudes have a three isotope slope of 1.71 ± 0.03 (1σ, N=23). Homogeneity of regression tests demonstrate that the differences in slope between our "vortex" and *Lämmerzahl* data and between our "midlatitude" and *Lämmerzahl* data are statistically significant at the 99% confidence interval (Table 2-S5). The dataset of Kawagucci *et al.* (39) shows much more variability, as is clear in Figures 2-1 and 2-S4, but the dataset is also much larger (N=58), resulting in an uncertainty in slope that appears relatively small. The three isotope slope calculated using all of their data is 1.67 ± 0.05 (1σ, N=58), and they conclude that their data support the *Lämmerzahl* slope of 1.7 throughout the stratosphere (39). Interestingly, visual inspection of the *Kawagucci* data (Fig. 2-1) does show some datapoints that appear to overlap with our SOLVE vortex data or our Balloon 2004 midlatitude data. Some of the visually overlapping data may represent real atmospheric variability, since they collected samples at times of year in which vortex air could have been intercepted and at midlatitudes when they might have intercepted filaments of air from the tropics. However, some datapoints also fall far below any of the three-isotope relationships in the high precision datasets. These variations do not appear to be explicable except perhaps by a lower precision for their new online, continuous flow CuO isotope exchange IRMS measurement technique compared with the previous dual inlet measurements or by an artifact. Availability of additional trace gas measurements and geophysical parameters other than the N_2O and altitude data that they report could help to objectively separate samples in their dataset into vortex, midlatitude and midlatitude-like, and tropically-influenced air, in order to check for coherent atmospheric variability within these subsets. Homogeneity of regression tests demonstrate that the differences in slope between our "vortex" and the *Kawagucci* data and between our "midlatitude" and the *Kawagucci* data are statistically significant at the 99% and 95% confidence intervals, respectively (Table 2-S5).

The rocket samples from the upper stratosphere and mesosphere near 30°N (40) have a three isotope slope of 1.39 ± 0.06 (1σ, N=23). A subset of these data (11) have a three isotope slope of 1.23 ± 0.08 (1σ, N=12). The smaller slopes of the higher altitude data have been attributed to an additional source of $O(^1D)$ from Lyman-α photolysis of O_2 in the mesosphere (41, 42). The $O(^1D)$ from O_2 photolysis is predicted to have massively large, mass-dependent enrichments in ^{17}O and ^{18}O, and thus draws the CO_2 isotope "slopes" downward from those produced from isotope exchange with $O(^1D)$ from O_3 photolysis alone (41, 42). The datasets reported here from the polar vortex and midlatitude middle stratosphere show a coherent transition to, and overlap with, the rocket sample data. Combined, they show that, at least in some parts of the stratosphere, the $\ln^{17}O$-$\ln^{18}O$ relationship is curvilinear, increasing and then decreasing as $\Delta^{17}O$ increases from its tropospheric value. The $\ln^{17}O$-$\ln^{18}O$ relationship is in fact, then, not always a straight line. A straight line would imply either a single source of $O(^1D)$, as in laboratory experiments, or the action of stratospheric transport and mixing processes that create straight lines from formerly curvilinear isotope relationships due to mixing of high-N_2O air with low N_2O air in the extratropics. We have still used the concept of "slopes" here, both to make historical comparisons and to determine that our datasets over the range of isotopic compositions we measured are in fact statistically different from earlier ones. However, it is now clear that calculating and comparing linear "slopes" should be done with great caution.

S2.2 Comparisons with previous atmospheric modeling

The 2D atmospheric model results of Liang *et al.* (41, 42) are highly relevant for our observations and their interpretation. First, their model predicts that the lifetime of CO_2 with respect to isotope exchange with O_3 in the stratosphere – what can be called τ_{chem} for the "chemistry timescale" – is at least an order of magnitude longer than the transport timescales, $\tau_{transprot}$, everywhere in the stratosphere. Even at 45 km in the tropics where $O(^1D)$ peaks and where τ_{chem} is the shortest, they calculate a lifetime for isotope exchange that is ~40 months, while the transport time scale there is only about ~4 months. Thus, CO_2 never reaches isotopic steady-state with $O(^1D)$ in the stratosphere and is always far from it, never getting closer to 10% of its steady-state value even in regions with the shortest τ_{chem}. These relative timescales mean that the CO_2 isotopic composition behaves as a long-lived tracer, which is key to understanding how the different slopes that we observe in the middle midlatitude stratosphere and the polar vortex can be created and maintained when and where they are observed. These relative timescales from the model also support our interpretation of mixing in the lower stratosphere and the variability in $\Delta\ln^{17}O/\Delta\ln^{18}O$ that we observe (Figure 2-S5). Specifically, $O(^1D)$ concentrations are very low and photochemical cycling is quite slow in the extratropical lower stratosphere. Thus transport and mixing alone will be almost entirely responsible for any change in $\ln^{17}O$ and $\ln^{18}O$ of CO_2 relative to the tropospheric entry value since τ_{chem} will be very long (much longer than τ_{chem} at 45 km in the tropics of >3years) compared to $\tau_{transport}$ of a few months. In other words, local photochemistry is too slow to result in an increase in the $\ln^{17}O$ and $\ln^{18}O$ values for CO_2 below 21 km in the extratropics, particularly at high latitudes in winter when there is very little photochemistry occurring in any case, as for the SOLVE samples. Any local changes in $\ln^{17}O$ and $\ln^{18}O$ in CO_2 in this region must be due to mixing with older, photochemically "aged" CO_2 that has derived its heavy isotopic signature from O_3 elsewhere.

Second, it is interesting to note that the *Liang* (41, 42) model results predict a value for $\ln^{17}O/\ln^{18}O$ of 1.5 throughout the extratropics, close to the previously expected value of 1.7, while we observe regional and seasonal differences in these values that are significantly larger. The insensitivity of their three-isotope slope for CO_2 to region could originate in uncertainties in the underlying isotope chemistry, in how this isotope chemistry is implemented in their model, in the transport and mixing characteristics of their model, or some combination of all of these issues. For example, the contribution from UV photolysis of ozone in their 2D model may be too low since they calculate that UV photolysis contributes only 10% to the isotopic enrichments in ozone. In contrast, measurements of stratospheric ozone isotopic compositions by Krankowsky *et al.* (38) suggest that photolysis contributes 20-25% and 25-30% of the total heavy isotope enrichments in ozone at midlatitudes and in the tropics, respectively. Since ozone photolysis mass-dependently enriches the remaining ozone, a larger contribution from such photolysis isotope effects in the stratosphere than in the Liang *et al.* model would result in a mass-dependent depletion of the $O(^1D)$ resulting from photolysis. As shown in our model sensitivities, a mass-dependent depletion of $O(^1D)$ results in a greater value for three-isotope slope in CO_2 after isotope exchange. Furthermore, the temperature and pressure dependences of the O_3 formation KIEs, especially for ^{17}O-containing isotopomers, are not well-known from experiments, which is why we estimated a number of those which have not been directly measured in order to include these dependencies as input for our 0D photochemical kinetics model. As such, the calculated temperature dependence of the ozone formation KIEs used in the *Liang* model may not be accurately simulating the underlying isotope chemistry and its latitude and altitude dependence. Interestingly, Liang *et al.* (41, 42) do note that in their 1-D and 2-D

models the "instantaneous" value of $\Delta\ln^{17}O/\Delta\ln^{18}O$ transferred from $O(^1D)$ to CO_2 can vary over a very wide range, from 1.3 to 3.0, due to differences in ozone photolysis at different altitudes in the stratosphere, but that these differences in instantaneous slopes in their model disappear due to transport and mixing. However, transport barriers between the tropics and midlatitudes and between vortex and non-vortex air, which create different CH_4:N_2O relationships in these different regions, are often difficult to simulate in 2D models (43). Simulating these differences to high accuracy may be a prerequisite for predicting different three-isotope slopes for CO_2 in different regions and times of year.

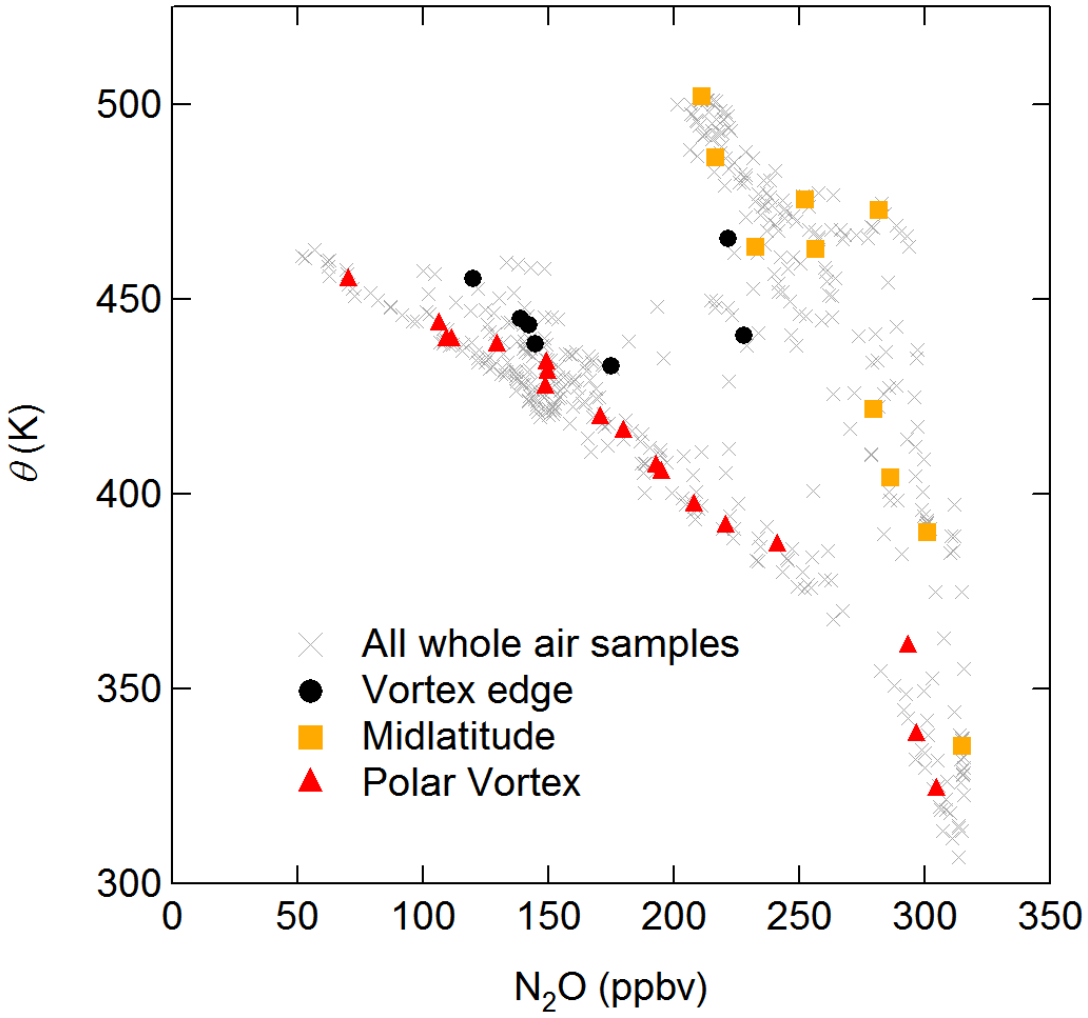

Fig. 2-S1. Measurements of potential temperature (θ) versus N_2O for whole air samples collected during the SOLVE mission. Samples for which CO_2 isotope measurements were also made appear as filled symbols. The method of Greenblatt *et al.* (10) was used to differentiate the samples into "polar vortex," "vortex edge," and "midlatitude"/"midlatitude-like" categories.

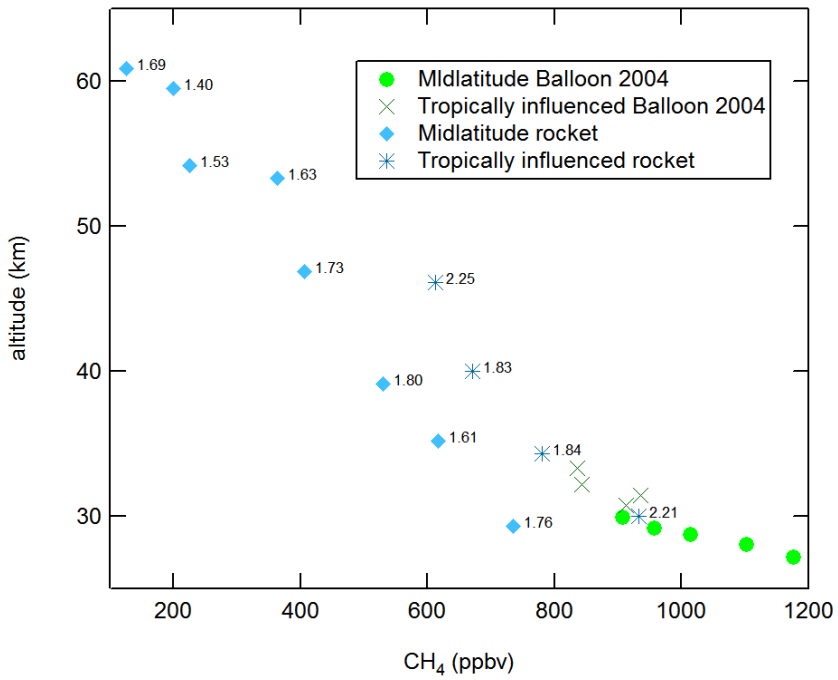

Fig. 2-S2. Altitude versus methane mixing ratio for the Balloon 2004 flight and the rocket data from Thiemens *et al.* (11). The influence of tropical air at several altitudes is evident in each set of samples as excursions to higher CH_4 mixing ratios in the profiles, and other tracers such as N_2O show similar trends. $\Delta\ln^{17}O/\Delta\ln^{18}O$ values (i.e., $\ln^{17}O/\ln^{18}O$ values relative to tropospheric CO_2) are shown as text labels for the rocket data. The tropically-influenced air samples in the rocket data, as identified by the excursions of higher CH_4 mixing ratio in the profiles, show a tendency towards $\Delta\ln^{17}O/\Delta\ln^{18}O$ values > 1.80. The balloon data are also shown on a finer scale in Fig. S3.

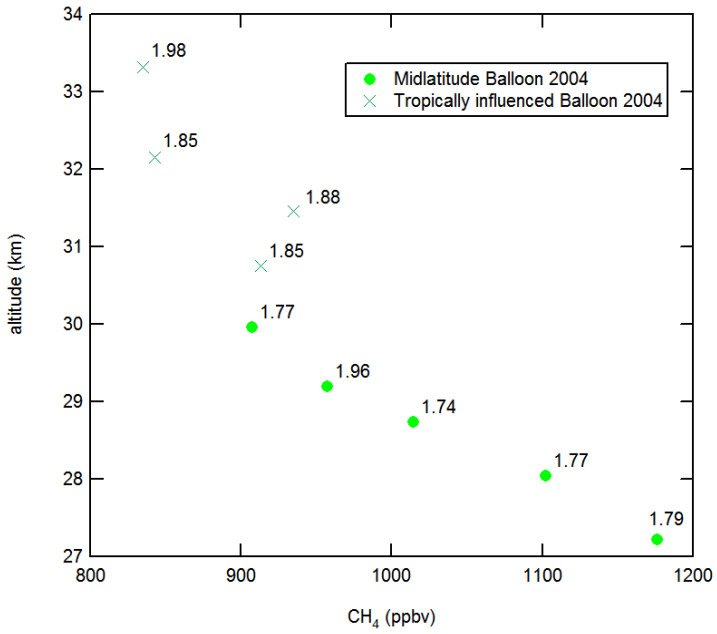

Fig. 2-S3. Altitude versus methane mixing ratio for the Balloon 2004 flight. The influence of more tropical air at several altitudes is evident as excursions to higher CH_4 mixing ratios in the profiles, and other tracers such as N_2O show similar trends. $\Delta\ln^{17}O/\Delta\ln^{18}O$ values (i.e., $\ln^{17}O/\ln^{18}O$ values relative to tropospheric CO_2) are shown as text labels. The tropically-influenced air samples, as identified by the excursions of higher CH_4 mixing ratio in the profiles, show a tendency towards $\Delta\ln^{17}O/\Delta\ln^{18}O$ values > 1.80, with the exception of the sample collected at 29.2 km with a high $\Delta\ln^{17}O/\Delta\ln^{18}O$ value of 1.96 but for which all the various tracer data suggest is midlatitude in character. The similarities between the rocket and balloon datasets both collected near 34ºN but with very different instrumentation 9 years apart and analyzed by different groups with different isotopic techniques suggests these variations are real and persistent.

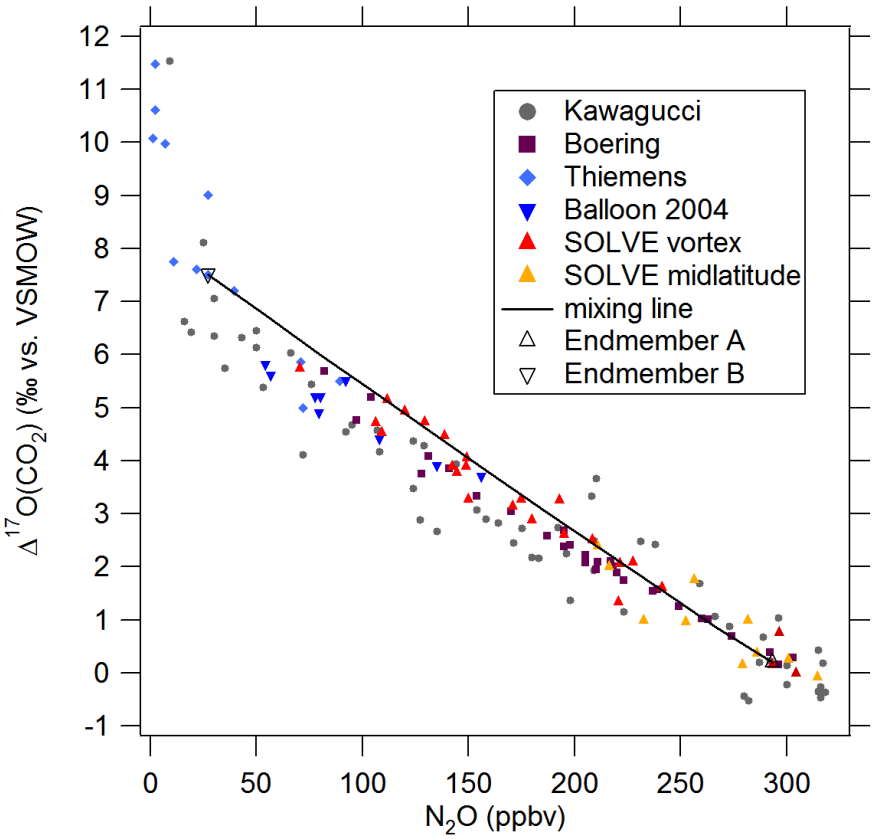

Fig. 2-S4. $\Delta^{17}O$ of CO_2 versus N_2O for this study and for previous observations: Thiemens *et al.* (11); Kawagucci *et al.* (39), Boering *et al.* (44). The two-endmember mixing line from Fig. 2-1 is also shown (see text).

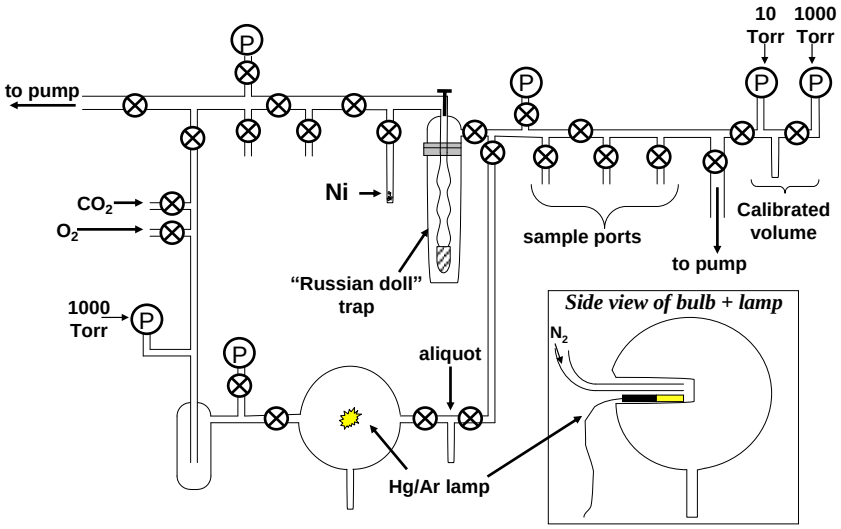

Fig. 2-S5. Schematic representation of vacuum line used for photochemical experiments.

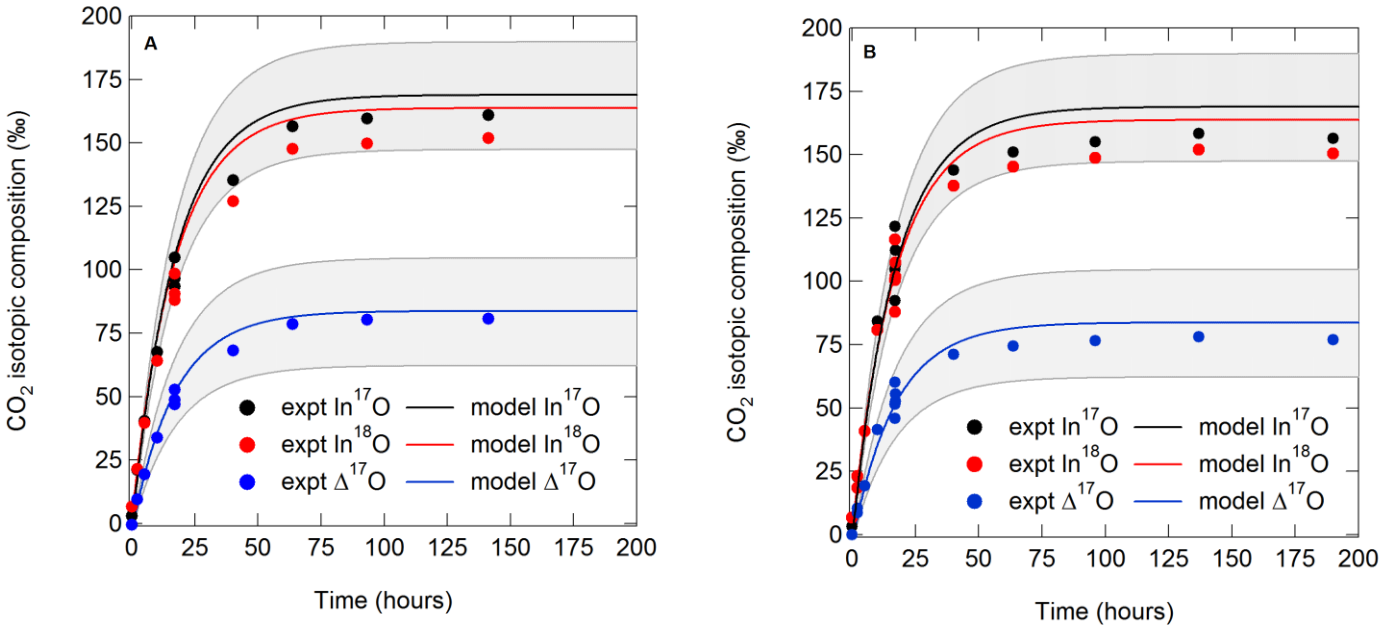

Fig. 2-S6. Predicted isotopic composition of CO_2 from the photochemical model using the base model scenario in the low pressure limit (lines) plotted along with the experimental results (symbols) at (**A**) 50 Torr and (**B**) 100 Torr total pressure.

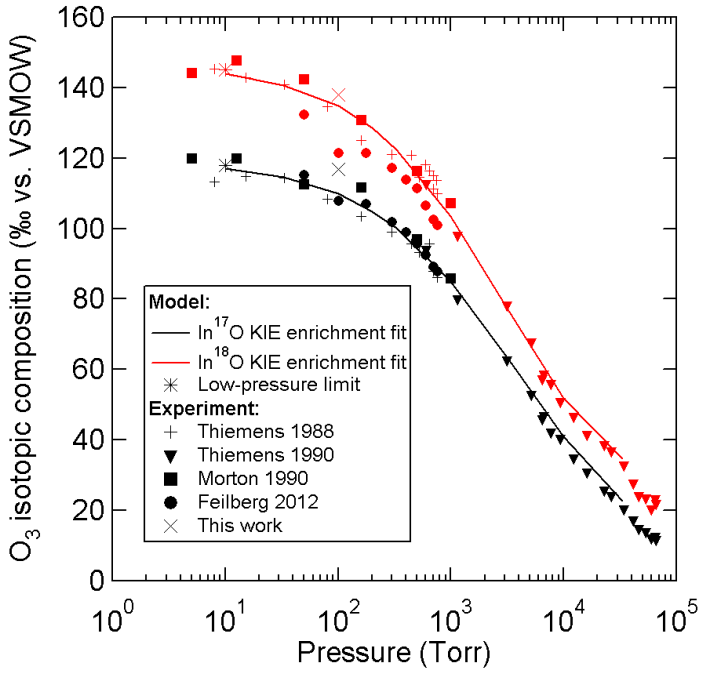

Fig. 2-S7. Photochemical model predictions for $ln^{17}O$ and $ln^{18}O$ of O_3 using the empirically-derived pressure dependence for the O_3 formation KIEs discussed in Section S1.6.2, along with previous experimental results (17, 22-24) and those from Table 2-S8.

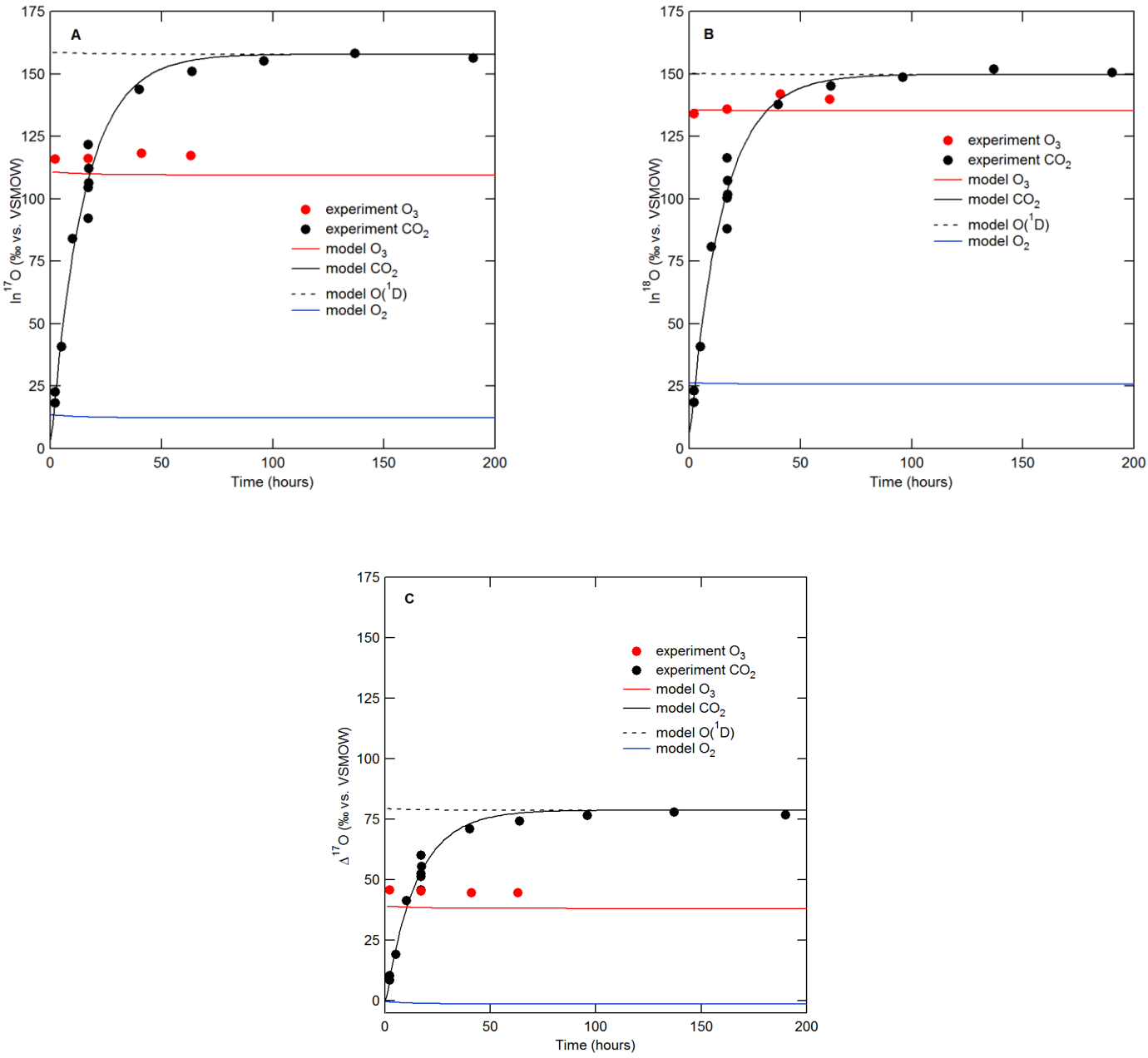

Figure 2-S8. Results for **(A)** $\ln^{17}O$, **(B)** $\ln^{18}O$, and **(C)** $\Delta^{17}O$ versus irradiation time for O_2, O_3, $O(^1D)$, and CO_2 at 100 Torr. Symbols show experimental results for O_3 (red) and CO_2 (black), while lines are the base model predictions.

Table 2-S1. Measurements on whole air samples collected during the SOLVE mission.

Flight date	UT(secs)	Altitude (km)	Latitude (°N)	Longitude (°W)	θ (K)	N_2O (ppbv)	CH_4 (ppbv)	CO_2 (ppmv)	$\ln^{13}C$ (‰ VPDB)	$\ln^{17}O$ (‰ VSMOW)	$\ln^{18}O$ (‰ VSMOW)	$\Delta^{17}O$ (‰ VSMOW) *	$\frac{\Delta\ln^{17}O}{\Delta\ln^{18}O}$ †	Region‡
1999-12-11	78452	16.2	31.6	-127.74	390	301	1695	366.4	-8.11	21.7	40.59	0.2	1.26	Midlatitude
1999-12-11	92199	11.2	35.0	-118.28	336	315	1770	367.2	-8.10	21.2	40.24	-0.1	0.31	Troposphere
2000-01-06	83678	19.6	24.0	-120	473	281	1596	365.5	-8.15	22.7	41.16	1.0	1.59	Midlatitude
2000-01-06	90463	19.4	29.4	-120	463	256	1495	364.1	-8.14	23.8	41.64	1.8	1.77	Midlatitude
2000-01-09	63083	20.1	40.6	-99.6	502	211	1330	362.0	-8.10	24.4	41.70	2.4	2.15	Midlatitude
2000-01-27	38501	19.4	57.8	31.84	441	228	1385	362.7	-8.13	24.2	41.93	2.1	1.75	Vortex Edge
2000-01-27	42165	19.5	51.7	36.57	465	222	1364	362.5	-8.12	24.2	41.98	2.1	1.70	Vortex Edge
2000-01-27	44072	16.2	54.4	34.5	404	286	1622	365.4	-8.11	22.0	40.87	0.4	1.15	Midlatitude
2000-01-27	47949	20.2	60.0	29.31	455	120	985	360.0	-8.13	28.0	43.61	4.9	1.98	Vortex Edge
2000-01-27	52216	19.8	66.2	22.61	445	139	1054	360.5	-8.20	27.3	43.14	4.5	2.06	Vortex Edge
2000-01-27	52761	12.3	67.0	21.87	338	296	1681	366.0	-8.17	22.3	40.83	0.8	1.79	Polar Vortex
2000-01-31	39005	19.2	72.6	17.94	433	175	1183	361.0	-8.15	25.6	42.24	3.3	2.14	Vortex Edge
2000-01-31	42070	19.5	77.9	13.25	433	149	1091	360.5	-8.13	26.8	43.17	4.0	1.90	Polar Vortex
2000-01-31	43541	17.9	77.8	13.36	405	195	1252	361.5	-8.11	24.9	42.22	2.6	1.83	Polar Vortex
2000-01-31	44628	18.3	76.0	15.32	416	180	1200	361.1	-8.12	25.2	42.31	2.9	1.90	Polar Vortex
2000-01-31	46080	19.9	73.4	17.35	444	142	1066	360.5	-8.14	26.4	42.72	3.9	2.08	Vortex Edge
2000-02-02	48616	19.6	73.7	41.61	439	145	1073	360.5	-8.11	26.4	42.81	3.8	1.99	Vortex Edge
2000-02-02	53598	19.7	77.7	12.6	438	129	1017	360.2	-8.16	27.5	43.18	4.7	2.12	Polar Vortex
2000-02-02	55680	19.3	74.0	16.81	431	150	1092	360.5	-8.13	25.7	42.53	3.3	1.94	Polar Vortex
2000-02-03	73606	17.1	71.7	26.06	397	208	1309	361.8	-8.11	24.7	42.07	2.5	1.88	Polar Vortex
2000-02-03	75105	17.6	70.4	27.54	407	193	1250	361.3	-8.12	25.5	42.19	3.3	2.18	Polar Vortex
2000-02-03	77028	18.7	73.0	24.93	419	171	1167	360.9	-8.11	25.6	42.45	3.1	1.93	Polar Vortex
2000-02-03	79886	14.5	68.4	24.36	361	293	1670	366.0	-8.19	21.7	40.86	0.2	0.84	Polar Vortex

2000-02-03	80167	11.7	68.3	23.4	324	305	1719	366.2	-8.15	21.4	40.52	0.0	0.65	Polar Vortex
2000-02-26	36727	19.0	73.3	12	427	149	1084	360.8	-8.11	26.6	43.02	3.9	1.92	Polar Vortex
2000-02-26	44427	17.1	82.7	12	392	221	1356	362.0	-8.13	23.4	41.84	1.3	1.37	Polar Vortex
2000-03-05	40019	16.8	68.2	54.18	387	241	1442	363.6	-8.12	23.7	41.84	1.6	1.53	Polar Vortex
2000-03-05	50946	19.9	79.2	19.33	455	70	789	359.8	-8.11	29.1	44.27	5.7	1.95	Polar Vortex
2000-03-11	40682	17.2	60.5	-0.89	422	279	1594	365.0	-8.11	21.9	41.11	0.1	0.75	Midlatitude
2000-03-11	46558	19.5	67.5	17.33	443	106	929	360.1	-8.13	27.7	43.44	4.7	1.99	Polar Vortex
2000-03-12	44489	19.1	70.1	52.18	439	109	941	360.2	-8.13	27.4	43.26	4.5	2.02	Polar Vortex
2000-03-12	50849	19.3	79.2	34.79	439	112	948	360.2	-8.17	28.2	43.61	5.2	2.05	Polar Vortex
2000-03-16	36822	18.5	61.9	-16.73	463	232	1405	363.1	-8.13	23.1	41.87	1.0	1.14	Midlatitude
2000-03-16	41327	18.9	59.5	-32.4	476	252	1471	364.1	-8.12	22.7	41.14	1.0	1.59	Midlatitude
2000-03-16	45827	19.2	55.8	-45.76	486	216	1338	362.5	-8.13	24.2	41.97	2.0	1.68	Midlatitude

* $\Delta^{17}O = \ln^{17}O - \lambda_{MD} \ln^{18}O$, where $\lambda_{MD} = 0.528$.

† $\Delta\ln^{17}O/\Delta\ln^{18}O$ is the $\ln^{17}O/\ln^{18}O$ value expressed relative to tropospheric CO_2, which was taken to be $\ln^{17}O = 21.16‰$ and $\ln^{18}O = 40.18‰$, and is given by:

$$\frac{\Delta \ln^{17}O}{\Delta \ln^{18}O} = \frac{\ln^{17}O - 21.16‰}{\ln^{18}O - 40.18‰}$$

‡ Based on simultaneous measurements of N_2O and potential temperature using the method of Greenblatt *et al.* (10); see Fig. 2-S1. Midlatitude and "midlatitude-like" high latitude points are grouped under the single heading "midlatitude" in the table.

Table 2-S2. The same measurements from the SOLVE mission from Table 2-S1, except the oxygen isotopic composition of CO_2 is reported relative to VSMOW-CO_2.

Flight date	UT(secs)	Altitude (km)	Latitude (°N)	N_2O (ppbv)	CO_2 (ppmv)	$\ln^{13}C$ (‰ VPDB)	$\ln^{17}O$ (‰ VSMOW-CO_2)	$\ln^{18}O$ (‰ VSMOW-CO_2)	$\Delta^{17}O$ (‰ VSMOW-CO_2) *	Region‡
1999-12-11	78452	16.2	31.6	301	366.4	-8.11	0.6	0.32	0.4	Midlatitude
1999-12-11	92199	11.2	35.0	315	367.2	-8.10	0.1	-0.04	0.1	Troposphere
2000-01-06	83678	19.6	24.0	281	365.5	-8.15	1.7	0.89	1.2	Midlatitude
2000-01-06	90463	19.4	29.4	256	364.1	-8.14	2.7	1.37	2.0	Midlatitude
2000-01-09	63083	20.1	40.6	211	362.0	-8.10	3.4	1.43	2.6	Midlatitude
2000-01-27	38501	19.4	57.8	228	362.7	-8.13	3.2	1.66	2.3	Vortex Edge
2000-01-27	42165	19.5	51.7	222	362.5	-8.12	3.2	1.71	2.3	Vortex Edge
2000-01-27	44072	16.2	54.4	286	365.4	-8.11	0.9	0.60	0.6	Midlatitude
2000-01-27	47949	20.2	60.0	120	360.0	-8.13	6.9	3.34	5.1	Vortex Edge
2000-01-27	52216	19.8	66.2	139	360.5	-8.20	6.2	2.87	4.7	Vortex Edge
2000-01-27	52761	12.3	67.0	296	366.0	-8.17	1.3	0.56	1.0	Polar Vortex
2000-01-31	39005	19.2	72.6	175	361.0	-8.15	4.5	1.97	3.5	Vortex Edge
2000-01-31	42070	19.5	77.9	149	360.5	-8.13	5.8	2.90	4.2	Polar Vortex
2000-01-31	43541	17.9	77.8	195	361.5	-8.11	3.8	1.95	2.8	Polar Vortex
2000-01-31	44628	18.3	76.0	180	361.1	-8.12	4.2	2.04	3.1	Polar Vortex
2000-01-31	46080	19.9	73.4	142	360.5	-8.14	5.4	2.45	4.1	Vortex Edge
2000-02-02	48616	19.6	73.7	145	360.5	-8.11	5.3	2.54	4.0	Vortex Edge
2000-02-02	53598	19.7	77.7	129	360.2	-8.16	6.5	2.91	4.9	Polar Vortex
2000-02-02	55680	19.3	74.0	150	360.5	-8.13	4.7	2.26	3.5	Polar Vortex
2000-02-03	73606	17.1	71.7	208	361.8	-8.11	3.7	1.80	2.7	Polar Vortex
2000-02-03	75105	17.6	70.4	193	361.3	-8.12	4.5	1.92	3.5	Polar Vortex
2000-02-03	77028	18.7	73.0	171	360.9	-8.11	4.5	2.18	3.3	Polar Vortex

2000-02-03	79886	14.5	68.4	293	366.0	-8.19	0.7	0.59	0.4	Polar Vortex
2000-02-03	80167	11.7	68.3	305	366.2	-8.15	0.3	0.25	0.2	Polar Vortex
2000-02-26	36727	19.0	73.3	149	360.8	-8.11	5.6	2.75	4.1	Polar Vortex
2000-02-26	44427	17.1	82.7	221	362.0	-8.13	2.4	1.57	1.5	Polar Vortex
2000-03-05	40019	16.8	68.2	241	363.6	-8.12	2.6	1.57	1.8	Polar Vortex
2000-03-05	50946	19.9	79.2	70	359.8	-8.11	8.1	4.00	5.9	Polar Vortex
2000-03-11	40682	17.2	60.5	279	365.0	-8.11	0.8	0.84	0.4	Midlatitude
2000-03-11	46558	19.5	67.5	106	360.1	-8.13	6.6	3.17	4.9	Polar Vortex
2000-03-12	44489	19.1	70.1	109	360.2	-8.13	6.3	2.99	4.7	Polar Vortex
2000-03-12	50849	19.3	79.2	112	360.2	-8.17	7.1	3.34	5.4	Polar Vortex
2000-03-16	36822	18.5	61.9	232	363.1	-8.13	2.0	1.60	1.2	Midlatitude
2000-03-16	41327	18.9	59.5	252	364.1	-8.12	1.6	0.86	1.2	Midlatitude
2000-03-16	45827	19.2	55.8	216	362.5	-8.13	3.1	1.70	2.2	Midlatitude

* $\Delta^{17}O = \ln^{17}O - \lambda_{MD} \ln^{18}O$, where $\lambda_{MD} = 0.528$.

‡ Based on simultaneous measurements of N_2O and potential temperature using the method of Greenblatt *et al.* (10); see Fig. 2-S1. Midlatitude and "midlatitude-like" high latitude points are grouped under the single heading "midlatitude" in the table.

Table 2-S3. Measurements on whole air samples collected over Ft. Sumner, New Mexico (34°N) on 2004-09-29.

Altitude (km)	θ (K)	N_2O (ppbv)	CH_4 (ppbv)	CO_2 (ppmv)	$\ln^{13}C$ (‰ VPDB)	$\ln^{17}O$ (‰ VSMOW)	$\ln^{18}O$ (‰ VSMOW)	$\Delta^{17}O$* (‰ VSMOW)	$\frac{\Delta\ln^{17}O}{\Delta\ln^{18}O}$ †	Region‡
33.3	931	54	835	360.2	-8.13	29.1	44.17	5.8	1.98	Tropical
32.2	896	56.7	843	360.2	-8.05	29.1	44.46	5.6	1.85	Tropical
31.5	882	79.6	935	360.2	-8.04	28.0	43.84	4.9	1.88	Tropical
30.8	862	77.8	913	360.2	-8.09	28.6	44.18	5.2	1.85	Tropical
30.0	795	80.2	907	360.2	-8.16	28.7	44.44	5.2	1.77	Midlatitude
29.2	778	92.1	957	360.2	-8.13	28.7	44.02	5.5	1.96	Midlatitude
28.7	758	107.9	1014	360.4	-8.10	27.5	43.84	4.4	1.74	Midlatitude
28.0	778	135.2	1102	361.0	-8.08	26.8	43.33	3.9	1.77	Midlatitude
27.2	710	155.9	1176	361.5	-8.09	26.5	43.17	3.7	1.79	Midlatitude

* $\Delta^{17}O = \ln^{17}O - \lambda_{MD} \ln^{18}O$, where $\lambda_{MD} = 0.528$.

† $\Delta\ln^{17}O/\Delta\ln^{18}O$ is the $\ln^{17}O/\ln^{18}O$ value expressed relative to tropospheric CO_2, which was taken to be $\ln^{17}O = 21.16‰$ and $\ln^{18}O = 40.18‰$, and is given by:

$$\frac{\Delta \ln^{17}O}{\Delta \ln^{18}O} = \frac{\ln^{17}O - 21.16‰}{\ln^{18}O - 40.18‰}$$

‡ "Tropical" indicates "tropically-influenced" air, based on higher excursions in CH_4 as a function of pressure altitude; see Fig. 2-S2 and 2-S3.

Table 2-S4. The same measurements from the 2004-09-29 balloon flight in Table 2-S3, except the oxygen isotopic composition of CO_2 is reported relative to VSMOW-CO_2.

Altitude (km)	θ (K)	N_2O (ppbv)	CH_4 (ppbv)	CO_2 (ppmv)	$\ln^{13}C$ (‰ VPDB)	$\ln^{17}O$ (‰ VSMOW-CO_2)	$\ln^{18}O$ (‰ VSMOW-CO_2)	$\Delta^{17}O$* (‰ VSMOW-CO_2)	Region†
33.3	931	54	835	360.2	-8.13	8.0	3.90	6.0	Tropical
32.2	896	56.7	843	360.2	-8.05	8.0	4.19	5.8	Tropical
31.5	882	79.6	935	360.2	-8.04	7.6	4.17	5.4	Tropical
30.8	862	77.8	913	360.2	-8.09	7.6	3.75	5.7	Tropical
30.0	795	80.2	907	360.2	-8.16	7.5	3.91	5.5	Midlatitude
29.2	778	92.1	957	360.2	-8.13	7.0	3.57	5.1	Midlatitude
28.7	758	107.9	1014	360.4	-8.10	6.5	3.57	4.6	Midlatitude
28.0	778	135.2	1102	361.0	-8.08	5.7	3.06	4.1	Midlatitude
27.2	710	155.9	1176	361.5	-8.09	5.4	2.90	3.9	Midlatitude

* $\Delta^{17}O = \ln^{17}O - \lambda_{MD} \ln^{18}O$, where $\lambda_{MD} = 0.528$

† "Tropical" indicates "tropically-influenced" air, based on higher excursions in CH_4 as a function of pressure altitude; see Fig. 2-S2 and 2-S3.

Table 2-S5. Homogeneity of regression tests of the statistical significance between different data sets.

Data Set 1	Data Set 2	F(df)	P
SOLVE vortex + vortex edge	Lämmerzahl *et al.* (13)	45.20 (1,45)	<0.01
SOLVE midlat. + Balloon 2004	Lämmerzahl *et al.* (13)	14.51 (1,39)	<0.01
SOLVE vortex + vortex edge	Kawagucci *et al.(39)*	10.86 (1,75)	<0.01
SOLVE midlat. + Balloon 2004	Kawagucci *et al.* (39)	4.45 (1,69)	<0.05

Table 2-S6. Mass fractions of endmembers A and B and the corresponding mixing ratios and CO_2 isotopic compositions (VSMOW) of the mixed air parcel.

M_A	M_B	N_2O (ppbv)	CO_2 (ppmv)	CH_4 (ppbv)	$\ln^{17}O$ (‰)	$\ln^{18}O$ (‰)	$\Delta^{17}O$ (‰)
1	0	293.3	366.0	1670	21.7	40.86	0.2
0.9	0.1	266.7	364.4	1565	22.8	41.48	0.9
0.8	0.2	240.0	362.9	1459	23.8	42.10	1.6
0.7	0.3	213.4	361.3	1354	24.9	42.73	2.3
0.6	0.4	186.8	359.8	1249	25.9	43.36	3.0
0.5	0.5	160.2	358.2	1144	27.0	44.00	3.8
0.4	0.6	133.5	356.7	1038	28.1	44.64	4.5
0.3	0.7	106.9	355.1	933	29.2	45.29	5.2
0.2	0.8	80.3	353.6	828	30.3	45.94	6.0
0.1	0.9	53.6	352.0	722	31.4	46.60	6.8
0	1	27.0	350.5	617	32.5	47.27	7.5

Table 2-S7. Measurements of the isotopic composition of CO_2 as a function of irradiation time in O_2-CO_2 mixtures at total pressures of ~100 Torr and ~50 Torr.

Irradiation time (hours)	Pressure O_2 (Torr)	Pressure CO_2 (mTorr)	CO_2 Yield	$\ln^{13}C$ (‰ vs. VPDB)	$\ln^{17}O$ (‰ vs. VSMOW)	$\ln^{18}O$ (‰ vs. VSMOW)	$\Delta^{17}O$ (‰ vs. VSMOW)
0	--	--		-40.0	3.4	6.6	-0.1
2	99.0	208	100%	-41.3	22.7	23.1	10.5
2	99.3	205	100%	-42.0	18.5	18.5	8.7
5	99.6	207	101%	-41.8	40.9	41.0	19.3
10	99.5	209	101%	-41.2	84.2	80.9	41.5
17	99.7	211	103%	-40.4	121.7	116.5	60.2
17	99.2	214	100%	-40.7	104.6	100.5	51.6
17	99.5	207	100%	-42.0	92.3	88.0	45.8
17.1	99.7	211	100%	-41.6	106.4	101.8	52.7
17.15	99.6	209	103%	-41.9	112.3	107.3	55.6
40	99.8	214	102%	-41.4	143.9	137.8	71.1
63.67	99.6	211	101%	-41.6	151.1	145.2	74.4
96	99.7	207	104%	-41.6	155.1	148.7	76.6
137	99.4	207	99.9%	-40.5	158.4	152.0	78.1
190	100.4	228	99.5%	-39.5	156.5	150.5	77.0
2	50.0	110	100.5%	-41.2	21.1	21.6	9.7
5.03	50.0	109	100.8%	-41.3	40.5	39.7	19.5
9.98	50.0	110	100.1%	-41.3	67.7	64.2	33.8
17	50.0	104	100.5%	-41.9	104.9	98.6	52.8
17	50.1	113	100.6%	-41.4	93.5	88.0	47.0
17	49.9	112	100.5%	-41.9	96.6	90.6	48.8
40.05	49.9	112	101.2%	-41.6	135.4	127.2	68.3
63.67	50.0	110	102.0%	-42.1	156.6	147.8	78.6
93.23	50.0	107	102.8%	-41.2	159.6	149.9	80.5
141.17	50.2	110	105.1%	-41.6	161.1	151.9	80.9

Table 2-S8. Measurements of the isotopic composition of O_3 as a function of irradiation time in O_2-CO_2 mixtures (in separate experiments) at total pressures of ~100 Torr.

Irradiation time (hours)	$P(O_2)$ (Torr)	$P(CO_2)$ (Torr)	$\ln^{17}O$ (‰ VSMOW)	$\ln^{18}O$ (‰ VSMOW)	$\Delta^{17}O$ (‰ VSMOW)
2	99.6	0	115.9	134.4	44.9
17	102.4	0.21	116.1	136.0	44.3
41	99.4	0.21	118.3	141.5	43.6
63	99.3	0.21	117.3	139.5	43.6
Average (1σ)			117 ± 1	138 ± 3	44.1 ± 0.6

Table 2-S9. Reactions included in the kinetics model

Reaction		Rate Coefficient	Source
S6	$O_2 + h\nu \rightarrow O + O$	2.2×10^{-7} s^{-1}	Cross section from Yoshino *et al.* (30); flux from CO_2 actinometry
S7	$O + O_2 + M \rightarrow O_3 + M$	$6.0\times10^{-34}(T/300)^{-2.4}$ cm^6 s^{-1}	Sander *et al.*(29)
S8a S8b	$O_3 + h\nu \rightarrow O_2 + O$ $O_3 + h\nu \rightarrow O_2(^1\Delta) + O(^1D)$	$0.1\times(1.8\times10^{-2}$ $s^{-1})$ $0.9\times(1.8\times10^{-2}$ $s^{-1})$	Flux estimated from CO_2 actinometry and 254/185 flux ratio (20); cross section and branching ratio from Sander *et al.* (29)
S9	$O_3 + O \rightarrow 2O_2$	8.0×10^{-12} exp(-2060/T) cm^3 s^{-1}	Sander *et al.* (29)
S10	$O_3 + O(^1D) \rightarrow 2O_2$	1.2×10^{-10} cm^3 s^{-1}	Sander *et al.* (29)
S11	$O_3 + O(^1D) \rightarrow O_2 + 2O$	1.2×10^{-10} cm^3 s^{-1}	Sander *et al.* (29)
S12	$O_3 + O_2(^1\Delta) \rightarrow 2O_2 + O$	5.2×10^{-11} exp(-2840/T) cm^3 s^{-1}	Sander *et al.* (29)
S13	$O_2(^1\Delta) + O_2 \rightarrow O_2 + O_2$	1.6×10^{-18} cm^3 s^{-1}	Sander *et al.* (29)
S14	$O_2(^1\Delta) + CO_2 \rightarrow O_2 + CO_2$	2×10^{-20} cm^3 s^{-1}	Sander *et al.* (29) (upper limit)
S15a S15b	$O(^1D) + O_2 \rightarrow O + O_2$ $O(^1D) + O_2 \rightarrow O + O_2(^1\Sigma)$	$0.2\times(3.2\times10^{-11}$exp(70/T) cm^3 $s^{-1})$ $0.8\times(3.2\times10^{-11}$exp(70/T) cm^3 $s^{-1})$	Sander *et al.* (29)and references therein re. yield of $O_2(^1\Sigma)$
S16	$O_2(^1\Sigma) + O_2 \rightarrow O_2(^1\Delta) + O_2$	4.0×10^{-17} cm^3 s^{-1}	Sander *et al.* (29)
S17a S17b	$O_2(^1\Sigma) + O_3 \rightarrow O_2(^1\Delta) + O_3$ $O_2(^1\Sigma) + O_3 \rightarrow O + 2O_2$	$0.3\times(2.2\times10^{-11}$ cm^3 $s^{-1})$ $0.7\times(2.2\times10^{-11}$ cm^3 $s^{-1})$	Sander *et al.* (29); assumed no $O_2(^3\Sigma)$ product Sander *et al.* (29)
S18	$O_2(^1\Sigma) + O \rightarrow O_2(^1\Delta) + O$	8.0×10^{-14} cm^3 s^{-1}	Sander *et al.* (29); assumed no $O_2(^3\Sigma)$ product
S19	$O_2(^1\Sigma) + CO_2 \rightarrow O_2(^1\Delta) + CO_2$	4.1×10^{-13} cm^3 s^{-1}	Sander *et al.* (29)
S20	$O(^1D) + CO_2 \rightarrow O + CO_2$	1.1×10^{-10} cm^3 s^{-1}	Sander *et al.* (29)
S21	O’ + OO → OO’ + O	3.4×10^{-12} $(T/300)^{-1.1}$ cm^3 s^{-1} [O’=^{18}O or ^{17}O]	Fleurat-Lessard *et al.* (32)
S22	O’ + OO ↔ OO’ + O	K_{eq}[O’=^{18}O] = 1.94 exp(32/T) K_{eq}[O’=^{17}O] = 1.96 exp(16.8/T)	Kaye and Strobel (33)

Table 2-S10. Isotope-specific rate coefficients for ozone formation containing a single heavy oxygen atom relative to that for $^{16}O^{16}O^{16}O$, and relative J-values for O_3 photolysis used in the model scenarios shown in Fig. 2-2C and Fig. 2-2D and Table 2-S9.

Reaction	Mauersberger *et al.* (27)	Janssen *et al.* (28)	Used in these calculations	Relative J-values for O_3 photolysis isotope effects		
				Liang *et al.* (31)	Normal isotope effect	Inverse isotope effect
$^{16}O + {}^{16}O^{16}O \rightarrow {}^{16}O^{16}O^{16}O$	1.00	1.00	1.00	1.00	1.00	1.00
$^{18}O + {}^{16}O^{16}O \rightarrow {}^{16}O^{16}O^{18}O$	0.93 ± 0.03	0.92 ± 0.04	0.92	1.0080×1/2	0.962×1/2	1.040×1/2
$^{16}O + {}^{16}O^{18}O \rightarrow {}^{16}O^{16}O^{18}O$	} 1.27 ± 0.03	1.45 ± 0.04	1.45	1.0080×1/2	0.990×1/2	1.010×1/2
$^{16}O + {}^{16}O^{18}O \rightarrow {}^{16}O^{18}O^{16}O$		1.08 ± 0.01	1.08	1.0131	0.990	1.010
$^{17}O + {}^{16}O^{16}O \rightarrow {}^{16}O^{16}O^{17}O$	1.03 ± 0.05	--	1.03	1.0042×1/2	0.980×1/2	1.020×1/2
$^{16}O + {}^{16}O^{17}O \rightarrow {}^{16}O^{16}O^{17}O$	} 1.17 ± 0.05	--	1.35	1.0042×1/2	0.995×1/2	1.005×1/2
$^{16}O + {}^{16}O^{17}O \rightarrow {}^{16}O^{17}O^{16}O$		--	0.99	1.0067	0.995	1.005

Table 2-S11. Isotopic compositions from photochemistry experiments and kinetics modeling at 100 Torr on the VSMOW scale. The modeled $O(^1D)$ isotopic composition is identical to that for CO_2 since isotope effects in the $O(^1D) + CO_2$ isotope exchange reaction were not included in these model scenarios.

Description	**CO_2***				**O_3†**			
	$\ln^{17}O$	**$\ln^{18}O$**	**$\ln^{17}O/\ln^{18}O$**	**$\Delta^{17}O$‡**	**$\ln^{17}O$**	**$\ln^{18}O$**	**$\ln^{17}O/\ln^{18}O$**	**$\Delta^{17}O$‡**
Experiment:	157 ± 2	150 ± 2	1.053 ± 0.003	77.2 ± 0.8	112 ± 5	130 ± 9	0.86 ± 0.07	44 ± 2
Model:								
Base Scenario	158	150	1.079	78.8	110	135	0.81	38.7
Liang photolysis IE §	160	155	1.060	78.7	108	131	0.82	38.8
Normal photolysis IE	143	121	1.212	78.9	114	144	0.79	38.0
Inverse photolysis IE	172	179	0.983	78.2	105	127	0.83	37.9
Tropopause O_2 and CO_2	153	142	1.29	78.9	106	129	0.82	37.9
" " and T = 250K	135	118	1.46	73.0	93	112	0.83	33.9
" " and T = 220K	121	99	1.70	69.2	83	99	0.84	30.7
" " and T = 200K	112	86	1.99	65.6	76	90	0.84	28.5

* Experimental results for CO_2 are an average (N=3, ±1σ) of the measured values at isotopic steady-state.

† Experimental results for O_3 are an average (N=8, ±1σ) of photochemistry experiments at 100 Torr from Feilberg, Wiegel, and Boering (22) and from Table 2-S8.

‡ $\Delta^{17}O = \ln^{17}O - 0.528 \ln^{18}O$.

§ Theoretical O_3 photolysis isotope effect at 254 nm (31).

SUPPLEMENTARY REFERENCES

1. Flocke F, *et al.* (1999) An examination of chemistry and transport processes in the tropical lower stratosphere using observations of long-lived and short-lived compounds obtained during STRAT and POLARIS. *J Geophys Res* 104:26625-26642.
2. Newman PA, *et al.* (2002) An overview of the SOLVE/THESEO 2000 campaign. *Journal of Geophysical Research-Atmospheres* 107(D20):8259.
3. Froidevaux L, *et al.* (2006) Early validation analyses of atmospheric profiles from EOS MLS on the Aura satellite. *IEEE Transactions on Geoscience and Remote Sensing* 44(5):1106-1121.
4. Lueb RA, Ehhalt DH, & Heidt LE (1975) Balloon-borne low temperature air sampler. *Rev. Sci. Instrum.* 46(6):702-705.
5. Assonov SS & Brenninkmeijer CAM (2001) A new method to determine the ^{17}O isotopic abundance in CO_2 using oxygen isotope exchange with a solid oxide. *Rapid Communications in Mass Spectrometry* 15(24):2426-2437.
6. Assonov SS & Brenninkmeijer CAM (2003) A redetermination of absolute values for R-17(VPDB-CO2) and R-17(VSMOW). *Rapid Communications in Mass Spectrometry* 17(10):1017-1029.
7. Luz B & Barkan E (2011) The isotopic composition of atmospheric oxygen. *Global Biogeochemical Cycles* 25:10.1029/2010gb003883.
8. Assonov SS & Brenninkmeijer CAM (2006) On the N_2O correction used for mass spectrometric analysis of atmospheric CO_2. *Rapid Communications in Mass Spectrometry* 20(11):1809-1819.
9. Boering KA, *et al.* (1996) Stratospheric mean ages and transport rates from observations of carbon dioxide and nitrous oxide. *Science* 274(5291):1340-1343.
10. Greenblatt JB, *et al.* (2002) Tracer-based determination of vortex descent in the 1999/2000 Arctic winter. *Journal of Geophysical Research-Atmospheres* 107(D20):8279.
11. Thiemens MH, Jackson T, Zipf EC, Erdman PW, & van Egmond C (1995) Carbon dioxide and oxygen isotope anomalies in the mesosphere and stratosphere. *Science* 270:969-972.
12. Cantrell CA (2008) Technical Note: Review of methods for linear least-squares fitting of data and application to atmospheric chemistry problems. *Atmospheric Chemistry and Physics* 8(17):5477-5487.
13. Lammerzahl P, Rockmann T, Brenninkmeijer CAM, Krankowsky D, & Mauersberger K (2002) Oxygen isotope composition of stratospheric carbon dioxide. *Geophysical Research Letters* 29(12):1582.
14. Criss RE (1999) *Principles of Stable Isotope Distribution* (Oxford Unviersity Press, New York) p 264.
15. Rex M, *et al.* (1999) Subsidence, mixing, and denitrification of Arctic polar vortex air measured During POLARIS. *Journal of Geophysical Research-Atmospheres* 104(D21):26611-26623.
16. Johnston JC, Rockmann T, & Brenninkmeijer CAM (2000) $CO_2 + O(^1D)$ isotopic exchange: Laboratory and modeling studies. *Journal of Geophysical Research* 105(D12):15213-15229.

17. Morton J, Barnes J, Schueler B, & Mauersberger K (1990) Laboratory studies of heavy ozone. *Journal of Geophysical Research* 95(D1):901-907.
18. Janssen C & Tuzson B (2010) Isotope Evidence for Ozone Formation on Surfaces. *Journal of Physical Chemistry A* 114(36):9709-9719.
19. Reader J, Sansonetti CJ, & Bridges JM (1996) Irradiances of spectral lines in mercury pencil lamps. *Appl. Optics* 35(1):78-83.
20. Okabe H (1978) *Photochemistry of Small Molecules* (John Wiley & Sons, New York) p 431.
21. Shaheen R, Janssen C, & Rockmann T (2007) Investigations of the photochemical isotope equilibrium between O_2, CO_2 and O_3. *Atmospheric Chemistry and Physics* 7:495-509.
22. Feilberg KL, Wiegel AA, & Boering KA (2013) Probing the unusual isotope effects in ozone formation: Bath gas and pressure dependence of the non-mass-dependent isotope enrichments in ozone. *Chemical Physics Letters* 556:1-8.
23. Thiemens MH & Jackson T (1988) New experimental evidence for the mechanism for production of isotopically heavy O_3. *Geophysical Research Letters* 15(7):639-642.
24. Thiemens MH & Jackson T (1990) Pressure dependency for heavy isotope enhancement in ozone formation. *Geophys. Res. Lett.* 17(6):717-719.
25. J.C. Ianni, Kintecus, Windows Version 2.80, 2002 (www.kintecus.com)
26. Cole AS & Boering KA (2006) Mass-dependent and non-mass-dependent isotope effects in ozone photolysis: Resolving theory and experiments. *Journal of Chemical Physics* 125(18):184301.
27. Mauersberger K, Erbacher B, Krankowsky D, Gunther J, & Nickel R (1999) Ozone isotope enrichment: Isotopomer-specific rate coefficients. *Science* 283:370-372.
28. Janssen C, Guenther J, Mauersberger K, & Krankowsky D (2001) Kinetic origin of the ozone isotope effect: a critical analysis of enrichments and rate coefficients. *Physical Chemistry Chemical Physics* 3(21):4718-4721.
29. Sander SP, *et al.* (2011) Chemical Kinetics and Photochemical Data for Use in Atmospheric Studies, Evaluation Number 17. in *Chemical Kinetics and Photochemical Data for Use in Atmospheric Studies, Evaluation Number 17, JPL Publication 10-6* (NASA JPL Publication 10-6 Pasadena).
30. Yoshino K, Esmond JR, Cheung ASC, Freeman DE, & Parkinson WH (1992) High-resolution Absorption Cross-sections in the Transmission Window Region of the Schumann-Runge Bands and Herzberg Continuum of O_2. *Planetary and Space Science* 40(2-3):185-192.
31. Liang MC, Blake GA, & Yung YL (2004) A semi-analytic model for photo-induced isotopic fractionation in simple molecules. *Journal of Geophysical Research-Atmospheres* 109(D10):D10308.
32. Fleurat-Lessard P, Grebenshchikov SY, Schinke R, Janssen C, & Krankowsky D (2003) Isotope dependence of the $O+O_2$ exchange reaction: Experiment and theory. *Journal of Chemical Physics* 119(9):4700-4712.
33. Kaye JA & Strobel DF (1983) Enhancement of heavy ozone in the Earth's atmosphere ? *Journal of Geophysical Research* 88:8447-8452.
34. Michalski G & Bhattacharya SK (2009) The role of symmetry in the mass independent isotope effect in ozone. *Proceedings of the National Academy of Sciences of the United States of America* 106(14):5493-5496.

35. Guenther J, Erbacher B, Krankowsky D, & Mauersberger K (1999) Pressure dependence of two relative ozone formation rate coefficients. *Chemical Physics Letters* 306(5-6):209-213.
36. Wen J & Thiemens MH (1993) Multi-isotope study of the $O(^1D) + CO_2$ exchange and stratospheric consequences. *J. Geophys. Res.* 98(D7):12801-12808.
37. Janssen C, Guenther J, Krankowsky D, & Mauersberger K (2003) Temperature dependence of ozone rate coefficients and isotopologue fractionation in O-16-O-18 oxygen mixtures. *Chemical Physics Letters* 367(1-2):34-38.
38. Krankowsky D, *et al.* (2007) Stratospheric ozone isotope fractionations derived from collected samples. *Journal of Geophysical Research-Atmospheres* 112(D8):D08301.
39. Kawagucci S, *et al.* (2008) Long-term observation of mass-independent oxygen isotope anomaly in stratospheric CO_2. *Atmospheric Chemistry and Physics* 8:6189-6197.
40. Zipf E & Erdman PW (1994) Trace constituents in the upper stratosphere and mesosphere using cryogenic whole sampling techniques. *1992-1993 UARP Research Summaries: Report to Congress*.
41. Liang MC, Blake GA, Lewis BR, & Yung YL (2007) Oxygen isotopic composition of carbon dioxide in the middle atmosphere. *Proceedings of the National Academy of the Sciences of the United States of America* 104(1):21-25.
42. Liang MC, Blake GA, & Yung YL (2008) Seasonal cycle of $C^{16}O^{16}O$, $C^{16}O^{17}O$, and $C^{16}O^{18}O$ in the middle atmosphere: Implications for mesospheric dynamics and biogeochemical sources and sinks of CO_2. *Journal of Geophysical Research* 113:D12305.
43. Prather M & Remsberg E (1993) The atmospheric effects of stratospheric aircraft: Report of the 1992 Models and Measurements Workshop. *NASA Ref. Publ. 1291*.
44. Boering KA, *et al.* (2004) Observations of the anomalous oxygen isotopic composition of carbon dioxide in the lower stratosphere and the flux of the anomaly to the troposphere. *Geophysical Research Letters* 31(3):L03109.

Chapter 3

Non-mass-dependent isotope fractionation generated from high energy isotope exchange collisions in UV irradiated mixtures of O_2 and CO_2

Abstract

Laboratory and atmospheric measurements have shown that stratospheric CO_2 is non-mass-dependently enriched in the rare stable isotopes ^{17}O and ^{18}O relative to ^{16}O and that the anomalous enrichments arise from $O(^1D)$-mediated isotope exchange produced by the photolysis of non-mass-dependently enriched O_3. However, laboratory measurements of the isotopic composition of UV-irradiated mixtures of O_2 and CO_2 in which the O_2/CO_2 mixing ratio is varied to levels far below the atmospheric mixing ratio show a dramatic decrease in the anomalous ^{17}O isotopic composition with decreasing O_2/CO_2 that cannot be explained by expectations of how the non-mass-dependent anomalous KIEs in O_3 formation could vary under these experimental conditions. In this study, additional laboratory measurements of the triple isotope composition of CO_2 from irradiating mixtures of CO_2 and O_2 as a function of the O_2/CO_2 mixing ratio at several different total pressures are reported and compared with predictions from a photochemical kinetics model. Of the many mechanisms investigated in the model, only two mechanisms were found to result in a O_2/CO_2 ratio dependence in the ^{17}O anomaly for CO_2 in the model, both arising from calculated changes in the non-thermal kinetic energy distributions for $^{16}O(^1D)$, $^{17}O(^1D)$, and $^{18}O(^1D)$ as the O_2/CO_2 ratio changes. Importantly, the sources of non-mass-dependent isotope fractionation did not appear to be directly related to the isotopic composition of ozone. Although the modeled O_2/CO_2 dependence is still a factor of ~5 too small compared to experiment, model sensitivities testing known systematic biases in the hard-sphere approximations used to calculate the energy distributions suggest that more accurate calculations of inelastic energy transfer in the relevant $O(^1D)$ isotope exchange reactions in this system are likely to go in the direction of reducing the current model-measurement discrepancies.

3.1. Introduction

The stable isotope ratios of chemical compounds can often provide useful information for understanding chemical mechanisms and geophysical processes that cannot be understood by using concentrations alone. Usually, changes in the stable isotope ratios are well predicted by statistical mechanics or statistical reaction rate theories.[1] For the three stable isotopes of oxygen (^{16}O, ^{17}O, and ^{18}O), these changes are reported relative to an international standard such as Vienna Standard Mean Ocean Water (VSMOW), and here we follow the logarithmic ratio convention suggested by Miller[2] in Eq. (1).

$$\ln {}^{18}O = \ln\left[\frac{\left({}^{18}O/{}^{16}O\right)_{\text{sample}}}{\left({}^{18}O/{}^{16}O\right)_{\text{standard}}}\right] = \ln(1+\delta^{18}O) \quad (1)$$

In this equation, $\delta^{18}O$ is the more commonly reported isotopic composition, but δ-values become non-linear for the large changes in the isotopic composition studied here. For most oxygen-containing compounds on Earth, $\ln^{17}O$ and $\ln^{18}O$ obey a "mass-dependent" relationship, shown

in Eq. (2) because the processes that affect the isotope ratios scale with the differences in masses.[3,4]

$$\ln {}^{17}\mathrm{O} = \lambda_{\mathrm{MD}} \times \ln {}^{18}\mathrm{O} \quad (2)$$

Values for λ_{MD} are typically 0.52, but the actual value can range from 0.5 to 0.53 depending on the physical or chemical process involved. Values of λ_{MD} are derived from ratios of partition functions in statistical mechanics or statistical reaction rate theories; conceptually, the value of λ_{MD} is approximately the ratio of the mass differences between ^{17}O and ^{16}O and between ^{18}O and ^{16}O. For these mass-dependent cases, the measurement of ^{17}O has until recently[5,6] been considered redundant and is often ignored.

In some special cases, the oxygen isotope ratios do not scale with the differences in mass and are instead called "anomalous" or "non-mass-dependent". The non-mass-dependent isotopic compositions are often quantified by Δ^{17}O, defined in Equation (3).[2,7]

$$\Delta^{17}\mathrm{O} = \ln {}^{17}\mathrm{O} - \lambda \times \ln {}^{18}\mathrm{O} \quad (3)$$

where λ is the $\ln{}^{17}\mathrm{O}/\ln{}^{18}\mathrm{O}$ relationship expected for mass-dependent fractionation. Non-mass-dependent isotopic compositions have been measured in stratospheric CO_2[8–12] and in several other oxygen-containing chemical species in the atmosphere, including O_3.[3,4] The ^{17}O isotope anomaly in stratospheric CO_2 was proposed[13] to originate in non-mass-dependent kinetic isotope effects (KIEs) in ozone formation, followed by the ultraviolet photolysis of ozone to form $O(^1D)$ (R2) and subsequent $O(^1D)$ quenching and isotope exchange (R3) with CO_2.

(R1) $O(^3P) + O_2 \rightarrow O_3^* + M \rightarrow O_3 + M^*$

(R2) $O_3 + h\nu \rightarrow O(^1D) + O_2(^1\Delta)$ $\lambda < 310$ nm

(R3) $O(^1D) + CO_2 \rightarrow CO_3^* \rightarrow O(^3P) + CO_2$

(R4) $O(^1D) + CO_2 \rightarrow CO_3^* \rightarrow O(^1D) + CO_2$

Subsequent crossed-molecular beam experiments by Perri et al. demonstrated that the "non-quenching" isotope exchange reaction (R4) also occurs and that its importance relative to (R3) increases with increasing collision energy between $O(^1D)$ and CO_2.[14,15] In Chapter 2, experiments and kinetics modeling of UV-irradiated mixtures of O_2 and CO_2 at an atmospheric O_2/CO_2 mixing ratio showed that the measured or derived non-mass-dependent isotope effects in ozone formation (R1)[16,17] and subsequent mass-dependent transfer from O_3 to CO_2 through $O(^1D)$ quantitatively accounts for the ^{17}O isotope anomaly of CO_2 in the laboratory. These results confirm that the ^{17}O isotope anomaly in CO_2 derives from transfer from O_3 and that no additional non-mass-dependent isotope effects beyond O_3 formation are needed at atmospheric mixing ratios of O_2 and CO_2.

While additional non-mass-dependent isotope effects are not necessary to explain the isotope anomaly in CO_2 measured in the laboratory at atmospheric mixing ratios or in the Earth's stratosphere, previous experiments by Shaheen et al.[18] in which the O_2/CO_2 mixing ratio ρ was varied showed systematically that the ^{17}O and ^{18}O enrichments and ^{17}O isotope anomaly of CO_2 relative to O_2 in the same experiment decreased significantly with decreasing ρ. These decreases in the enrichments of CO_2 relative to O_2 with decreasing ρ could explain many of the differences between previous experiments[19,20] and were much larger than any expected change in the isotopic composition of O_3 on changing the bath gas M in (R1) from O_2 to CO_2.[21] Indeed,

subsequent measurements by Feilberg, Wiegel, and Boering[22] of the isotopic composition of O_3 formed in a CO_2 bath gas confirmed that the differences in the isotopic composition of O_3 formed in O_2 versus CO_2 were small and thus not large enough to be responsible for the measured ρ dependence of the relative isotopic compositions in CO_2 in the Shaheen et al.[18] experiments.

Because the ρ dependence of the relative isotopic composition of CO_2 formed in UV-irradiated mixtures of O_2 and CO_2 could not be explained by expected changes in the ozone in a CO_2 bath gas, Shaheen et al.[18] postulated that an additional unknown non-mass-dependent isotope effect beyond O_3 formation becomes important as ρ decreases. They argued that the ρ dependence might arise from a decrease in the branching ratio of quenching (R3) to non-quenching (R4) in the $O(^1D) + CO_2$ isotope exchange reactions as ρ decreased if $O(^1D)$ from O_3 photolysis (R2) is thermalized less efficiently in a CO_2-dominated mixture than in an O_2-dominated mixture. They based their hypothesis on the following experimental and theoretical studies. First, the cross-beam experiments on the $O(^1D) + CO_2$ isotope exchange ((R3) and (R4)) discussed above had demonstrated that the relative importance of (R4) over (R3) increases with increasing collision energy between $O(^1D)$ and CO_2.[15] Second, Mebel et al.[23] had used the experimental crossed-beam results and RRKM theory to calculate the isotope-specific branching ratios for (R3) and (R4) for ^{16}O and ^{18}O and concluded that the isotope effects for (R3) and (R4) may not only be different from each other but may also show a different collision energy dependence. Third, the excess translational energy from the $O(^1D)$ produced from UV photolysis of O_3 (R2) at a wavelength of 254 nm[24] is only partially thermalized by collisions with O_2 based on calculations of $O(^1D)$ thermalization in O_2 using the hard sphere approximation for collisions.[25,26] Using all of these ideas, Shaheen et al.[18] hypothesized that if the steady-state translational energy distribution of $O(^1D)$ in CO_2-dominated mixtures (i.e., low ρ) contained a larger population of high kinetic energy $O(^1D)$ than the distribution in O_2-dominated mixtures (i.e., at high ρ), then the increasing importance of the non-quenching $O(^1D) + CO_2$ isotope exchange reaction (R4) at low ρ might produce $O(^1D)$ with a different isotopic composition than $O(^1D)$ at high ρ. A change in the isotopic composition of $O(^1D)$ with decreasing ρ could thus potentially lead to large changes in the isotopic composition of CO_2. To date, however, steady-state translational energy distributions for $O(^1D)$ in UV irradiated mixtures of O_2 and CO_2 at low ρ have not been calculated. Thus, whether the translational energy distribution for $O(^1D)$ in the high CO_2 (low ρ) experiments had a greater population of high energy $O(^1D)$ atoms than the low CO_2 (high ρ) experiments and what effects, if any, such differences in the $O(^1D)$ translational energy distributions might have on the measured CO_2 isotopic composition in these experiments are unknown. As such, calculations of the steady-state translational energy distribution for $O(^1D)$ in these experiments are needed to investigate how changes in the translational energy distributions for $O(^1D)$ could affect the isotopic compositions of CO_2 and O_2.

To investigate the ρ dependence of the isotopic composition of CO_2 relative to O_2 and its possible origin(s), new experiments measuring the triple isotope compositions of UV-irradiated mixtures of O_2 and CO_2 at both 50 Torr and 170 Torr were performed, including a special emphasis on experiments near ρ =1 where the relative enrichments were found to change rapidly. The experimental results are then compared with results from a photochemical kinetics model in KINTECUS[27] similar to the one used in Chapter 2. A number of model scenarios were designed to investigate the effects of reaction rates, known and unknown isotope effects, and the $O(^1D)$ kinetic energy distributions as a function of the O_2/CO_2 mixing ratio ρ, some of which might lead to a ρ dependence in the isotopic composition of CO_2 relative to O_2 observed in the experiments.

3.2. Materials and Methods

3.2.1. Experimental Methods

Mixtures of O_2 and CO_2 were irradiated with ultraviolet light from a mercury lamp using the same photochemistry apparatus (Figure 3-1) used in Chapter 2 and then measured for the triple isotope compositions of O_2 and CO_2 using dual inlet isotope ratio mass spectrometry (IRMS). Several differences exist between the experiments in this chapter and the experiments reported here. The main difference between the experiments reported here and in Chapter 2 is that instead of separating the CO_2 directly from the irradiated mixture, for most runs, two aliquots of the irradiated mixture were taken at the end of each experiment. In these experiments, two aliquots of the irradiated mixture were taken instead because there was far more CO_2 in these experiments than in the experiments of Chapter 2. After the gases in the larger of the two aliquots were separated cryogenically, the isotopic composition of O_2 was measured directly on the IRMS, and the isotopic composition of CO_2 was measured using the cerium oxide equilibration technique.[28] The second, smaller aliquot of the reaction mixture was used to measure ρ (i.e. the ratio of O_2 to CO_2) directly and accurately because the gases did not completely mix when introduced into the vacuum line and photolysis bulb.

In each experiment, O_2 (Scott Specialty Gases, 99.999% purity) and CO_2 (Scott Specialty Gases, 99.999% purity) were introduced into the line without further purification to reach a total pressure of either 50 Torr or 170 Torr in the 2.2L borosilicate glass bulb as measured by a Baratron capacitance manometer (MKS Instrument 627B, 1000 Torr full-scale, 0.1% accuracy). The amounts of O_2 and CO_2 at the different total pressures were varied to reach the different O_2/CO_2 mixing ratios, ρ. After the gases were introduced into the photolysis line, the glass bulb was isolated from the vacuum, and irradiation by the mercury/argon pen lamp (Oriel Instruments) was started. In blank experiments without irradiation, measurements of the separated O_2 and CO_2 on the IRMS showed that the gas mixtures contained no impurities and that the fractionation in O_2 and CO_2 from the gas handling and separation process was less than 0.5‰ for $\ln^{18}O$. The gas mixtures were irradiated for at least 90 hours so that the isotopic compositions of O_2 and CO_2 reached steady state. Experiments conducted at longer irradiation times confirmed that steady state was reached in 90 hours because the isotopic composition changed by less than 0.5‰. After the 90 hours of irradiation, two aliquots on port A (~3mL) and port B (~30mL) (Figure 3-1) were filled with aliquots of the gas mixture from the photolysis bulb. The O_2 and CO_2 in the sample tube on port A were used to determine the experimental value of ρ, while the O_2 and CO_2 in the sample tube on port B were separated cryogenically to measure their isotopic compositions, as follows. For the measurement of ρ, the sample tube on port A was heated to 80°C for 30 minutes to convert the small amount of O_3 (~$1/1000^{th}$ of the mixture) back to O_2 on the surface of the nickel shavings. The sample tube was then returned to room temperature, and the total pressure in the sample tube and the part of the vacuum line leading to a Baratron capacitance manometer (MKS Instruments 627B, 10 Torr full-scale, 0.1% accuracy,) was measured once the pressure gauge gave a stable reading for 5 minutes. Liquid nitrogen was then placed on the sample tube to condense CO_2 back to the sample tube. Once the CO_2 was frozen, the line was opened to the vacuum pump to remove O_2. The sample tube and the part of the vacuum line leading to the Baratron was then isolated, and the sample tube was allowed to return to room temperature. Once the pressure reading was stable for 5 minutes, the pressure of CO_2 was measured in the same volume used for the total pressure measurement. The

measured pressure of CO_2 and the measured total pressure were then used to calculate ρ. In blank experiments with no irradiation, determinations of ρ using the same initial pressures of O_2 and CO_2 in the bulb gave a reproducibility of ±2% (1σ, N=3) for the calculated value for ρ.

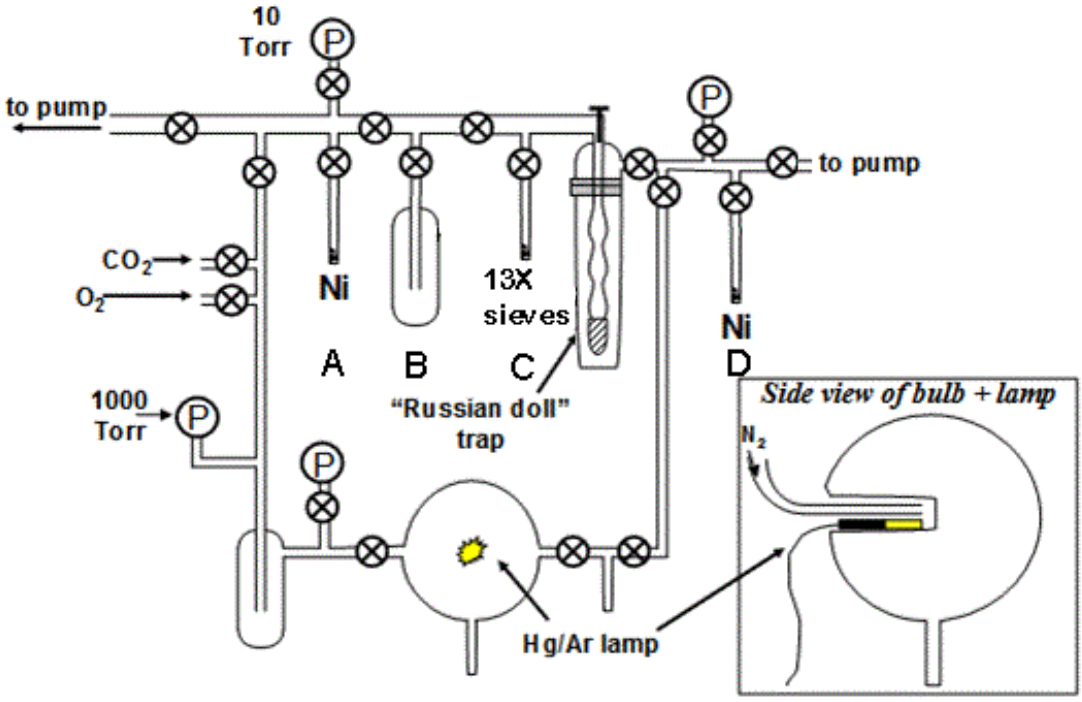

Figure 3-1. Schematic of the borosilicate glass manifold used for the photochemistry experiments. The letters A, B, C, and D indicate different ports to the glass manifold.

After the determination of ρ for an experimental run, the O_2 and CO_2 in the second aliquot from the photolysis bulb in the sample tube on port B (Figure 3-1) were separated cryogenically using liquid nitrogen so that their isotopic compositions could be determined. The part of the vacuum line that includes the Russian doll trap, the sample tube on port D, and the area above ports A, B, C, and D was isolated from vacuum and the rest of the photolysis line. The sample tube on port B was opened to allow the gas mixture into that part of the photolysis line, and liquid nitrogen was placed on the Russian doll trap[29] to condense CO_2 and O_3 from the

mixture but not O_2. During the separation, the pressure in the isolated part of the photolysis line was monitored by the Baratron gauge above port A and a convection gauge calibrated for air above port D. After approximately 45 to 60 minutes, the sample tube on port C containing evacuated 13X molecular sieve (Sigma-Aldrich) was immersed in liquid nitrogen and then opened to allow O_2 to condense onto the sieve. Once O_2 had completely condensed, the sample tube containing the sieve was isolated from the photolysis line and used for measurement of the isotopic composition of O_2. After the O_2 was separated, the CO_2 and O_3 in the Russian doll trap were cryogenically transferred to the sample tube on port D containing nickel shavings. This sample tube was heated to 80°C for 30 minutes to convert the remaining O_3 to O_2. After heating, the sample tube was immersed in liquid nitrogen again to condense the CO_2, and the line was opened to vacuum to pump away the O_2 from O_3 decomposition. The frozen CO_2 was then isolated in the sample tube and its isotopic composition determined. The isotopic composition of O_3 was not measured in these experiments because the amount of O_3 in the aliquots was too small for IRMS analysis.

The isotopic compositions of O_2 and CO_2 in these experiments was then measured by IRMS. The CeO_2 technique originally developed by Assonov and Brenninkmeijer[28] was used to determine the values of $\ln^{17}O$ and $\Delta^{17}O$ of CO_2 as described in detail Chapter 2. The parameters used in this chapter to calculate the isotopic composition of CO_2 were ${}^{13}R_{PDBCO2} = 0.0112372$, ${}^{17}R_{PDBCO2} = 0.00039511$, ${}^{18}R_{PDBCO2} = 0.00208835$, and $\lambda_{std} = 0.528$.[30] Measurements of four anomalous and two mass-dependently fractionated laboratory standards (N=130) using this method yielded an external 1σ measurement precision for CO_2 of ±0.2‰, ±0.05‰, and ±0.2‰ for $\ln^{17}O$, $\ln^{18}O$, and $\Delta^{17}O$, respectively. The accuracy of the determination of the isotopic composition of CO_2 can also be affected by the small ^{17}O anomaly (≈0.1-0.2‰) generated from the CeO_2 equilibration itself.[6] In addition, a small amount of mass-dependent fractionation was introduced through the cryogenic separation and sample handling processes; for example, processing the gases through the experimental procedure without irradiation changed the measured isotopic compositions of both O_2 and CO_2 by less than 0.3‰ and 0.5‰ for $\ln^{17}O$ and $\ln^{18}O$, respectively. The combined 1σ uncertainty from these considerations of accuracy and precision was approximately ±0.5‰, ±0.5‰, and ±0.5‰ for $\ln^{17}O$, $\ln^{18}O$, and $\Delta^{17}O$ for CO_2, respectively. Similarly, for O_2, due mostly to the small mass-dependent fractionation induced by the cryogenic separation, the estimated 1σ uncertainty for these measurements was approximately ±0.3, ±0.5, and ±0.5 for $\ln^{17}O$, $\ln^{18}O$, and $\Delta^{17}O$ for O_2, respectively.

Finally, as ρ is varied between experiments, the isotopic compositions of O_2 and CO_2 relative to VSMOW will change simply due to reservoir effects. That is, even if all the reactions and the associated isotope effects remain the same as ρ decreased, the isotopic compositions will change differently over the course of the irradiation at different experimental ρ as the heavy isotopes initially contained in the O_2 are redistributed and sequestered in the CO_2 weighted by the concentrations of O_2 and CO_2. To account for such a reservoir effect at different experimental ρ, the measured isotopic composition of CO_2 relative to the measured isotopic composition of O_2 at steady-state from the same experiment was calculated using Eq. (4) and Eq. (5), which is similar to the relative isotopic composition for δ-values used in Shaheen et al.[18]

$$\ln {}^{18}O_{O_2}(CO_2) = \ln {}^{18}O_{VSMOW}(CO_2) - \ln {}^{18}O_{VSMOW}(O_2) \tag{4}$$

$$\Delta^{17}O_{O_2}(CO_2) = \Delta^{17}O(CO_2) - \Delta^{17}O(O_2) \tag{5}$$

These relative isotopic compositions will change with ρ only if the isotope effects in reactions such as O_3 formation or $O(^1D)+CO_2$ also change with ρ. For example, if the KIEs in ozone formation were to decrease significantly in low ρ experiments, the relative isotopic composition of CO_2 would decrease accordingly in a way that would not be obvious from the isotopic composition of O_2 and CO_2 relative to VSMOW. As such, for every experiment, the isotopic compositions of O_2 and CO_2 relative to VSMOW and the isotopic composition of CO_2 relative to O_2 will both be given.

To more easily compare different experiments, an empirical fit to the isotopic composition of CO_2 relative to O_2 to the Hill function in Eq. (6) will also be reported.

$$E(\rho) = base + \frac{max - base}{1 + (\rho/\rho_0)^{rate}} \quad (6)$$

In this equation, the isotopic composition of CO_2 relative to O_2, E, as a function of ρ was fit using the following parameters: *max* is the high ρ plateau for the relative isotopic composition of CO_2, *base* is the low ρ plateau for the relative isotopic composition of CO_2, ρ_0 is the midway point for the transition from *base* to *max*, and *rate* is the rate that the transition from *base* to *max* occurs. The linear least squares fitting method to the Hill function applied the Levenberg-Marquardt algorithm to find a set of coefficients that minimized the chi-squared deviation of the fit from the data.

3.2.2. Photochemical kinetics model description

The kinetics model of the laboratory experiments developed in KINTECUS[27] described in Chapter 2 was used in this chapter to investigate potential mechanisms that could generate the observed ρ dependence of the isotopic compositions of O_2 and CO_2 using various model scenarios. A list of reactions used in the base model and their rate coefficients for species that contain only ^{16}O is shown in Table 3-1. In addition to the reactions in Table 3-1, the model included each possible variant for the reactions that involved substitution of ^{17}O or ^{18}O for one or two of the ^{16}O atoms in the chemical species shown in Table 3-1.

Table 3-1. Reactions included in the kinetics model and the corresponding rate coefficients for the ^{16}O-containing isotopologues.

Reaction		Rate Coefficient	Source
(R1)	$O + O_2 + M \rightarrow O_3 + M$	$6.0\times10^{-34}(T/300)^{-2.4}$ cm^6 s^{-1}	Sander et al.[31]
(R2a)	$O_3 + h\nu \rightarrow O_2 + O$	$0.1\times(2.2\times10^{-2}$ s$^{-1})$	Flux estimated from CO_2 actinometry and 254/185 flux ratio [32]; cross section and branching ratio from Sander et al.[31]
(R2b)	$O_3 + h\nu \rightarrow O_2(^1\Delta) + O(^1D)$	$0.9\times(2.2\times10^{-2}$ s$^{-1})$	
(R3)	$O(^1D) + CO_2 \rightarrow O + CO_2$	1.1×10^{-10} cm^3 s^{-1} (thermal)	Sander et al.[31]; calculated in non-thermal model
(R4)	$O(^1D) + CO_2 \rightarrow O(^1D) + CO_2$	Calculated from non-thermal velocity distribution of $O(^1D)$l	
(R5a)	$O(^1D) + O_3 \rightarrow 2O_2$	1.2×10^{-10} cm^3 s^{-1}	Sander et al.[31]
(R5b)	$O(^1D) + O_3 \rightarrow O_2 + 2O$	1.2×10^{-10} cm^3 s^{-1}	Sander et al.[31]
(R6a)	$O(^1D) + O_2 \rightarrow O + O_2$	$0.2\times(3.2\times10^{-11}\exp(70/T)$ cm^3 s$^{-1})$	Sander et al.[31]
(R6b)	$O(^1D) + O_2 \rightarrow O + O_2(^1\Sigma)$	$0.8\times(3.2\times10^{-11}\exp(70/T)$ cm^3 s$^{-1})$	
(R7)	$O_2 + h\nu \rightarrow O + O$	1.9×10^{-7} s^{-1}	Cross section from Yoshino et al.;[33] flux from CO_2 actinometry
(R8)	$O_3 + O_2(^1\Delta) \rightarrow 2O_2 + O$	$5.2\times10^{-11}\exp(-2840/T)$ cm^3 s^{-1}	Sander et al.[31]
(R9)	$O_2(^1\Delta) + O_2 \rightarrow O_2 + O_2$	1.6×10^{-18} cm^3 s^{-1}	Sander et al.[31]
(R10)	$O_2(^1\Delta) + CO_2 \rightarrow O_2 + CO_2$	2×10^{-20} cm^3 s^{-1}	Sander et al.[31] (upper limit)
(R11)	$O_2(^1\Sigma) + O_2 \rightarrow O_2(^1\Delta) + O_2$	4.0×10^{-17} cm^3 s^{-1}	Sander et al.[31]
(R12)	$O_2(^1\Sigma) + O_3 \rightarrow O_2(^1\Delta) + O_3$	$0.3\times(2.2\times10^{-11}$ cm^3 s$^{-1})$	Sander et al.[31]; assumed no $O_2(^3\Sigma)$ product
(R13)	$O_2(^1\Sigma) + O_3 \rightarrow O + 2O_2$	$0.7\times(2.2\times10^{-11}$ cm^3 s$^{-1})$	Sander et al.[31]
(R14)	$O_2(^1\Sigma) + O \rightarrow O_2(^1\Delta) + O$	8.0×10^{-14} cm^3 s^{-1}	Sander et al.[31]; assumed no $O_2(^3\Sigma)$ product
(R15)	$O_2(^1\Sigma) + CO_2 \rightarrow O_2(^1\Delta) + CO_2$	4.1×10^{-13} cm^3 s^{-1}	Sander et al.[31]
(R16)	$O(^1D) + CO_2 \rightarrow O + CO_2$	1.1×10^{-12} cm^3 s^{-1}	Sander et al.[31]
(R17)	O' + OO → OO' + O	3.4×10^{-12} (T/300)$^{-1.1}$ cm^3 s^{-1} [O'=^{18}O or ^{17}O]	Fleurat-Lessard et al.[34]
(R18)	O' + OO ↔ OO' + O	$K_{eq}[O'=^{18}O] = 1.94\exp(32/T)$ $K_{eq}[O'=^{17}O] = 1.96\exp(16.8/T)$	Kaye and Strobel[35]

Table 3-2. Rate coefficients for ozone formation containing a single heavy oxygen atom relative to $^{16}O^{16}O^{16}O$.

Reaction	Mauersberger et al.[16]	Janssen et al.[17]	Used in these calculations
$^{16}O + {}^{16}O^{16}O \rightarrow {}^{16}O^{16}O^{16}O$	1.00	1.00	1.00
$^{18}O + {}^{16}O^{16}O \rightarrow {}^{16}O^{16}O^{18}O$	0.93 ± 0.03	0.92 ± 0.04	0.92
$^{16}O + {}^{16}O^{18}O \rightarrow {}^{16}O^{16}O^{18}O$	} 1.27 ± 0.03	1.45 ± 0.04	1.45
$^{16}O + {}^{16}O^{18}O \rightarrow {}^{16}O^{18}O^{16}O$		1.08 ± 0.01	1.08
$^{17}O + {}^{16}O^{16}O \rightarrow {}^{16}O^{16}O^{17}O$	1.03 ± 0.05	--	1.03
$^{16}O + {}^{16}O^{17}O \rightarrow {}^{16}O^{16}O^{17}O$	} 1.17 ± 0.05	--	1.35
$^{16}O + {}^{16}O^{17}O \rightarrow {}^{16}O^{17}O^{16}O$		--	0.99

Table 3-3. Description of the various model scenarios used in the kinetics model.

Scenario	Scenario description
Base	
1	$O_2(^1\Sigma) + O_3$ mass-dependent KIE from Cole and Boering[36]
2	10kcal/mol branching ratios for $O(^1D) + CO_2$ calculated by Mebel et al.[23]
3	Isotopic specific non-thermal rate coefficients for all $O(^1D)$ reactions calculated from hard-sphere model
3A	Same as 3 but with O_3 KIEs set to 1
3B	Halved elastic cross sections for $O(^1D) + CO_2$
3C	Same as 3B but also with doubled inelastic cross sections for $O(^1D) + CO_2$
3D	Same as 3, but with initial kinetic energy distribution for $O(^1D)$ from O_3 photolysis at 245 nm
3E	Non-thermal rate coefficients for all $O(^1D)$ calculated from O_3 photolysis energy distribution at 255 nm (i.e. with no elastic or inelastic collisions)

The "base" scenario included kinetic isotope effects only in ozone formation (0) their pressure and bath-gas dependence, and the equilibrium constants for oxygen-atom exchange (R18), as in Chapter 2. The pressure dependence for the ozone KIEs was derived in Chapter 2 from measurements of the ozone enrichments[22,37–39] by assuming that the pressure dependence of the ozone formation KIEs was mostly caused by the asymmetric formation channels $^{16}O + {}^{16}O^{17}O$ and $^{16}O + {}^{16}O^{18}O$.[40,41] To account for the effect of bath gas, an "effective pressure" parameter was used to estimate the ozone formation KIEs at a given ρ and total pressure p using Equation (7).

$$p_{\text{eff}} = p\left(\frac{2.1+\rho}{1+\rho}\right) \tag{7}$$

For example, at $\rho = 1$ and $p = 50$ Torr, Eq. (7) yields a p_{eff} of 77.5 Torr that is used to calculate the ozone formation KIEs for this set of initial conditions. This parameter was used in addition to multiplying the rate coefficient for formation of $^{16}O^{16}O^{16}O$ by a factor 2.1 to account for the the increased efficiency of CO_2 collisions in forming ozone with M = CO_2 in (R63).[42] Overall, this "base" scenario used in the photochemical kinetics model quantitatively predicts the isotopic composition of CO_2 in the high ρ experiments (i.e. $\rho \approx 450$), as detailed in Chapter 2.

In addition to the base model, a number of model scenarios were also considered. The subset of the model scenarios that will be discussed explicitly in this chapter are shown in Table 3-3. In Scenario 1, a mass-dependent isotope effect in the reaction $O_2(^1\Sigma) + O_3$ (R13) was included, motivated in part because previous kinetics modeling of ozone photolysis experiments suggested that mass-dependent isotope effects in this reaction may be potentially important in determining the isotopic composition of O_3.[36] While mass-dependent isotope effects in this reaction or in any of other reaction occurring in the experiments cannot by definition change the relative isotope anomaly $\Delta^{17}O_{O2}(CO_2)$, they may still affect the ρ dependence of $\ln{}^{17}O_{O2}(CO_2)$ and $\ln{}^{18}O_{O2}(CO_2)$. The KIEs used for the $O_2(^1\Sigma) + O_3$ reaction in Scenario 1 were 0.9714 and 0.945 for ^{17}O-substituted and ^{18}O-substituted reactions, respectively, since these KIEs appeared to be consistent with the modeled[36] time evolution of the isotopic composition of O_3 in UV photolysis experiments.[43]

In Scenarios 2, 3, and 3A through 3E, the isotope-specific branching ratios for the $O(^1D) + CO_2$ quenching (R3) and non-quenching (R4) isotope exchange reactions calculated by Mebel et al.[23] were used to test the effect of the non-quenching isotope exchange reaction (R4).[14,15] For ^{18}O and ^{16}O, the RRKM calculations by Mebel et al.[23] using a barrier height of 49.2 kcal/mol for the CO_3* transition state *s*-TS0 were used since the calculations using that barrier height best predicted the branching ratio results of the crossed-beam experiments.[14,15] Because Mebel et al.[23] did not calculate isotope-specific branching ratios for ^{17}O-substituted reactions, the branching ratio $^{17}\xi$ was calculated using the following equation:

$$^{17}\xi = \frac{1}{2}\,{}^{16}\xi - \lambda_{\text{MD}}\left(\frac{1}{2}\,{}^{16}\xi - {}^{18}\xi\right) \tag{8}$$

where $^{16}\xi$ is the branching ratio for the reactions with all ^{16}O, $^{18}\xi$ is the branching ratio for the ^{18}O-substituted reactions, and λ_{MD} is the mass-dependent slope, which is taken to be 0.52 here. The isotope-specific branching ratios $^{16}\xi$, $^{17}\xi$, and $^{18}\xi$ were slightly different from each other and thus produced mass-dependent fractionation. For example, at 10 kcal/mol, the branching ratios of quenching (R3) to non-quenching isotope exchange (R4) for $^{16}\xi$, $^{17}\xi$, and $^{18}\xi$ were 57.07%:42.93%, 56.60%:43.40%, and 56.16%:43.84%, respectively; these differences in the

branching ratios resulted in mass-dependent KIEs in the non-quenching isotope exchange reaction (R4) that were 0.992 and 0.984 for ^{17}O and ^{18}O, respectively. For the purposes of the non-thermal rate coefficient calculations in Scenarios 3 and 3A through 3E, the trend in the branching ratios of quenching and non-quenching isotope exchange was extrapolated from 10kcal/mol to the 16kcal/mol collision energy needed for these calculations. These branching ratios $^{16}\xi$, $^{17}\xi$, and $^{18}\xi$ for quenching and non-quenching isotope exchange as a function of collision energy are shown in Figure 3-2. In addition to the branching ratios of quenching (R3) and non-quenching (R4) $O(^1D) + CO_2$, the branching ratios for the products of isotope exchange were also considered. For example, at 10 kcal/mol, once these branching ratios for the different products of isotope are taken into account, the ratio of $^{18}O(^1D)/^{16}O(^1D)$ products from $^{18}O(^1D) + C^{16}O^{16}O$ and the ratio of $^{17}O(^1D)/^{16}O(^1D)$ products from $^{17}O(^1D) + C^{16}O^{16}O$ were 2.034 and 2.018. The branching ratios of quenching and non-quenching isotope exchange as well as the possible products of the isotope exchange were used in Scenario 2, and in the calculation of non-thermal rate coefficients in Scenarios 3 through 3E.

In Scenario 2, these calculated isotope-specific branching ratios for the non-quenching and quenching $O(^1D) + CO_2$ isotope exchange reactions at a collision energy of 10kcal/mol were multiplied by the thermal rate coefficient for $O(^1D) + CO_2$ quenching at room temperature (i.e., 1.1×10^{-10} cm^3 s^{-1}); in other words, the increase in collision frequencies at a collision energy of 10kcal/mol was not considered in this particular scenario. Although this hypothetical scenario is thus physically inconsistent – that is, using non-thermal branching ratios multiplied by a thermal rate coefficient at room temperature in the model, Scenario 2 provides a way to investigate whether the ρ dependence of the isotopic composition of CO_2 relative to O_2 could arise from a dramatic increase in importance of the non-quenching $O(^1D) + CO_2$ isotope exchange (R4) and its associated kinetic isotope effects calculated by Mebel et al.[23] in these experiments, regardless of the actual $O(^1D)$ kinetic energy distributions. In addition to Scenario 2, a scenario with a full kinetics scheme that included all the intermediates in Mebel et al.,[23] such as CO_3* (s3) was also developed and tested, but it did not produce meaningfully different results from the simplified model described here for Scenario 2 so it will not be discussed or shown

For the Scenarios 3 and 3A through 3E described below, the isotope-specific branching ratios for the quenching (R3) and non-quenching (R4) $O(^1D) + CO_2$ isotope exchange reactions shown in Figure 3-2 were also used in the derivation of non-thermal rate coefficients for these reactions. In Scenario 3, the non-thermal rate coefficients were obtained by integrating over the energy dependence of the products of the energy-dependent reactive cross sections and branching ratios for the reactions of $^{16}O(^1D)$, $^{17}O(^1D)$, and $^{18}O(^1D)$ with O_2, O_3, and CO_2 and the isotope-specific non-thermal $O(^1D)$ translational energy distributions calculated using a hard-sphere collision model, which is described in detail below in section 3.2.3. In Scenario 3A, the same non-thermal rate coefficients from Scenario 3 are used, but the KIEs for O_3 formation are set to 1. A comparison of model results from Scenario 3 and Scenario 3A allows us to test whether non-mass-dependent isotope fractionation in this system occurs separately from the KIEs in O_3 formation. In Scenarios 3B through 3E, the effects of varying the calculated isotope-specific non-thermal $O(^1D)$ translational energy distributions by various processes and considerations are also investigated; these are described in detail below in section 3.2.3.

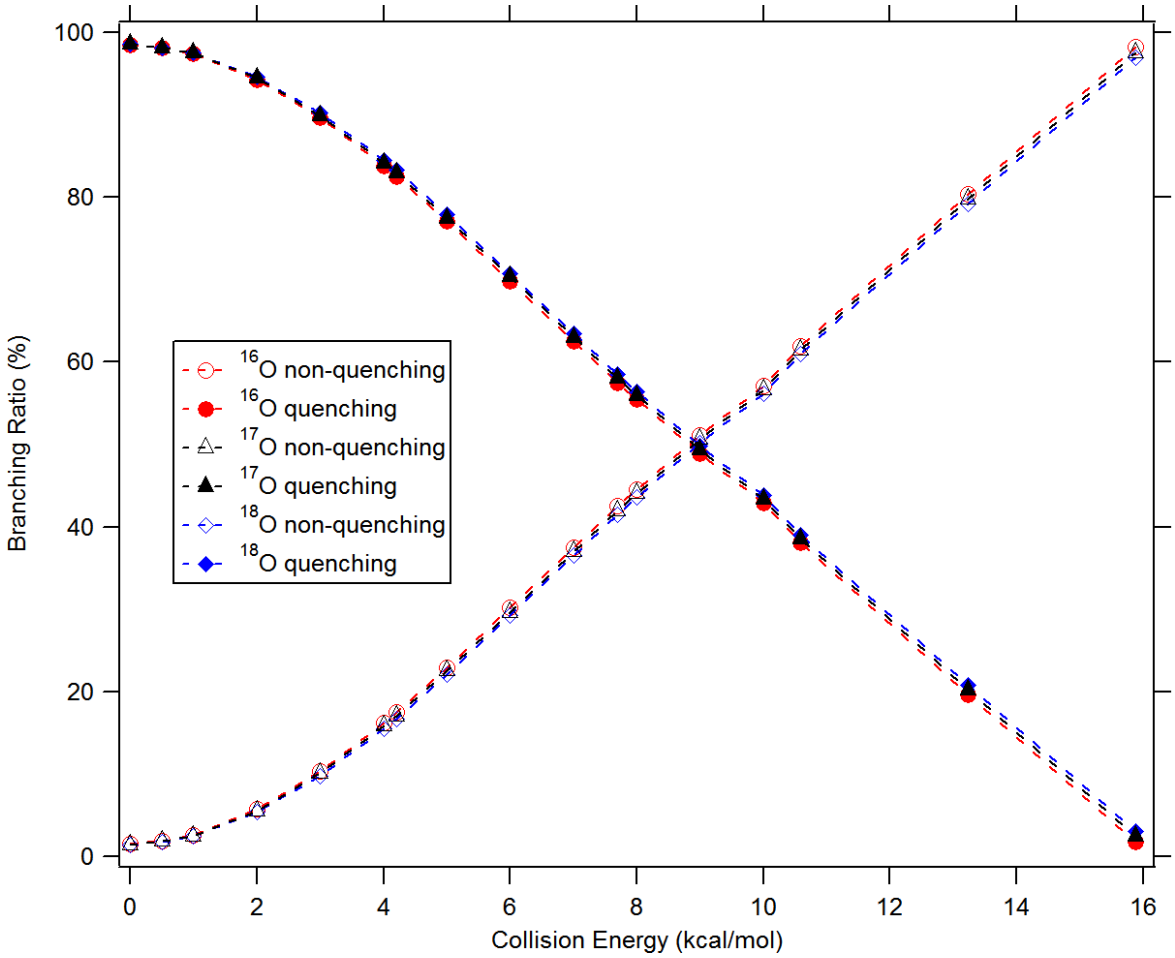

Figure 3-2. Branching ratios for the quenching (R3) versus non-quenching (R4) $O(^1D) + CO_2$ isotope exchange reactions as a function of the collision energy between $O(^1D)$ and CO_2, where the isotope label indicates the incoming $O(^1D)$ atom. The branching ratios for ^{16}O and ^{18}O are taken from the calculations of Mebel et al.,[23] while the branching ratios for ^{17}O were calculated from the Mebel et al.[23] results for ^{18}O using the mass-dependent relationship in Eqn. (8). Values for the branching ratios above 10kcal/mol were extrapolated from the Mebel calculations to higher collision energies based on the trend at lower collision energies.

3.2.3. Calculation of non-thermal rate coefficients

Steady-state non-thermal translational energy distributions for $^{16}O(^1D)$, $^{17}O(^1D)$, and $^{18}O(^1D)$ were calculated for several different mixing ratios ρ to investigate whether any notable differences between the isotope-specific kinetic energy distributions of $O(^1D)$ (and thus the rate coefficients for its reactions) in O_2-dominated mixtures versus in CO_2-dominated mixtures exist, as postulated by Shaheen et al.[18] The initial translational energy distribution of $O(^1D)$ from UV photolysis of O_3, the loss rates of $O(^1D)$ from chemical reactions at different translational energies, and the energy transfer induced by both elastic and inelastic collisions of $O(^1D)$ with O_2 and CO_2 are all needed to calculate the non-thermal $O(^1D)$ translational energy distributions at steady state. Other initial conditions needed for the calculations, such as the rate of production of $O(^1D)$ from O_3 photolysis and the concentration of O_3, were obtained from the base scenario results from the kinetics model for ρ = 1000, 10, 1, 0.1, and 0.01. Once calculated, the translational energy distributions of $^{16}O(^1D)$, $^{17}O(^1D)$, and $^{18}O(^1D)$ can then be used to calculate the isotope-specific non-thermal rate coefficients for the reactions of $O(^1D)$ with O_2, O_3, and CO_2 predicted for the experimental conditions. These calculated non-thermal rate coefficients were used as input into the kinetics model, described in Section 3.2.2 above, in model Scenarios 3 and Scenarios 3A through 3E.

The translational energy distributions of $^{16}O(^1D)$, $^{17}O(^1D)$, and $^{18}O(^1D)$ and their corresponding isotope-specific non-thermal rate coefficients for the reactions of $O(^1D)$ with other species were calculated as follows. Non-thermal translational energy distributions were defined for $^{16}O(^1D)$, $^{17}O(^1D)$, and $^{18}O(^1D)$ on an energy interval $(0,E_{max}]$ where E_{max} is chosen to be greater than the upper energy limit of $O(^1D)$ produced from ozone photolysis. Within this interval, the probability distribution was represented as a discretized $f(x)$ where each point represents the probability of finding $O(^1D)$ at the dimensionless reduced energy $x = E/kT$ at T = 300K. For these calculations, the step-size Δx and E_{max} were chosen to be $0.1kT$ and $30kT$, respectively, so that the length of $f(x)$ was N = 300.

The non-thermal kinetic energy distribution for $^{16}O(^1D)$, $^{17}O(^1D)$, and $^{18}O(^1D)$ were then calculated using the steady-state solution to the linear Boltzmann equation for a homogeneous Maxwell gas at temperature T using Eqn. (9).

$$f(x) = \frac{\int_0^\infty B(x|x')f(x')dx' + Q(x)}{\int_0^\infty B(x'|x)dx' + \gamma(x)} \tag{9}$$

In this equation, $B(x|x')$ is the collision kernel that describes the rate of energy transfer from laboratory frame energy $x' \rightarrow x$ caused by elastic and inelastic collisions of $O(^1D)$ with O_2 and CO_2, $Q(x)$ is the production rate of $O(^1D)$ at each energy x, and $\gamma(x)$ is the rate of reactions that remove $O(^1D)$ at each energy x. This calculation was done in a similar fashion to other previous work in which, for example, the non-thermal kinetic energy distributions of $O(^1D)$ in the stratosphere and mesosphere, and $O(^3P)$ and $N(^4S)$ in the thermosphere, were calculated.[26,44–46] Each of the terms in Eq. (9) can be calculated from the physical and chemical parameters of $O(^1D)$, O_2, and CO_2 as described below.

For elastic collisions, the hard sphere approximation was used to calculate the collision kernel $B(x'|x)$ analytically as in previous studies — e.g. for the non-thermal translational energy distribution of $O(^1D)$ in the stratosphere and mesosphere.[46] For O_2, an effective hard-sphere cross section that had been previously shown to best approximate elastic and inelastic collisions

between $O(^1D)$ and O_2 was used.[26] For CO_2, an elastic cross section was estimated from the total $O(^1D) + CO_2$ collision cross section and an estimated reactive cross section similar to a previous study of the total cross section for $O(^3P) + CO_2$ collisions.[47] The total cross section for collisions σ_{total} can be estimated from the Lennard-Jones parameters for O and CO_2 using the expression in Eq. (10).

$$\sigma_{\text{total}} = \pi b_{\text{max}}^2 \tag{10}$$

where b_{max} is the collision radius beyond which no collision will occur. This parameter can be estimated using the Lennard-Jones potential[48] in Eq. (11):

$$V(r) = 4\varepsilon\left[\left(\frac{\sigma(\text{O}+\text{CO}_2)}{r}\right)^{12} - \left(\frac{\sigma(\text{O}+\text{CO}_2)}{r}\right)^{6}\right] \tag{11}$$

where ε and $\sigma(O+CO_2)$ correspond to the well depth and collision diameter for $O(^1D) + CO_2$ collisions. The value for $\sigma(O+CO_2)$ can be estimated from the individual $\sigma(O)$ and $\sigma(CO_2)$ using Eqn. (12).[49]

$$\sigma(\text{O}+\text{CO}_2) = \frac{1}{2}[\sigma(\text{O}) + \sigma(\text{CO}_2)] \tag{12}$$

Using the values $\sigma(\text{O}) = 2.78 \times 10^{-10}\text{m}$ and $\sigma(\text{CO}_2) = 3.90 \times 10^{-10}\text{m}$ estimated previously[49,50] gives $\sigma(\text{O}+\text{CO}_2) = 3.34 \times 10^{-10}\text{m}$. Setting $b_{\text{max}} = \sigma(\text{O}+\text{CO}_2)$ yields a total cross section $\sigma_{\text{total}} = 3.50 \times 10^{-15}\text{cm}^2$. The total cross section σ_{total} was then used with the reactive cross section σ_{rxn} to estimate the elastic cross section $\sigma_{elastic}$. The reactive cross section for $O(^1D) + CO_2$ (for both (R3) and (R4)) was estimated from the thermal rate coefficient k and the reduced mass of the collision μ using Eq. (13):

$$\sigma_{\text{rxn}} = k\sqrt{\frac{\pi\mu}{8kT}} \tag{13}$$

For $O(^1D) + CO_2$, σ_{rxn} was estimated as $1.50 \times 10^{-15}\text{cm}^2$. Using the total and reactive cross sections for $O(^1D) + CO_2$ collisions, the elastic cross section was then estimated to be $2.00 \times 10^{-15}\text{cm}^2$. This estimated elastic cross section was used as the hard sphere cross section for collisions with CO_2 in the collision kernel $B(x'|x)$ used in Eq. (9).

The inelastic part of the collision kernel $B(x'|x)$ for CO_2 in Eq. (9) was also calculated using the reactive cross section for $O(^1D) + CO_2$ ((R3) and (R4)) calculated in Eq. (13) and the branching ratios taken from Mebel et al.[23] or derived from Mebel et al.[23] using Eq. (8). In this case, the reactive cross section σ_{rxn} for $O(^1D) + CO_2$ was assumed to be a hard sphere collision cross section with an additional branching ratio term that depended on the center-of-mass energy, x_r, of the collision. This inelastic cross section was calculated using Equation (14):

$$\Xi_{\text{in}}(x_r) = \frac{\sigma_{\text{rxn}}}{4\pi}\xi(x_r) \tag{14}$$

where $\xi(x_r)$ is the branching ratio between the quenching (R3) and non-quenching (R4) $O(^1D) + CO_2$ reaction. This term was then substituted into the general expression for the collision kernel $B(x'|x)$ in Eq. (21) of Kharchenko et al.[46] Because the inelastic part of the collision kernel could no longer be evaluated analytically after this substitution, the kernel $B(x'|x)$ was calculated at each laboratory frame energy pair x and x' using Monte Carlo integration. The approximation of inelastic scattering using the hard sphere cross section (i.e. as isotropic elastic scattering) likely

underestimates the energy transfer since it has been shown that nearly 50% of the energy of the collision is deposited into the internal energy of CO_2 before dissociation of the CO_3* complex.[15,51] On the other hand, approximating the *elastic* scattering using a hard sphere cross section is expected to overestimate large energy losses in elastic collisions.[52] As such, the combined errors induced by using the hard sphere approximation for both elastic and inelastic scattering to calculate the translational distributions of $^{16}O(^1D)$, $^{17}O(^1D)$, and $^{18}O(^1D)$ could in principle roughly cancel each other out. The sensitivity of the model results to varying the magnitudes of the elastic and inelastic hard-sphere cross sections was tested in Scenarios 3B and 3C as described further below.

In addition to the energy transfer due to elastic and inelastic collisions of $O(^1D)$ with O_2 and CO_2, estimates of the chemical loss rates for $O(^1D)$ are also needed for Eqn. (9). To estimate the chemical loss rates, the reactive cross sections from Eq. (13) above were also used to calculate the chemical loss rates $\gamma(x)$ of $O(^1D)$ in Eq. (9) through the quenching $O(^1D) + CO_2$ isotope exchange (R3) and other reactions at each energy x, specifically the quenching $O(^1D) + CO_2$ isotope exchange reactions (R3), and the reactions of $O(^1D)$ with O_3 (R5) and O_2 (R6).

(R5a) $O(^1D) + O_3 \rightarrow 2O_2$

(R5b) $O(^1D) + O_3 \rightarrow O_2 + 2O(^3P)$

(R6a) $O(^1D) + O_2 \rightarrow O(^3P) + O_2$

(R6b) $O(^1D) + O_2 \rightarrow O(^3P) + O_2(^1\Sigma)$

For (R5a) and (R5b), the collision cross section was calculated from the thermal rate coefficient using Eq. (13), and no collision energy dependence was considered explicitly. For 0, the reactive cross section and collisional energy dependence derived in Taniguchi et al.[53] from measurements of the translational and electronic quenching of $O(^1D)$ by O_2 was used. For electronic quenching of $O(^1D)$ by CO_2 (R3), the cross section calculated above was used along with the collisional energy-dependent and isotope-specific branching ratios between the quenching (R3) and non-quenching (R4) $O(^1D) + CO_2$ isotope exchange reactions calculated form Mebel et al.[23] above. Using these reactive cross sections and their collisional energy dependence, $\gamma(x)$ was calculated for each chemical reaction of $^{16}O(^1D)$, $^{17}O(^1D)$, and $^{18}O(^1D)$ by transforming each lab frame reduced energy x into a center-of-mass energy x_r distribution for a Maxwell-Boltzmann gas at temperature T[26,54] and integrating over the center-of-mass energy as shown in Equations (15) and (16):

$$\gamma_{\mathrm{g}}(x) = n_{\mathrm{g}} \int_0^{\infty} dx_r \sqrt{\frac{2x_r kT}{\mu}}\, \sigma_{\mathrm{rxn}}(x_r)\rho_T(x, x_r) \tag{15}$$

$$\rho_T(x, x_r) = \sqrt{\frac{m_0 + m_{\mathrm{g}}}{\pi x \mu}} \sinh\left(\frac{2m_g}{m_0}\sqrt{\frac{x x_r m_0}{\mu}}\right) \exp\left(-\frac{x_r m_{\mathrm{g}}}{\mu} - \frac{x m_{\mathrm{g}}}{m_0}\right) \tag{16}$$

where n_{g} is the number density of the reactant, m_O is the mass of the isotope-specific oxygen, m_{g} is the mass of the reactant, and μ is the reduced mass of the collision partners. The sum of $\gamma_{\mathrm{g}}(x)$ for each reactant (i.e. g = O_2, CO_2, and O_3) was used as the total $\gamma(x)$ for the Boltzmann calculation in Eq. (9).

Finally, in addition to the kernels for collisional energy transfer $B(x'|x)$ and the chemical loss rate $\gamma(x)$ for $^{16}O(^1D)$, $^{17}O(^1D)$, and $^{18}O(^1D)$, the isotope-specific production rates of $O(^1D)$, $Q(x)$, at various translational energies from O_3 photolysis were also needed in Eq. (9). The center-of-mass kinetic energy distribution for the $O(^1D) + O_2(^1\Delta)$ photolysis products of ozone photolysis was obtained from the measurements of Dylewski et al.[24] at 255 nm. To convert to the laboratory frame energy x needed for $Q(x)$, the center-of-mass energy x_r was multiplied by the factor in Eqn. (16) using the appropriate masses of the O_3 and O_2 fragments for photolysis of $^{16}O^{16}O^{16}O$, $^{16}O^{16}O^{17}O$, and $^{16}O^{16}O^{18}O$.

$$x = \frac{m_{O_2}}{m_{O_3}} x_r \tag{17}$$

The resulting normalized $Q(x)$ for $^{16}O(^1D)$, $^{17}O(^1D)$, and $^{18}O(^1D)$ are shown in Figure 3-3. The normalized kinetic energy distributions were then multiplied by the rates of $O(^1D)$ production obtained from the kinetics model at each set of initial conditions to obtain isotope-specific $Q(x)$ for different mixing ratios ρ. For these calculations, the differences in zero point energy between $^{16}O^{16}O^{16}O$, $^{16}O^{16}O^{17}O$, and $^{16}O^{16}O^{18}O$ were not considered for the kinetic energy distributions resulting from ozone photolysis because these zero point energy differences are small compared to k_BT (<0.1k_BT at T = 300K). Similarly, differences in the overlap of the isotope-specific vibrational wave functions between the ground electronic state of O_3 and the dissociative state could potentially result in slight changes in the energies of the local maxima in the initial kinetic energy distributions for $^{16}O(^1D)$, $^{17}O(^1D)$, and $^{18}O(^1D)$. There may also be a small increase in kinetic energy between the $O(^1D)$ distribution from ozone photolysis measured at 255 nm[24] and the actual distribution of kinetic energy at the wavelength of O_3 photolysis (254nm) in the experiments reported here and in Shaheen et al.[18] Most of these differences between the actual initial $O(^1D)$ kinetic energy distribution and the likely experimental initial $O(^1D)$ kinetic energy distribution should be small, however, so the calculated isotope-specific initial distributions of $O(^1D)$ from O_3 photolysis should be well estimated by the distributions shown in Figure 3-3.

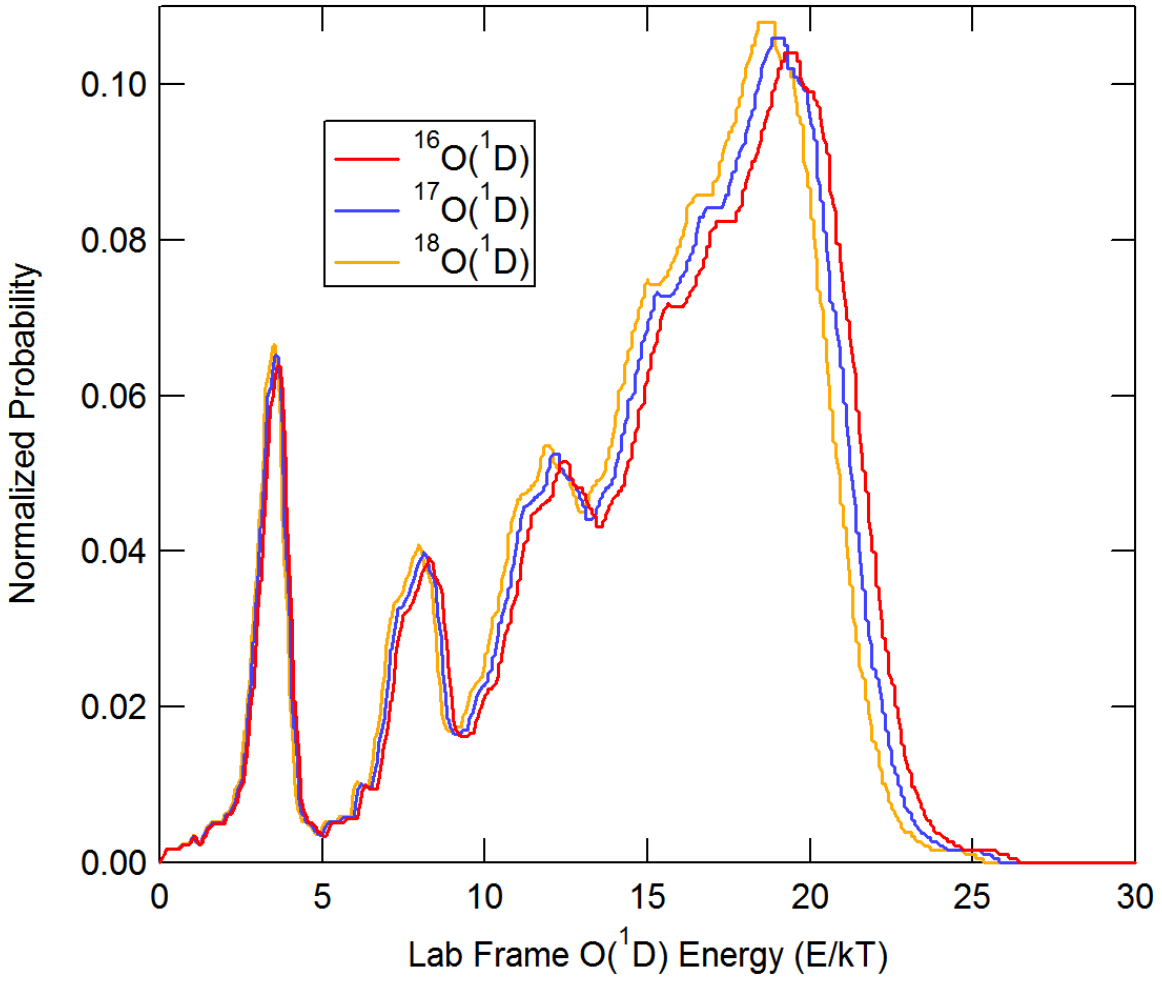

Figure 3-3. Laboratory frame translational energy distributions for $O(^1D)$ from ozone photolysis at 255 nm. The distributions for $^{16}O(^1D)$, $^{17}O(^1D)$, and $^{18}O(^1D)$ were calculated from the center-of-mass kinetic energy distribution from Dylweski et al. using Equation (17).[24] These non-thermal distributions were used as the initial $O(^1D)$ kinetic energy distributions in the model for Scenarios 3, 3A, 3B, 3C, and 3E.

In addition to the initial $O(^1D)$ kinetic energy distribution from O_3 photolysis, production rates for $O(^1D)$ from the non-quenching isotope exchange reactions shown in (R19) and (R20) are also needed to calculate the production rates $Q(x)$ for $^{17}O(^1D)$ and $^{18}O(^1D)$.

(R19) $^{16}O(^1D) + C^{17}O^{16}O \rightarrow {}^{17}O(^1D) + C^{16}O^{16}O$

(R20) $^{16}O(^1D) + C^{18}O^{16}O \rightarrow {}^{18}O(^1D) + C^{16}O^{16}O$

These production rates were calculated by convolving the $^{16}O(^1D)$ kinetic energy distribution, $^{16}f(x)$, calculated below with the inelastic kernel for non-quenching isotope exchange as shown in Equation (18).

$$Q_{\text{ex}}^{17}(x) = \int_0^\infty B_{\text{ex}}^{16\rightarrow 17}(x|x')\,{}^{16}f(x')dx' \tag{18}$$

While the additional production rates of $^{17}O(^1D)$ and $^{18}O(^1D)$ from the non-quenching isotope $O(^1D) + CO_2$ exchange reactions (R19) and (R20) were needed, the production rate of $^{16}O(^1D)$ from the non-quenching $O(^1D) + CO_2$ isotope exchange reactions between the rare isotopes $^{17}O(^1D)$ and $^{18}O(^1D)$ and $C^{16}O^{16}O$ ((R21) and (R22), i.e., the reverse reactions of (R19) and (R20)) was not included in $Q(x)$ because it was much slower than the production rate of $^{16}O(^1D)$ from the UV photolysis of $^{16}O^{16}O^{16}O$ (see Figure 3-10).

(R21) $^{17}O(^1D) + C^{16}O^{16}O \rightarrow {}^{16}O(^1D) + C^{17}O^{16}O$

(R22) $^{18}O(^1D) + C^{16}O^{16}O \rightarrow {}^{16}O(^1D) + C^{18}O^{16}O$

The loss rates of $^{17}O(^1D)$ and $^{18}O(^1D)$ through the isotope exchange reactions (R21) and (R22) were also considered in the calculation of the kinetic energy distributions for $^{17}O(^1D)$ and $^{18}O(^1D)$. Including both the production and loss rates of $^{17}O(^1D)$ and $^{18}O(^1D)$ from the non-quenching $O(^1D) + CO_2$ isotope exchange reactions (R19) through (R22) increased the population of low kinetic energy $^{17}O(^1D)$ and $^{18}O(^1D)$; this has important consequences for the kinetics discussed below.

Using the production rates $Q(x)$ for $^{16}O(^1D)$, $^{17}O(^1D)$, and $^{18}O(^1D)$, the isotope-specific collision kernels $B(x'|x)$ that include both elastic and inelastic scattering by O_2 and CO_2, and the isotope-specific chemical loss rates of $O(^1D)$, the kinetic energy distributions for $^{16}O(^1D)$, $^{17}O(^1D)$, and $^{18}O(^1D)$ ($^{16}f(x)$, $^{17}f(x)$, and $^{18}f(x)$, respectively) were then determined using Eq. (9). Equation (9) was solved iteratively until the differences between solutions converged to less than 1% for each point along the isotopic-specific $f(x)$.

The kinetic energy distributions calculated for $^{16}O(^1D)$, $^{17}O(^1D)$, and $^{18}O(^1D)$ were then used to calculate the non-thermal rate coefficients to be used in the kinetics model in the various "non-thermal" model scenarios. For each possible reactant with $^{16}O(^1D)$, $^{17}O(^1D)$, and $^{18}O(^1D)$, the isotope-specific rate coefficient for that reaction was calculated using the center-of-mass transformation $\rho_T(x,x_r)$ from Eq. (16) and Equation (19).[26]

$$k_{\text{rxn}} = \int_0^\infty dx \int_0^\infty dx_r \sqrt{\frac{2x_r kT}{\mu}}\,\sigma_{\text{rxn}}(x_r)\rho_T(x,x_r)f(x) \tag{19}$$

The rate coefficients calculated for each set of reaction conditions (i.e. as a function of ρ) were then used in the photochemical kinetics model for the reactions of $O(^1D)$ in Scenario 3. Values

for the isotope-specific non-thermal rate coefficients used in Scenario 3 are summarized in Table 3-4.

In Scenarios 3B through 3E, the sensitivity of the isotopic composition of CO_2 relative to O_2 to different isotope-specific non-thermal reaction rate coefficients resulting from changes in the non-thermal translational energy distributions of $^{16}O(^1D)$, $^{17}O(^1D)$, and $^{18}O(^1D)$ can be tested. Because the hard sphere kernel is known to overestimate the probability of large energy transfers in elastic collisions,[46,52] the $O(^1D)$ kinetic energy distributions for $\rho < 10$ could have a much greater population of high kinetic energy $O(^1D)$ atoms than for $\rho > 10$. To test the sensitivity of the isotopic composition of CO_2 to such a systematic bias, in Scenario 3B, the non-thermal kinetic energy distributions for $^{16}O(^1D)$, $^{17}O(^1D)$, and $^{18}O(^1D)$ and their resulting non-thermal rate coefficients were calculated with a value for the hard-sphere collision cross section in elastic collisions with CO_2 reduced by a factor of 2. In addition to *overestimating* the probability of large energy transfers in elastic collisions, the hard sphere assumption also likely *underestimates* the probability of large energy transfers in inelastic collision between $O(^1D)$ and CO_2 since it is known that nearly 50% of the collision energy between $O(^1D)$ and CO_2 is deposited into the internal degrees of freedom of CO_2.[15,51] To test the combined effect of more effective inelastic collisions along with less effective elastic collisions, in Scenario 3C the cross section for inelastic collisions between $O(^1D)$ and CO_2 was doubled, while the same halved cross section for elastic collisions in Scenario 3B was also included. To test the sensitivity of the isotopic composition of CO_2 to the initial kinetic energy distribution of $O(^1D)$ from ozone photolysis, in Scenario 3D, the isotope-specific non-thermal rate coefficients were derived by using the center-of-mass translational energy distribution for O_3 photolysis at 245 nm[24] in $Q(x)$ instead of that at 255 nm. Finally, to completely remove the effect of energy transfer in elastic and inelastic collisions, in Scenario 3E, the non-thermal rate coefficients were calculated by integrating the kinetic energy-dependent reactive cross sections with the normalized kinetic energy distributions for $^{16}O(^1D)$, $^{17}O(^1D)$, and $^{18}O(^1D)$ from O_3 photolysis at 255 nm (Figure 3-3). In other words, elastic, inelastic , and reactive collisions of $O(^1D)$ with O_2, CO_2, and O_3 were not considered, and the initial $O(^1D)$ kinetic energy distributions from O_3 photolysis remained constant.

Table 3-4. Rate coefficients for reactions of $O(^1D)$ in different model scenarios using isotope-specific branching ratios in or derived from Mebel et al.[23] at 10kcal/mol (Scenario 2 in column 2) or using the non-thermal isotope-specific $O(^1D)$ kinetic energy distributions calculated by the hard-sphere approximations outlined in Section 3.2.3 at various mixing ratios ρ (Scenario 3 in columns 3 through 6).

Reaction	10 kcal/mol k ($cm^3\ s^{-1}$)	ρ = 1000 k ($cm^3\ s^{-1}$)	ρ = 10 k ($cm^3\ s^{-1}$)	ρ = 1 k ($cm^3\ s^{-1}$)	ρ = 0.01 k ($cm^3\ s^{-1}$)
$^{16}O(^1D) + C^{16}O^{16}O \rightarrow {}^{16}O(^1D) + C^{16}O^{16}O$	6.85×10^{-11}	1.36×10^{-11}	1.59×10^{-11}	2.65×10^{-11}	3.83×10^{-11}
$^{16}O(^1D) + C^{16}O^{16}O \rightarrow {}^{16}O(^3P) + C^{16}O^{16}O$	4.15×10^{-11}	1.26×10^{-10}	1.30×10^{-10}	1.48×10^{-10}	1.66×10^{-10}
$^{16}O(^1D) + C^{17}O^{16}O \rightarrow {}^{16}O(^1D) + C^{17}O^{16}O$	4.54×10^{-11}	8.99×10^{-12}	1.06×10^{-11}	1.76×10^{-11}	2.55×10^{-11}
$^{16}O(^1D) + C^{17}O^{16}O \rightarrow {}^{16}O(^3P) + C^{17}O^{16}O$	2.80×10^{-11}	8.38×10^{-11}	8.67×10^{-11}	9.85×10^{-11}	1.11×10^{-10}
$^{16}O(^1D) + C^{17}O^{16}O \rightarrow {}^{17}O(^1D) + C^{16}O^{16}O$	2.25×10^{-11}	4.33×10^{-12}	5.10×10^{-12}	8.52×10^{-12}	1.24×10^{-11}
$^{16}O(^1D) + C^{17}O^{16}O \rightarrow {}^{17}O(^3P) + C^{16}O^{16}O$	1.40×10^{-11}	4.19×10^{-11}	4.34×10^{-11}	4.94×10^{-11}	5.56×10^{-11}
$^{16}O(^1D) + C^{18}O^{16}O \rightarrow {}^{16}O(^1D) + C^{18}O^{16}O$	4.53×10^{-11}	8.83×10^{-12}	1.04×10^{-11}	1.73×10^{-11}	2.52×10^{-11}
$^{16}O(^1D) + C^{18}O^{16}O \rightarrow {}^{16}O(^3P) + C^{18}O^{16}O$	2.84×10^{-11}	8.40×10^{-11}	8.69×10^{-11}	9.89×10^{-11}	1.11×10^{-10}
$^{16}O(^1D) + C^{18}O^{16}O \rightarrow {}^{18}O(^1D) + C^{16}O^{16}O$	2.23×10^{-11}	4.29×10^{-12}	5.05×10^{-12}	8.45×10^{-12}	1.23×10^{-11}
$^{16}O(^1D) + C^{18}O^{16}O \rightarrow {}^{18}O(^3P) + C^{16}O^{16}O$	1.41×10^{-11}	4.17×10^{-11}	4.31×10^{-11}	4.91×10^{-11}	5.52×10^{-11}
$^{16}O(^1D) + {}^{16}O^{16}O \rightarrow {}^{16}O(^3P) + {}^{16}O^{16}O$	3.3×10^{-11}	3.73×10^{-11}	3.88×10^{-11}	4.51×10^{-11}	5.18×10^{-11}
$^{16}O(^1D) + {}^{16}O^{16}O^{16}O \rightarrow$ Products	2.4×10^{-10}	3.05×10^{-10}	3.20×10^{-10}	3.83×10^{-10}	4.50×10^{-10}
$^{16}O(^1D) + {}^{17}O^{16}O \rightarrow {}^{16}O(^3P) + {}^{17}O^{16}O$	3.3×10^{-11}	3.72×10^{-11}	3.86×10^{-11}	4.50×10^{-11}	5.17×10^{-11}
$^{16}O(^1D) + {}^{18}O^{16}O \rightarrow {}^{16}O(^3P) + {}^{17}O^{16}O$	3.3×10^{-11}	3.70×10^{-11}	3.85×10^{-11}	4.48×10^{-11}	5.15×10^{-11}
$^{17}O(^1D) + C^{16}O^{16}O \rightarrow {}^{16}O(^1D) + C^{17}O^{16}O$	4.54×10^{-11}	8.37×10^{-12}	9.78×10^{-12}	1.62×10^{-11}	2.35×10^{-11}
$^{17}O(^1D) + C^{16}O^{16}O \rightarrow {}^{16}O(^3P) + C^{17}O^{16}O$	2.80×10^{-11}	8.18×10^{-11}	8.45×10^{-11}	9.58×10^{-11}	1.08×10^{-10}
$^{17}O(^1D) + C^{16}O^{16}O \rightarrow {}^{17}O(^1D) + C^{16}O^{16}O$	2.25×10^{-11}	4.03×10^{-12}	4.72×10^{-12}	7.83×10^{-12}	1.14×10^{-11}
$^{17}O(^1D) + C^{16}O^{16}O \rightarrow {}^{17}O(^3P) + C^{16}O^{16}O$	1.40×10^{-11}	4.09×10^{-12}	4.23×10^{-11}	4.80×10^{-11}	5.41×10^{-11}
$^{17}O(^1D) + {}^{16}O^{16}O \rightarrow {}^{17}O(^3P) + {}^{16}O^{16}O$	3.3×10^{-11}	3.63×10^{-11}	3.77×10^{-11}	4.36×10^{-11}	5.00×10^{-11}
$^{17}O(^1D) + {}^{16}O^{16}O^{16}O \rightarrow$ Products	2.4×10^{-10}	2.96×10^{-10}	3.09×10^{-10}	3.68×10^{-10}	4.33×10^{-10}
$^{18}O(^1D) + C^{16}O^{16}O \rightarrow {}^{16}O(^1D) + C^{18}O^{16}O$	4.53×10^{-11}	7.64×10^{-12}	8.91×10^{-12}	1.47×10^{-11}	2.14×10^{-11}
$^{18}O(^1D) + C^{16}O^{16}O \rightarrow {}^{16}O(^3P) + C^{18}O^{16}O$	2.84×10^{-11}	8.01×10^{-11}	8.27×10^{-11}	9.37×10^{-11}	1.05×10^{-10}
$^{18}O(^1D) + C^{16}O^{16}O \rightarrow {}^{18}O(^1D) + C^{16}O^{16}O$	2.23×10^{-11}	3.71×10^{-12}	4.33×10^{-12}	7.17×10^{-12}	1.04×10^{-11}
$^{18}O(^1D) + C^{16}O^{16}O \rightarrow {}^{18}O(^3P) + C^{16}O^{16}O$	1.41×10^{-11}	3.98×10^{-11}	4.10×10^{-11}	4.65×10^{-11}	5.23×10^{-11}
$^{18}O(^1D) + {}^{16}O^{16}O \rightarrow {}^{18}O(^3P) + {}^{16}O^{16}O$	3.3×10^{-11}	3.53×10^{-11}	3.66×10^{-11}	4.23×10^{-11}	4.84×10^{-11}
$^{18}O(^1D) + {}^{16}O^{16}O^{16}O \rightarrow$ Products	2.4×10^{-10}	2.87×10^{-10}	3.00×10^{-10}	3.56×10^{-10}	4.17×10^{-10}

3.3. Results and Discussion

The isotopic composition of CO_2 relative to O_2 measured at 50 Torr and 170 Torr is shown as a function of the O_2/CO_2 mixing ratio ρ in Figure 3-4 and listed in Table 3-5 and Table 3-6. The empirical Hill-function fits to $\ln^{17}O_{O2}(CO_2)$, $\ln^{18}O_{O2}(CO_2)$, and $\Delta^{17}O_{O2}(CO_2)$ are also shown in Figure 3-4, as the solid and dashed lines for 50 Torr and 170 Torr, respectively, and given in Table 3-7. At both 50 and 170 Torr, values for $\ln^{17}O_{O2}(CO_2)$, $\ln^{18}O_{O2}(CO_2)$, and $\Delta^{17}O_{O2}(CO_2)$ decreased quite dramatically with decreasing ρ. At 50 Torr, for example, $\Delta^{17}O_{O2}(CO_2)$ decreased from a high-ρ plateau value of 82‰ to a low-ρ plateau value of 29‰. Based on the fitted value of ρ_0 at both pressures, the midway point between the transition from the high-ρ plateau to the the low-ρ plateau occurs at $\rho \approx 3$, and similarly for $\ln^{17}O_{O2}(CO_2)$ and $\ln^{18}O_{O2}(CO_2)$. At high ρ, the values for $\ln^{17}O_{O2}(CO_2)$, $\ln^{18}O_{O2}(CO_2)$, and $\Delta^{17}O_{O2}(CO_2)$ decreased as the pressure decreased from 50 Torr to 170 Torr because of the pressure dependence of the KIEs in ozone formation;[22,37–40] for example, the values for the empirical fit to $\Delta^{17}O_{O2}(CO_2)$ at the high ρ plateau were 81.6‰ and 68.3‰ at 50 Torr and 170 Torr, respectively. The values for the empirical fit to $\Delta^{17}O_{O2}(CO_2)$ at the low ρ plateau also decreased as the pressure was increased from 50 Torr to 170 Torr, but the difference between the two pressures was much smaller: 29.1‰ at 50 Torr and 25.3‰ at 170 Torr. For the low ρ case, the pressure dependence of the ozone KIEs may still have caused some decrease in $\Delta^{17}O_{O2}(CO_2)$ as the pressure was increased from 50 to 170 Torr, but the smaller magnitude of the decrease from 50 to 170 Torr suggests that some other non-mass-dependent process starts to become important at $\rho < 10$, as hypothesized by Shaheen et al.[18]

The $\ln^{17}O_{O2}(CO_2)$, $\ln^{18}O_{O2}(CO_2)$, and $\Delta^{17}O_{O2}(CO_2)$ measurements reported here show similar magnitudes and ρ-dependence to those at 170 Torr from Shaheen et al.,[18] with a few differences. The differences may be due to differences in the experimental conditions, to differences in how the ^{17}O isotopic compositions were derived from the CeO_2 technique measurements, or both. For example, the Shaheen et al.[18] experiments involved a smaller reactor size and a higher photon flux from a different manufacturer's mercury lamp. A higher lamp flux and smaller reactor volume could affect the isotopic compositions through an increase in the relative importance of mass-dependent isotope effects in O_3 photolysis[36,55] or through an increase in the temperature of the gases in the bulb and thus the magnitudes of the ozone formation KIEs, which are known to be temperature dependent.[56,57] Differences in the values used for the isotope ratios of the international standard (i.e. $(^{17}O/^{16}O)_{VSMOW}$) and the actual value of the mass-dependent factor λ_{MD} used can also lead to different calculated values for the isotopic composition of CO_2 [30]. Because the original measurements relative to VSMOW and the parameters used in the derivation of the isotopic composition of the CO_2 reported in Shaheen et al.[18] are not retrievable, their measurements are not necessarily directly comparable to ours, particularly for $\ln^{17}O$ and $\Delta^{17}O$.

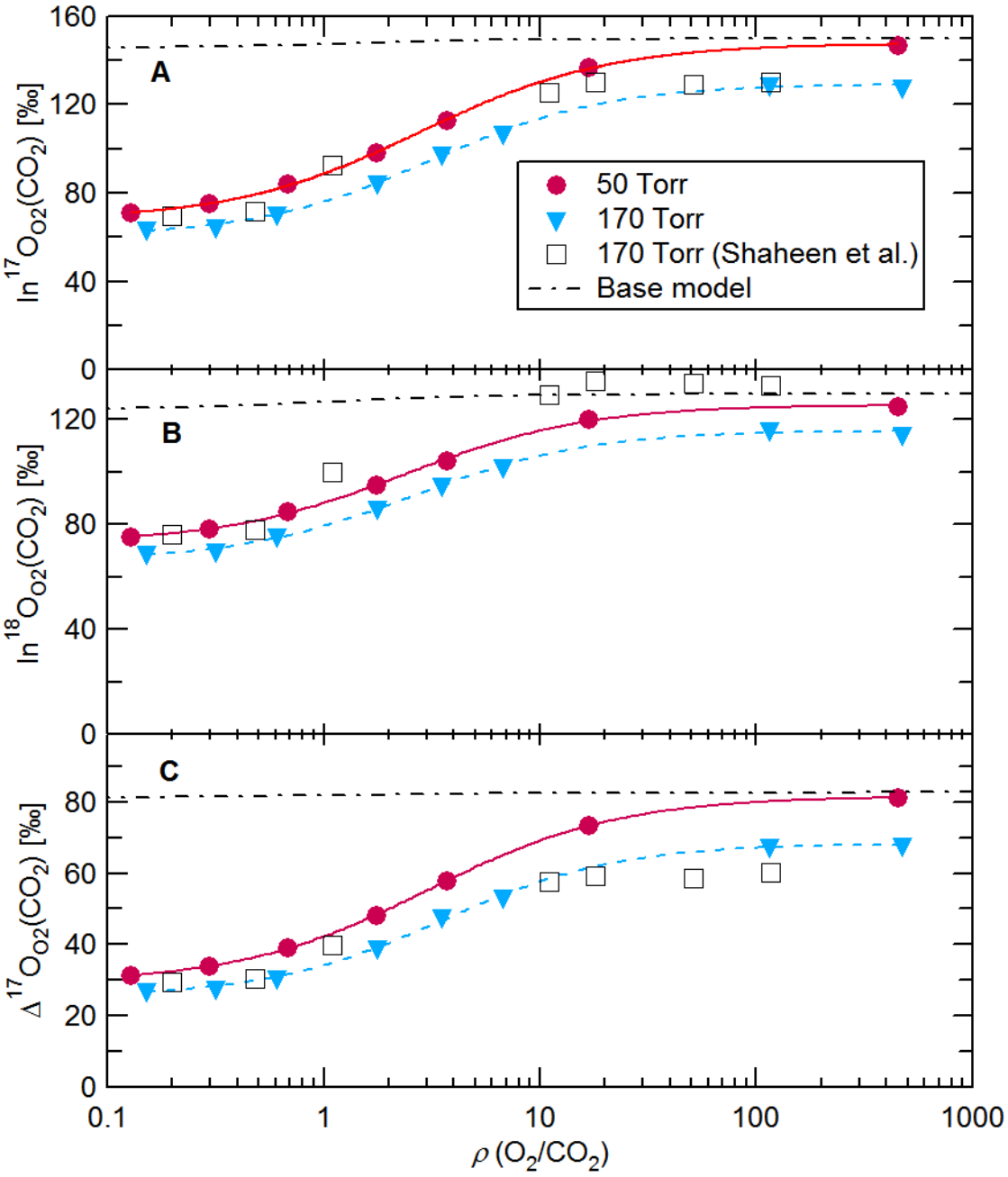

Figure 3-4. Measurements of the isotopic composition of CO_2 relative to O_2 in a mixture of the UV-irradiated gases. Measurements shown are (**A**) $\ln^{17}O_{O2}(CO_2)$, (**B**) $\ln^{18}O_{O2}(CO_2)$, and (**C**) $\Delta^{17}O_{O2}(CO_2)$ as a function of the O_2/CO_2 mixing ratio ρ. Model predictions from the base scenario are also shown as dot-dashed black line.

Table 3-5. Experimental results for the isotopic composition of CO_2 and O_2 relative to VSMOW in ‰, as a function of various values of ρ at total pressure of 50 Torr and of 170 Torr. The reported uncertainties for N > 1 are the 1σ standard errors of the mean.

ρ (O_2/CO_2)	O_2			CO_2			
	$\ln^{17}O$	$\ln^{18}O$	$\Delta^{17}O$	$\ln^{17}O$	$\ln^{18}O$	$\Delta^{17}O$	N
N/A (Initial)	13.7 ± 0.1	26.5 ± 0.1	-0.3 ± 0.1	3.4± 0.2	6.6± 0.3	-0.1± 0.2	3
			*50 Torr**				
0.128 ± 0.009	-59.0 ± 0.6	-58.2 ± 0.6	-28.29 ± 0.06	11.9 ± 0.7	16.8 ± 0.7	3.0 ± 0.3	2
0.295 ± 0.006	-53.6 ± 0.4	-50.68 ± 0.11	-26.8 ± 0.3	21.62 ± 0.09	27.58 ± 0.04	7.05 ± 0.07	2
0.683 ± 0.013	-43.9 ± 0.3	-37.2 ± 0.4	-24.26 ± 0.11	40.3 ± 0.6	47.9 ± 0.5	15.0 ± 0.3	3
1.76 ± 0.04	-27.8 ± 0.2	-17.3 ± 0.2	-18.69 ± 0.05	70.26 ± 0.09	77.49 ± 0.18	29.34 ± 0.01	2
3.72 ± 0.15	-14.8 ± 0.2	-2.3 ± 0.2	-13.6 ± 0.1	98.3 ± 0.9	102.06 ± 0.05	44.4 ± 0.9	2
16.7 ± 0.5	4.4 ± 0.3	17.8 ± 0.3	-5.0 ± 0.2	141.3 ± 0.3	138.15 ± 0.03	68.4 ± 0.3	2
449 ± 9	13.33 ± 0.01	26.16 ± 0.01	-0.49 ± 0.01	160.3 ± 0.7	150.9 ± 1.0	80.7 ± 0.2	2
			*170 Torr**				
0.151 ± 0.003	-51.3 ± 0.2	-51.57 ± 0.2	-24.06 ± 0.03	12.38 ± 0.07	17.30 ± 0.01	3.24 ± 0.07	2
0.317 ± 0.006	-45.6 ± 0.9	-43.8 ± 1.1	-22.4 ± 0.3	19.2 ± 0.4	26.0 ± 0.3	5.5 ± 0.2	2
0.61 ± 0.02	-38.7 ± 0.3	-34.7 ± 0.5	-20.38 ± 0.07	31.97 ± 0.04	40.88 ± 0.11	10.39 ± 0.09	2
1.78 ± 0.04	-22.9 ± 0.2	-14.3 ± 0.5	-15.38 ± 0.09	61.8 ± 0.6	71.9 ± 0.6	23.8 ± 0.3	2
3.52 ± 0.07	-11.4 ± 0.3	-0.1 ± 0.3	-11.40 ± 0.11	86.59 ± 0.17	95.0 ± 0.3	36.4 ± 0.4	2
6.79 ± 0.14	-2.6 ± 0.4	9.9 ± 0.4	-7.84 ± 0.14	105 ± 2	112.1 ± 1.0	45.4 ± 1.6	2
115 ± 2[†]	12.4 ± 0.3	25.3 ± 0.5	-0.9 ± 0.5	141.4 ± 0.5	141.4 ± 0.5	66.7 ± 0.5	1
470 ± 9[†]	13.0 ± 0.3	25.6 ± 0.5	-0.6 ± 0.5	141.3 ± 0.5	140.0 ± 0.5	67.3 ± 0.5	1

*The average pressure in the "50 Torr" and "170 Torr" experiments was 50.5 ± 0.1 Torr (1σ) and 170.8 ± 0.8 Torr (1σ), respectively.

[†] For N=1, the reported uncertainties are the 1σ values for the combined measurement precision and accuracy described in Section 2.1.

Table 3-6. Experimental results for the isotopic composition of CO_2 relative to the O_2 isotopic composition in ‰, as a function of ρ at a total pressure of 50 Torr and of 170 Torr. The reported uncertainties for N > 1 are the 1σ standard errors of the mean.

ρ (O_2/CO_2)	$CO_2 - O_2$			
	$\ln^{17}O$	$\ln^{18}O$	$\Delta^{17}O$	N
		*50 Torr**		
0.128 ± 0.009	70.9 ± 0.3	75.01 ± 0.07	31.3 ± 0.2	2
0.295 ± 0.001	75.2 ± 0.5	78.26 ± 0.15	33.9 ± 0.4	2
0.683 ± 0.003	84.2 ± 0.5	85.1 ± 0.6	39.2 ± 0.3	3
1.755 ± 0.015	98.08 ± 0.09	94.77 ± 0.10	48.04 ± 0.06	2
3.72 ± 0.15	113.2 ± 1.1	104.4 ± 0.2	58.1 ± 1.0	2
16.7 ± 0.5	136.9 ± 0.6	120.3 ± 0.3	73.4 ± 0.5	2
449 ± 5	147.0 ± 0.7	124.7 ± 1.0	81.2 ± 0.2	2
		*170 Torr**		
0.151 ± 0.001	63.7 ± 0.3	68.9 ± 0.2	27.31 ± 0.10	2
0.317 ± 0.002	64.8 ± 1.3	69.8 ± 1.5	27.9 ± 0.6	2
0.61 ± 0.02	70.6 ± 0.3	75.6 ± 0.6	30.76 ± 0.02	2
1.78 ± 0.02	84.7 ± 0.4	86.14 ± 0.13	39.2 ± 0.4	2
3.52 ± 0.05	98.03 ± 0.11	95.1 ± 0.6	47.80 ± 0.19	2
6.79 ± 0.07	107 ± 3	102.2 ± 1.4	53.3 ± 1.8	2
115 ± 2†	128.9 ± 0.8	116.2 ± 1.0	67.6 ± 1.0	1
470 ± 9†	128.3 ± 0.8	114.4 ± 1.0	67.9 ± 1.0	1

*The average pressure in the "50 Torr" and "170 Torr" experiments was 50.5 ± 0.1 Torr (1σ) and 170.8 ± 0.8 Torr (1σ), respectively.

† For N=1, the reported uncertainties are the 1σ values for the combined measurement precision and accuracy described in Section 2.1.

Table 3-7. Empirically fit parameters for $\ln^{17}O_{O2}$, $\ln^{18}O_{O2}$, $\Delta^{17}O_{O2}$ of CO_2 using the Hill function (Eq. (6)) at 50 and 170 Torr.

	50 Torr			*170 Torr*		
	$\ln^{17}O_{O_2}$	$\ln^{18}O_{O_2}$	$\Delta^{17}O_{O_2}$	$\ln^{17}O_{O_2}$	$\ln^{18}O_{O_2}$	$\Delta^{17}O_{O_2}$
max	147.7	125.5	81.6	120.4	115.7	68.3
base	67.6	72.9	29.1	60.2	66.0	25.3
ρ_0	2.77	2.38	3.02	3.1	2.6	3.5
rate	-1.00	-1.03	-0.98	-1.06	-1.06	-1.07

Results for $\ln^{17}O_{O2}(CO_2)$, $\ln^{18}O_{O2}(CO_2)$, and $\Delta^{17}O_{O2}(CO_2)$ predicted by the photochemical kinetics model using the "base" scenario are shown in Figure 3-4 and Figure 3-5. While the base scenario model predictions for $\ln^{17}O_{O2}(CO_2)$, $\ln^{18}O_{O2}(CO_2)$, and $\Delta^{17}O_{O2}(CO_2)$ at a total pressure of 50 Torr are all within 4‰ of the measurements at high ρ, the base model showed only a small ρ dependence as ρ decreases from 1000 to 0.1, unlike the dramatic ρ dependence in the experiments. The small decreases of ~4‰, ~6‰ and ~1‰ for $\ln^{17}O_{O2}(CO_2)$, $\ln^{18}O_{O2}(CO_2)$, and $\Delta^{17}O_{O2}(CO_2)$ from high to low ρ for the base scenario results arise from the "effective pressure" mechanism used to modify the KIEs for O_3 formation as pressure and ρ were varied, as detailed in Feilberg, Wiegel, and Boering.[22] Yet these small decreases are clearly inadequate to describe the experimental behavior of the isotopic composition of CO_2 as a function of ρ. Indeed, that the isotopic composition of ozone formed in a CO_2 bath gas was very similar to that formed in an O_2 bath gas also suggested that the ρ dependence of the isotopic composition of CO_2 relative to O_2 cannot be explained simply by changes in the KIEs for O_3 formation when CO_2 is the bath gas instead of O_2.[22] Thus, the base model results compared with the experiments confirmed that the dramatic dependence of $\ln^{17}O_{O2}(CO_2)$, $\ln^{18}O_{O2}(CO_2)$, and $\Delta^{17}O_{O2}(CO_2)$ values on ρ is unlikely due to changes in the magnitude of the KIEs for O_3 formation from the increased ozone formation quenching efficiency for CO_2, which is a factor of 2.1 larger than the quenching efficiency for O_2.[42]

As described in Section 3.2, a number of different mechanisms with potential ρ dependencies were introduced into the kinetics model using various scenarios. In the following, we discuss results for Scenarios 1 through 3E. As described below, the introduction of various mechanisms in most of the scenarios tested worsened the agreement with the experimental $\ln^{17}O_{O2}(CO_2)$ and $\ln^{18}O_{O2}(CO_2)$ values at high ρ, where the base scenario in the model had performed well, but had only a small effect on $\Delta^{17}O_{O2}(CO_2)$. Furthermore, each of the model scenario results showed little ρ dependence. In comparing the results from various scenarios below, since we were interested in the relative differences that could lead to a possible ρ-dependence for the isotopic composition of CO_2 relative to O_2, we report the model results in Table 3-8 as a difference between the isotopic composition of CO_2 relative to O_2 predicted by the model at ρ = 1000 and at ρ = 0.01. Some of the model predictions using various scenarios are also shown in Figure 3-5.

In Scenario 1, hypothetical mass-dependent isotope effects in the reaction $O_2(^1\Sigma) + O_3$ (R13) were added to the base scenario since a previous modeling study by Cole and Boering[36] of isotope effects in ozone photolysis experiments[43] had indicated that such effects might be consistent with the experiments. Including such isotope effects in the model decreased the $\ln^{17}O_{O2}(CO_2)$ and $\ln^{18}O_{O2}(CO_2)$ values by 6.4‰ and 12.4‰, respectively as ρ was decreased from 1000 to 0.1 (see Figure 3-5 and Table 3-8). Because the rate coefficient for electronic quenching of $O_2(^1\Sigma)$ by CO_2 is 10^4 times greater than electronic quenching by O_2, the concentration of $O_2(^1\Sigma)$ relative to O_3 also decreased in the model as ρ decreased. This led to a decrease in the relative importance of the isotope effects in $O_2(^1\Sigma) + O_3$, and thus to a decrease in the values of $\ln^{17}O_{O2}(CO_2)$ and $\ln^{18}O_{O2}(CO_2)$ with decreasing ρ. At the same time, however, the $\Delta^{17}O_{O2}(CO_2)$ value did not change. While mass-dependent isotope effects in this or any of the other reactions in the experiments will not by definition change the value of $\Delta^{17}O_{O2}(CO_2)$, the Scenario 1 model results show that such mass-dependent isotope effects may at least play a potentially important role in changing the values of $\ln^{17}O_{O2}(CO_2)$ and $\ln^{18}O_{O2}(CO_2)$ as ρ changes.

Table 3-8. Comparison of the change in the isotopic composition of CO_2 relative to O_2 between ρ = 1000 and ρ = 0.1 for the different model scenarios at 50 Torr and between ρ = 449 and ρ = 0.128 for the experiments at 50 Torr.

Name	$\Delta(\ln^{17}O_{O_2}(CO_2))$	$\Delta(\ln^{18}O_{O_2}(CO_2))$	$\Delta(\Delta^{17}O_{O_2}(CO_2))$
Expt (50 Torr)	-76.1‰	-49.7‰	-49.9‰
Base Scenario	-4.5‰	-6.2‰	-1.3‰
Scenario 1	-11.8‰	-20.2‰	-1.1‰
Scenario 2	-18.0‰	-32.3‰	-1.2‰
Scenario 3	-11.6‰	-13.9‰	-4.4‰
Scenario 3A	-6.8‰	-7.6‰	-2.8‰
Scenario 3B	-13.2‰	-15.8‰	-5.0‰
Scenario 3C	-21.4‰	-21.9‰	-10.0‰
Scenario 3D	-12.7‰	-15.2‰	-4.8‰
Scenario 3E	-17.6‰	-21.3‰	-6.6‰

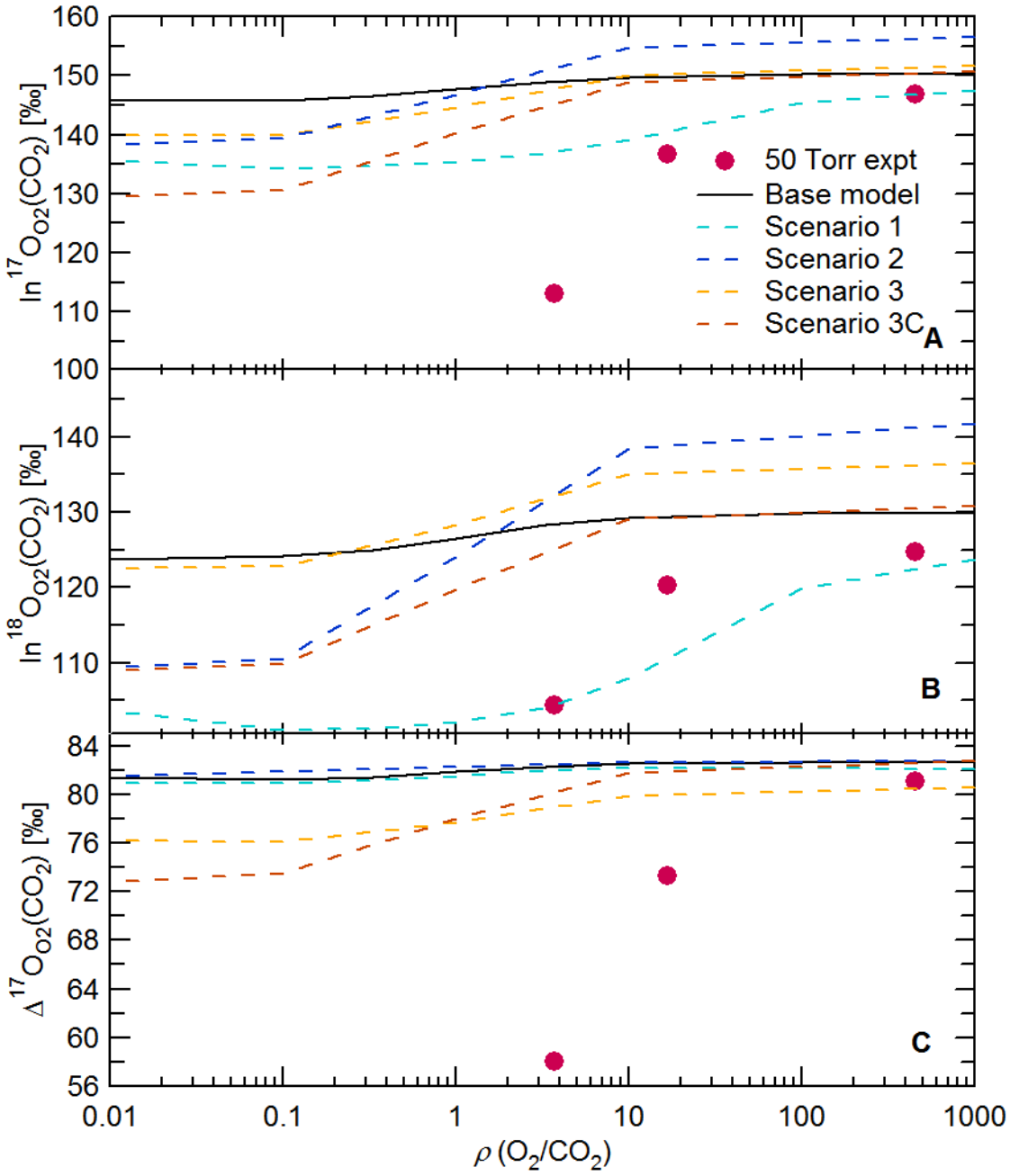

Figure 3-5. The isotopic composition of CO_2 relative to O_2 in the 50 Torr experiments compared with results from several model scenarios. The isotopic compositions shown are (**A**) $\ln^{17}O_{O2}(CO_2)$, (**B**) $\ln^{18}O_{O2}(CO_2)$, and (**C**) $\Delta^{17}O_{O2}(CO_2)$ as a function of the O_2/CO_2 mixing ratio ρ. Note the difference in *y*-axis scale from Figure 3-4. See Section 3.2.2 for a detailed description and Table 3-3 as a short-hand guide for each scenario.

For Scenario 2, the isotope-specific branching ratios for the quenching (R3) and non-quenching (R4) isotope exchange between $O(^1D)$ and CO_2 at a collision energy of 10 kcal/mol calculated by or derived from Mebel et al.[23] at thermal collision frequencies (see section 3.2.2) were added to the base scenario. At this high collision energy, the branching ratio calculated by Mebel for $^{16}O(^1D) + C^{16}O^{16}O$ for non-quenching to quenching maximized to 57%:43%, so this scenario tested the sensitivity of the relative isotopic composition of CO_2 to a large increase in the relative importance of the non-quenching $O(^1D) + CO_2$ isotope exchange reaction. This scenario resulted in a mass-dependent ρ-dependence in which $\ln^{17}O_{O2}(CO_2)$ and $\ln^{18}O_{O2}(CO_2)$ values decreased by 18‰ and 32‰ respectively (see Table 3-8) as ρ decreased from 1000 to 0.1, while $\Delta^{17}O_{O2}(CO_2)$ did not change. The results from Scenario 2 show that large changes in the relative importance of the non-quenching $O(^1D) + CO_2$ isotope exchange reaction on its own did not result in a ρ dependence for $\Delta^{17}O_{O2}(CO_2)$, at least when only thermal collision energies are considered.

For Scenario 3 and Scenarios 3A through 3E, recall from Section 3.2.3 that translational energy distributions for $^{16}O(^1D)$, $^{17}O(^1D)$, and $^{18}O(^1D)$ at several different mixing ratios ρ were calculated and then used to calculate non-thermal rate coefficients for all the reactions of $O(^1D)$ in the model. The calculated kinetic energy distributions for $^{16}O(^1D)$, $^{17}O(^1D)$, and $^{18}O(^1D)$ change significantly with decreasing ρ, and these differences between the isotope-specific kinetic energy distributions at high ρ and low ρ are key to understanding the results of Scenario 3 and Scenarios 3A through 3E. The normalized translational energy distributions for $^{16}O(^1D)$ for Scenario 3 at ρ = 1000, 1, and 0.01 are shown in Figure 3-6 along with a Maxwell-Boltzmann distribution for T = 300K. The translational energy distributions for $^{16}O(^1D)$ at these values of ρ show large populations of high kinetic energy $^{16}O(^1D)$, with 15%, 33%, and 50% of $^{16}O(^1D)$ atoms populating the high energy tail ($E > 5k_BT$) at ρ = 1000, 1, and 0.01, respectively, compared with <2% for a Maxwell-Boltzmann distribution for T = 300K. A larger proportion of $O(^1D)$ atoms populated the high energy tail in CO_2-dominated mixtures at low ρ compared with O_2 dominated mixtures at high ρ because the larger difference in mass between $O(^1D)$ and CO_2 than between $O(^1D)$ and O_2 resulted in less efficient energy transfer in elastic collisions between $O(^1D)$ and CO_2 than in elastic collisions between $O(^1D)$ and O_2.[58] In addition, in part because of more efficient energy transfer in elastic collisions when the differences in mass are smaller, at ρ = 0.01 the translational energy distributions of $^{18}O(^1D)$ and $^{17}O(^1D)$ also had a smaller population of high energy $O(^1D)$ atoms compared with the translational energy distribution for $^{16}O(^1D)$ (Figure 3-7). Furthermore, the translational energy distributions for $^{18}O(^1D)$ and $^{17}O(^1D)$ were also "colder" than the distribution for $^{16}O(^1D)$ due to the differences in the initial kinetic energy distributions for $^{16}O(^1D)$, $^{17}O(^1D)$, and $^{18}O(^1D)$ both from the UV photolysis of O_3 (Figure 3-3) and due to the increased importance at low ρ of the $^{17}O(^1D)$ and $^{18}O(^1D)$ produced from the non-quenching isotope exchange reaction of $^{16}O(^1D)$ with $C^{17}O^{16}O$ (R19) and with $C^{18}O^{16}O$ (R20), as discussed further below.

For Scenario 3, the combination of the larger population of high kinetic energy $O(^1D)$ at ρ = 0.01 and the differences between the translational energy distributions for $^{16}O(^1D)$, $^{17}O(^1D)$, and $^{18}O(^1D)$ led to calculated non-thermal rate coefficients for the various reactions of $O(^1D)$ that were quite different than the thermal rate coefficients (see Table 3-4). When used in the kinetics model, these calculated non-thermal rate coefficients produced a non-mass-dependent decrease in the relative isotopic composition of CO_2 even though the KIEs were either 1 for the reactions $O(^1D) + O_2$ and $O(^1D) + O_3$ or mass-dependent at a given kinetic energy for the $O(^1D) + CO_2$ reactions. Inclusion of these non-thermal rate coefficients in Scenario 3 decreased $\Delta^{17}O_{O2}(CO_2)$

by 4.4‰ as ρ decreased from 1000 to 0.01, which is an additional 3.1‰ decrease over the base scenario. While this ρ dependence is still an order of magnitude too small compared to the experiment, most other realistic mechanisms included in the various scenarios (including many not explicitly discussed in this chapter) did not produce any significant ρ dependence for the value of $\Delta^{17}O_{O2}(CO_2)$ at all.

In Scenario 3A, the same non-thermal rate coefficients for the reactions of $O(^1D)$ as in Scenario 3 were used, but the non-mass-dependent KIEs in ozone formation were all set to 1. The model results for Scenario 3A also showed a ρ dependence for $\Delta^{17}O_{O2}(CO_2)$ with $\Delta^{17}O_{O2}(CO_2)$ decreasing by 2.8‰ from ρ = 1000 to ρ = 0.01, compared with 1.3‰ for the base scenario and 4.4‰ for Scenario 3 (see Table 3-8). Importantly, this model scenario showed that a ρ dependence for $\Delta^{17}O_{O2}(CO_2)$ can arise from the non-thermal rate coefficients for the reactions of $O(^1D)$ alone and can occur in the absence of ozone formation KIEs and non-mass-dependently fractionated ozone. In other words, the results from Scenario 3A compared with Scenario 3 and the base model scenario suggest that non-thermal isotope exchange between $O(^1D)$ and CO_2 can produce changes in the ^{17}O isotope anomaly of O_2 and CO_2 regardless of the source of the non-thermal $O(^1D)$.

Results for Scenarios 3B through 3E showed that an increase in the population of $O(^1D)$ in the high-energy part of the translational energy distributions yielded larger ρ dependences for the value of $\Delta^{17}O_{O2}(CO_2)$, as shown in Table 3-8 and in Figure 3-8. For Scenario 3B, the elastic hard-sphere cross section for CO_2 was reduced by a factor of 2, so the translational energy distributions for $^{16}O(^1D)$, $^{17}O(^1D)$, and $^{18}O(^1D)$ had greater populations of high kinetic energy atoms than in Scenario 3. This resulted in a ρ dependence in which the value of $\Delta^{17}O_{O2}(CO_2)$ decreased by 5.0‰ from ρ = 1000 to ρ = 0.01 compared with 4.4‰ in Scenario 3 (Table 3-8). For Scneario 3D, using the initial kinetic energy distribution for $O(^1D)$ from O_3 photolysis at 245 nm instead of 255 nm also created isotope-specific translational energy distributions for $O(^1D)$ with a greater population of high kinetic energy $O(^1D)$ atoms. Using the non-thermal rate coefficients in Scenario 3D calculated from these $O(^1D)$ kinetic energy distributions led to a ρ dependence in which the value of $\Delta^{17}O_{O2}(CO_2)$ decreased by 4.8‰ from ρ = 1000 to ρ = 0.01. For Scenario 3E, the initial translational energy distribution of $O(^1D)$ from O_3 photolysis at 255 nm shown in Figure 3-3 was used to calculate the non-thermal rate coefficients directly (i.e. no collisional energy transfer at all), so a relatively large population of high kinetic energy $O(^1D)$ atoms in the $O(^1D)$ translational energy distributions remained. This led to a ρ dependence in which the value of $\Delta^{17}O_{O2}(CO_2)$ decreased by 6.6‰ from ρ = 1000 to ρ = 0.01. Comparing each of these model scenarios, an increase in the population of high energy $O(^1D)$ in the kinetic energy distributions led to larger ρ dependences for $\Delta^{17}O_{O2}(CO_2)$.

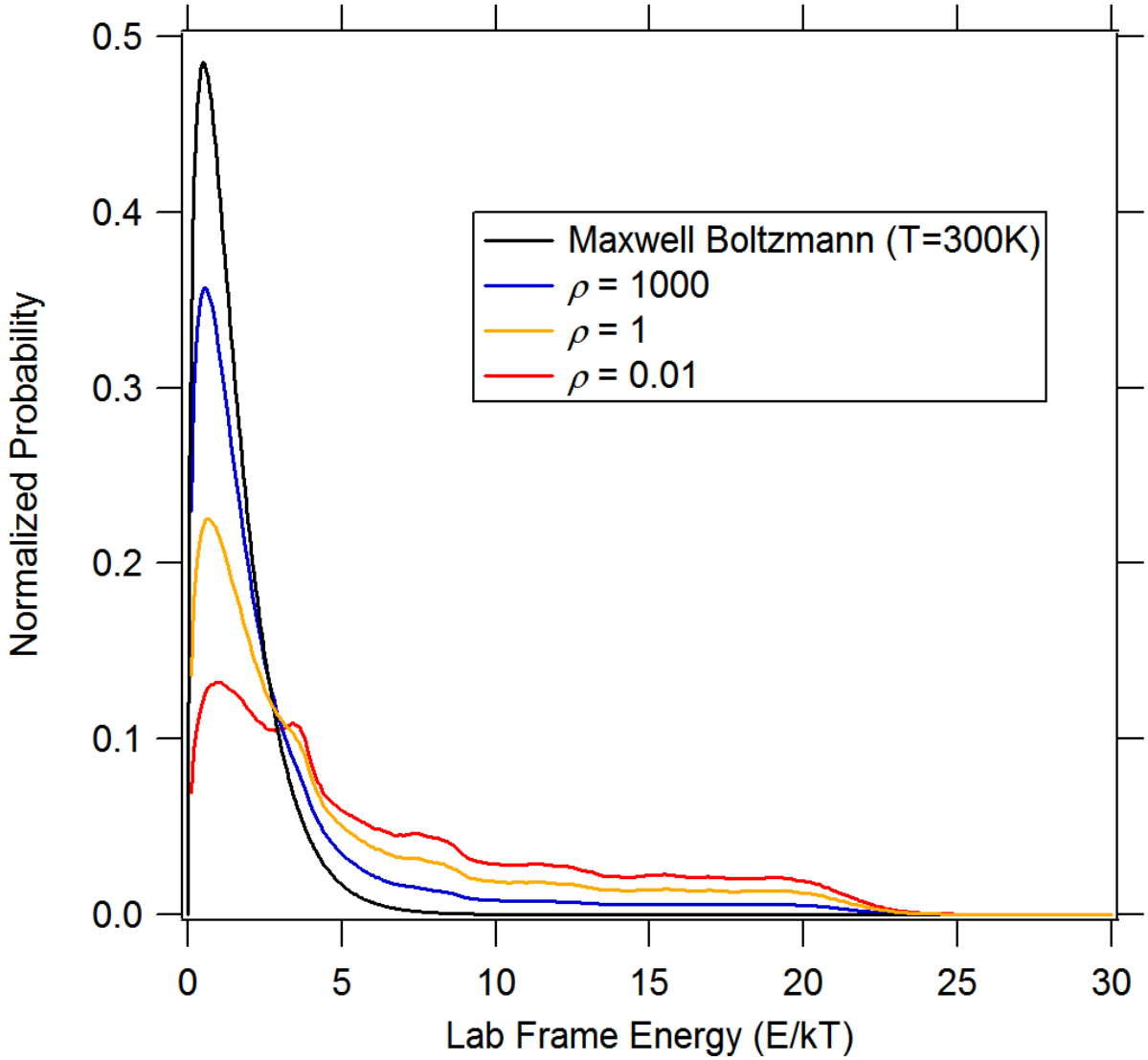

Figure 3-6. Normalized translational energy distributions for $^{16}O(^1D)$ in Scenario 3 at various O_2/CO_2 mixing ratios ρ, compared with a Maxwell Boltzmann distribution at T = 300K. For clarity, the distributions for ρ = 10 and ρ = 0.1 are not shown.

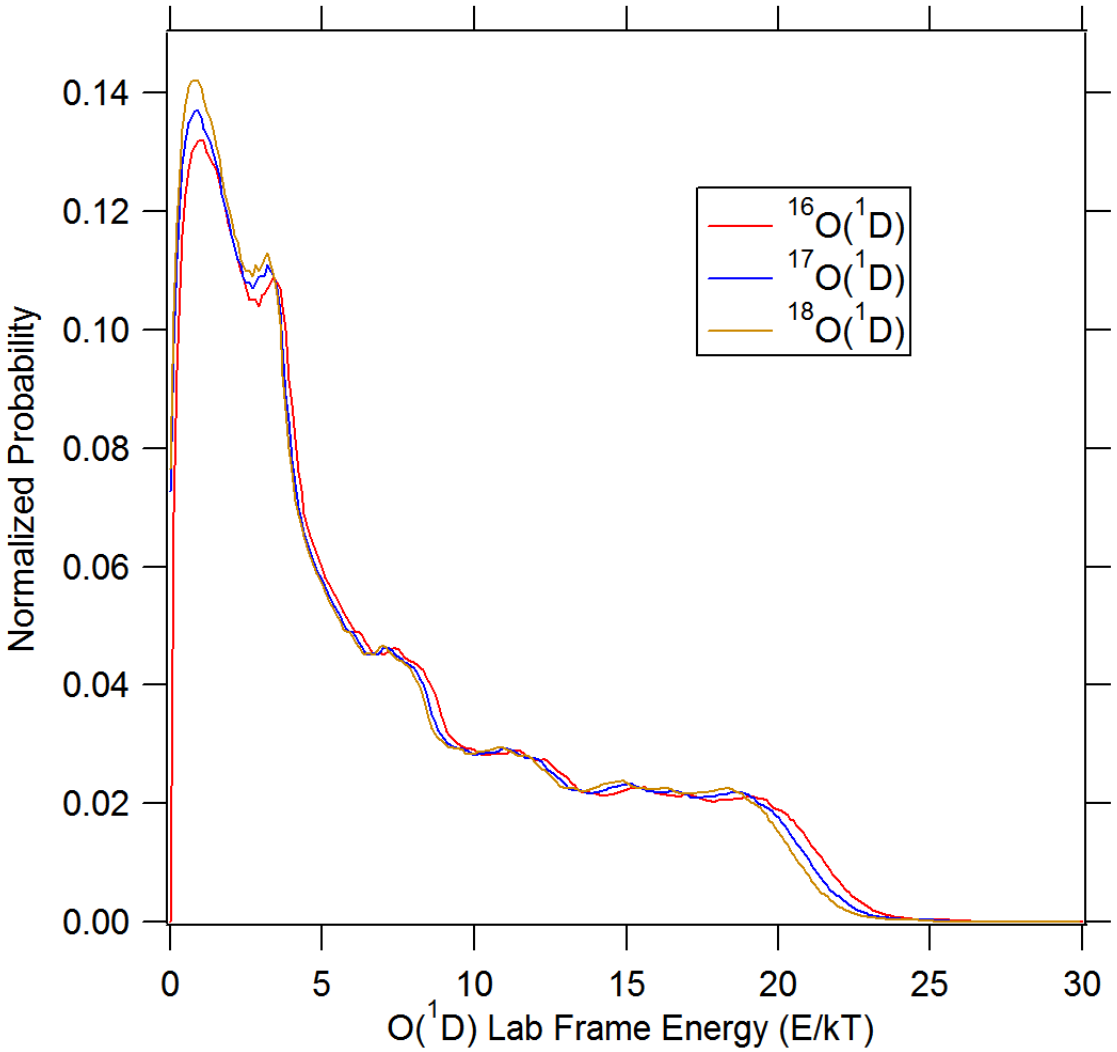

Figure 3-7. Normalized translational energy distributions calculated for $^{16}O(^1D)$, $^{17}O(^1D)$, and $^{18}O(^1D)$ at a mixing ratio of $\rho = 0.01$ in Scenario 3.

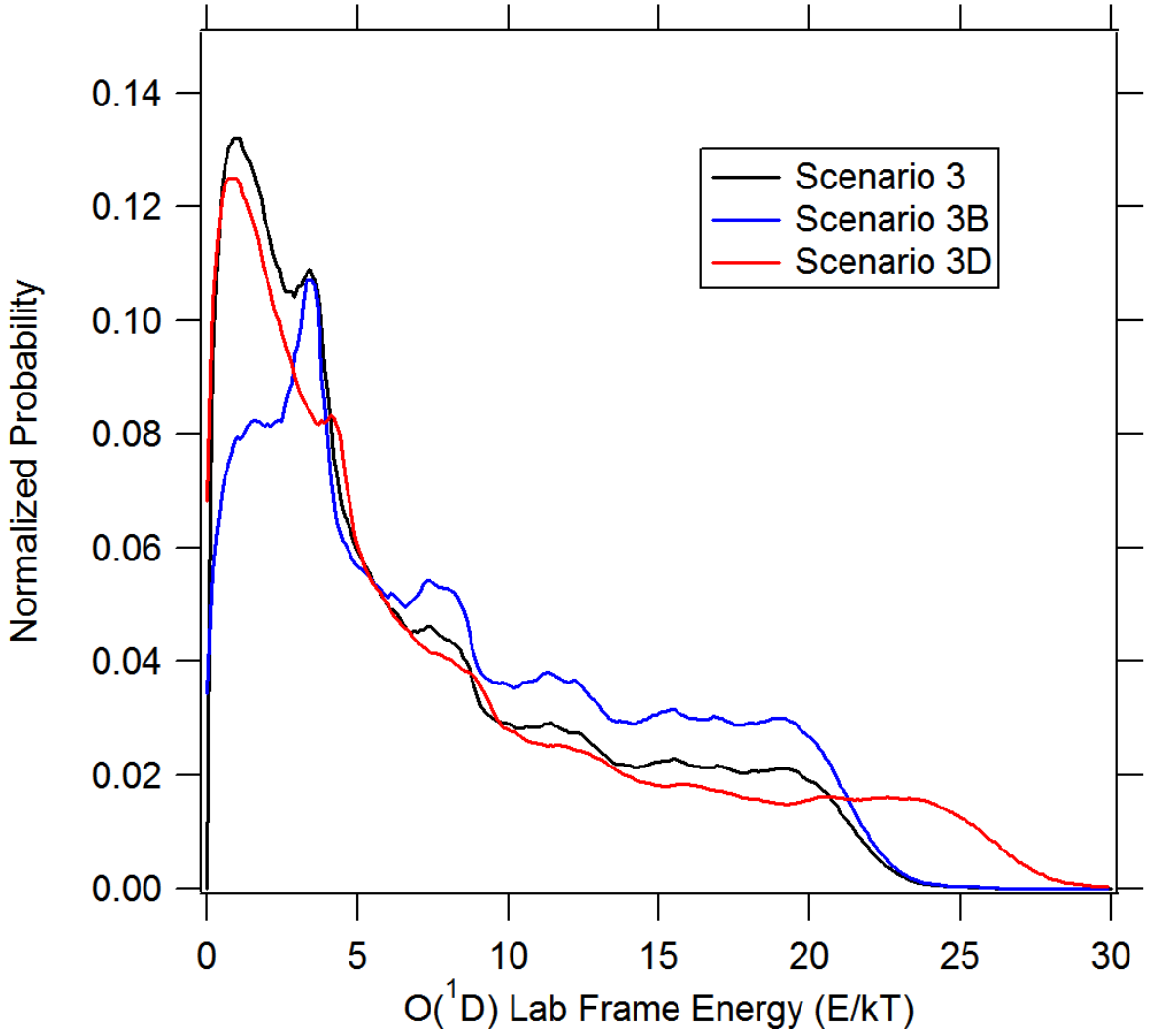

Figure 3-8. Calculated translational energy distributions for $^{16}O(^1D)$ for different model scenarios at $\rho = 0.01$. In Scenario 3B, the elastic cross section in the hard sphere kernel $B(x'|x)$ was reduced by half. In Scenario 3D, the translational energy distribution for $O(^1D)$ from O_3 photolysis at 245 nm was used as the initial distribution instead of that for 255 nm, which was used in the other model scenarios.

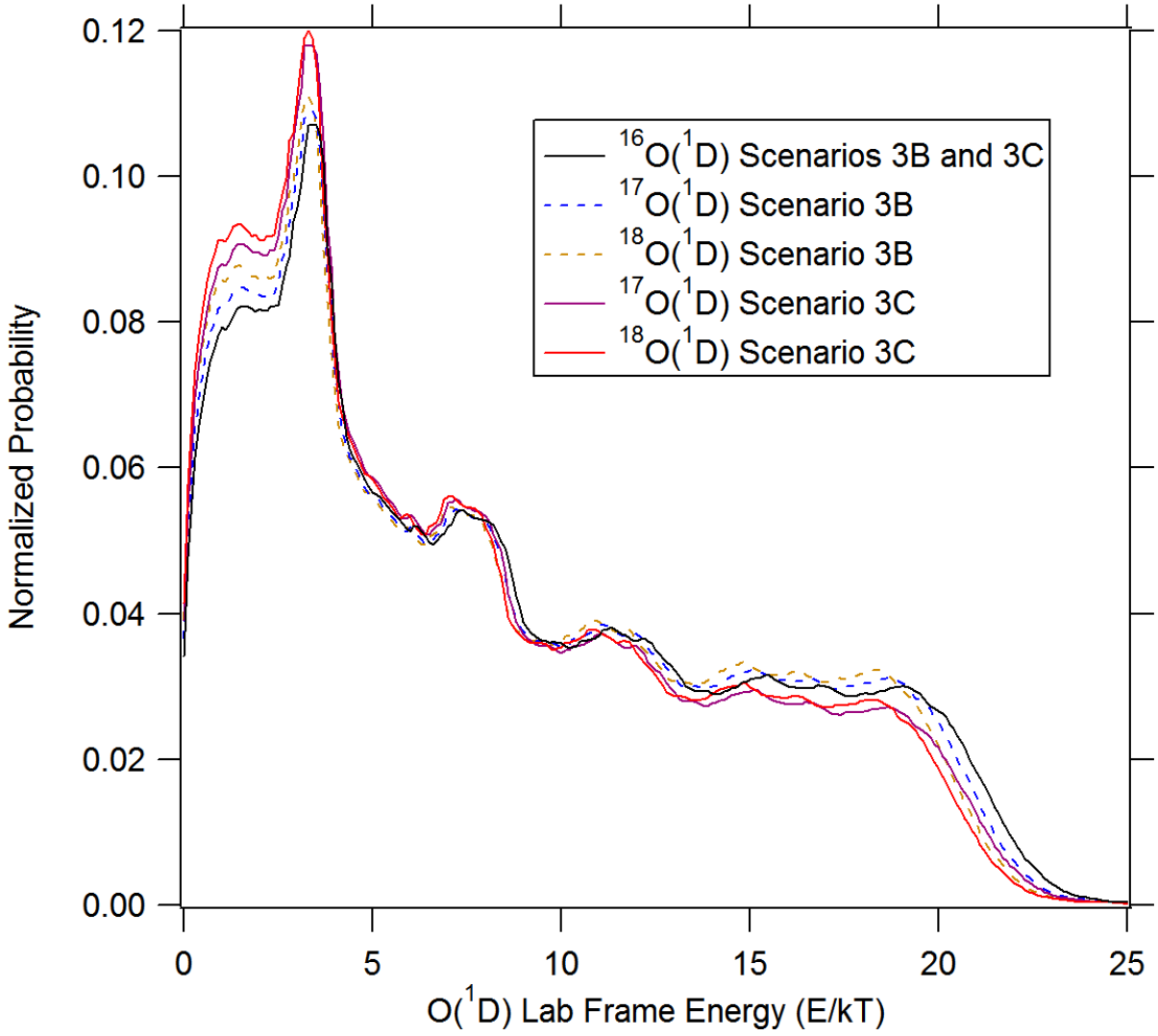

Figure 3-9. Calculated translational energy distributions of $^{16}O(^1D)$, $^{17}O(^1D)$, and $^{18}O(^1D)$ for Scenario 3B (halved elastic cross section) and Scenario 3C (halved elastic cross section and doubled inelastic cross section) at $\rho = 0.01$. The differences between the translational energy distributions for $^{16}O(^1D)$ for Scenarios 3B and 3C are very small, while the differences for $^{17}O(^1D)$ and $^{18}O(^1D)$ between Scenario 3B and Scenario 3C are large.

Comparing results from Scenario 3C with those from Scenarios 3 and 3B, we infer that, in addition to a higher population of high-energy $O(^1D)$ atoms, larger divergences of the translational energy distributionss for $^{17}O(^1D)$ and $^{18}O(^1D)$ from the translational energy distribution for $^{16}O(^1D)$ also produced larger ρ dependences for the value of $\Delta^{17}O_{O2}(CO_2)$. In Scenario 3C, doubling the inelastic scattering cross section for collisions between $O(^1D)$ and CO_2 did not have much effect on the translational energy distribution for $^{16}O(^1D)$ at any ρ. However, at lower values of ρ, the translational energy distributions for $^{17}O(^1D)$ and $^{18}O(^1D)$ both shifted towards lower kinetic energies because of an increase in the rate of the non-quenching isotope exchange reactions of $^{16}O(^1D)$ with $C^{17}O^{16}O$ and $C^{18}O^{16}O$ (Figure 3-9). In other words, as these non-quenching $O(^1D) + CO_2$ isotope exchange reactions increased in importance as ρ decreased, they began to make an important contribution to lowering the population of high kinetic energy $^{17}O(^1D)$ and $^{18}O(^1D)$ in their translational energy distributions. When the translational energy distributions were integrated to yield the non-thermal rate coefficients used in Scenario 3C, the larger divergence in the translational energy distrbituions of $^{17}O(^1D)$ and $^{18}O(^1D)$ from the translational energy distribution of $^{16}O(^1D)$ resulted in a ρ dependence in which the value of $\Delta^{17}O_{O2}(CO_2)$ decreased by 10.0‰ from $\rho = 1000$ to $\rho = 0.01$ (see Table 3-8). This ρ dependence in the value of $\Delta^{17}O_{O2}(CO_2)$ was the largest of all of the model scenarios results reported here, although it was still 5 times smaller than the results of the experiments (-49.9‰).

In addition to all the model scenarios and results described above, a number of other mechanisms were also tested as scenarios in the photochemical model, including CO_2 photolysis and isotope effects in CO + OH (to test for any effect of trace water contaminants in the experiments), among others. Of these mechanisms tested, none of them produced a significant decrease in $\Delta^{17}O_{O2}(CO_2)$ with decreasing ρ, except for Scenario 3. In Scenario 3, non-thermal rate coefficients for all the reactions of $O(^1D)$ with other species were included, and the inclusion of these non-thermal rate coefficients produced non-mass-dependently fractionated CO_2 even when the ozone KIEs were set to 1. As such, it is useful to investigate the Scenario 3 results further.

Comparing the model sensitivities to different scenarios, including and not including isotope-specific non-thermal rate coefficients for all the reactions of $O(^1D)$, thee calculated non-thermal rate coefficients led to a ρ dependence in the value of $\Delta^{17}O_{O2}(CO_2)$ for two different reasons. First, non-quenching isotope exchange between $O(^1D)$ and CO_2 (R4) became a much more important reaction at low ρ because of the larger population of high kinetic energy $O(^1D)$ in CO_2-dominated mixtures. The population of high kinetic energy $O(^1D)$ was larger since energy transfer from $O(^1D)$ to CO_2 in elastic collisions is less efficient than to O_2 due to the larger relative mass difference between $O(^1D)$ and CO_2 than between $O(^1D)$ and O_2 Second, the translational energy distributions of $^{17}O(^1D)$ and $^{18}O(^1D)$ diverged from the translational energy distribution of $^{16}O(^1D)$ towards much lower energies as ρ decreased. When the isotope-specific kinetic energy distributions were then integrated with the energy dependence of the branching ratios to calculate the rate coefficients for $O(^1D) + CO_2$ isotope exchange (and for other reactions of $O(^1D)$), the non-quenching $O(^1D) + CO_2$ isotope exchange reaction (R4) produced "colder" $^{17}O(^1D)$ and $^{18}O(^1D)$ that both had slower loss rates from $O(^1D) + CO_2$ isotope exchange than the loss rate from $O(^1D) + CO_2$ isotope exchange for the "hotter" $^{16}O(^1D)$. The combination of the high population of high kinetic energy $O(^1D)$ in the translation energy distributions and the divergence of the translational energy distributions of $^{17}O(^1D)$ and $^{18}O(^1D)$ from the distribution of $^{16}O(^1D)$ at low ρ led to the ρ-dependence of $\Delta^{17}O_{O2}(CO_2)$ in the Scenario 3 model results, as described in more detail below.

We can explore the first effect as follows. Because of the larger population of high kinetic energy $O(^1D)$ in a CO_2-dominated mixture, the non-quenching $O(^1D) + CO_2$ isotope exchange reaction (R4) became a more important reaction pathway at low ρ than at high ρ. For example, the calculated non-thermal rate coefficient for the non-quenching isotope exchange $^{16}O(^1D) + C^{16}O^{16}O$ increased by a factor of ~3 from 1.36×10^{-11} cm^3 s^{-1} at ρ = 1000 to 3.83×10^{-11} cm^3 s^{-1} at ρ = 0.01. While the non-thermal rate coefficient increased at least in part due to the higher collision frequencies at the higher translational energies, the rate coefficient also increased the branching ratio of the non-quenching $O(^1D) + CO_2$ isotope exchange reaction from 9.7% at ρ = 1000 to 18.8% at ρ = 0.01. Importantly, the increase in the non-thermal rate coefficient and in the concentration of CO_2 at low ρ for a given total pressure increased the rates of both (R19) and (R20) so that they produced $^{17}O(^1D)$ and $^{18}O(^1D)$ at rates comparable to the rates from ozone photolysis.

(R19) $^{16}O(^1D) + C^{17}O^{16}O \rightarrow {}^{17}O(^1D) + C^{16}O^{16}O$

(R20) $^{16}O(^1D) + C^{18}O^{16}O \rightarrow {}^{18}O(^1D) + C^{16}O^{16}O$

Under the same conditions, however, the reverse reactions (R21) and (R22) did not lead to a significant change in the production rate for $^{16}O(^1D)$, as the production rate from ozone photolysis is still orders of magnitude larger.

(R21) $^{17}O(^1D) + C^{16}O^{16}O \rightarrow {}^{16}O(^1D) + C^{16}O^{16}O$

(R22) $^{18}O(^1D) + C^{16}O^{16}O \rightarrow {}^{16}O(^1D) + C^{16}O^{16}O$

The relative rates for these reactions as a function of ρ in Scenario 3 are shown in Figure 3-10. At ρ = 0.01, the production rate of $^{17}O(^1D)$ from ozone photolysis was 1.55×10^8 cm^{-3} s^{-1} while the production rate from non-quenching $O(^1D) + CO_2$ isotope exchange (R19) was 2.30×10^7 cm^{-3} s^{-1}, so the two production rates of $^{17}O(^1D)$ were within an order of magnitude. Indeed, for both $^{17}O(^1D)$ and $^{18}O(^1D)$, the rates of non-quenching $O(^1D) + CO_2$ isotope exchange were each approximately 13% of the total production rate of $O(^1D)$ at ρ = 0.01 (Figure 3-10). In contrast, at ρ = 0.01 the production rate of $^{16}O(^1D)$ from ozone photolysis was 3.98×10^{11} cm^{-3} s^{-1} while the production rate of $^{16}O(^1D)$ from the non-quenching $O(^1D) + CO_2$ isotope exchange reaction (R21) was 2.26×10^7 cm^{-3} s^{-1}, so the two production rates of $^{16}O(^1D)$ were different by 4 orders of magnitude even at small ρ. Notably, the non-quenching $O(^1D) + CO_2$ isotope exchange reactions started to yield significant production rates for $^{17}O(^1D)$ and $^{18}O(^1D)$ compared to O_3 photolysis (i.e. >1% of the total $O(^1D)$ production rate) at ρ < 10, where the ρ dependence for $\Delta^{17}O_{O2}(CO_2)$ started to occur in the experiments.

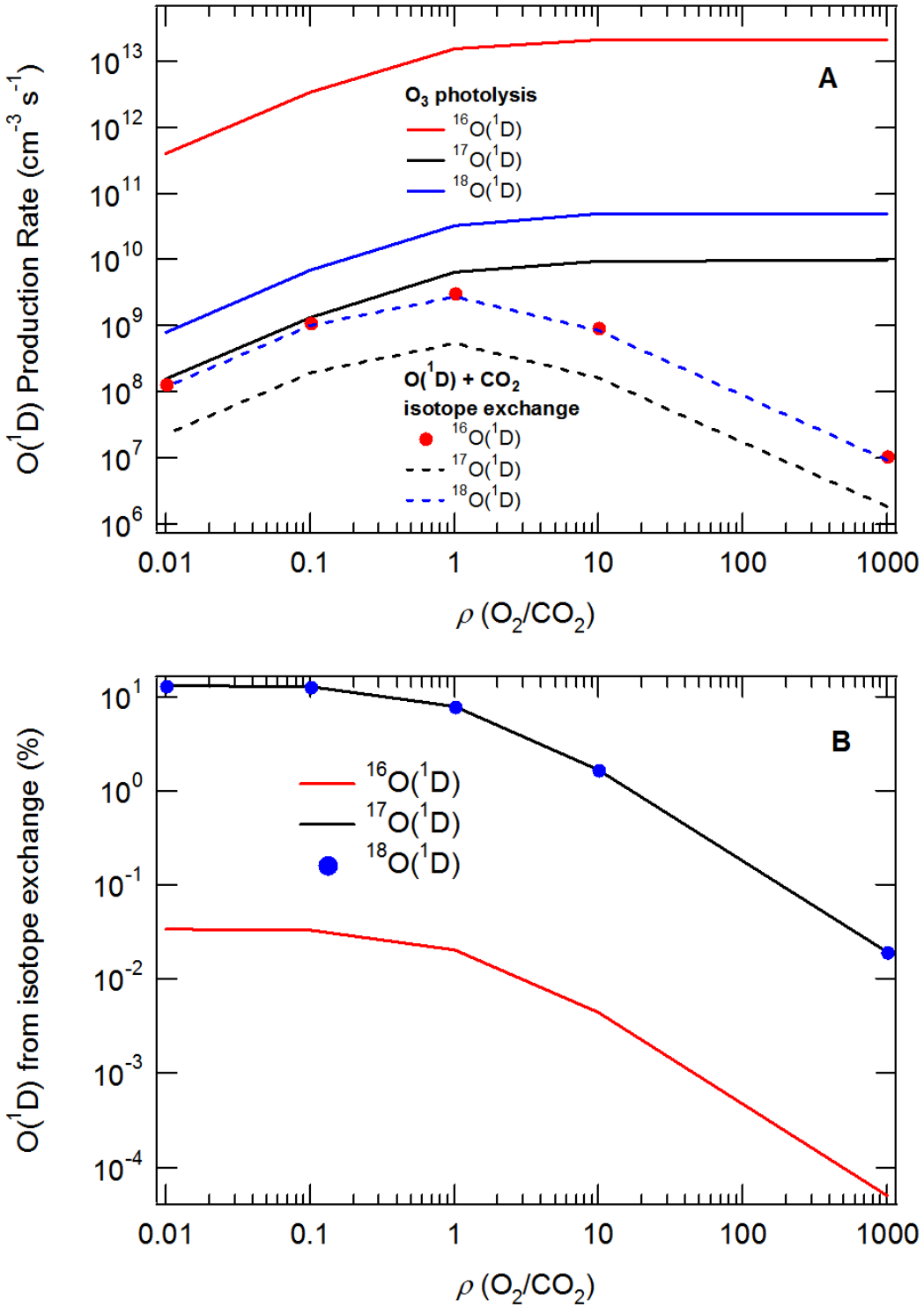

Figure 3-10. (**A**) The production rates for $^{16}O(^1D)$, $^{17}O(^1D)$, and $^{18}O(^1D)$ from O_3 photolysis and for the non-quenching $O(^1D) + CO_2$ isotope exchange reaction in Scenario 3, and (**B**) the percentage of $O(^1D)$ production from the non-quenching $O(^1D) + CO_2$ isotope exchange reaction as a total of the O_3 photolysis and non-quenching $O(^1D) + CO_2$ isotope exchange reaction.

However, simply increasing the relative importance of the non-quenching $O(^1D) + CO_2$ isotope exchange reactions, as in Scenario 2, still did not produce a ρ dependence for $\Delta^{17}O_{O2}(CO_2)$ in the model results, as the ρ dependence for $\Delta^{17}O_{O2}(CO_2)$ in Scenario 2 was essentially the same as that for the base scenario. Thus, an additional effect of the non-thermal kinetic energy distributions for $O(^1D)$ used to calculate the non-thermal rate coefficients in addition to simply increasing relative importance of the non-quenching $O(^1D) + CO_2$ isotope exchange at low ρ must also be necessary to account for the larger ρ-dependence in the Scenario 3 results. Rather, the magnitude of the ρ dependence for $\Delta^{17}O_{O2}(CO_2)$ calculated in the various scenarios is largest for those scenarios with the largest divergences for the kinetic energy distributions for $^{17}O(^1D)$ and $^{18}O(^1D)$ from the distribution of $^{16}O(^1D)$ (see, e.g., Figure 3-9). For model scenarios 3 and 3A through 3E, the divergence in the kinetic energy distributions for $^{16}O(^1D)$, $^{17}O(^1D)$, and $^{18}O(^1D)$ depended on the differences in mass as in, for example, ozone photolysis where $^{16}O(^1D)$, $^{17}O(^1D)$, and $^{18}O(^1D)$ carry 32/48, 32/49, and 32/60 of the center-of-mass energy from ozone photolysis, respectively (see Eq. (2) and Figure 3-3). In addition to differences in mass in the products of O_3 photolysis, the non-quenching $O(^1D) + CO_2$ isotope exchange reactions (R19) and (R20) of $^{16}O(^1D)$ with ^{17}O- or ^{18}O-substituted CO_2 led to greater production of less energetic $^{17}O(^1D)$ and $^{18}O(^1D)$, and thus the distributions of $^{17}O(^1D)$ and $^{18}O(^1D)$ diverged even more from the distribution of $^{16}O(^1D)$ towards lower kinetic energies when these non-quenching reactions were included. In turn, because the distributions for $^{17}O(^1D)$ and $^{18}O(^1D)$ exhibited even lower populations of high energy $O(^1D)$ atoms, both the collision frequency with CO_2 and the branching ratio of non-quenching to quenching isotope exchange decreased for $^{17}O(^1D)$ and $^{18}O(^1D)$ compared with $^{16}O(^1D)$. Due to this decrease in the frequency of collisions of $^{17}O(^1D)$ and $^{18}O(^1D)$ with CO_2 and in the branching ratios for non-quenching to quenching in the $O(^1D) + CO_2$ isotope exchange reactions, the non-quenching isotope exchange reactions (R21) and (R22) removed less $^{17}O(^1D)$ and $^{18}O(^1D)$ than the $^{17}O(^1D)$ and $^{18}O(^1D)$ produced from the non-quenching isotope exchange reactions (R19) and (R20). For example, in Scenario 3 at $\rho = 0.01$, the rate of production of $^{18}O(^1D)$ from (R20) was 1.19×10^8 cm^{-3} s^{-1}, while the loss rate of $^{18}O(^1D)$ from (R22) was 1.10×10^8 cm^{-3} s^{-1}. The loss rates of $^{17}O(^1D)$ and $^{18}O(^1D)$ from non-quenching $O(^1D) + CO_2$ isotope exchange both decreased due to their "colder" distributions but the loss rate of $^{16}O(^1D)$ did not decrease, so these reductions in the loss rates of both $^{17}O(^1D)$ and $^{18}O(^1D)$ caused non-mass-dependent fractionation for each of the non-thermal scenarios as a function of ρ.

Of the non-thermal model Scenarios 3 and 3A through 3E, Scenario 3C produced the largest ρ dependence for $\Delta^{17}O_{O2}(CO_2)$ because the translational energy distributions for $^{17}O(^1D)$ and $^{18}O(^1D)$ diverged the most from the distribution for $^{16}O(^1D)$ (see Figure 3-9). The larger divergence of the isotope-specific $O(^1D)$ kinetic energy distributions not only reduced the loss rates of $^{17}O(^1D)$ and $^{18}O(^1D)$ through the non-quenching isotope exchange reactions as in Scenario 3 but also caused the collision frequencies for $^{17}O(^1D)$, and $^{18}O(^1D)$ with all other gas-phase species to decrease from the collision frequencies of $^{16}O(^1D)$ in addition to the typical mass-dependent decrease in collision frequencies. In other words, when the isotope-specific non-thermal rate coefficients were calculated by integrating over the translational energy distributions for $^{16}O(^1D)$, $^{17}O(^1D)$, and $^{18}O(^1D)$, each of the reactions with $O(^1D)$, including with O_2 and O_3, resulted in non-mass-dependent isotope fractionation in the Scenario 3C. To illustrate this, a triple isotope slope for the isotope fractionation that arises from the calculated non-thermal rate coefficients for each reaction of $O(^1D)$ from integration of these translational energy distributions

with the energy-dependent reactive cross sections and branching ratios was calculated using Equation (20).

$$\lambda = \frac{\ln\left({}^{17}k/{}^{16}k\right)}{\ln\left({}^{18}k/{}^{16}k\right)} \quad (20)$$

The triple isotope slopes for each of the non-thermal reactions of $O(^1D)$ are plotted as a function of ρ on Figure 3-11 for Scenarios 3 and 3C. For Scenario 3, the values of λ for each reaction of $O(^1D)$ shown were within the range of mass-dependent values (0.5 to 0.53). In contrast, for Scenario 3C, the values of λ started near 0.52 for the reactions with $O(^1D)$ at ρ = 1000, but by ρ = 0.01, the values of λ had increased to near 0.65 for each reaction with $O(^1D)$. At low ρ, the non-mass-dependent kinetic isotope effects for $O(^1D)$ in the $O(^1D) + CO_2$ reaction non-mass-dependently enriched $O(^1D)$, and thus eventually O_2 through subsequent quenching to $O(^3P)$ and isotope exchange with O_2. At the same time, CO_2 was non-mass-dependently depleted, leading to the largest modeled ρ-dependence for $\Delta^{17}O_{O2}(CO_2)$ (see Table 3-8). Notably, the non-mass-dependent KIEs were generated from reactions that are typically mass-dependent at any given kinetic energy but became non-mass-dependent when the differences between the kinetic energy distributions for $^{16}O(^1D)$, $^{17}O(^1D)$, and $^{18}O(^1D)$ are accounted for.

Given that the inelastic non-quenching isotope exchange reaction between $O(^1D)$ and CO_2 (R4) played a critical role in generating a ρ-dependence for $\Delta^{17}O_{O2}(CO_2)$ in Scenario 3C and that the hard sphere approximation underestimates the inelastic collision cross sections, more accurate calculations of inelastic scattering in isotope exchange collisions might lead to larger ρ dependences in for $\Delta^{17}O_{O2}(CO_2)$ than the approximate calculations performed here. As such, semi-classical or quantum mechanical calculations of the collisions between $O(^1D)$ and CO_2 using the CO_3* potential energy surface[23] such as those done for $N+N_2$ scattering[59] could lead to a more accurate collision kernel $B(x'|x)$ that is needed for calculating the non-thermal kinetic energy distributions. If the new collision kernel for $O(^1D)$ and CO_2 from such scattering calculations results in greater divergences between the kinetic energy distributions of $^{17}O(^1D)$ and $^{18}O(^1D)$ and the distribution of $^{16}O(^1D)$, then the ρ dependence for $\Delta^{17}O_{O2}(CO_2)$ predicted by the non-thermal scenarios in the kinetics model, which ranges from ≈3‰ to ≈10‰ from ρ = 1000 to ρ = 0.01, might be much closer to the experimentally observed ρ dependence of ~50‰ from $\rho \approx 450$ to $\rho \approx 0.1$.

The initial kinetic energy distribution used in the calculation of the translational energy distributions for $^{16}O(^1D)$, $^{17}O(^1D)$, and $^{18}O(^1D)$ may also not be accurate under these experimental conditions because O_3 was continuously being formed and destroyed in the photochemistry bulb. As such, the O_3 in these experiments could have a non-thermal vibrational distribution because the rovibrationally excited O_3* initially formed in (R1) does not start to relax to the ground state until after 50 μs.[60] With a greater population of vibrationally excited O_3, the initial translational energy of $O(^1D)$ produced from O_3 photolysis at 254 nm in these experiments could be much "hotter" than $O(^1D)$ produced from photolysis of ground-state O_3 at 254 nm. Based on the results of Scenario 3D (Table 3-8) in which the initial kinetic energy distribution for $O(^1D)$ from O_3 photolysis at 245 nm was used, the change to the ρ dependence in the value of $\Delta^{17}O_{O2}(CO_2)$ from a "hotter" initial energy distribution for $O(^1D)$ might not be large. However, with more accurate inelastic scattering, a greater population of high energy $O(^1D)$ might lead to more non-quenching $O(^1D) + CO_2$ isotope exchange and thus a larger divergence between the energy distributions of $^{17}O(^1D)$ and $^{18}O(^1D)$ and the distribution of $^{16}O(^1D)$.

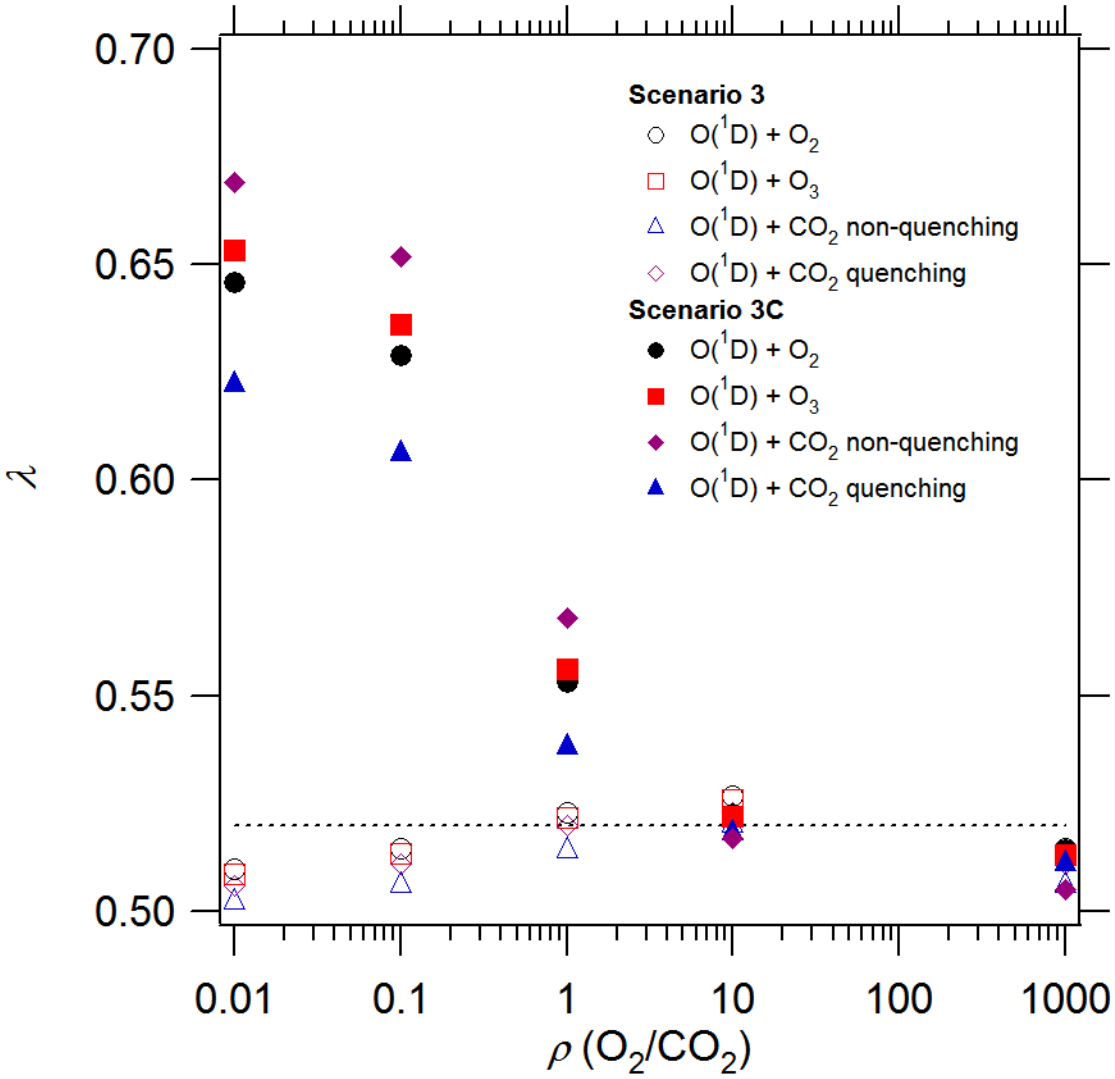

Figure 3-11. Values for the triple isotope slope, λ, calculated using Eq. (19) for each of the reactions of $O(^1D)$ as a function of the mixing ratio ρ for Scenario 3 and Scenario 3C. For Scenario 3C, the large divergences in the translational energy distributions for $^{17}O(^1D)$ and $^{18}O(^1D)$ from the translational energy distribution for $^{16}O(^1D)$ lead to non-mass-dependent values for λ from an increased divergence of the translational energy distributions of $^{17}O(^1D)$ and $^{18}O(^1D)$ from the distribution of $^{16}O(^1D)$ towards lower energies (see Figure 3-9). The dotted line is the approximate mass-dependent value (0.52) for λ for reference.

Due to inaccuracies in the hard sphere approximation used for calculating the non-thermal kinetic energy distributions of the isotopes of $O(^1D)$, additional experiments that measure the ρ dependence of the isotopic composition of CO_2 relative to O_2 using different UV lamps, buffer gases, or sources of $O(^1D)$ could provide additional constraints on the possible mechanisms that lead to the observed ρ dependence. To date, all published experiments studying the photochemical transfer of the isotope anomaly from O_3 to CO_2 have been conducted with mercury lamps that have primary emission lines at 185 nm and 254 nm.[12,18–20,61] Because a large population of high energy $O(^1D)$ was necessary to generate a ρ dependence in the model, experiments conducted with UV lamps having shorter and longer wavelengths that produce $O(^1D)$ at higher and lower translational energies or different chemical sources of $O(^1D)$ such as N_2O should also be performed. If the experimentally observed ρ-dependence is related strongly to the non-thermal character of the $O(^1D)$, then experiments in which $O(^1D)$ at lower energies is produced should have a much less pronounced ρ-dependence, and experiments that produce $O(^1D)$ at higher energies should have a more sensitive ρ-dependence. In addition to different lamps or different sources of oxygen atoms, such as N_2O, experiments that use a buffer gas that is more effective at thermalizing $O(^1D)$ than CO_2 might also reduce the population of high energy $O(^1D)$ and thus also generate a less sensitive ρ dependence.

Because the ρ-dependence of the non-mass-dependent isotopic composition of CO_2 relative to O_2 may not be wholly related to the KIEs in O_3 formation, we infer that other non-thermal isotope exchange reactions might also produce non-mass-dependent isotope effects. For example, Yeung et al.[47] suggested that the non-thermal $O(^3P) + CO_2$ isotope exchange reaction could be partially responsible for the ρ-dependence of the isotopic composition of CO_2 in the experiments of Shaheen et al.[18] Since O_3 photolysis near 254 nm and 185 nm also produces $O(^3P)$ with excess translational energy at ~50 [62] and ~70 kcal/mol, [63] respectively, the $O(^3P)$ atoms could have enough energy to overcome the ~25kcal/mol energy barrier to this reaction. Non-thermal $O(^3P) + CO_2$ isotope exchange could in principle lead to steady-state isotope-specific kinetic energy distributions for which the kinetic energy distributions of $^{17}O(^3P)$ and $^{18}O(^3P)$ diverge from the distribution of $^{16}O(^3P)$ in a similar manner to the calculations performed in this chapter. However, we developed a hard sphere collisional model for $O(^3P)$ similar to the one used for $O(^1D)$, and our preliminary calculations of the translational energy distributions for $^{16}O(^3P)$, $^{17}O(^3P)$, and $^{18}O(^3P)$ showed that the population of high energy $O(^3P)$ was negligible ($<10^{-10}$ %) for the experimental conditions reported here or for the experiments of Shaheen et al.[18] Thus, the non-thermal rate coefficients for $O(^3P) + CO_2$ isotope exchange calculated from the cross sections in Yeung et al.[47] were also very small at ~10^{-24} cm^3 s^{-1} for $\rho = 0.01$. This small rate coefficient produces a rate of ~10 cm^{-3} s^{-1} for the $^{16}O(^3P) + CO_2$ isotope exchange reaction at $\rho = 0.01$, compared with a rate of ~10^8 cm^{-3} s^{-1} for the $^{16}O(^1D) + CO_2$ isotope exchange reaction. However, as in the calculations for $O(^1D)$, the hard sphere collision kernel overestimates large energy transfers for elastic collisions especially for high energy collisions,[59] leading to an underestimate of the amount of non-thermal $O(^3P)$ and thus the rate coefficient for the $O(^3P) + CO_2$ isotope exchange reaction. These results suggest, though, that at least for the experiments reported here, the non-thermal $O(^3P) + CO_2$ isotope exchange reaction is unlikely to produce a ρ dependence in $\Delta^{17}O_{O2}(CO_2)$, although with different UV lamps or sources of $O(^3P)$, such as the ones suggested above, non-thermal isotope exchange between $O(^3P)$ and CO_2 may still be potentially important.

Given the possibility of non-mass-dependent isotope effects in other non-thermal oxygen atom isotope exchange reactions, understanding the ρ-dependence for $\Delta^{17}O_{O2}(CO_2)$ is important

not only for providing a more mechanistic understanding of the chemical physics of non-mass-dependent isotope effects but perhaps also for applications to planetary atmospheres such as on Mars[64] and Venus in which CO_2 is the dominant species. Ozone has been observed in the Martian atmosphere since the 1970s [65] and more recently in the Venusian atmosphere,[66] but, in contrast to Earth's atmosphere, CO_2 photolysis is the primary source of O_2 and O_3 in the atmospheres of Venus and Mars.[67] UV photolysis of O_3 or other trace gases produced in these atmospheres could lead to significant non-thermal $O(^1D)$ (or $O(^3P)$) distributions that could potentially have unusual isotope effects when undergoing isotope exchange with CO_2. However, the isotopic composition of CO_2 itself is unlikely to be non-mass-dependent since the measurements in the experiments at low ρ do not show only a small increase (~10‰) in the isotopic composition of CO_2 relative to VSMOW (see Table 3-5) and since ρ is much lower on Mars or Venus than in the experiments here. Other trace species related to ozone and carbon dioxide such as O_2 might potentially have unusual isotopic signatures beyond those from the non-mass-dependent KIEs in ozone formation.

3.4. Conclusions

The results from new experiments in which mixtures of O_2 and CO_2 were irradiated with UV light from a mercury lamp clearly showed the dependence of the ^{17}O isotope anomaly in CO_2 relative to O_2, or $\Delta^{17}O_{O2}(CO_2)$, on ρ, the O_2/CO_2 mixing ratio, at two different total pressures of 50 Torr and 170 Torr. These experiments expanded the number of available measurements of the ρ dependence for $\Delta^{17}O_{O2}(CO_2)$, particularly near where $\Delta^{17}O_{O2}(CO_2)$ is changing most rapidly. While a kinetics model of the reaction system could predict the relative isotope enrichments at high ρ relevant to the Earth's atmosphere,[12] as shown in Chapter 2, the base model could not predict the decrease in the value of $\Delta^{17}O_{O2}(CO_2)$ with decreasing ρ due to expected changes in the ozone formation KIEs alone. A number of mechanisms with potential ρ dependences for $\Delta^{17}O_{O2}(CO_2)$ were tested in the model using different model scenarios. However, only model scenarios that included non-thermal rate coefficients for reactions of $O(^1D)$ with other species, calculated from integration of non-thermal kinetic energy distributions for $^{16}O(^1D)$, $^{17}O(^1D)$, and $^{18}O(^1D)$ calculated using a hard sphere model and the energy dependence of the reactive cross sections and branching ratios, resulted in any ρ dependence for $\Delta^{17}O_{O2}(CO_2)$.

Analysis of the translational energy distributions and model kinetics showed that this non-mass-dependent fractionation of oxygen isotopes in CO_2 arises from the divergence of the translational energy distributions for $^{17}O(^1D)$ and $^{18}O(^1D)$ from the distribution for $^{16}O(^1D)$. The divergence was created by the production of lower kinetic energy $^{17}O(^1D)$ and $^{18}O(^1D)$ atoms from the non-quenching isotope exchange reactions of $^{16}O(^1D)$ with $C^{17}O^{16}O$ and $C^{18}O^{16}O$. These non-quenching isotope exchange reactions occurred at significant rates compared to the production of $O(^1D)$ from O_3 photolysis at low ρ because the concentration of CO_2 is high and the $O(^1D)$ kinetic energy distributions have a greater population of high kinetic energy $O(^1D)$ due to the lower $O(^1D)$ translational energy quenching efficiency for CO_2 than for O_2. The divergence of the kinetic energy distributions for $^{17}O(^1D)$ and $^{18}O(^1D)$ from the distribution for $^{16}O(^1D)$ reduced the loss rates for $^{17}O(^1D)$ and $^{18}O(^1D)$ through the non-quenching $O(^1D) + CO_2$ isotope exchange reaction but not for $^{16}O(^1D)$, leading to non-mass-dependent fractionation. Furthermore, results for an additional model scenario in which these non-thermal rate coefficients for the reactions of $O(^1D)$ were used but with the KIEs for ozone formation set to 1 suggested that the ρ dependence in the value of $\Delta^{17}O_{O2}(CO_2)$ was not entirely related to the non-mass-dependent KIEs in ozone formation. As such, non-thermal isotope exchange reactions in

other systems may in principle also produce non-mass-dependent isotope fractionation through reactions that are mass-dependent under thermal conditions. Interestingly, in a model scenario in which the rates for the inelastic non-quenching $O(^1D) + CO_2$ isotope exchange reactions were doubled, the divergence of the translational energy distributions for $^{17}O(^1D)$ and $^{18}O(^1D)$ from the distribution for $^{16}O(^1D)$ became large enough to generate non-mass-dependent isotope effects in all reactions between $O(^1D)$ and the other gases in the reaction mixture. These results suggest that a more accurate collisional energy transfer model for inelastic isotope exchange between $O(^1D)$ and CO_2 should be used to investigate the robustness and magnitude of this latter effect. While the results from the model scenarios in which these calculated non-thermal rate coefficients for the reactions of $O(^1D)$ are factors of 5 to 10 smaller than the ρ dependence for $\Delta^{17}O_{O2}(CO_2)$ experiments, this mechanism was the only one of the many tested that created any significant ρ dependence in the model. Non-thermal rate coefficients used in the model scenarios here are also a novel mechanism for producing non-mass-dependent isotope fractionation that has not, to our knowledge, been described before. While the isotope fractionation studied here in the $O(^1D) + CO_2$ isotope exchange reaction may only have limited relevance to the ^{17}O isotope anomaly in CO_2 in Earth's atmosphere due to the high O_2/CO_2 mixing ratio, they could potentially be important for oxygen-containing trace species in planetary atmospheres that primarily contain CO_2, such as those on Mars and Venus.

References

[1] J. Bigeleisen and M.G. Mayer, J. Chem. Phys. **15**, 261 (1947).

[2] M.F. Miller, Geochim. Cosmochim. Acta **66**, 1881 (2002).

[3] C. a M. Brenninkmeijer, C. Janssen, J. Kaiser, T. Röckmann, T.S. Rhee, and S.S. Assonov, Chem. Rev. **103**, 5125 (2003).

[4] M.H. Thiemens, Annu. Rev. Earth Planet. Sci. **34**, 217 (2006).

[5] E. Barkan and B. Luz, Rapid Commun. Mass Spectrom. **26**, 2733 (2012).

[6] M.E.G. Hofmann and A. Pack, Anal. Chem. **82**, 4357 (2010).

[7] J. Kaiser and T. Röckmann, Rapid Commun. Mass Spectrom. **22**, 3997 (2008).

[8] M.H. Thiemens, T. Jackson, E.C. Zipf, P.W. Erdman, and C. Van Egmond, Science **270**, 969 (1995).

[9] B. Alexander, M.K. Vollmer, T. Jackson, and R.F. Weiss, J. Geophys. Res. **28**, 4103 (2001).

[10] P. Lämmerzahl, T. Röckmann, C.A.M. Brenninkmeijer, D. Krankowsky, and K. Mauersberger, Geophys. Res. Lett. **29**, 1582 (2002).

[11] S. Kawagucci, U. Tsunogai, S. Kudo, F. Nakagawa, H. Honda, S. Aoki, T. Nakazawa, M. Tsutsumi, and T. Gamo, Atmos. Chem. Phys. **8**, 6189 (2008).

[12] A.A. Wiegel, A.S. Cole, K.J. Hoag, E.L. Atlas, S.M. Schauffler, and K.A. Boering, Proc. Natl. Acad. Sci. U. S. A. **110**, 17680 (2013).

[13] Y.L. Yung, a Y. Lee, F.W. Irion, W.B. DeMore, and J. Wen, J. Geophys. Res. **102**, 10857 (1997).

[14] M.J. Perri, A.L. Van Wyngarden, K.A. Boering, J.J. Lin, and Y.T. Lee, J. Chem. Phys. **119**, 8213 (2003).

[15] M.J. Perri, A.L. Van Wyngarden, J.J. Lin, Y.T. Lee, and K.A. Boering, J. Phys. Chem. A **108**, 7995 (2004).

[16] K. Mauersberger, B. Erbacher, D. Drankowsky, J. Gunther, and R. Nickel, Science **283**, 370 (1999).

[17] C. Janssen, J. Guenther, K. Mauersberger, and D. Krankowsky, Phys. Chem. Chem. Phys. **3**, 4718 (2001).

[18] R. Shaheen, C. Janssen, and T. Röckmann, Atmos. Chem. Phys. **7**, 495 (2007).

[19] J. Wen and M.H. Thiemens, J. Geophys. Res. **98**, 12801 (1993).

[20] J.C. Johnston, T. Röckmann, and C.A.M. Brenninkmeijer, J. Geophys. Res. **105**, 15213 (2000).

[21] J. Guenther, D. Krankowsky, and K. Mauersberger, Chem. Phys. Lett. **324**, 31 (2000).

[22] K.L. Feilberg, A.A. Wiegel, and K.A. Boering, Chem. Phys. Lett. **556**, 1 (2013).

[23] A.M. Mebel, M. Hayashi, V. V. Kislov, and S.H. Lin, J. Phys. Chem. A **108**, 7983 (2004).

[24] S.M. Dylewski, J.D. Geiser, and P.L. Houston, J. Chem. Phys. **115**, 7460 (2001).

[25] K. Takahashi, N. Taniguchi, Y. Sato, and Y. Matsumi, J. Geophys. Res. **107**, 4290 (2002).

[26] V. Kharchenko and A. Dalgarno, J. Geophys. Res. **109**, 1 (2004).

[27] J.C. Ianni, *A Comparison of the Bader-Deuflhard and the Cash-Karp Runge-Kutta Integrators for the GRI-MECH 3.0 Model Based on the Chemical Kinetics Code Kintecus* (2003), pp. 1368–1372.

[28] S.S. Assonov and C.A.M. Brenninkmeijer, Rapid Commun. Mass Spectrom. **15**, 2426 (2001).

[29] C.A.M. Brenninkmeijer and T. Röckmann, Anal. Chem. **68**, 3050 (1996).

[30] S.S. Assonov and C.A.M. Brenninkmeijer, Rapid Commun. Mass Spectrom. **17**, 1017 (2003).

[31] S.P. Sander, R.R. Friedl, J.R. Barker, D.M. Golden, M.J. Kurylo, G.E. Sciences, P.H. Wine, J.P.D. Abbatt, J.B. Burkholder, C.E. Kolb, G.K. Moortgat, R.E. Huie, and V.L. Orkin, JPL Publ. **10-6**, (2011).

[32] H. Okabe, *Photochemistry of Small Molecules* (1978), p. 431.

[33] K. Yoshino, J.R. Esmond, A.S.-C. Cheung, D.E. Freeman, and W.H. Parkinson, Planet. Space Sci. **40**, 185 (1991).

[34] P. Fleurat-Lessard, S.Y. Grebenshchikov, R. Schinke, C. Janssen, and D. Krankowsky, J. Chem. Phys. **119**, 4700 (2003).

[35] J.A. Kaye and D.F. Strobel, J. Geophys. Res. **88**, 8447 (1983).

[36] A.S. Cole and K.A. Boering, J. Chem. Phys. **125**, 184301 (2006).

[37] M.H. Thiemens and T. Jackson, Geophys. Res. Lett. **15**, 639 (1988).

[38] M.H. Thiemens and T. Jackson, Geophys. Res. Lett. **17**, 717 (1990).

[39] J. Morton, J. Barnes, B. Schueler, and K. Mauersberger, J. Geophys. Res. **95**, 901 (1990).

[40] J. Guenther, B. Erbacher, D. Krankowsky, and K. Mauersberger, Chem. Phys. Lett. **306**, 209 (1999).

[41] G. Michalski and S.K. Bhattacharya, Proc. Natl. Acad. Sci. U. S. A. **106**, 5493 (2009).

[42] K. Luther, K. Oum, and J. Troe, Phys. Chem. Chem. Phys. **7**, 2764 (2005).

[43] S. Chakraborty and S.K. Bhattacharya, J. Chem. Phys. **118**, 2164 (2003).

[44] B. Shizgal and M.J. Lindenfeld, Planet. Space Sci. **27**, 1321 (1979).

[45] K. Stamnes, Ø. Lie-Svendsen, and M.H. Rees, Planet. Space Sci. **39**, 1436 (1991).

[46] V. Kharchenko, N. Balakrishnan, and a. Dalgarno, J. Atmos. Solar-Terrestrial Phys. **60**, 95 (1998).

[47] L.Y. Yeung, M. Okumura, J. Zhang, T.K. Minton, J.T. Paci, A. Karton, J.M.L. Martin, J.P. Camden, and G.C. Schatz, J. Phys. Chem. A **116**, 64 (2012).

[48] J.O. Hirschfelder, C.F. Curtiss, and R.B. Bird, *Molecular Theory of Gases and Liquids* (John Wiley & Sons; Inc., New York, 1964).

[49] J.O. Hirschfelder and W.J. Meath, in *Adv. Chem. Phys.*, edited by J.O. Hirschfelder (Interscience Publishers, New York, 1967).

[50] G. Némethy, M.S. Pottle, and H.A.J. Scheraga, J. Phys. Chem. **87**, 1883 (1983).

[51] H.-F. Chen, H.-C. Chiang, H. Matsui, S. Tsuchiya, and Y.-P. Lee, J. Phys. Chem. A **113**, 3431 (2009).

[52] V. Kharchenko, J. Tharamel, and A. Dalgarno, J. Atmos. Solar-Terrestrial Phys. **59**, 107 (1997).

[53] N. Taniguchi, K. Hirai, K. Takahashi, and Y. Matsumi, J. Phys. Chem. A **104**, 3894 (2000).

[54] E.C. Whipple, J. Chem. Phys. **60**, 1345 (1974).

[55] M.-C. Liang, G.A.G. Blake, and Y.L.Y. Yung, J. Geophys. Res. **109**, D10308 (2004).

[56] C. Janssen, J. Guenther, D. Krankowsky, and K. Mauersberger, Chem. Phys. Lett. **367**, 34 (2003).

[57] D. Krankowsky, P. Lämmerzahl, K. Mauersberger, C. Janssen, B. Tuzson, and T. Röckmann, J. Geophys. Res. **112**, 1 (2007).

[58] K. Andersen and K.E. Shuler, J. Chem. Phys. **633**, 633 (1964).

[59] N. Balakrishnan, V. Kharchenko, and A. Dalgarno, J. Chem. Phys. **108**, 943 (1998).

[60] J.A. Joens, J.B. Burkholder, and E.J. Bair, J. Chem. Phys. **76**, 5902 (1982).

[61] S. Chakraborty and S.K. Bhattacharya, J. Geophys. Res. **108**, 4724 (2003).

[62] M. -a. Thelen, T. Gejo, J. a. Harrison, and J.R. Huber, J. Chem. Phys. **103**, 7946 (1995).

[63] D. Stranges, X. Yang, J.D. Chesko, and A.G. Suits, J. Chem. Phys. **102**, 6067 (1995).

[64] M.H. Thiemens, T.L. Jackson, and C.A.M. Brenninkmeijer, Geophys. Res. Lett. **22**, 255 (1995).

[65] C. Barth and C. Hord, Science **173**, 197 (1971).

[66] F. Montmessin, J.-L. Bertaux, F. Lefèvre, E. Marcq, D. Belyaev, J.-C. Gérard, O. Korablev, a. Fedorova, V. Sarago, and a. C. Vandaele, Icarus **216**, 82 (2011).

[67] Y.L. Yung and W.B. DeMore, *Photochemistry of Planetary Atmospheres* (1999).

Chapter 4

Measurements and modeling of the isotopic composition of O_3 formed in air-like mixtures of O_2 and N_2

4.1. Introduction

Measurements of the oxygen isotopic composition of ozone formed in the laboratory[1–3] and in the atmosphere[4–6] revealed unusual enrichments in the two heavy, stable isotopes, ^{17}O and ^{18}O. The enrichments in ^{17}O and ^{18}O relative to ^{16}O are very large — greater than 10% compared with more typical enrichments or depletions for oxygen isotopes of 0.1-1%. Even more unusually, the isotopic composition of ozone is "non-mass-dependent", which means that the isotope enrichments in ^{17}O and ^{18}O relative to ^{16}O do not depend on the mass differences between each of the isotopes.

In most cases, kinetic and equilibrium isotope effects affect the ratios of ^{17}O and ^{18}O relative to ^{16}O such that the relationship between the $\ln^{17}O$ and $\ln^{18}O$ values form a "mass-dependent" line with a slope, λ_{MD}, of approximately 0.5 to 0.53,[7] with $\ln^{x}O$ defined in Equation (1).

$$\ln^{x}O = \ln\left[\frac{\left({}^{x}O/{}^{16}O\right)_{\text{sample}}}{\left({}^{x}O/{}^{16}O\right)_{\text{standard}}}\right] \quad (1)$$

In this equation, ^{x}O is either ^{17}O or ^{18}O, and $^{x}O/^{16}O$ is the ratio of abundances of ^{x}O and ^{16}O in the sample or standard.[8,9] The "mass-dependent" relationship between $\ln^{17}O$ and $\ln^{18}O$ with $\lambda_{MD} \approx 0.5$ is expected because isotope effects generally scale with the relative differences in molecular velocities, rotational energies, and vibrational energies of the reactants, transition states, or products that in turn scale with the differences in masses between the isotopes.[10]

For the isotopic composition of ozone, however, $\ln^{17}O$ and $\ln^{18}O$ values deviate from the mass-dependent line by a quantity $\Delta^{17}O$, called the "^{17}O isotope anomaly", defined in Equation (2).

$$\Delta^{17}O = \ln^{17}O - \lambda_{MD} \times \ln^{18}O \quad (2)$$

where λ_{MD} is the expected mass-dependent $\ln^{17}O/\ln^{18}O$ relationship for the system and typically ranges from 0.5 to 0.53 depending on the species or reactions involved, as noted above. In other words, $\Delta^{17}O$ will be non-zero for a non-mass-dependent oxygen isotopic composition. The ^{17}O isotope anomaly in ozone has been found to originate in the ozone three-body recombination reaction (R1)[11–13]

(R1) $\quad O(^3P) + O_2(^3\Sigma) \rightarrow O_3^* + M \rightarrow O_3 + M^*$

and depends on temperature[11,14], pressure[11,15–18], and the identity of the bath gas M.[18]

Measurements of the kinetic isotope effects (KIEs) in the ozone formation reaction (R1) showed that formation of some isotopologues of ozone had unusually high rate coefficient enhancements over the formation of $^{16}O^{16}O^{16}O$ as shown in (R2), (R3), and (R4).[12,13,19]

(R2) $^{18}O^{16}O + {}^{16}O + M \rightarrow {}^{18}O^{16}O^{16}O$ KIE = 1.45

(R3) $^{18}O + {}^{16}O^{16}O + M \rightarrow {}^{18}O^{16}O^{16}O$ KIE = 0.92

(R4) $^{16}O + {}^{18}O^{16}O + M \rightarrow {}^{16}O^{18}O^{16}O$ KIE = 1.08

In these measurements, the formation of asymmetrically substituted ozone isotopologues (e.g., $^{18}O^{16}O^{16}O$ in (R2) and (R3)) depended sensitively on the change in zero-point energy (ΔZPE) between the two possible reactant O_2 isotopologues (i.e., $^{16}O^{16}O$ and $^{18}O^{16}O$). In addition, the formation of symmetrically substituted ozone isotopologues (e.g., $^{16}O^{18}O^{16}O$ in (R4)) was found to have a ~18% lower rate coefficient compared with the ΔZPE trend for KIEs for formation of the asymmetric isotopologues. This difference between the formation rate coefficients for the symmetric and asymmetric complexes was termed the "η-effect", named for the *ad hoc* non-statistical correction factor η that was invoked to reduce the densities of states for symmetric O_3* complexes by 18% from the effective densities of states for asymmetric O_3* complexes, originally in semi-empirical RRKM calculations,[20–22] but later in semi-classical trajectory[23,24] calculations as well. In other words, while the formation of O_3 is non-statistical in all cases, the symmetric O_3* complexes needed a larger, additional non-statistical correction factor of 18% compared with the asymmetric O_3* complexes.

The origin of the η-effect had remained somewhat elusive; Feilberg, Wiegel, and Boering[18] and Marcus[25] give brief historical overviews up to 2012. Recently, however, a mixed approach to the collision dynamics that treats translations and rotations classically and vibrations quantum mechanically by Ivanov and Babikov[26] finally suggests a quantitatively plausible origin for the η-effect for O_3 formation. In their calculations, the substitution of a heavy oxygen isotope at one of the terminal atom positions in the excited ozone complex distorts the vibrational wave function of $^{18}O^{16}O^{16}O$ towards the formation channel for asymmetric O_3 isotopolgoues shown in (R2). For (R2), this distortion allows tunneling through the centrifugal barrier on the potential energy surface (PES) so that these vibrational O_3* states receive population from O + O_2 collisions more effectively (i.e., the vibrational O_3* states are better connected to the entrance channel). In contrast, the vibrational wave functions for the symmetric isotopologues of O_3 such as $^{16}O^{18}O^{16}O$ in (R4) are undistorted, such that tunneling through the centrifugal barrier on the O_3* PES is less effective. Because the undistorted vibrational O_3* states for symmetric O_3 isotopologues are thus only weakly connected to the the formation channel, symmetric O_3* states also receive population from O + O_2 collisions less effectively than in the formation of asymmetric O_3 isotopologues. Thus, the η-effect could be explained by the differences in the quantum mechanical tunneling rates for the O_3* complexes of the symmetric and asymmetric isopotologues. Interestingly, the η-effect is not strictly a quantum symmetry effect as had been presumed, although the symmetry of the O_3 isotopologues indirectly affects the relative rates of ozone formation through distortion of the vibrational wavefunctions.

While the recent work of Ivanov and Babikov[26] introduces the first chemical physics mechanism that appears to be able to quantitatively predict the non-mass-dependent KIEs in ozone formation from first principles, additional measurements of the isotopic composition of ozone at different pressures with different bath gases M are still needed to test this new theory in particular. Recent measurements of the isotopic composition of ozone formed in different bath gases by Feilberg, Wiegel, and Boering[18] showed that the values of $\Delta^{17}O$ of ozone formed at a given pressure followed the pattern Ar > O_2 > CO_2 > SF_6. This pattern follows the trend in values of the average energy transferred per collision with O_3* $\langle\Delta E\rangle$ of 18 cm^{-1}, 25 cm^{-1}, 150 cm^{-1}, and

280 cm^{-1}, respectively, inferred from ozone kinetics experiments for $^{16}O^{16}O^{16}O$ and assuming that the value for O_2 is similar to that for N_2.[27] Remarkably, however, the difference between $\Delta^{17}O$ values for O_3 formed in CO_2 and those formed in SF_6 was quite dramatically large, while the difference between $\Delta^{17}O$ values for O_3 formed in O_2 and those formed in CO_2 was quite small. In fact, the KIEs for ozone formation are essentially eliminated at 700 Torr of SF_6 (i.e., $\Delta^{17}O \approx 0‰$), while experiments conducted in O_2 and CO_2 at 700 Torr still have large ^{17}O isotope anomalies (i.e., $\Delta^{17}O \approx 35‰$).[18,28] This dramatic difference between O_3 formed in CO_2 and SF_6 led Feilberg, Wiegel, and Boering[18] to postulate that a $\langle\Delta E\rangle$ of 280 cm^{-1} for SF_6 (or some other collision property) allows it to bypass the most isotope-selective part of the O_3 PES in a way that other bath gases such as CO_2 do not, despite its many degrees of freedom and large $\langle\Delta E\rangle$ of 150 cm^{-1} for O_3 formation. Indeed, based on the results of the calculations of Ivanov and Babikov,[26] the larger $\langle\Delta E\rangle$ for SF_6 to stabilize O_3* complexes of 280 cm^{-1} may outcompete the faster tunneling rates for formation of asymmetric O_3* complexes from $O + O_2$ collisions, thus eliminating the η-effect and the non-mass-dependent KIEs in O_3 formation.

Feilberg, Wiegel, and Boering[18] also speculated that the differences in the ^{17}O isotope anomalies for ozone formed in the different bath gases might also be explained by differences in the relative contributions of the energy transfer (ET) and radical complex (RC) mechanisms of ozone formation between the different bath gases. In contrast to the ET mechanism for ozone formation shown in (R1), in the RC mechanism, an O_2 molecule or $O(^3P)$ atom first forms a loosely bound van der Waals complex with the bath gas M (R5 or R7, respectively) before colliding with $O(^3P)$ or O_2 to form O_3 (R6 or R8, respectively).

(R5) $O_2 + M \rightarrow O_2{\cdot}M$

(R6) $O_2{\cdot}M + O(^3P) \rightarrow O_3 + M$

(R7) $O(^3P) + M \rightarrow O(^3P){\cdot}M$

(R8) $O(^3P){\cdot}M + O_2 \rightarrow O_3 + M$

Troe and co-workers[27,29] have estimated that the RC mechanism accounts for about 40% of ozone formation at room temperature and at atmospheric pressures of N_2 and Ar versus about 60% for the ET mechanism. In addition, the contribution of the RC mechanism over the ET mechanism increases as the temperature is lowered or as the pressure is increased above 200 atm.[27,29] If the non-mass-dependent KIEs in O_3 formation are associated only with the ET mechanism, as some have postulated before[26,28–30] or have assumed in their calculations of the KIEs,[26] then the observed decrease in the value of $\Delta^{17}O$ for O_3 with decreasing temperatures[11,14] may be partially explained by a decrease in the relative contribution of the ET mechanism versus the RC mechanism with decreasing temperature. Similarly, as Feilberg, Wiegel, and Boering[18] speculated, different bath gases, M, in ozone formation might also affect the relative contributions of the ET and RC mechanisms and thus the values of $\Delta^{17}O$ for ozone through differences in the stabilities of the radical complexes in (R5) and (R7), in the rates at which these complexes form ozone in (R6) and (R8), or in both. Indeed, the trends in $\Delta^{17}O$ of ozone formed in different bath gases are inversely correlated not only with the trend in the $\langle\Delta E\rangle$ for a given bath gas for the ET mechanism but also with the expected trend for the radical complex stabilities with O_2 or $O(^3P)$: $SF_6 > CO_2 > O_2 > Ar$. A decrease in the relative contribution of the ET mechanism versus the RC mechanism for ozone formation in SF_6 could be one possible explanation for the dramatically lower $\Delta^{17}O$ values for O_3, apart from or in addition to the differences in $\langle\Delta E\rangle$ of the bath gases in the ET mechanism.

Given that differences between the properties of bath gases, such as the average energy transferred per collision, $\langle \Delta E \rangle$, for the ET mechanism or the radical-complex stabilities for the RC mechanism, could lead to differences in the effective magnitudes of the ozone formation KIEs, additional measurements of the isotopic composition of O_3 in various bath gases may provide additional clues to the origins of the dramatic difference in $\Delta^{17}O$ between ozone formed in SF_6 versus other bath gases. While additional experiments on the bath gases CF_4 and C_2F_6 are currently ongoing in our research group, a comparison of the isotopic composition of O_3 formed in an air-like mixture of N_2 and O_2 versus pure O_2 is also of interest. Small differences between the $\Delta^{17}O$ values of ozone formed in pure O_2 and in an air-like N_2/O_2 mixture at a given pressure have been measured, [11,15] although the measurements were limited by small sample sizes and large uncertainties. These differences, if real, may provide additional insight into the specifics of the bath gas dependence of the isotopic composition of ozone. Additional experiments on ozone formation in air-like N_2/O_2 mixtures, along with kinetics modeling of these experiments, may also provide new insights into other previous experiments involving ozone, including understanding the isotopic composition of ozone in ozone photolysis experiments. For example, measurements of the isotopic composition of O_3 after UV photolysis showed an increase in the three isotope slope, λ, from 0.6 to 1.0 as N_2 was added to the experiments.[31] Isotope-specific kinetics modeling of these ozone photolysis experiments by Cole and Boering[32] suggested that changes in the relative importance of unknown mass-dependent isotope effects in various reactions of O_3 with the products of O_3 photolysis as N_2 was added led to most of the observed increase in the slope. Understanding these mass-dependent isotope effects are key not only to understanding isotope effects specific to ozone but also to modeling the isotopic composition and three isotope slopes λ (although not $\Delta^{17}O$) of species that obtain their non-mass-dependent isotopic composition from O_3, such as CO_2,[33] sulfates,[34] or nitrates.[35]

To investigate the isotopic composition of O_3 formed in an air-like mixture of O_2 and N_2 further, the isotopic composition of O_3 formed in O_2 and N_2 at air-like mixing ratios was measured at several different total pressures. A kinetics model of the experiment at 40 Torr of O_2 and 160 Torr of N_2 was developed to directly compare the results of the experiments reported here with the measurements by Mauersberger and co-workers[12,13] of the KIEs for ozone formation at these same pressures of O_2 and N_2. The sensitivity of the model results to mass-dependent isotope effects in various reactions and changes in the relative importance of the ET and RC mechanisms of O_3 formation were also tested to investigate how different bath gases might affect the isotopic composition of O_3.

4.2. Methods

The apparatus (Figure 4-1) and experimental procedures used here are the similar to those used in a previous study of the isotopic composition of ozone formed in different bath gases.[18] A description of those procedures as they apply to experiments with N_2 follows. Oxygen (Scott Specialty Gases, 99.999% purity) and N_2 (Praxair, 99.999% purity) were introduced into a 2.2L borosilicate glass bulb without additional purification and were allowed to mix for 12 to 14 hours. For most experiments, N_2 and O_2 were introduced into the glass bulb until they reached an air-like mixing ratio of 80% and 20%, as measured on a Baratron capacitance manometer (MKS Instruments 627B, 1000 Torr full-scale, 0.1% accuracy), except for one set of experiments at 100 Torr with a 1:1 ratio of O_2 to N_2 (i.e. 50 Torr O_2 and 50 Torr N_2. The total pressures used in the experiments were 100 Torr, 200 Torr, 300 Torr, 500 Torr, and 700 Torr. The temperature in the

bulb was not monitored directly but was assumed to be in equilibrium with the laboratory temperature, which ranged from 18-22°C, as the bulb was not warm to the touch. Ozone formation was initiated by photodissociation of O_2 at 185 nm from a mercury/argon pen ray lamp (Oriel Instruments, Inc.) After 30 to 180 minutes, the lamp was turned off, and the ozone produced was allowed to condense into a Russian doll trap[36] at liquid nitrogen temperature. After five to ten minutes, the trap was then opened to vacuum to remove the excess O_2 and N_2. Because ozone has a significant vapor pressure at liquid nitrogen temperature (0.7 mTorr at -196ºC),[37] the trap was pumped at a rate sufficiently fast to avoid evaporation of O_3 but also slow enough to cryogenically trap O_3; both processes can introduce mass-dependent artifacts into the final measurement of the isotopic composition. After separation from O_2 and N_2 on the Russian doll trap, the O_3 was transferred cryogenically to a ~3mL glass sample tube on port D (Figure 4-1) containing nickel shavings. The sample tube was then heated to 80°C for 10 to 15 minutes to catalytically convert the O_3 to O_2. The amount of O_2 produced from O_3 was then measured manometrically in the calibrated volume of the upper vacuum line using another Baratron capacitance manometer (MKS Instruments 627B, 10 Torr full scale, 0.1% accuracy). The amount of O_2 produced in these experiments varied from approximately 20 to 80 μmol depending on the total pressure and irradiation time. The O_2 was then transferred cryogenically to another ~3mL glass sample tube on port B (Figure 4-1) containing 13X molecular sieve (Sigma Aldrich) using liquid nitrogen.

The O_2 from decomposition of the O_3 produced photochemically in the bulb was analyzed on a dual inlet Finnigan MAT 252 isotope ratio mass spectrometer to measure $\ln^{17}O$, $\ln^{18}O$, and $\Delta^{17}O$ relative to the starting O_2. The isotopic composition of the reactant O_2 was $\ln^{17}O$=13.7±0.2‰ (2σ) and $\ln^{18}O$=26.5±0.2‰ (2σ)on the VSMOW scale, as measured by Feilberg, Wiegel, and Boering.[18] For each pressure, the experiment was repeated 3 times, so 95% confidence intervals for the measurements were calculated using the standard error of the sample mean $SE_{\bar{x}}$ and a *t*-distribution with $df = 2$. A major contributor to the measured uncertainty is likely from the cryogenic separation of O_3 from O_2 and N_2 and the subsequent cryogenic transfers between sample tubes, which can introduce mass-dependent artifacts of approximately ±0.25‰ and ±0.5‰ for $\ln^{17}O$ and $\ln^{18}O$, respectively.[18] In addition, variations in the lamp flux between experiments could also affect mass-dependent isotope effects in the system directly through changes in the rate of ozone photolysis or indirectly through changes in the rates of other reactions in the system such as $O_2(^1\Sigma)+O_3$ that potentially have large mass-dependent isotope effects.[18,32] Differences in temperature in the experiments caused by changes in the lamp flux or the ambient lab temperature could also lead to changes in the isotopic composition and ^{17}O isotope anomaly of ozone. Using the previously measured temperature dependence of the ozone isotope enrichments,[11,38] we calculate that a change of ±2.5°C could lead to changes in $\ln^{17}O$, $\ln^{18}O$, and $\Delta^{17}O$ of ±0.6‰, ±0.75‰, and ±0.20‰, respectively. Because most of the sources of random or systematic error are mass-dependent in nature, the overall uncertainties for $\Delta^{17}O$ are smaller than those for $\ln^{17}O$ and $\ln^{18}O$ by about a factor of 2.

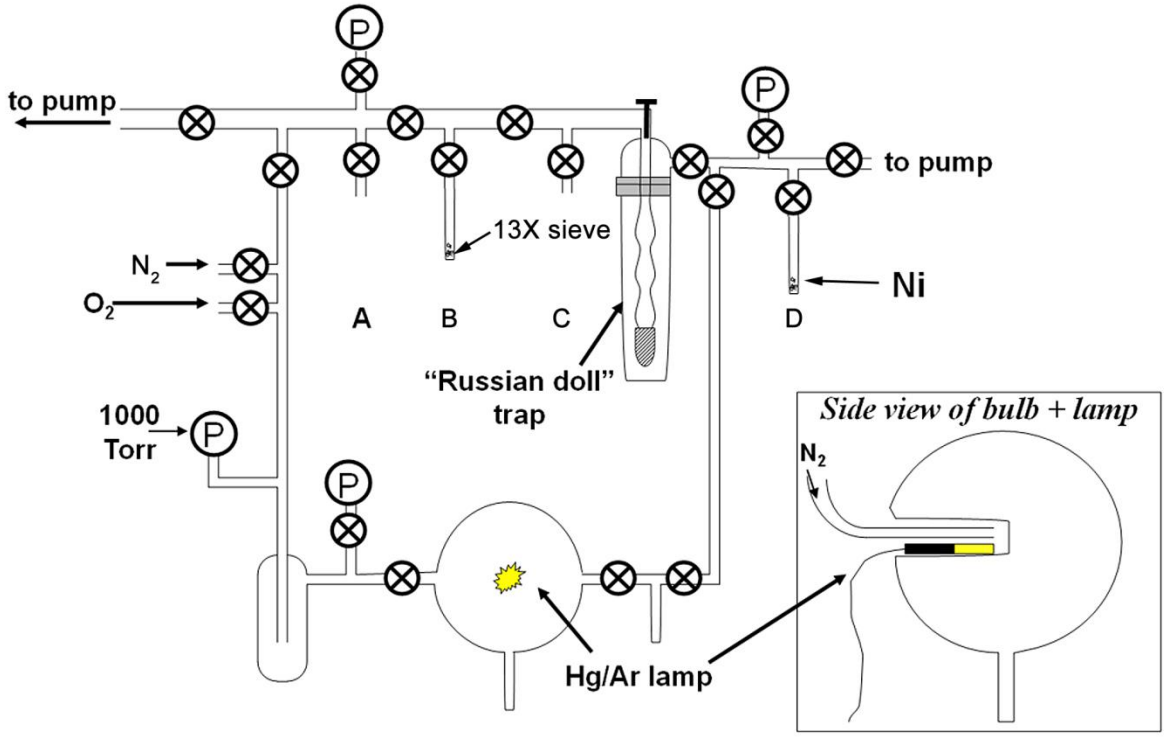

Figure 4-1. Schematic of the bulk photochemical apparatus for production of ozone from photolysis of O_2.

For comparison with the experimental results, a photochemical kinetics model developed in KINTECUS[39] was used to predict the steady state isotopic composition of O_3. The model used here was similar to models used in previous studies of both the isotopic compositions of O_3 and CO_2 in other experiments[18,32,33,40] and has been described in a previous publication.[33] A brief summary follows here, highlighting important features of the model. A list of the reactions and rate coefficients used in the model for reactions is shown in Table 1 for the non-isotopically substituted reactions. The rate coefficients for photolysis of O_3 and O_2 were estimated from the photon flux and geometry of the bulb using CO_2 actinometry[18,33] and the reported power output of the lamp.[41] The KIEs in ozone formation measured by Mauersberger and co-workers[12,13] were used directly in the model to compare with the experiments because these KIEs were measured at the same total pressure (200 Torr) and mole fractions of O_2 and N_2 (20% and 80%, respectively) as one of our set of experiments. Since no direct measurements of the KIEs of the individual channels for formation of $^{16}O^{16}O^{17}O$ and $^{16}O^{17}O^{16}O$ from $^{16}O + {}^{16}O^{17}O$ are available, the KIEs for these channels were derived from the total (i.e., overall) relative rate coefficient for ozone formation for $^{16}O + {}^{16}O^{17}O$ and the ΔZPE relationship between the relative rate coefficients for formation of the asymmetric isotopologues.[32,33] These rate coefficients are shown in Table 4-2. In addition to the KIEs in ozone formation, isotope effects derived from the rate coefficient for $O + O_2$ isotope exchange[42] and the calculated equilibrium constants of Kaye and Strobel[43] were also used. A parameterization of the KIEs as a function of total effective pressure was not used in this model. This kinetics model without KIEs in any reactions but ozone formation and $O + O_2$ isotope exchange is referred to as the "Base Scenario".

A number of modifications were also made to the Base Scenario to test the sensitivity of the isotopic composition of O_3 to various mass-dependent isotope effects. For each model scenario, a "^{17}O factor" and "^{18}O factor" for photolysis isotope effects and any isotope effects in other reactions are given in Table 4-3. Details for each model scenario and why they were selected appear in the following paragraphs. These model scenarios were then run at two conditions: (1) 40 Torr of O_2 and 160 Torr of N_2 and (2) 200 Torr of O_2, so that the model results could be compared with the results of the photochemistry experiments reported here and with the 175 Torr O_2 experiments of Feilberg, Wiegel, and Boring.[18]

In Scenarios 1, 2, and 3, different mass-dependent isotope effects were used for the UV photolysis of O_3 (see Table 4-3) in order to compare the model results for the isotopic composition of O_3 with experiments and with different theoretical calculations now available for the isotope-specific cross sections for O_3 photolysis. In Scenario 1, hypothetical mass-dependent isotope effects for ozone photolysis were selected that best predicted the values of $\ln^{17}O$ and $\ln^{18}O$ for O_3 measured in our experiments at 40 Torr of O_2 and 160 Torr of N_2. In Scenario 2, the isotope-specific O_3 photolysis cross sections from the recent quantum mechanical calculations by Ndengué[47] are used in the calculated rate coefficients for O_3 photolysis. In Scenario 3, the isotope-specific O_3 photolysis cross sections from the semi-analytic calculations by Liang et al.[48] are used in the calculated rate coefficients for O_3 photolysis.

Table 4-1. Reactions included in the kinetics model.

Reaction	Rate Coefficient	Source
$O_2 + h\nu \rightarrow O + O$	2.2×10^{-7} s^{-1}	Cross section from Yoshino *et al.*[44]; flux from CO_2 actinometry
$O + O_2 + M \rightarrow O_3 + M$	$6.0\times10^{-34}(T/300)^{-2.4}$ cm^6 s^{-1}	Sander *et al.*[45]; assumed rate coefficient for O_2 and N_2 were the same
$O_3 + h\nu \rightarrow O_2 + O$	$0.1\times(1.8\times10^{-2}$ $s^{-1})$	Flux estimated from CO_2 actinometry and 254/185 flux ratio[46]; cross section and branching ratio from Sander *et al.*[45]
$O_3 + h\nu \rightarrow O_2(^1\Delta) + O(^1D)$	$0.9\times(1.8\times10^{-2}$ $s^{-1})$	
$O_3 + O \rightarrow 2O_2$	8.0×10^{-12} exp(-2060/T) cm^3 s^{-1}	Sander *et al.*[45]
$O_3 + O(^1D) \rightarrow 2O_2$	1.2×10^{-10} cm^3 s^{-1}	Sander *et al.*[45]
$O_3 + O(^1D) \rightarrow O_2 + 2O$	1.2×10^{-10} cm^3 s^{-1}	Sander *et al.*[45]
$O_3 + O_2(^1\Delta) \rightarrow 2O_2 + O$	5.2×10^{-11} exp(-2840/T) cm^3 s^{-1}	Sander *et al.*[45]
$O_2(^1\Delta) + O_2 \rightarrow O_2 + O_2$	1.6×10^{-18} cm^3 s^{-1}	Sander *et al.*[45]
$O_2(^1\Delta) + N_2 \rightarrow O_2 + N_2$	1×10^{-20} cm^3 s^{-1}	Sander *et al.*[45] (upper limit)
$O(^1D) + O_2 \rightarrow O + O_2$	$0.2\times(3.2\times10^{-11}$exp(70/T) cm^3 $s^{-1})$	Sander *et al.*[45]
$O(^1D) + O_2 \rightarrow O + O_2(^1\Sigma)$	$0.8\times(3.2\times10^{-11}$exp(70/T) cm^3 $s^{-1})$	
$O_2(^1\Sigma) + O_2 \rightarrow O_2(^1\Delta) + O_2$	4.0×10^{-17} cm^3 s^{-1}	Sander *et al.*[45]
$O_2(^1\Sigma) + O_3 \rightarrow O_2(^1\Delta) + O_3$	$0.3\times(2.2\times10^{-11}$ cm^3 $s^{-1})$	Sander *et al.*[45]; assumed no $O_2(^3\Sigma)$ product
$O_2(^1\Sigma) + O_3 \rightarrow O + 2O_2$	$0.7\times(2.2\times10^{-11}$ cm^3 $s^{-1})$	Sander *et al.*[45]
$O_2(^1\Sigma) + O \rightarrow O_2(^1\Delta) + O$	8.0×10^{-14} cm^3 s^{-1}	Sander *et al.*[45]; assumed no $O_2(^3\Sigma)$ product
$O_2(^1\Sigma) + N_2 \rightarrow O_2(^1\Delta) + N_2$	4.1×10^{-13} cm^3 s^{-1}	Sander *et al.*[45]
$O(^1D) + N_2 \rightarrow O + N_2$	2.15×10^{-11} exp(-110/T) cm^3 s^{-1}	Sander *et al.*[45]
O' + OO → OO' + O	3.4×10^{-12} $(T/300)^{-1.1}$ cm^3 s^{-1} [O'=^{18}O or ^{17}O]	Fleurat-Lessard *et al.*[42]
O' + OO ↔ OO' + O	K_{eq}[O'=^{18}O] = 1.94 exp(32/T) K_{eq}[O'=^{17}O] = 1.96 exp(16.8/T)	Kaye and Strobel[43]

Table 4-2. Isotope-specific rate coefficients for ozone formation containing a single heavy oxygen atom relative to that for $^{16}O^{16}O^{16}O$ at 40 Torr O_2 and 160 Torr N_2 measured by Mauersberger et al.[12] and by Janssen et al.,[13] used in the Base Scenario (left), and used as the KIEs for the energy transfer and radical complex mechanisms in Scenario 4 (right).

				Scenario 4	
Reaction	Mauersberger et al. [12]	Janssen et al.[13]	Base Scenario	Energy Transfer	Radical Complex
$^{16}O + {}^{16}O^{16}O \rightarrow {}^{16}O^{16}O^{16}O$	1.00	1.00	1.00	1.00	1.00
$^{18}O + {}^{16}O^{16}O \rightarrow {}^{16}O^{16}O^{18}O$	0.93 ± 0.03	0.92 ± 0.04	0.93	0.880	1.00
$^{16}O + {}^{16}O^{18}O \rightarrow {}^{16}O^{16}O^{18}O$	} 1.27 ± 0.03	1.45 ± 0.04	1.45	1.771	1.00
$^{16}O + {}^{16}O^{18}O \rightarrow {}^{16}O^{18}O^{16}O$		1.08 ± 0.01	1.08	1.137	1.00
$^{17}O + {}^{16}O^{16}O \rightarrow {}^{16}O^{16}O^{17}O$	1.03 ± 0.05	--	1.03	1.051	1.00
$^{16}O + {}^{16}O^{17}O \rightarrow {}^{16}O^{16}O^{17}O$	} 1.17 ± 0.05	--	1.35	1.600	1.00
$^{16}O + {}^{16}O^{17}O \rightarrow {}^{16}O^{17}O^{16}O$		--	0.99	0.983	1.00

In Scenarios A, B, C, and D, mass-dependent KIEs for several of the reactions of O_3 with other species in the photochemistry bulb are introduced. These mass-dependent isotope effects were derived in Cole and Boering[32] to fit the time dependence of the isotopic composition of O_3 measured in the ozone photolysis experiments of Chakraborty and Bhattacharya.[31] In Scenarios A, B, C, and D, mass-dependent isotope effects are considered in the reactions $O(^1D)+O_3$, $O(^3P)+O_3$, $O(^1\Delta)+O_3$, and $O(^1\Sigma)+O_3$, respectively (see Table 4-3). In Scenarios 3A, 3B, 3C, 3D, and 3AD, the mass-dependent O_3 photolysis isotope effects calculated in Scenario 3 from Liang et al.[48] are combined with the mass-dependent KIEs in the same reactions for O_3 loss as in Scenarios A, B, C, and D, respectively, or a combination of the KIEs for O_3 loss reactions used in Scenarios A and D for Scenario 3AD.

In several scenarios tested but not reported explicitly here, possible mechanisms that could result in mass-dependent fractionation of O_3 formed in air-like O_2/N_2 were also introduced into the model to try to account for differences between the experiments and the model predictions. These scenarios involved N_2O formation from $O(^1D) + N_2 + M$ and subsequent N_2O photolysis, leading to formation of NO and NO_2. In these scenarios, mass-dependent KIEs in the reactions of NO and NO_2 with O_3 did not lead to any significant changes in the isotopic composition of O_3 in the model results.

Table 4-3. Isotope effects in all mass-dependent model scenarios for experiments involving the UV photolysis of ozone.

Model scenario	O_3 photolysis isotope effect		Other isotope effect(s)		
	^{18}O factor	^{17}O factor	Reaction	^{18}O factor	^{17}O factor
Base scenario	-	-	-	-	-
Scenario 1	1.0285 asym, 1.0590 sym	1.0147 asym, 1.0303 sym	-	-	-
Scenario 2	1.0103 asym, 1.0204 sym	1.0054 asym, 1.0106 sym	-	-	-
Scenario 3	1.0073 asym, 1.012 sym	1.0038 asym, 1.0063 sym	-	-	-
Scenario A	-	-	$O_3 + O(^1D)$	0.945	0.9714
Scenario B	-	-	$O_3 + O(^3P)$	0.99	0.9948
Scenario C	-	-	$O_3 + O_2(^1\Delta)$	0.975	0.987
Scenario D	-	-	$O_3 + O_2(^1\Sigma)$	0.89	0.9428
Scenario 3A	1.0073 asym, 1.012 sym	1.0038 asym, 1.0063 sym	$O_3 + O(^1D)$	0.925	0.961
Scenario 3B	1.0073 asym, 1.012 sym	1.0038 asym, 1.0063 sym	$O_3 + O(^3P)$	0.985	0.9922
Scenario 3C	1.0073 asym, 1.012 sym	1.0038 asym, 1.0063 sym	$O_3 + O_2(^1\Delta)$	0.965	0.9818
Scenario 3D	1.0073 asym, 1.012 sym	1.0038 asym, 1.0063 sym	$O_3 + O_2(^1\Sigma)$	0.85	0.922
Scenario 3AD	1.0073 asym, 1.012 sym	1.0038 asym, 1.0063 sym	$O_3 + O_2(^1\Sigma)$	0.85	0.922
			$O_3 + O(^1D)$	0.95	0.974

In Scenario 4, potential non-mass-dependent fractionation is considered due to changes that may occur as a function of the identity of the bath gas M or of temperature by including two separate ozone formation channels: the energy transfer (ET) mechanism and the radical-complex (RC) mechanism. The two possible mechanisms for ozone formation are not modeled step-wise as shown in (R1) for ET or (R5) through (R8) for RC but as two separate single-step three-body reactions. The two ozone formation mechanisms have the different rate coefficients and different temperature dependences inferred by Luther et al.[27] for O_3 formed in N_2, as shown in Table 4-4. Because the non-mass-dependent KIEs are thought to occur in the ET mechanism,[26,28,29] KIEs are included in this model scenario only in the ET mechanism reactions. Since the RC mechanism accounts for about 40% of ozone formation at room temperature,[27] the KIEs for the ET mechanism reactions for ozone formation have to be re-scaled so that the combined ET + RC KIEs for ozone formation are the same as the measured KIEs (Table 4-2). Scenario 4 was run under several different conditions in addition to the 200 Torr of O_2 and 40 Torr of O_2 and 160 Torr of N_2 at T = 300 K used for the Base Scenario and the mass-dependent Scenarios shown in Table 4-3. To compare possible temperature dependences for the isotopic composition of O_3, the Base Scenario and Scenario 4 were also run at T = 400 K, 250 K, 200 K, 175 K. Scenario 4 was also run using 50 Torr of O_2 and 150 Torr of SF_6 to compare with the results from Feilberg, Wiegel, and Boering.[18] While the rate coefficients and temperature dependence for ozone formed by the ET and RC mechanisms in N_2 are the same as those inferred by Luther et al.[27] for $^{16}O^{16}O^{16}O$, the rate coefficients used in Scenario 4 for the RC and ET ozone formation channels in O_2 were iteratively adjusted until the model predictions for the value of $\Delta^{17}O$ for O_3 are the same as the measured $\Delta^{17}O$ values for O_3 formed in 175 Torr of O_2 (see Table 4-4). Similarly, for ozone formation in SF_6, the rate coefficients used in Scenario 4 for the RC and ET formation channels in SF_6 were iteratively adjusted until the model predictions for the value of $\Delta^{17}O$ for O_3 are the same as the measured $\Delta^{17}O$ values for O_3 formed in 50 Torr of O_2 and 125 Torr of SF_6 (see Table 4-4). While this is overall a somewhat crude model that uses parameters fit to the measurements, Scenario 4 still allows us to investigate the possible role of the ET and RC mechanisms in affecting the non-mass-dependent isotopic composition of O_3 formed in different bath gases and at different temperatures.

Table 4-4. Rate coefficients for the energy transfer (ET) and radical complex (RC) mechanisms for ozone formation in the bath gases N_2, O_2, and SF_6 used in Scenario 4, along with the percentage of ozone formation that proceeds through the radical complex mechanism.

	k_{N2} ($cm^6\ s^{-1}$)*	k_{O2} ($cm^6\ s^{-1}$)†	k_{SF6} ($cm^6\ s^{-1}$)†
Energy Transfer	$3.5 \times 10^{-34}(T/300)^{-1.5}$	$3.7 \times 10^{-34}(T/300)^{-1.5}$	6.4×10^{-34}
Radical Complex	$2.5 \times 10^{-34}(T/300)^{-3.3}$	$2.3 \times 10^{-34}(T/300)^{-3.3}$	2.5×10^{-33}
% RC	41.7%	38.3%	80%

*Inferred by Luther et al.[27]

†Inferred from iteration of the Scenario 4 results for the isotopic compositions of O_3 formed in O_2 and SF_6 in Feilberg, Wiegel, and Boering[18]

4.3. Results and Discussion

The experimental results for the isotopic composition of ozone formed in mixtures of N_2 and O_2 as a function of total pressure are shown in Figure 4-2 and Table 4-5, along with the measurements from Feilberg, Wiegel, and Boering et al.[18] in Ar, O_2, and CO_2. The isotopic composition of ozone formed in N_2/O_2 decreases with total pressure, similar to previous laboratory measurements.[11,15,16,18] However, the values for $\Delta^{17}O$ of ozone formed in an air-like N_2/O_2 mixture are nearly the same as the values of $\Delta^{17}O$ of ozone formed in CO_2 at the same total pressures and are lower than the values for ozone formed in pure O_2 by about 2‰ at most of the pressures measured. Although small, these differences between $\Delta^{17}O$ of O_3 formed in an air-like N_2/O_2 mixture and in pure O_2 in the experiments at 200, 300, and 700 Torr are statistically significant at the 95% significance level using two-sample *t*-tests.

Comparison of the measured isotopic composition of O_3 formed in an air-like N_2/O_2 mixture at 40 Torr of O_2 and 160 Torr of N_2 with results of the Base Scenario in the kinetics model in Figure 4-2 shows that the model can quantitatively predict the value for $\Delta^{17}O$ of ozone (≈42‰) using only the KIEs measured or derived from Mauersberger et al.[12] and Janssen et al.[13] at the same partial pressures of O_2 and N_2 as the experiments reported here. As such, an additional non-mass-dependent isotope effect in UV photolysis is not required, as has been suggested previously,[31] because UV photolysis of O_3 in the experiments of Mauersberger et al.[12] and Janssen et al.[13,19] is negligible given the wavelength of UV radiation (180nm) and short irradiation times (<2 min). These combined experimental results and model predictions show directly that the ^{17}O isotope anomaly in ozone in these experiments originates in KIEs in ozone formation without an additional non-mass-dependent isotope effect in UV photolysis of ozone.

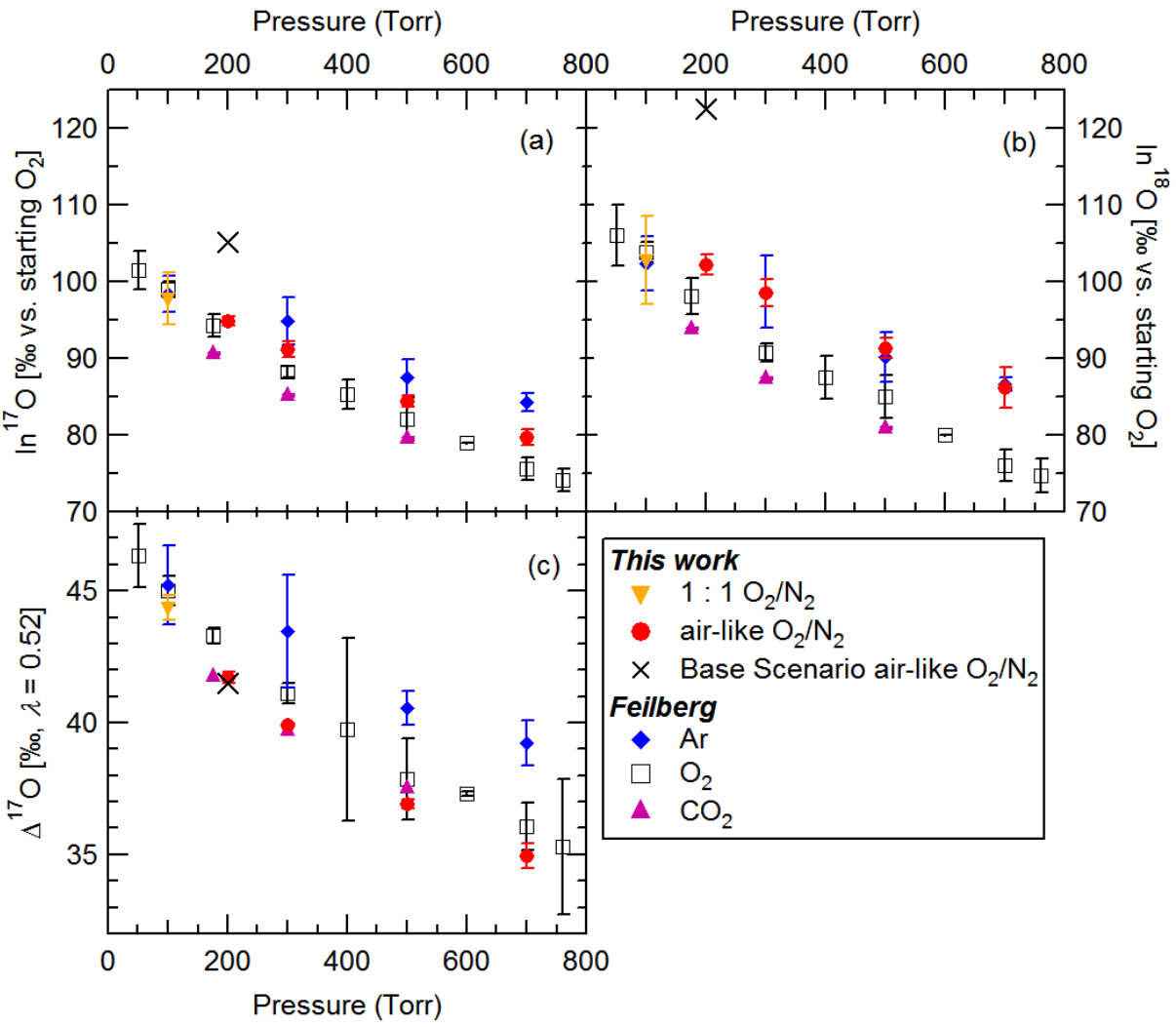

Figure 4-2. Measured (a) $\ln^{17}O$, (b) $\ln^{18}O$, and (c) $\Delta^{17}O$ of ozone as a function of total pressure for ozone formed in either air-like (red circles) or 1:1 mixtures of O_2 and N_2 (gold triangles) for the experiments reported here, along with the same for ozone formed in Ar, O_2, and CO_2 from Feilberg, Wiegel, and Boering.[18] The error bars represent the 95% confidence intervals derived from the standard error of the mean $SE_{\bar{x}}$ with N = 3 and the two sided *t*-statistic for each set of measurements. The Base Scenario model results for an air-like mixture of O_2/N_2 are also shown. The vertical axes do not start at zero to better show the differences between the bath gases.

Table 4-5. The isotopic composition of ozone formed by the irradiation of O_2 and N_2 at different pressures with the 95% confidence intervals from the *t*-statistic and the standard error of the mean $SE_{\bar{x}}$ with N = 3 for each.

P O_2 (Torr)	P N_2 (Torr)	$\ln^{17}O$ (‰)*		$\ln^{18}O$ (‰)*		$\Delta^{17}O$ (‰)†		Slope
50	50	97.8	± 3.4	102.9	± 5.7	44.4	± 0.5	0.95
40	160	94.8	± 0.5	102.1	± 1.4	41.7	± 0.2	0.93
60	240	91.1	± 1.0	98.5	± 1.8	39.92	± 0.02	0.92
100	400	84.4	± 0.7	91.3	± 1.3	36.94	± 0.17	0.93
140	560	79.7	± 1.0	86.2	± 2.7	34.9	± 0.5	0.93

* Relative to the starting O_2

† The value of λ_{MD} used was 0.52

While the experimental and predicted $\Delta^{17}O$ values for ozone formed in an air-like mixture of O_2/N_2 at 200 Torr agree to within 0.2‰, the $\ln^{17}O$ and $\ln^{18}O$ values for ozone are mass-dependently lower relative to the model predictions using the Base Scenario by 10‰ and 20‰, respectively (see Figure 4-2 and Table 4-6). The model-measurement differences for an air-like mixture of O_2/N_2 at 200 Torr can potentially be resolved under these conditions by assuming that mass-dependent isotope effects account for all of this difference as in Scenario 1 (see Table 4-3). However, these same mass-dependent isotope effects in photolysis in Scenario 1 do not resolve the mass-dependent differences between the Base Scenario model results and the experiment with O_2 at 175 Torr from Feilberg, Wiegel, and Boering,[18] as the values of $\ln^{17}O$ and $\ln^{18}O$ in the model are greater by 5‰ and 10‰ over the experimental values after adjusting for the difference between the values of $\Delta^{17}O$ for O_3 formed in O_2 and in an air-like mixture of O_2/N_2. Furthermore, the mass-dependent isotope effects in photolysis used in Scenario 1 are three times larger than those calculated by Ndengué et al.[47] from quantum mechanical calculations (Scenario 2) and five times larger than those calculated by Liang et. al.[48] from a semi-analytic model (Scenario 3) (see Table 4-3). As such, the mass dependent isotope effects in O_3 photolysis used in Scenarios 2 and 3 cannot resolve the model-measurement differences either at 200 Torr of an air-like O_2/N_2 mixture or at 175 Torr of pure O_2 (See Table 4-6). These model results for Scenarios 1, 2, and 3 at 200 Torr for both an air-like mixture of O_2/N_2 and pure O_2 suggest that some additional mass-dependent isotope effects that deplete the O_3 of ^{17}O and ^{18}O are missing at least one of the reactions included in the model.

Several possible reactions that might have mass-dependent isotope effects are explored in Scenarios A through D using the isotope effects derived in the study by Cole and Boering[32] modeling the isotopic composition of O_3 in UV photolysis experiments;[31] the results for these scenarios are shown in Table 4-6. In Scenarios A and B, mass-dependent isotope effects in reactions of $O(^1D)$ and $O(^3P)$ with O_3 do not change the isotopic composition of O_3 formed in O_2 or in an air-like O_2/N_2 mixture. In Scenario C, mass-dependent KIEs in the reaction of $O_2(^1\Delta)$

with O_3 increase the values of $\ln^{17}O$ and $\ln^{18}O$ for ozone formed in both an air-like O_2/N_2 mixture at 200 Torr and O_2 at 175 Torr by ≈5‰ and ≈10‰, respectively. In Scenario D, mass-dependent KIEs in the reaction of $O_2(^1\Sigma)$ with O_3 increase the values of $\ln^{17}O$ and $\ln^{18}O$ for O_3 formed in an air-like mixture O_2/N_2 at 200 Torr by ≈3‰ and ≈6‰, respectively, but the enrichment gets much larger (≈12‰ and ≈24‰ for $\ln^{17}O$ and $\ln^{18}O$) in pure O_2 at 175 Torr due to the higher concentrations of the ground state $O_2(^3\Sigma)$ and thus $O_2(^1\Sigma)$ through the reaction $O(^1D) + O_2(^3\Sigma)$. In summary, based on the model results for Scenarios A through D, the mass-dependent KIEs derived in Cole and Boering[32] in the reactions of $O(^1D)$ or $O(^3P)$ with O_3 (Scenarios A, B, 3A, and 3B) are consistent with the experimental differences between measurements of O_3 formed in O_2 and in an air-like O_2/N_2 mixture simply because they have only a very small effect on the modeled isotopic composition of O_3 formed in the experiments reported here and by Feilberg, Wiegel, and Boering.[18] The mass-dependent KIEs in the reactions of $O_2(^1\Delta)$ and $O_2(^1\Sigma)$ with O_3 (Scenarios C, D, 3C, 3D, and 3AD), however, are inconsistent with the experimental results for the isotopic composition of O_3 formed in both O_2 and air-like O_2/N_2 because they result in enrichments in the heavy isotopes over the Base Scenario, which was already too enriched compared with the experiments. These results from Scenarios C, D, 3C, 3D, and 3AD suggest that if mass-dependent KIEs large enough to be considered do exist in the reactions of $O_2(^1\Delta)$ and $O_2(^1\Sigma)$ with O_3, the mass-dependent KIEs should actually be inverse KIEs (i.e., >1) to cause a depletion in the heavy isotopes of ozone, as needed to better simulate the experimental results.

These new model and experimental results suggest some modifications to the mass-dependent KIEs derived by Cole and Boering[32] from the time dependence of the isotopic composition of O_3 in the UV photolysis experiments of Chakraborty and Bhattacharya[31]. In particular, Cole and Boering[32] found that mass-dependent KIEs in the reaction of $O_2(^1\Sigma)$ and O_3 — in addition to mass-dependent KIEs in the reaction of $O(^1D) + O_3$ as in Scenarios A, 3A, and 3AD — were one possible source of mass-dependent fractionation that increased the three isotope slope λ from a value of 0.6 to 1.0 in experiments involving photolysis of O_3 in the presence of N_2. In contrast, the kinetics modeling of the experimental results for the isotopic composition of O_3 reported here suggests that such KIEs in $O_2(^1\Sigma) + O_3$ would generate large mass-dependent enrichments that are in fact inconsistent with the isotopic compositions of O_3 formed in both O_2 and air-like O_2/N_2 (see Table 4-6). As such, the mass-dependent KIEs in the reaction $O_2(^1\Sigma) + O_3$ used in Scenarios D, 3D, or 3AD are unlikely to exist unless the increase in λ for O_3 photolysis with increasing N_2 in the experiments of Chakraborty and Bhattacharya[31] arises from mass-dependent artifacts from, e.g., the cryogenic separation of O_3, a possibility discussed by Cole and Boering.[32] The mass-dependent KIEs in the $O(^1D) + O_3$ reaction in Scenarios A or 3A cannot be ruled out, however, since they had so little effect on the isotopic composition of O_3 in those model scenarios.

Table 4-6. Comparison of the isotopic composition of O_3 from experiments at 200 Torr and from different mass-dependent model scenarios with the isotopic composition of O_3 reported relative to the starting O_2.

Scenario	200 Torr air-like O_2/N_2*		200 Torr O_2†	
	$\ln^{17}O$ (‰)	$\ln^{18}O$ (‰)	$\ln^{17}O$ (‰)	$\ln^{18}O$ (‰)
Experiment	94.8	102.1	93.3‡	95.1‡
Base Scenario	105.2	122.5	105.2	122.5
Scenario 1	94.8	102.0	97.0	106.4
Scenario A	105.3	122.5	105.3	122.6
Scenario B	105.2	122.5	105.3	122.5
Scenario C	110.4	132.5	109.8	131.2
Scenario D	108.2	128.3	117.4	146.1
Scenario 2	101.5	115.2	102.3	116.8
Scenario 3	102.8	117.7	103.3	118.8
Scenario 3A	102.8	117.8	103.4	118.9
Scenario 3C	109.9	131.5	109.6	130.9
Scenario 3D	106.9	125.6	119.9	151.0
Scenario 3AD	106.9	125.7	120.0	151.1

* The value of $\Delta^{17}O$ for all model scenarios and the air-like O_2/N_2 experiment at 200 Torr are both ≈41.7‰

† Experiments are the 175 Torr experiments in O_2 from Feilberg, Wiegel, and Boering.[18] The actual isotopic composition at 200 Torr in O_2 will be slightly lower because of the pressure dependence of the KIEs in ozone formation.

‡ The value of $\Delta^{17}O$ for ozone in the experiment at 175 Torr of O_2 is 43.8‰

The differences between the isotopic composition of O_3 formed in the experiments and those predicted by the various mass-dependent model Scenarios 1 through 3 and Scenarios A through D might also result from the participation of significant amounts of vibrationally and rotationally excited states of O_3 or other species in the bulb. For example, the difference between the hypothetical isotope effects in photolysis used in Scenario 1 and those calculated theoretically by Ndengué et al.[47] (Scenario 2) could potentially arise from the presence of a significant amount of vibrationally and rotationally excited ozone in our experiments. In studies

in which the population of vibrationally excited O_3* after ozone recombination was measured, ozone in its vibrational ground state does not start to have any appreciable population until 50 μs after the start of ozone formation.[49] In the experiments reported here, ozone is more rapidly destroyed and reformed than in the atmosphere or in some other experiments such as UV photolysis experiments[31], so the population of vibrationally excited O_3* may not be thermalized before UV photodissociation or before removal through other reactions. The photodissociation of these vibrationally excited states could potentially lead to larger photolysis isotope effects due to differences in the Franck-Condon factors for overlap of the excited vibrational state and the dissociative electronically excited state of O_3. In particular, slight asymmetries in the excited vibrational modes for asymmetrically substituted O_3* isotopologues could in principle lead to better overlap between the isotopically substituted O_3 and the dissociative state of O_3 and thus to larger mass-dependent isotope effects in photolysis than those calculated for ozone with a thermal distribution of vibrationally excited states, as in Ndengue et al.[47] or Liang et al.[48] Calculations of isotope-specific UV photodissociation cross sections for vibrationally excited states of O_3 are needed to test this hypothesis and to show how vibrational excitation of O_3 could affect the magnitudes of mass-dependent isotope effects in O_3 photolysis.

Notably, the presence of vibrationally excited O_3* from O_3 recombination is unlikely to be important in the experiments of Charkaborty and Bhattacharya[31] since the O_3 starts in thermal equilibrium with the laboratory. However, other sources of non-thermal isotope effects could be one possible explanation for the increase in the three isotope slope, λ, of O_3 as N_2 is added to the experiments. In the UV photolysis experiments, $O(^1D)$ and $O_2(^1\Delta)$ from ozone photolysis at 254 nm likely have translational energies as large as ≈14 kcal/mol,[50] which is well in excess of the thermal energy at 300K of 0.529 kcal/mol. As N_2 is added to the UV photolysis experiments, These translational energy distributions from photolysis of O_3 would then lose population of high kinetic energy $O(^1D)$ and $O_2(^1\Delta)$ the experiment continues through increased translational and electronic quenching rates in collisions with N_2. A decrease in the population of high kinetic energy $O(^1D)$ and $O_2(^1\Delta)$ in their translational distributions would reduce the collision frequencies of $O(^1D)$ and $O_2(^1\Delta)$ with O_3 as N_2 is added, leading to decreased loss rates for O_3 through chemical reactions with both, and thus a decrease in the relative importance of mass-dependent isotope effects in the reactions of $O(^1D)$ and $O_2(^1\Delta)$ with O_3. Such a decrease in the relative importance of mass-dependent KIEs in the reactions of $O(^1D)$ and $O_2(^1\Delta)$ as N_2 is added could potentially lead to the increase in the three isotope slope, λ, of O_3 that was measured by Chakraborty and Bhattacharya[31] as N_2 was added.

In addition to the mass-dependent differences between O_3 formed or photolyzed in O_2 or in an air-like O_2/N_2 mixture, recall that the value for $\Delta^{17}O$ of O_3 formed in air-like O_2/N_2 at a given pressure was lower than that for O_3 formed in pure O_2 in by ≈2‰ and was nearly the same as that for O_3 formed in CO_2 (see Figure 4-2). Differences in the ability of O_2, N_2, and CO_2 to stabilize O_3* in the energy transfer mechanism are unlikely to be the origin of the values of $\Delta^{17}O$ for O_3 formed in these three bath gases because the average energy transferred per collision, $\langle\Delta E\rangle$, for collisions of N_2 and CO_2 with O_3* are quite different at 25 cm^{-1} and 150 cm^{-1}, respectively. Furthermore, although the value of $\langle\Delta E\rangle$ for collisions of O_3* with O_2 is unknown, the value of $\langle\Delta E\rangle$ for O_2 and N_2 are likely nearly the same since ozone formation in O_2 and N_2 have very close three-body recombination rate coefficients.[51] As such, using Scenario 4, the relative contributions of the energy transfer (ET) and radical complex (RC) mechanisms for O_3 formation were varied with O_2 as the bath gas until the model results best simulated the value for $\Delta^{17}O$ of O_3 (≈43‰) formed in pure O_2 at 175 Torr, as explained in Methods. The resulting value

used in Scenario 4 for the relative contribution of the RC mechanism was ≈38% of the total ozone formation rate in pure O_2, compared with ≈42% of the total ozone formation rate in N_2 (see entries Table 4-4). This smaller value for the relative contribution of the RC mechanism in O_2 than that in the N_2/O_2 mixture is expected since the value for $\Delta^{17}O$ of O_3 formed in pure O_2 is 2‰ greater than that for O_3 formed in an air-like O_2/N_2 mixture and since the non-mass-dependent KIEs in ozone formation are associated with the ET mechanism and not the RC mechanism. While such a small difference in the contributions of each mechanism probably could not be inferred from a master equation model, these estimated contributions of the RC and ET mechanisms to O_3 formation do not seem unreasonable.

Scenario 4 was also used to estimate the possible contributions of the RC and ET mechanism to O_3 formation in SF_6 that could lead to the observed value of $\Delta^{17}O$ for O_3 (≈17‰) formed in 50 Torr of O_2 and 125 Torr of SF_6 in Feilberg, Wiegel, and Boering.[18] By comparing the model results with the experimental results, the relative contribution of the RC mechanism in this case was nearly 80% of the total rate of ozone formation in SF_6 compared with ≈42% of the total rate of ozone formation in N_2. In contrast, the contribution of the RC mechanism to O_3 formation in SF_6 inferred by Luther et al.[27] from a master equation model is ≈31% at T = 300K and low pressures. As such, while the RC mechanism may contribute to the dramatic difference in the $\Delta^{17}O$ values for O_3 formed in SF_6 versus O_2 and other bath gases, the dramatic difference is more likely due to the improved quenching efficiency of collisions of SF_6 with O_3* for all isotopologues versus the other bath gases studied, as discussed in Feilberg, Wiegel, and Boering.[18]

The model results at different temperatures for the isotopic composition of O_3 for Scenario 4 and for the Base Scenario were also compared to test whether the temperature dependence of the isotopic composition of ozone could be caused by changes in the relative contributions of the RC and ET mechanisms at different temperatures, as has been suggested previously.[14,27,30] The modeled temperature dependences of the isotopic composition of O_3 for the Base Scenario and for Scenario 4 along with the experimental temperature dependence of the isotopic composition of O_3 are shown in Figure 4-3. While the isotopic composition of O_3 in the Base Scenario has only a slight dependence on temperature, the predicted temperature dependence of the isotopic composition of O_3 from Scenario 4 qualitatively follows the same trend as the experimental temperature dependence. Importantly, the model results for Scenario 4 produce the same qualitative temperature dependence of the isotopic composition of O_3 using only the rate coefficients for ozone formation by the ET and RC mechanisms without an explicit temperature dependence in the KIEs, as hypothesized previously.[14,29,30] While these results are somewhat speculative, they do suggest that the assumption that the RC mechanism does not have any KIEs used here and in Ivanov and Babikov[26] is at least somewhat realistic.

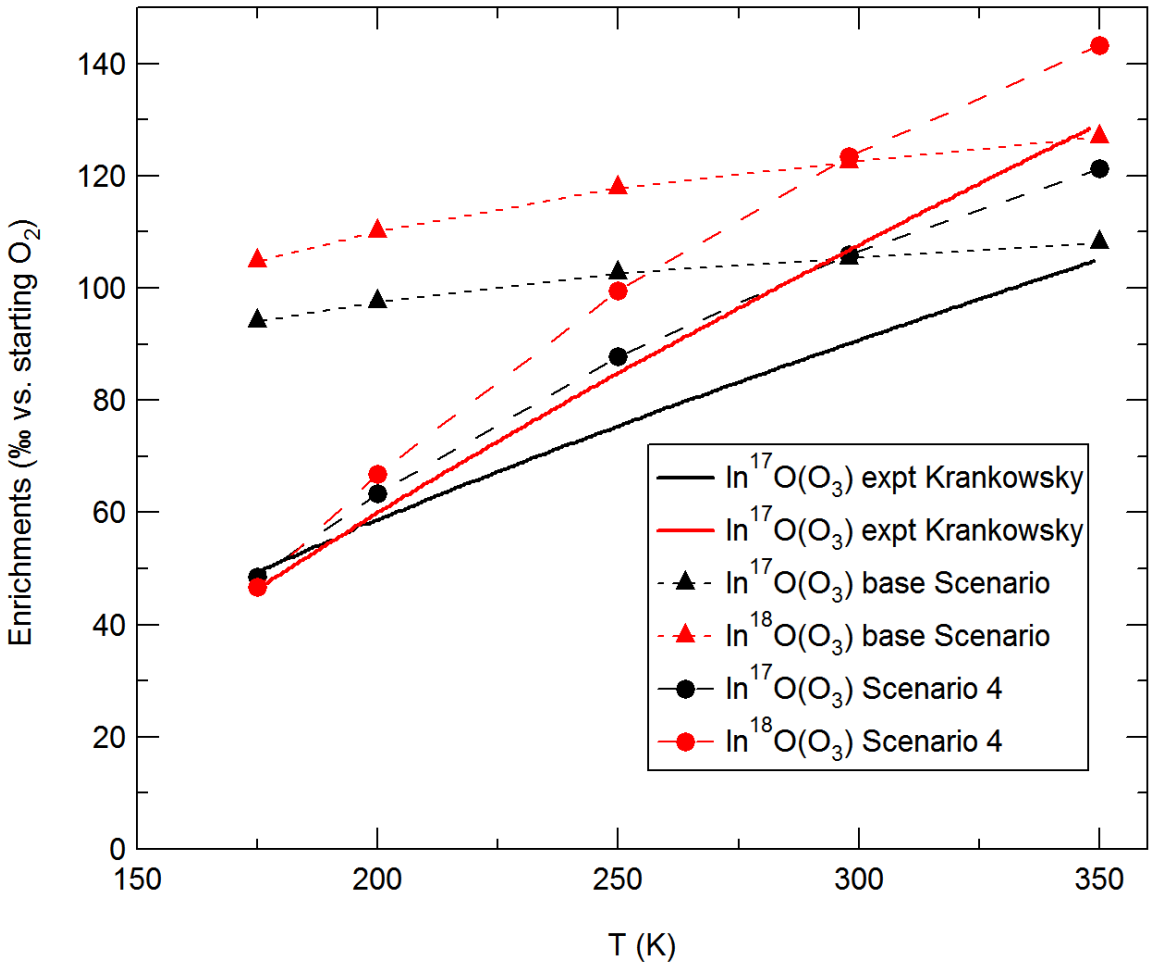

Figure 4-3. Comparison of the temperature dependence of the ozone enrichments between the experiments and model results for the Base Scenario and Scenario 4. The experimental temperature dependence of the ozone enrichments was derived by Krankowsky et al.[38]

4.4. Conclusions

In the experiments reported here, ozone formed in an air-like O_2/N_2 mixture exhibited small but statistically significant differences in its values for $\Delta^{17}O$ of 2‰ lower than ozone formed in pure O_2 at several different total pressures. A kinetics model was used to quantitatively predict the value for $\Delta^{17}O$ of O_3 formed in these experiments at 40 Torr O_2 and 160 Torr N_2 using previously measured non-mass-dependent KIEs for O_3 formation[12,13] under the same experimental conditions. Given that the value for $\Delta^{17}O$ of O_3 can be predicted very well by the measured KIEs for O_3 formation, the existence of a non-mass-dependent isotope effect in UV photolysis of O_3, as argued by Chakraborty and Bhattacharya[31] from their laboratory experiments involving ozone photolysis, is implausible. Rather, background O_3 formation and mass-dependent isotope effects in reaction of O_3 with $O(^1D)$ are instead the likely sources of the increase in the three isotope slope λ of O_3 that they observe as N_2 is added to their experiments, as argued by Cole and Boering[32].

Various model Scenarios that included mass-dependent isotope effects in O_3 photolysis or the reactions of O_3 with $O(^3P)$, $O(^1D)$, $O_2(^1\Delta)$, and $O_2(^1\Sigma)$ are used to compare with the measured isotopic compositions of O_3 formed in an air-like mixture of N_2/O_2 or pure O_2. While strict quantification of the isotope effects in these reactions is not possible from the experiments or modeling here, the model results do help rule out large mass-dependent KIEs in the reaction of $O_2(^1\Sigma) + O_3$, for example. Understanding the mass-dependent isotope effects in reactions involving O_3 or O_3 photolysis is important not only for predicting the isotopic composition of O_3 but also the isotopic compositions of various other species that obtain their non-mass-dependent oxygen isotopic composition from O_3, such as stratospheric CO_2.

References

[1] M.H. Thiemens and J.E. Heidenreich, Science **219**, 1073 (1983).

[2] J.E. Heidenreich and M.H. Thiemens, J. Chem. Phys. **84**, 2129 (1986).

[3] J.E. Heidenreich and M.H. Thiemens, J. Chem. Phys. **78**, 892 (1983).

[4] K. Mauersberger, Geophys. Res. Lett. **8**, 935 (1981).

[5] K. Mauersberger, Geophys. Res. Lett. **14**, 80 (1987).

[6] K. Mauersberger, P. Lämmerzahl, and D. Krankowsky, Geophys. Res. Lett. **28**, 3155 (2001).

[7] M.H. Thiemens, Annu. Rev. Earth Planet. Sci. **34**, 217 (2006).

[8] M.F. Miller, Geochim. Cosmochim. Acta **66**, 1881 (2002).

[9] S.S. Assonov and C.A.M. Brenninkmeijer, Rapid Commun. Mass Spectrom. **19**, 627 (2005).

[10] J. Bigeleisen and M.G. Mayer, J. Chem. Phys. **15**, 261 (1947).

[11] J. Morton, J. Barnes, B. Schueler, and K. Mauersberger, J. Geophys. Res. **95**, 901 (1990).

[12] K. Mauersberger, B. Erbacher, D. Drankowsky, J. Gunther, and R. Nickel, Science **283**, 370 (1999).

[13] C. Janssen, J. Guenther, K. Mauersberger, and D. Krankowsky, Phys. Chem. Chem. Phys. **3**, 4718 (2001).

[14] C. Janssen, J. Guenther, D. Krankowsky, and K. Mauersberger, Chem. Phys. Lett. **367**, 34 (2003).

[15] M.H. Thiemens and T. Jackson, Geophys. Res. Lett. **15**, 639 (1988).

[16] M.H. Thiemens and T. Jackson, Geophys. Res. Lett. **17**, 717 (1990).

[17] J. Guenther, B. Erbacher, D. Krankowsky, and K. Mauersberger, Chem. Phys. Lett. **306**, 209 (1999).

[18] K.L. Feilberg, A.A. Wiegel, and K.A. Boering, Chem. Phys. Lett. **556**, 1 (2013).

[19] C. Janssen, J. Guenther, D. Krankowsky, and K. Mauersberger, J. Chem. Phys. **111**, 7179 (1999).

[20] Y.Q. Gao and R.A. Marcus, Science **293**, 259 (2001).

[21] Y.Q. Gao and R.A. Marcus, J. Chem. Phys. **116**, 137 (2002).

[22] Y.Q. Gao and R.A. Marcus, J. Chem. Phys. **127**, 244316 (2007).

[23] R. Schinke, S.Y. Grebenshchikov, M. V Ivanov, and P. Fleurat-Lessard, Annu. Rev. Phys. Chem. **57**, 625 (2006).

[24] R. Schinke and P. Fleurat-Lessard, J. Chem. Phys. **122**, 094317 (2005).

[25] R.A. Marcus, Proc. Natl. Acad. Sci. U. S. A. **110**, 17703 (2013).

[26] M. V Ivanov and D. Babikov, Proc. Natl. Acad. Sci. U. S. A. 1 (2013).

[27] K. Luther, K. Oum, and J. Troe, Phys. Chem. Chem. Phys. **7**, 2764 (2005).

[28] J. Guenther, D. Krankowsky, and K. Mauersberger, Chem. Phys. Lett. **324**, 31 (2000).

[29] H. Hippler, R. Rahn, and J. Troe, J. Chem. Phys. **93**, 6560 (1990).

[30] R.A. Marcus, in *Adv. Quantum Chem.* (2008), pp. 5–19.

[31] S. Chakraborty and S.K. Bhattacharya, J. Chem. Phys. **118**, 2164 (2003).

[32] A.S. Cole and K.A. Boering, J. Chem. Phys. **125**, 184301 (2006).

[33] A.A. Wiegel, A.S. Cole, K.J. Hoag, E.L. Atlas, S.M. Schauffler, and K.A. Boering, Proc. Natl. Acad. Sci. U. S. A. **110**, 17680 (2013).

[34] C.C.-W. Lee, J. Savarino, and M.H. Thiemens, Geophys. Res. Lett. **28**, 1783 (2001).

[35] G. Michalski, Z. Scott, M. Kabiling, and M.H. Thiemens, Geophys. Res. Lett. **30**, 1870 (2003).

[36] C.A.M. Brenninkmeijer and T. Röckmann, Anal. Chem. **68**, 3050 (1996).

[37] D. Hanson and K. Mauersberger, J. Chem. Phys. **85**, 4669 (1986).

[38] D. Krankowsky, P. Lämmerzahl, K. Mauersberger, C. Janssen, B. Tuzson, and T. Röckmann, J. Geophys. Res. **112**, 1 (2007).

[39] J.C. Ianni, *A Comparison of the Bader-Deuflhard and the Cash-Karp Runge-Kutta Integrators for the GRI-MECH 3.0 Model Based on the Chemical Kinetics Code Kintecus* (2003), pp. 1368–1372.

[40] J.C. Johnston, T. Röckmann, and C.A.M. Brenninkmeijer, J. Geophys. Res. **105**, 15213 (2000).

[41] J. Reader, C.J. Sansonetti, and J.M. Bridges, Appl. Opt. **35**, 78 (1996).

[42] P. Fleurat-Lessard, S.Y. Grebenshchikov, R. Schinke, C. Janssen, and D. Krankowsky, J. Chem. Phys. **119**, 4700 (2003).

[43] J.A. Kaye and D.F. Strobel, J. Geophys. Res. **88**, 8447 (1983).

[44] K. Yoshino, J.R. Esmond, A.S.-C. Cheung, D.E. Freeman, and W.H. Parkinson, Planet. Space Sci. **40**, 185 (1991).

[45] S.P. Sander, R.R. Friedl, J.R. Barker, D.M. Golden, M.J. Kurylo, G.E. Sciences, P.H. Wine, J.P.D. Abbatt, J.B. Burkholder, C.E. Kolb, G.K. Moortgat, R.E. Huie, and V.L. Orkin, JPL Publ. **10-6**, (2011).

[46] H. Okabe, *Photochemistry of Small Molecules* (1978), p. 431.

[47] S.A. Ndengué, F. Gatti, R. Schinke, H.-D. Meyer, and R. Jost, J. Phys. Chem. A **114**, 9855 (2010).

[48] M.-C. Liang, G.A.G. Blake, and Y.L.Y. Yung, J. Geophys. Res. **109**, D10308 (2004).

[49] J.A. Joens, J.B. Burkholder, and E.J. Bair, J. Chem. Phys. **76**, 5902 (1982).

[50] S.M. Dylewski, J.D. Geiser, and P.L. Houston, J. Chem. Phys. **115**, 7460 (2001).

[51] F. Kaufman and J.R. Kelso, J. Chem. Phys. **46**, 4541 (1967).